

Magazine of Civil Engineering

105(5), 2021

ISSN
2712-8172





ПОЛИТЕХ
Санкт-Петербургский
политехнический университет
Петра Великого

Инженерно-строительный институт
Центр дополнительных профессиональных программ
195251, г. Санкт-Петербург, Политехническая ул., 29,
тел/факс: 552-94-60, www.stroikursi.spbstu.ru,
stroikursi@mail.ru

**Приглашает специалистов организаций, вступающих в СРО,
на курсы повышения квалификации (72 часа)**

Код	Наименование программы	Виды работ*
Курсы по строительству		
БС-01-04	«Безопасность и качество выполнения общестроительных работ»	п.1,2, 3, 5, 6, 7, 9, 10, 11, 12, 13, 14
БС-01	«Безопасность и качество выполнения геодезических, подготовительных и земляных работ, устройства оснований и фундаментов»	1,2,3,5
БС-02	«Безопасность и качество возведения бетонных и железобетонных конструкций»	6,7
БС-03	«Безопасность и качество возведения металлических, каменных и деревянных конструкций»	9,10,11
БС-04	«Безопасность и качество выполнения фасадных работ, устройства кровель, защиты строительных конструкций, трубопроводов и оборудования»	12,13,14
БС-05	«Безопасность и качество устройства инженерных сетей и систем»	15,16,17,18,19
БС-06	«Безопасность и качество устройства электрических сетей и линий связи»	20,21
БС-08	«Безопасность и качество выполнения монтажных и пусконаладочных работ»	23,24
БС-12	«Безопасность и качество устройства мостов, эстакад и путепроводов»	29
БС-13	«Безопасность и качество выполнения гидротехнических, водолазных работ»	30
БС-14	«Безопасность и качество устройства промышленных печей и дымовых труб»	31
БС-15	«Осуществление строительного контроля»	32
БС-16	«Организация строительства, реконструкции и капитального ремонта. Выполнение функций технического заказчика и генерального подрядчика»	33
Курсы по проектированию		
БП-01	«Разработка схемы планировочной организации земельного участка, архитектурных решений, мероприятий по обеспечению доступа маломобильных групп населения»	1,2,11
БП-02	«Разработка конструктивных и объемно-планировочных решений зданий и сооружений»	3
БП-03	«Проектирование внутренних сетей инженерно-технического обеспечения»	4
БП-04	«Проектирование наружных сетей инженерно-технического обеспечения»	5
БП-05	«Разработка технологических решений при проектировании зданий и сооружений»	6
БП-06	«Разработка специальных разделов проектной документации»	7
БП-07	«Разработка проектов организации строительства»	8
БП-08	«Проектные решения по охране окружающей среды»	9
БП-09	«Проектные решения по обеспечению пожарной безопасности»	10
БП-10	«Обследование строительных конструкций и грунтов основания зданий и сооружений»	12
БП-11	«Организация проектных работ. Выполнение функций генерального проектировщика»	13
Э-01	«Проведение энергетических обследований с целью повышения энергетической эффективности и энергосбережения»	
Курсы по инженерным изысканиям		
И-01	«Инженерно-геодезические изыскания в строительстве»	1
И-02	«Инженерно-геологические изыскания в строительстве»	2,5
И-03	«Инженерно-гидрометеорологические изыскания в строительстве»	3
И-04	«Инженерно-экологические изыскания в строительстве»	4
И-05	«Организация работ по инженерным изысканиям»	7

*(согласно приказам Минрегионразвития РФ N 624 от 30 декабря 2009 г.)

**По окончании курса слушателю выдается удостоверение о краткосрочном повышении
квалификации установленного образца (72 ак. часа)**

Для регистрации на курс необходимо выслать заявку на участие, и копию диплома об образовании по телефону/факсу: 8(812) 552-94-60, 535-79-92, , e-mail: stroikursi@mail.ru.

Magazine of Civil Engineering

SCHOLAR JOURNAL

ISSN 2712-8172

Свидетельство о государственной регистрации:
Эл № ФС77-77906 от 19.02.2020,
выдано Роскомнадзором

Специализированный научный журнал.

Выходит с 09.2008.

Включен в Перечень ВАК РФ

Индексируется в БД Scopus

Периодичность: 8 раз в год

Учредитель и издатель:

Санкт-Петербургский политехнический университет
Петра Великого

Адрес редакции:

195251, СПб, ул. Политехническая, д. 29

Главный редактор:

Екатерина Александровна Линник

Научный редактор:

Виталий Владимирович Сергеев

Заместитель главного научного редактора:

Галина Леонидовна Козинец

Редакционная коллегия:

PhD, проф. Т. Аввад;
д.т.н., проф. М.И. Бальзанников;
д.т.н., проф. А.И. Белостоцкий;
к.т.н., проф. А.И. Боровков;
д.т.н., проф. А. Бородинец;
PhD, проф. М. Велькович;
PhD, проф. Р.Д. Гарг;
PhD, М.Р. Гарифуллин;
Dr.-Ing, проф. Т. Грис;
д.т.н., проф. Т.А. Дацюк;
д.т.н., проф. В.В. Елистратов;
Dr.-Ing., проф. Т. Кэрки;
д.т.н., проф. Д.В. Козлов;
д.т.н., доцент С.В. Корниенко;
д.т.н., проф. Ю.Г. Лазарев;
д.т.н., проф. М.М. Мухаммадиев;
Dr.-Ing. Habil., проф. Х. Пастернак;
Dr.-Ing., проф. Ф. Рёгинер;
д.т.н., проф. Т.З. Султанов;
д.т.н., проф. М.Г. Тягунов;
акад. РАН, д.т.н., проф. М.П. Федоров;
Dr.-Ing., проф. Д. Хеэцк;
д.г.-м.н. А.Г. Шашкин;
д.т.н. В.Б. Штильман

Дата выхода: 24.09.2021

© ФГАОУ ВО СПбПУ, 2021

© Иллюстрация на обложке: Илья Смагин

Magazine of Civil Engineering

SCHOLAR JOURNAL

ISSN 2712-8172

Peer-reviewed scientific journal

Start date: 2008/09

8 issues per year

Publisher:

Peter the Great St. Petersburg Polytechnic University

Indexing:

Scopus, Web of Science (ESCI, RSCI), Compendex,
EBSCO, Google Academia, Index Copernicus, ProQuest,
Ulrich's Serials Analysis System, CNKI

Corresponding address:

29 Polytechnicheskaya st., Saint-Petersburg, 195251,
Russia

Editor-in-chief:

Ekaterina A. Linnik

Science editor:

Vitaly V. Sergeev

Deputy chief science editor:

Galina L. Kozinetc

Editorial board:

T. Awwad, PhD, professor
M.I. Balzannikov, D.Sc., professor
A.I. Belostotsky, D.Sc., professor
A.I. Borovkov, PhD, professor
A. Borodinecs, Dr.Sc.Ing., professor
M. Veljkovic, PhD, professor
R.D. Garg, PhD, professor
M. Garifullin, PhD, postdoctorant
T. Gries, Dr.-Ing., professor
T.A. Datsyuk, D.Sc., professor
V.V. Elistratov, D.Sc., professor
T. Kärki, Dr.-Ing., professor
D.V. Kozlov, D.Sc., professor
S.V. Korniyenko, D.Sc., professor
Yu.G. Lazarev, D.Sc., professor
M.M. Muhammadiev, D.Sc., professor
H. Pasternak, Dr.-Ing.habil., professor
F. Rögener, Dr.-Ing., professor
T.Z. Sultanov, D.Sc., professor
M.G. Tyagunov, D.Sc., professor
M.P. Fedorov, D.Sc., professor
D. Heck, Dr.-Ing., professor
A.G. Shashkin, D.Sc.
V.B. Shtilman, D.Sc.

Date of issue: 24.09.2021

© Peter the Great St. Petersburg Polytechnic University.

All rights reserved.

© Coverpicture – Ilya Smagin

Contacts:

E-mail: mce@spbstu.ru

Web: <http://www.engstroy.spbstu.ru>

Contents

Al-Rousan, R. The impact of depth on shear behavior of strengthened beams	10501
Babafemi, A.J., Akinola, O.T., Kolawole, J.T., Paul, S.C., Miah, M.J. Effect of sawdust ash and laterite on the electrical resistivity of concrete	10502
Galishnikova, V.V., Elroba, S.H., Nassar, M., Sakna, A. Self-healing bacterial mortar with calcium lactate and improved properties	10503
Abid, S.R., Ali, S.H., Goaiz, H.A., Al-Gasham, T.S., Kadhim, A.L. Impact resistance of steel fiber-reinforced self-compacting concrete	10504
Bashir, M.T., Daniyal, M., Alzara, A., Elkady, M., Armghan, A. Self-sensing cement composite for traffic monitoring in intelligent transport system	10505
Fedotov, A.A., Vahnina, T.N., Susoeva, I.V. Resistance to temperature and humidity changes of construction plywood and thermal-insulation boards	10506
El-Nadoury, W.W. Production of sustainable concrete using sawdust	10507
Basri, K., Zainorabidin, A., Mohamad, H.M., Musta, B. Determining the peat soil dynamic properties using geophysical methods	10508
Kaldar-ool, A-Kh.B., Glukhikh, V.N., Opbul, E.K., Saaya, S.S. Stress condition of brick barrel vaults in view of anisotropic properties	10509
Kozhurova, A.V., Shipilov, A.V. Assessment of wave impact on hydraulic structures of the Flood Prevention Facility Complex of St. Petersburg obtained from field observations	10510
Sprince, A., Gailitis, R., Pakrastins, L., Kozlovskis, T., Vatin, N. Long-term properties of cement mortar under compression, tension, and 3-point bending	10511
Koyankin, A.A., Mitsov, V.M. A deformed state of the composite frame with phased installation	10512
Kabantsev, O.V., Perelmuter, A.V. Plastic behavior particularities of structures subjected to seismic loads	10513
Gravit, M.V., Dmitriev, I.I. Thin-walled compressed steel constructions under fire load	10514



DOI: 10.34910/MCE.105.1

The impact of depth on shear behavior of strengthened beams

R. Al-Rousan 

Jordan University of Science and Technology, Irbid, Jordan

E-mail: rzalrousan@just.edu.jo

Keywords: reinforced concrete, beam depth, shear, flexural strength, fiber reinforced polymer, nonlinear, finite element analysis

Abstract. The main aim of this work is to investigate the influence of the beam's depth on the behavior of the externally-strengthened-with-CFRP beams, having shear deficiency. The Nonlinear Finite Element Analysis (NLFEA) has been utilized to construct and validate study models, which had been subjected to load till failure aiming to monitor their performance. Also, the cracking's first appearance, the increase rate of cracking according to loadings, and ductility were all put to observation. The NLFEA results indicated that strengthening the RC beams with externally-bonded CFRP enhanced the beams' shear capacity, in accordance to the study parameters. The strips of CFRP enhanced the beam's ultimate load by 15–19 %. In the NLFEA modelled beams, it had been noticed that the more the beam's depth, the less the shear span-to-depth ratio; as that ratio was 2.7 at a depth of 225 mm, where the ratio became 1.2 at a depth of 450 mm. The depth, of strengthened and control beams, was more influential on the beam's ultimate load than the resultant deflections. Also, the attained findings pointed out that the RC beam's depth had affected the cracking angle; as it was: 33°, 44°, 50°, and 54° at a beam's shear span-to-depth ratio of: 2.7, 1.9, 1.5, and 1.2, respectively. Had a shear crack exceeded the length of a CFRP strip, the stirrup would fail to get to its yield strength. In this case, the influence of the beams' depth is limited. Finally, the obtained NLFEA results were evaluated by comparing them to well-known shear strength models.

1. Introduction

For RC beams, the depth of the beam is directly proportional to the shear span. In other words, an increase in the beam's depth results in the shear capacity. It is a common, recommended even, that upon designing RC beams, and the shear capacity must exceed the flexural capacity, to prevent the occurrence of brittle shear failure. Nevertheless, any RC beam could become subjected to lose its shear capacity when it encounters a big variation in the applied loads or steel corrosion, caused by inadequate covering of concrete. Another reason for the RC beam to lose its shear capacity is when it is strengthened in bending. In the light of the lingering issues of RC beams' structural shear capacity and resistance, there must be further researching to come up with proper solutions.

Concrete structures (for example: buildings, bridge decks, girders, offshore structures, parking lots) are subjected to be harmed or damaged because of: improper maintenance, steel corrosion, ageing, faulty design or construction, additional excessive loading such as heavy traffic, the seismic movements, and harsh environmental condition. Due to the old codes of design, or not abiding by the new ones as in some countries, many structures are endangered, and need to be strengthened and/or rehabilitation [1]. It has been reported that 23 % of the concrete bridges in the USA are deficient or not in service [2].

Deficient structure can be repaired or demolished. However, the latter could cause damages, sometimes severe, to the adjacent structures, causing financial losses. Therefore, the need arises to find adequate techniques and materials to strengthen and/or repair such structures. The strengthening

Al-Rousan, R. The impact of depth on shear behavior of strengthened beams. Magazine of Civil Engineering. 2021. 105(5). Article No. 10501. DOI: 10.34910/MCE.105.1

© Al-Rousan R., 2021. Published by Peter the Great St.Petersburg Polytechnic University.



This work is licensed under a CC BY-NC 4.0

technique of bonding, externally, carbon-fiber reinforced polymer (CFRP) laminates has been widely adopted to repair, strengthen, and rehabilitate deficient or damaged structure [3–6]. The externally-bonded CFRP technique extends the structural life span and serviceability, and decreases the cost and time of maintenance. A great number of researches have highlighted the efficiency of the CFRP material in enhancing the structural flexural strength. When enduring excessive loads, an adequately-designed RC beam possesses a flexural strength enough to guarantee having a flexural failure mode, which is brittle and ductile. Therefore, RC beams must be availed with a satisfactory margin of safety to withstand more critical, sudden modes of failure, such as shear failure. RC beams must be strengthened to improve their shear capacity; and this capacity must be examined upon strengthening a beam in flexure. It is worth mentioning that RC beams shear failures could be disastrous. When overloading a deficient-in-shear-strength RC beam, an abrupt shear failure is likely to take place, with no pre-warning; unlike the flexural failure, which is not sudden in nature, and is preceded by big cracks and deflections, as pre-warnings. Further, the shear failure mode lessens the structural strength, to a limit less than the flexural capacity, resulting in a significant decrease in ductility. Therefore, it is imperative to enhance the shear capacity of RC beams by proper means of shear strengthening to make sure that the beam's failure mode is the ductile flexural. Among the various types of the fiber-reinforced polymers (FRP) materials, the CFRP one is the most advantageous for its high tensile strength and remarkable fatigue characteristics. FRP materials are widely utilized to rehabilitate and strengthen actually-standing RC structures. That is because these materials have great features, as they are: durable, flexible, ductile, resistant to corrosion, easy to shape and erect, high strength-to-weight ratio, and remarkably resistant to fatigue; making this material highly desired in many RC applications, for example: beams, slabs and columns [3–5]. These properties have made it possible to prolong the life span and the serviceability of structures [1]. The RC structures, commonly, fail or be defected in shear or flexure. Between these two, the deficiency in shear is way more serious because it occurs in sudden, without giving the element the chance to deal with the developed internal stresses. The shear failure could be due to improper designing, reduction in shear reinforcement (RFT) that is caused by steel corrosion or overloading. It has been evident that the use of externally-bonded FRP material's efficiency, in enhances the shear capacity [7–11], is governed, mainly, by its: tensile strength, the ratio of shear reinforcement, the used configuration. In addition, the FRP's efficiency is also affected by: the inclination angle of shear cracks, the concrete's compressive strength, and the yield strength of both the shear reinforcement and steel bars, adding to its ratio of tensile reinforcement. Reinforcing RC structural elements with externally-bonded FRP has been the focus of many researches [12–14]; as several analytical investigations have been carried out to study the strengthened RC beams' shear performance [15–20]. According to these studies, the ultimate shear capacity, of strengthened RC beams, is controlled by; the strength of concrete, the adequacy of steel, and the material's type of the FRP materials.

Although the abundant studies related to the shear behavior of RC beams, there is so little information about the depth of beams, upon the beams' overloading and failure; as this information elaborates the factual condition of the developed stress, the changes of actions, and the mechanisms upon loading. Such information is, urgently, required to better understand the resistance of the concrete and laminates to shear. Further, the detailed formation and distribution of developed strains, throughout the length of the transverse and longitudinal reinforcement, can be employed to adjust the finite element modelling, particularly the bonding adequacy. Keeping in mind the fact that the structural shear strength is formed by the total internal actions together. It is imperative for the numerical model to avail the actual value of each internal action by itself. Hence, this research introduces a new approach that consists of erecting, externally, the CFRP sheets on RC beams that were different in depth. The main aim, of this study, is to examine the influence of shear span-to-depth (a/d) ratio of externally-strengthened-with-CFRP RC beams on the structural shear strength. To achieve this aim, the nonlinear finite element analysis (NLFEA) method has been utilized. The study investigated the impacts of 4 main methods of strengthening, namely: 1) RC beams with a depth of 225 mm (shear span-to-depth ratio of 2.7) strengthened externally with CFRP composite at a spacing of 100 mm, center to center; 2) RC beams with a depth of 300 mm (shear span-to-depth ratio of 1.9) strengthened externally with CFRP composite at a spacing of 100 mm, center to center; 3) RC beams with a depth of 375 mm (shear span-to-depth ratio of 1.5) strengthened externally with CFRP composite at a spacing of 100 mm, center to center; and 4) RC beams with a depth of 450 mm (shear span-to-depth ratio of 1.2) strengthened externally with CFRP composite at a spacing of 100 mm, center to center. Eight models have been built and experimented under four points loading. According to the experimental findings of Shbeeb et al. [21], the models of this research were validated after they had been simulated, utilizing the ANSYS software. The parameter of this study was the depth of the RC beam models.

2. Methods

The NLFEA method is adopted to analyze complicated designs of structures, effectively; as this method is operated on virtual structures, which allows the user to study the effect of any parameter, leading to considerable savings in efforts, time, and cost. Also, this method enables the user to alter any setting or

variable to explore its effect on the structure. Also, it facilitates the ability to record the resultant values, due to the change of load levels, of stresses, strains, and displacements, at any point. To examine the influence of various parameters, six full-scale, strengthened-with-CFRP models were modelled.

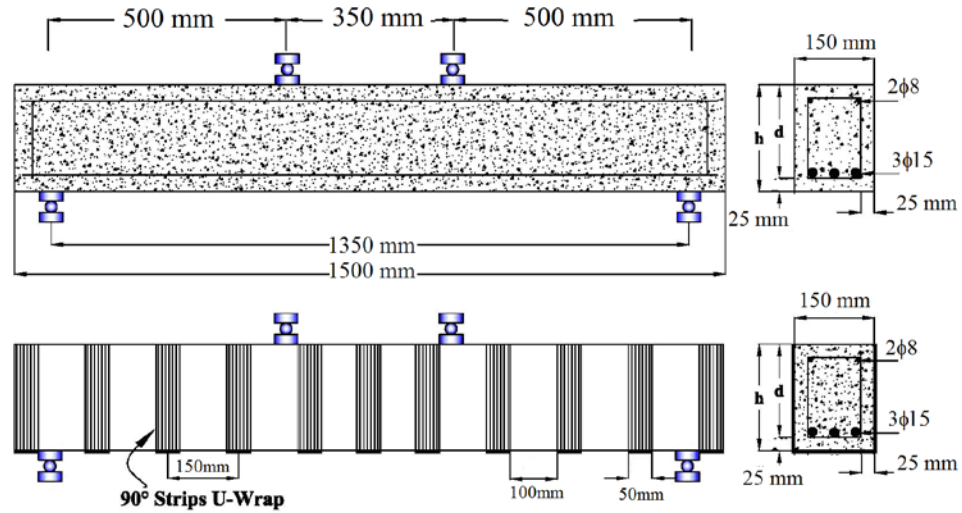


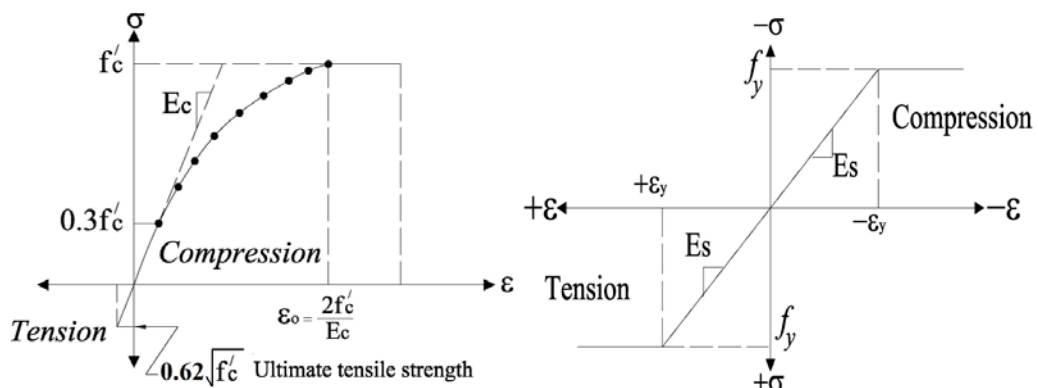
Figure 1. Setup and reinforcement details of the beams [21].

2.1. Experimental Work Review

The finite element models were validated in accordance with the study carried out by Shbeeb et al. [21]. Highly-strengthened RC beams were constructed, dimensioned as 100×150×1400 mm, without being reinforced in shear. Stirrups were put in the zone of constant moment, for the ease of placing the flexural reinforcement, availing a proper concrete confinement, as illustrated in Fig. 1. The experimental specimens consisted of 22 rectangular RC beams, with dimensions of 150×225 mm and a total length of 1500 mm. The top side of the specimens was reinforced with 2φ8 bars, 3φ15 bars at the lower side, and with stirrups of φ8 located at 250 mm, center to center, throughout the beams' total length. The design variables were set to make sure that shear failure would take place within the beams. Four of the specimens were left un-strengthened to be the control, or reference, beams; while the remaining 22 specimens were strengthened with CFRP strips and sheets, in various schemes (Fig. 1). A specially-designed, built-up rigid steel frame was employed to test the specimens, as simply supported. Also, a hydraulic jack was utilized to add an extensive load, within a hydraulic cylinder, to a spread steel beam, so as to generate a two-point loading state, to create an area of constant moment, at mid-span.

2.2. Description of Non-linear Finite Element Analysis (NLFEA)

Concrete seems to be a brittle material, and does not exhibit the same behavior, in compression and tension. SOLID65 was used because it can predict, utilizing the smeared crack approach, the concrete's: nonlinear behavior, failure mode, in addition to the failure in crushing as well as in cracking. To determine the concrete surface failure mode, both the ultimate uniaxial tensile and compressive strengths need to be specified. Hence, it was possible to compute for the default value of the multi-axial stress states that cause concrete failure. For all the specimens: the Poisson's ratio was made 0.2, as most of the previous studies used a value between 0.05 and 0.25; the shear transfer coefficient (β_t) was in the range from 0.0 (no shear transfer) to 1.0 (complete shear transfer). The concrete, used in this work, had a compressive strength of 55 MPa, and an initial young's modulus (E_c) of 35063 MPa.



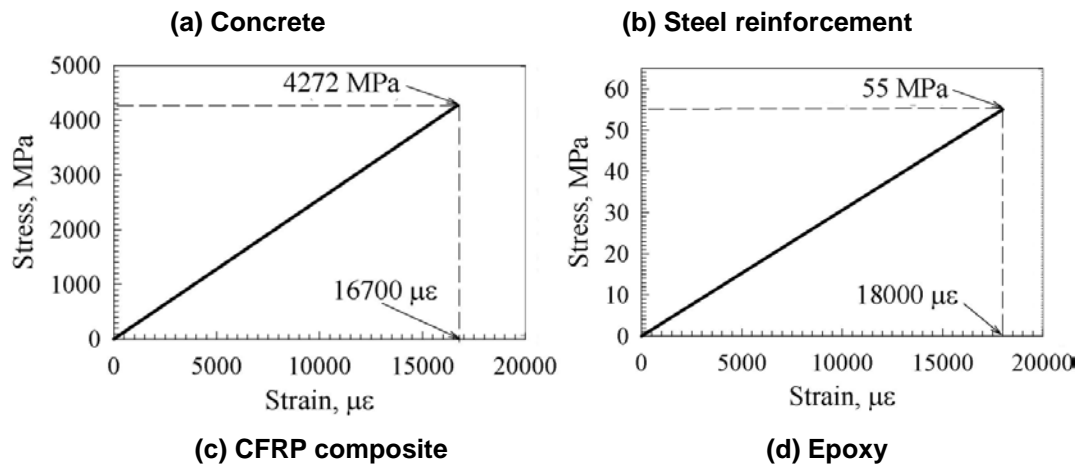


Figure 2. Stress-strain curves [21].

Prior to the point of the ultimate tensile strength, the concrete's stress-strain curve was presumed linear and elastic. Then, cracks emerged in concrete and the strength dropped down, drastically, reaching to zero (Fig. 2). The designed finite element models were reinforced with, presumably an elastic-perfectly plastic, steel, having the same behavior in tension as well as compression. The steel's Poisson's ratio was 0.3, and its yield stress was 413 MPa. Good results were attained upon utilizing the 3D LINK180 uniaxial tension-compression spar in the simulation of the steel reinforcement, separately, to make it possible to predict: the impact of plasticity, huge and rotational stains, and deflections. Fig. 5-2b depicts the relation between the stress and the strain. The two beam's ends were reinforced with steel plates to avail a better distribution of stresses over the support regions. These plates were presumed linearly-elastic, with a modulus of elasticity of 200 GPa, and the Poisson's ratio of 0.3. The SOLID46 element had been used in preparing the adhering material (epoxy) and the, presumably orthotropic, CFRP laminates. The CFRP material had: a thickness of 0.165 mm, a tensile strength of 3790 MPa, an elastic modulus of 228 GPa, and an ultimate tensile strain of 0.017 mm/mm. As the epoxy, it had a thickness of 0.343 mm, the ultimate tensile strength was 55 MPa, the modulus of elasticity of 30 GPa, and the ultimate tensile strain of 0.018 mm/mm. When perpendicular to the direction of the fiber, the CFRP's modulus of elasticity was assumingly 10^{-6} of the main direction. Both the epoxy and the sheets of CFRP had assumingly linearly-elastic characteristics.

The total amount of the exerted load was split to a several load increments; each of which was subjected to the Newton–Raphson equilibrium iterations to be availed with a convergence at its ends, with a tolerance of 0.001. The maximum and minimum sizes of each Load increment were specified, automatically, by ANSYS. As it is stipulated, the concrete structure endures cracking when the main tensile stress is not located inside the failure surface, regardless the direction. Post cracking, the concrete's modulus of elasticity becomes zero, parallel to the prime tensile stress. Concrete crushing takes place, out of the failure surface, when all of the main stresses are compressive. Consequently, the element vanishes and the elastic modulus is set to zero, in all directions. When the concrete's capability of crushing is on, the finite element model fails, in an impulsive manner. Once the concrete's crushing began, it extended in of the areas exposed to direct loads. Then, the neighboring concrete structural elements crushed, as well, leading to a significant decrease in the local stiffness. Lastly, the model exhibited a huge displacement, where the solution diverged. In consequence, the crushing capability was off, and concrete cracking controlled the models' failure. While the concrete was cracking and the emergence of so many cracks, the loads were added, step by step, with smaller increments of load. The models' failure occurred when the load increment of 0.0045 kN did not converge.

CONTA174 element was used to prepare the concrete-epoxy bonding layer. This element is an 8-node element used for analysis in the cases of the general rigid-flexible and flexible-flexible contact. In the general analysis of a contact between two materials or more, the area of contact area cannot be specified in advance. Also, the CONTA174 element is viable for 3-D geometries, and the contact area between solid shells or bodies. Lu et al. [22] introduced the most reliable model of bond stress slip, valid to be included into the finite element analysis. The mechanical behavior of the FRP-concrete bond is described by the relationship between the local shear stress (τ) and the relative displacement (s). In addition, the authors suggested three simplified bond slips, sorted as per their sophistication level, namely: the precise, the simplified, and the bilinear. In the current study, the simplified model (Fig. 3) was adopted for its simplicity.

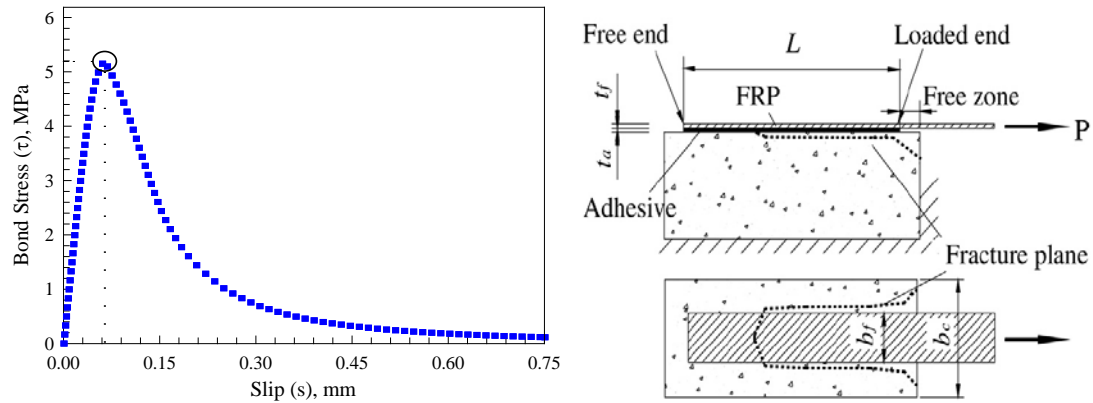


Figure 3. CFRP to concrete bond slip model [22].

The volume-mapped command was utilized to construct rectangular and square structural elements, for the rectangular volumes (concrete, CFRP, epoxy, and steel plates). This facilitates the setting of the steel's length and width to suit the concrete nodes and elements. The suitable mesh density was specified by a convergence study (Fig. 4). Each element was modelled; whereas, the essential concrete meshing measurements were set before the creation of every reinforcement section. The SOLID46 elements, for CFRP and epoxy, had a mesh the same as SOLID65 ones, to ensure that the concrete nodes were allocated over the nodes of each element.

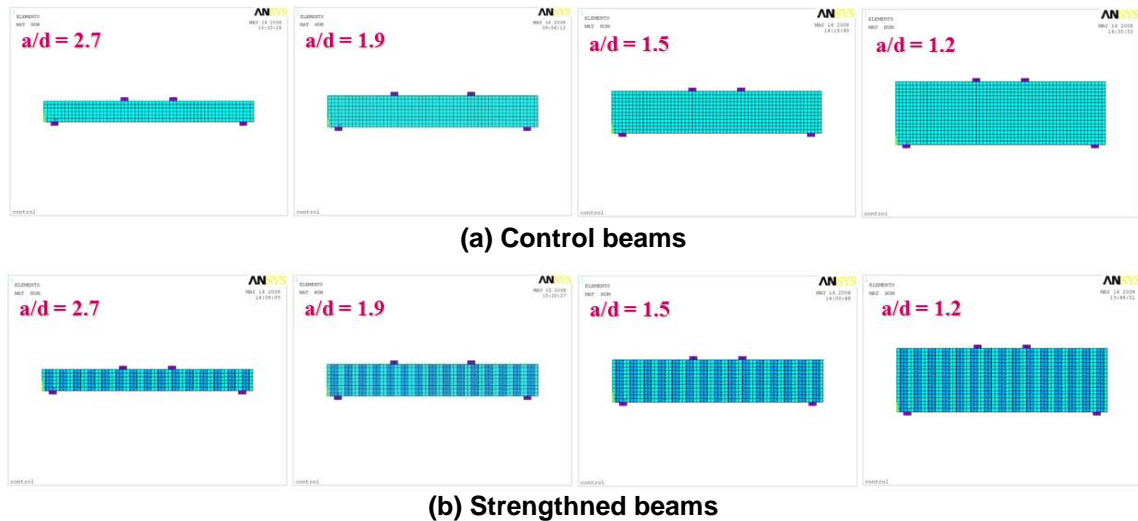


Figure 4. Typical finite element meshing of the beams.

The command merge item has been utilized to merge separate entities that are located in the same place, into a single entity. To make sure that the modeling process was done properly, the displacement boundary conditions had been set before they were used at the planes of symmetry; where these planes could be designated by the nodes that defined a certain plane across the beam's cross-sectional section, at the beam's center. To permit the beam to move around the support, a hinge and a roller were installed at the support. The force was exerted throughout the length of the steel plate's centerline. The analysis of the specimens was carried out by simulating a 4-point loading case, at a distance of 550 mm, between the two loading points. The total load had been split to small increments of load, each of which was 0.45 kN. The modified Newton–Raphson equilibrium iterations were utilized to monitor the convergence at every increment's end, with a tolerance margin of 0.001. In order to investigate the specimens' behavior, the static analysis type was used. The model failure took place when the solution of the load increment of 0.0045 kN failed to converge.

2.3. Validation Process

Fig. 5 depicts the load-deflection curves that represent the behavior of both the experimental and NLFEA. Considering Fig. 5, the curves indicated that, for the strengthened specimens, consisted of straight segment indicating the no cracking stage (or pre-cracking); then, there was a variation in the curve's slope, indicating the emergence of cracks (or after-cracking). Continuing raising the exerted load, the strengthened-with-CFRP beams experienced a shear failure, prior to the ultimate flexural capacity limit, as a result of the de-bonding of the CFRP-concrete bond.

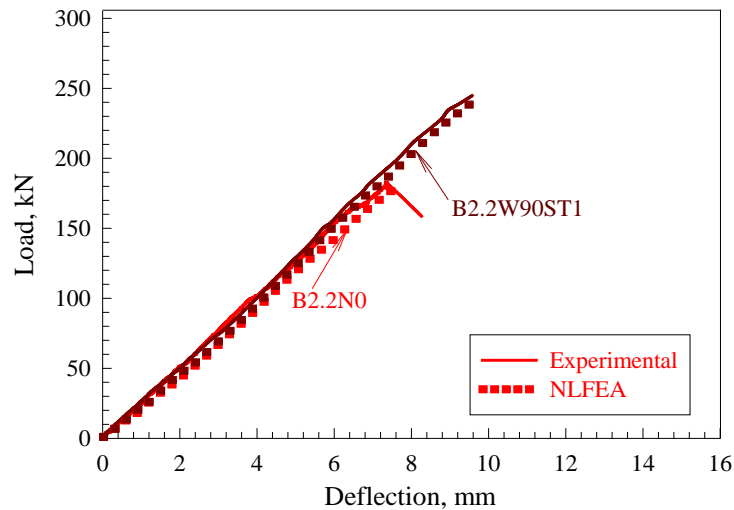


Figure 5. Experimental [21] and NLFEA load-deflection curves.

Referring the obtained values, of the control and strengthened specimens' ultimate strengths and the resultant increase in the ultimate shear strength, indicated that the shear-deficient beams' performance improved due to the CFRP laminates. Considering Fig. 5, the curve of load vs mid-span displacement showed a big agreement between the results of the NLFEA and the experimental ones (with a margin of less than 5 %), when exerting low and high loads. However, at medium loads, there was a slight deviation. This is substantiated by the slight difference between the experimental and the NLFEA's ultimate load, whatever configuration was used. Fig. 6 illustrates typical stress contours of the control and strengthened beams.

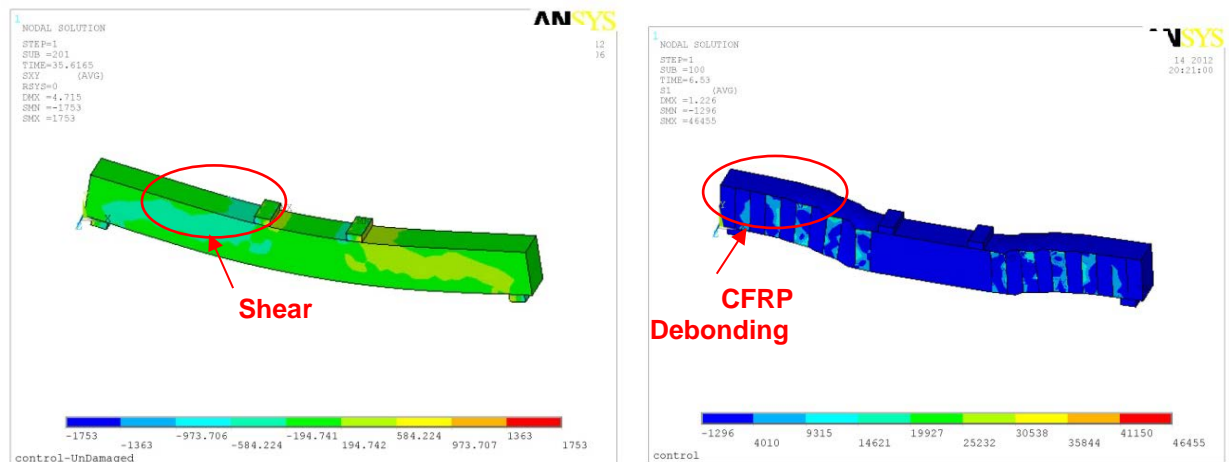


Figure 6. Typical NLFEA stress contours of NLFEA beams.

3. Results and Discussion

3.1. Failure Mode

The control, with no reinforcement, beam specimens had the first flexural crack at the beam's center; later, many cracks appeared away from the mid-section. While raising the exerted load, one of the following cases occurred: either a flexural crack stretched diagonally close to either support, or a diagonal crack emerged suddenly at the beam's mid height, in the shear span region. After the emergence of the diagonal crack, the specimen had a splitting failure, across the tension reinforcement. The mode's type of the ultimate failure was determined by the a/d ratio, and it was either shear or flexural. A representative cracking pattern for the control beams is shown in Fig. 7.

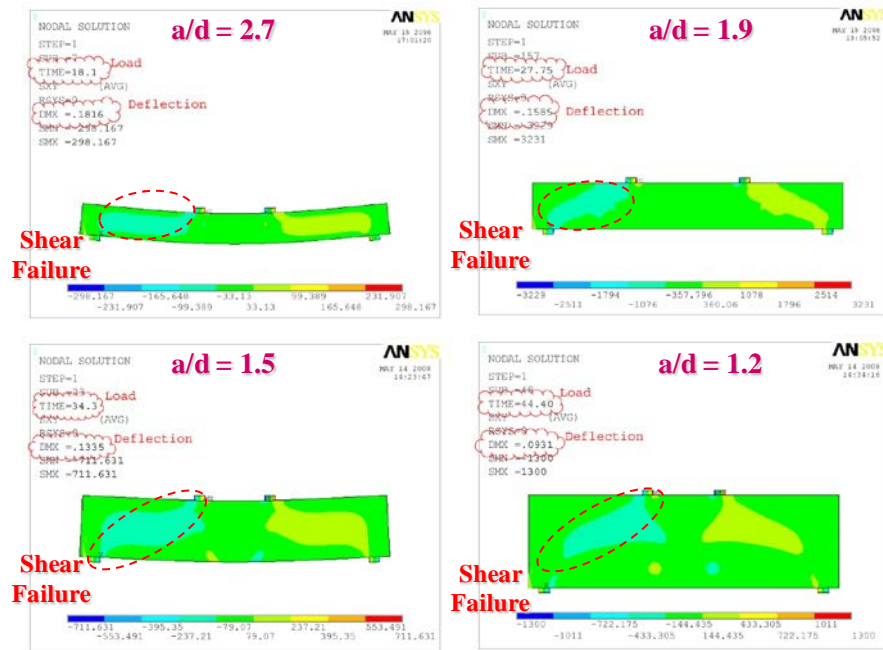


Figure 7. Typical NLFEA stress contours of control NLFEA beams.

Fig. 8 depicts the patterns of cracking of the strengthened NLFEA beam with a/d of 2.7. At a load of 34.2 kN, the first emergence of flexural crack was at the beam's center, inside the constant moment zone. At higher loads, the cracks stretched towards the top fiber; then, more cracks developed, along the length of the beam. At 112.5 kN of load, a shear crack – with an angle of 33° – appeared, not related to the previous ones, at the shear span's center. It was noticed that the strip No. 4 de-bonded at 139.2 kN, followed by strip No. 3 at 142.8 kN. At a load of 146.0 kN, strip No.5 de-bonded, leading to complete failure of the beam, as explicated in Fig. 4 and Table 1. De-bonding is a term that describes the de-lamination of the strip of the CFRP-concrete bond, caused when the bonding strength is higher than the developed stresses, at the end of the strip. Fig. 8 illustrates the patterns of cracking, exhibited by the strengthened NLFEA beam that had an a/d of 1.9. The very first flexural crack emerged at a load of 42.3 kN, at the beam's center, inside the area of constant moment. At a higher load, cracks stretched in the direction of the top fiber. Then, more flexural cracks appeared along the beam. At a load of 124.5 kN, a shear crack, angled at 44° , emerged, not related to the earlier ones, at the shear span's center. The strip No. 4 began to de-bond at 245.0 kN, followed by strip No. 5 at 246.0 kN; then strip No. 2 – closest to the support – de-bonded at a load of 247.2 kN, leading to the beam's shear failure, as illustrated in Fig. 8 and Table 1.

Table 1. The details, ultimate load and mode of failure of NLFEA shear beams.

Beam Designation	h , mm	d , mm	a/d	Type of Strengthening	Ultimate load, kN	Failure mode
B2.7N0	225	185	2.7	None	127.3	Shear failure followed by 33° diagonal crack
B1.9N0	300	263	1.9	None	213.2	Shear failure followed by 44° diagonal crack
B1.5N0	375	333	1.5	None	248.4	Shear failure followed by 50° diagonal crack
B1.2N0	450	417	1.2	None	403.2	Shear failure followed by 54° diagonal crack
B2.7U90ST1	225	185	2.7	Strip@ 90° U-wrap	146.0	Shear failure followed by 33° diagonal crack and debonding of CFRP sheets
B1.9U90ST1	300	263	1.9	Strip@ 90° U-wrap	247.2	Shear failure followed by 44° diagonal crack, debonding of CFRP sheets, and ripping of concrete
B1.5U90ST1	375	333	1.5	Strip@ 90° U-wrap	294.2	Shear failure followed by 50° diagonal crack, debonding of CFRP sheets, and ripping of concrete
B1.2U90ST1	450	417	1.2	Strip@ 90° U-wrap	475.1	Shear failure followed by 54° diagonal crack, debonding of

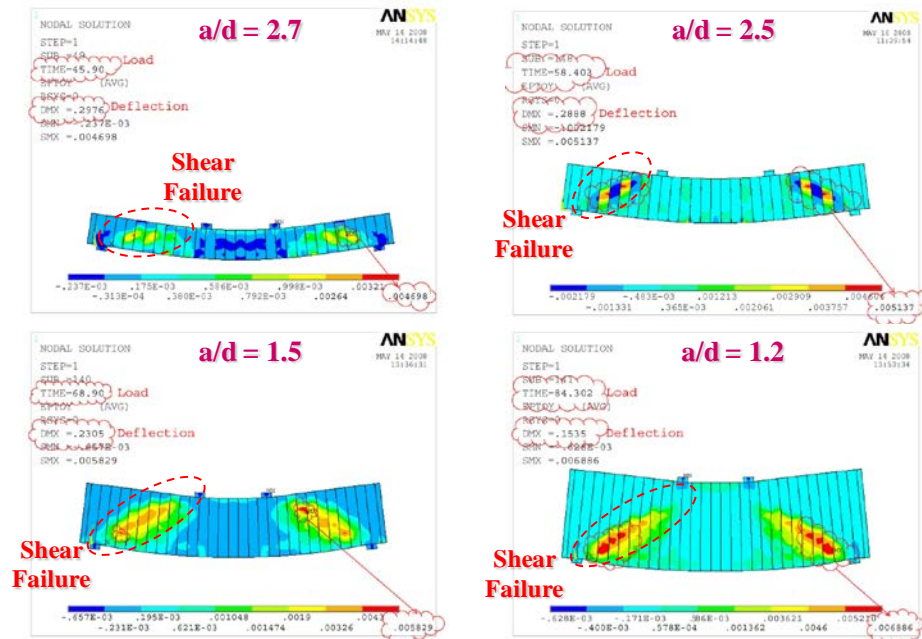


Figure 8. Typical NLFEA stress contours of strengthened NLFEA beams.

Fig. 8 illustrates the cracking patterns, exhibited by the strengthened NLFEA beam, with an a/d ratio of 1.5. The very first emergence of flexural cracks was at a load of 51.6 kN, at the beam's center, in the zone of constant moment. Beyond 51.6 kN, the cracks stretched in the direction of the top fiber. Later, more cracks appeared throughout the length of the beam. At 133.4 kN of load, a shear crack, with an angle of 50° , emerged by itself, in the shear span's center. Upon incrementing the load, the strip No. 4 de-bonded at a load of 287.6 kN, followed by strip No. 5 at 293.4 kN. The beam experienced a shear failure at 294.2 kN, as illustrated in Fig. 8 and Table 1.

Fig. 8 illustrates the cracking patterns exhibited by the strengthened NLFEA beam, with an a/d ratio of 1.2. The first flexural crack appeared at a load of 84.5 kN, at the beam's center, in the zone of constant moment. When exceeding that load, cracks stretched to the top fiber; while, more flexural cracks appeared, along the beam. At a load of 164.6 kN, a shear crack, with an angle of 54° , appeared, separately, at the shear span's center. The strip No. 4 de-bonded at a load of 465.0 kN, followed by strip No. 5 at 475.8 kN. When the load was at 475.1 kN, the beam had a shear failure, as explicated in Fig. 8 and Table 1.

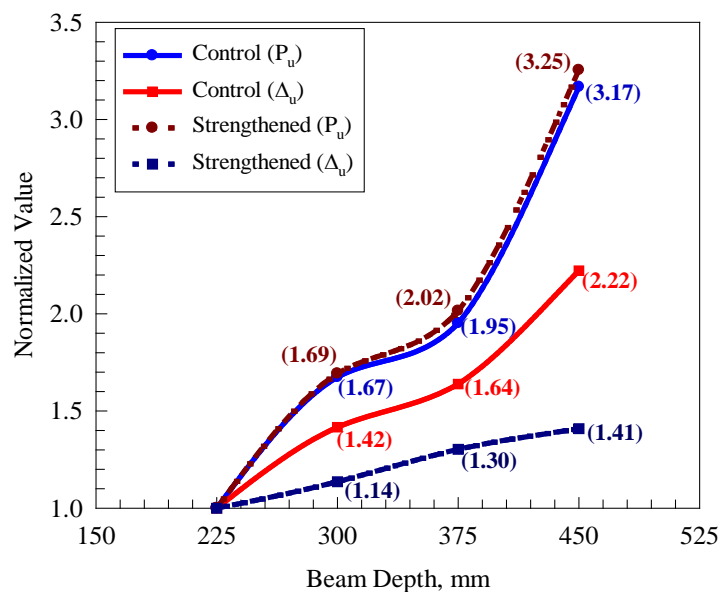


Figure 9. The normalized ultimate load and deflection with respect to control beam.

3.2. Ultimate load capacity

Fig. 9 depicts the strengthened beams' modified ultimate loads and deflections, according to the control beam, having a depth of 225 mm. Referring to Fig. 9, the control beam's ultimate load capacity raised by: 69 %, 102 %, and 225 %, when the depth of the beam increased by: 33 % (300 mm), 67 % (375 mm), and 100 % (450 mm), respectively. The depth's impact on the ultimate load was the same for the strengthened and the control beams. Also, Fig. 9 illustrates that the ultimate deflection, exhibited by the control beams, was higher by: 42 %, 64 %, and 122 %, when the depth was raised by: 33 % (300 mm), 67 % (375 mm), and 100 % (450 mm), respectively. Further, the beam depth's influence on the strengthened beams' ultimate deflection was the same as on the control ones, with enhancement percentages of: 14 %, 30 %, and 41 %, at depths of: 300 mm, 375 mm, and 450 mm, respectively.

3.3. Load-deflection behavior

Fig. 10 illustrates the curves of load vs deflection, for the NLFEA beams. All of the strengthened beams had, nearly, a liner relation between the load and deflection, up to the load of: 129.9, 201.1, 222.8, and 389.2 kN, the same as the failure loads of the beams: B2.7N0, B1.9N0, B1.5N0, and B1.2N0, respectively. This was an indicator that the CFRP conveyed the load after the diagonal shear had developed. Fig. 10 depicts that the beams' ultimate load capacity and beams' stiffness were higher when the effective depth was increased. That was observed by monitoring the angle of rotation, during the elastic phase of the curve, regarding the NLFEA beams. Also, Fig. 10 indicates that the beams' ductility enhanced with the width increase of the anchoring system, which reflected, precisely, the failure mode.

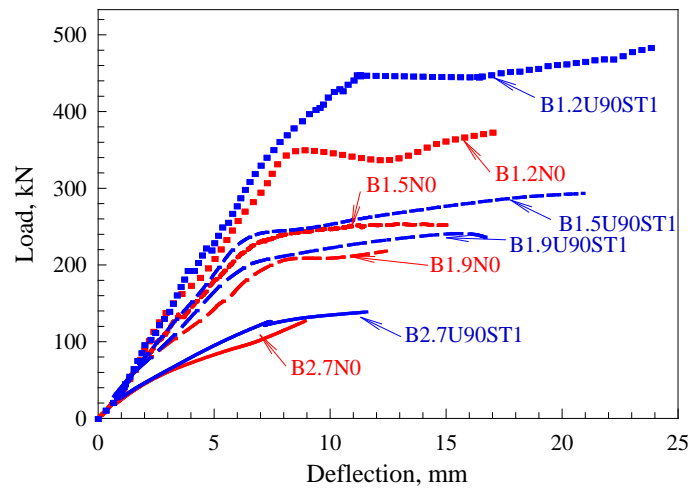


Figure 10. NLFEA load-deflection curves.

3.4. Concrete compressive strain

Fig. 11 depicts the relationship of the NLFEA beam's load and the compressive strain of concrete. Inspecting Fig. 11, it is shown that increasing the beam's effective depth (d) resulted in a rise in the concrete's compressive strength and strain, as well. In general, the highest level of strain was in the strengthened RC beam (B1.2U90ST1).

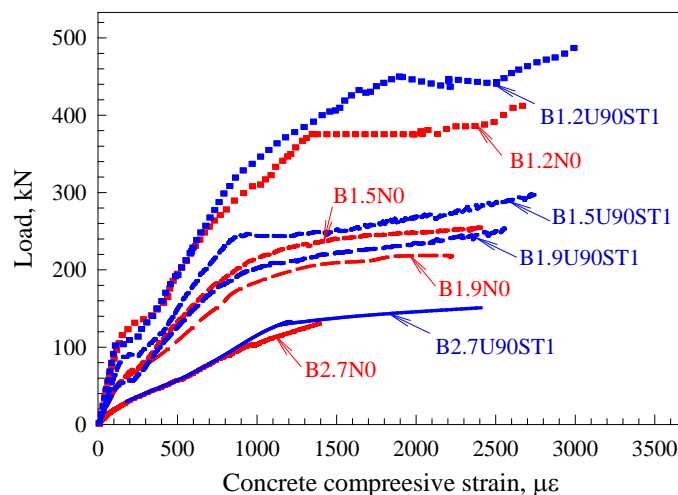


Figure 11. NLFEA load-concrete compressive strain curves.

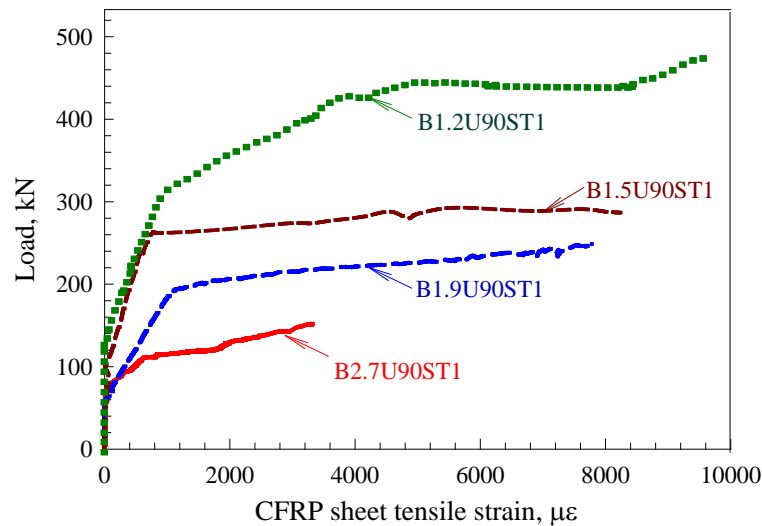


Figure 12. NLFEA load- steel tensile strain curves.

3.5. Steel tensile strain

For NLFEA beams, the curves, that represents the relation between the exerted load and the tensile strain of CFRP sheet, are illustrated in Fig. 12. The curves indicated the emergence of the sheet's tension strain occurred after the formation of the diagonal shear crack, at load levels of: 77.0, 78.3, 79.2, and 84.5 kN, for the beams: B2.7U90ST1, B1.9U90ST1, B1.5U90ST1, and B1.2U90ST1, respectively. In addition, Fig. 12 indicates that the beams: B2.7U90ST1, B1.9U90ST1, and B1.5U90ST1 witnessed sluggish strains, at a load level of 77.8 kN, approximately. Furthermore, Fig. 12 shows that increasing the beam's effective depth (d) resulted in a rise in the tensile sheet strain. In addition, it been found that the reduction of the effective depth delays the emergence of the strain. At the ultimate level of load, the sheets' tensile strains were: $3165\mu\epsilon$, $7720\mu\epsilon$, $8615\mu\epsilon$, and $9640\mu\epsilon$, in the beams: B2.7U90ST1, B1.9U90ST1, B1.5U90ST1, and B1.2U90ST1, respectively, equivalent to: $0.19\epsilon_{fu}$, $0.46\epsilon_{fu}$, $0.51\epsilon_{fu}$, and $0.57\epsilon_{fu}$, respectively. The enhanced values of CFRP strip's strains prove that the using the CFRP bonded length of beam depth is highly efficient in strengthening shear-deficient beams.

3.6. Crack opening behavior

Fig. 13 illustrates the curves of the load vs crack opening, for the NLFEA models. The curves have illustrated that the crack began to widen after the initiation of the diagonal shear cracks, at loads of: 88.5, 109.4, 137.4, 159.2, 98.7, 157.9, 180.6, and 192.2 kN, in the beams: B2.7N0, B1.9N0, B1.5N0, B1.2N0, B2.7U90ST1, B1.9U90ST1, B1.5U90ST1, and B1.2U90ST1, respectively. It was, also, found that, in all beams, the cracks widened to almost 0.25 mm, in a more sluggish manner. The development of cracks was slower in rate when the effective depth (d) was increased. At the ultimate level of load, the ultimate crack width was: 1.78, 2.56, 2.81, 3.07, 1.14, 1.78, 2.43, and 2.71 mm, in the beams: B2.7N0, B1.9N0, B1.5N0, B1.2N0, B2.7U90ST1, B1.9U90ST1, B1.5U90ST1, and B1.2U90ST1, respectively; while the beam B2.7U90ST1 exhibited a less crack width under the same load.

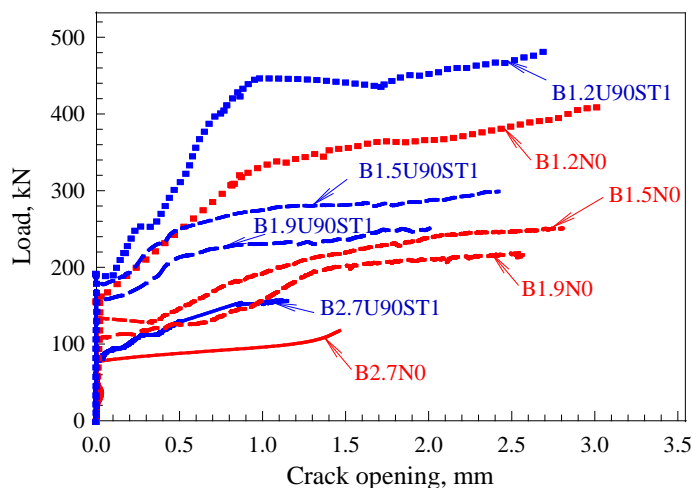


Figure 13. NLFEA load-crack opening curves.

Table 2. Comparison of results obtained with different models.

Beam Designation	NLFEA Ultimate load, kN	Chen and Teng model [23] $(\frac{V_{f,NLFEA}}{V_{f,mod}})$	Chen et al. model [24] $(\frac{V_{f,NLFEA}}{V_{f,mod}})$	ACI 440.2R model [25] $(\frac{V_{f,NLFEA}}{V_{f,mod}})$
B2.7N0	127.3	0.932	0.942	2.058
B1.9N0	213.2	0.923	0.933	2.038
B1.5N0	248.4	0.990	1.000	2.186
B1.2N0	403.2	1.000	1.010	2.208
B2.7U90ST1	146.0	1.011	1.021	2.232
B1.9U90ST1	247.2	0.914	0.924	2.019
B1.5U90ST1	294.2	0.980	0.990	2.163
B1.2U90ST1	475.1	0.941	0.951	2.078
Average	----	0.962	0.971	2.123
CoV (%)	----	37	40	98

3.7. Comparison of NLFEA with theoretical models

For all of the theoretical modeling methods, the first step had to be validated to confirm the methods' efficiency, and to prove their ability of prediction, against the so many experiments, conducted on beams with different properties, geometrically and mechanically, e.g.: the strength of concrete, and the reinforcement quantity and strength, internally and externally. The proposed model has been applied to experimental results as well as the literature test results. The NLFEA model was compared with ACI model, in terms of the obtained results. It was obvious that the guidance of the ACI model had been extracted from the NLFEA data, and they were, only, valid for the external FRP reinforcement. The results of the experimental validation are discussed below.

The comparison, conducted between NLFEA and other analytical methods, namely: Chen and Teng model [23], Chen et al. model [24], and ACI model [25]), as illustrated in Table 2. It is worth noticing that the ACI model was adjusted to the CFRP; whereas, this method must be utilized, cautiously, with other materials. The predictions of the ACI model were not as acceptable, when the mean value ($V_{f,exp}/V_{f,ACI}$) of 2.122, and a COV of 98 %. Referring to Table 2, the models of Chen and Teng [23] and Chen et al. [24] models were better in predicting the NLFEA data. Therefore, Chen and Teng [23] and Chen et al. [24] models have been found to be viable for the externally-bonded beams, regardless the material used (steel or CFRP).

4. Conclusions

1. The CFRP composites technique has proven a great efficiency in improving the RC beams' shear capacity. The externally-bonded CFRP laminates enhance, greatly, the beam's shear capacity to be 15–19 % more than control beams, based on the study parameters.
2. The most monitored mode of failure, of beams strengthened with CFRP strips, was the de-bonding of two or more strips. The test results, of this study, indicated that the de-bonding failure could be avoided by increasing the length of the CFRP strips, at the top side of the beam.
3. The study results pointed out that the depth of the beam depth affected the angle of the main crack; as this angle was: 33, 44, 50, and 54, for the beam's a/d of: 2.7, 1.9, 1.5, and 1.2, respectively.
4. In control and strengthened beams, the beam depth affected the ultimate load more than it did on the deflection.
5. Rising the RC beam's effective depth from 185 mm to 417 mm (corresponding to an a/d ratio of 2.7 to 1.2) reduced the average interface bond stress, and enhanced the effective CFRP sheet's strain, at failure. This had delayed, or even eliminated, the de-bonding failure, and raised the shear capacity, compared with the un-anchored, U-wrapped beams.
6. The extent of the main cracks' inclination affected the shear strength, affecting, in consequence, the overall strength. This study has shown that the shear crack angle had a big role in determining the number of CFRP strips that could be crossed by the crack, and whether the crossed strips were highly effective, or not.

References

1. Ahmed, A., Kodur, V. The experimental behavior of FRP-strengthened RC beams subjected to design fire exposure. *Engineering Structures*. 2011. 33(1). Pp. 2201–2211. DOI: 10.1016/j.engstruct.2011.03.010
2. Mabsout, M., Tarhini, K., Jabakhanji, R., Awwad, E. Wheel load distribution in simply supported concrete slab bridges. *J Bridge Eng*. 2004. 9(2). Pp. 293–306. DOI: 10.1061/(ASCE)1084-0702(2004)9:2(147)
3. Al-Rousan, R., Abo-Msamh, I. Bending and torsion behaviour of CFRP strengthened RC beams. *Magazine of Civil Engineering*. 2019. 92(8). Pp. 48–62. DOI: 10.18720/MCE.92.4
4. Al-Rousan, R. Behavior of two-way slabs subjected to drop-weight. *Magazine of Civil Engineering*. 2019. 90(6). Pp. 62–71. DOI: 10.18720/MCE.90.6
5. Al-Rousan, R. The impact of cable spacing on the behavior of cable-stayed bridges. *Magazine of Civil Engineering*. 2019. 91(7). Pp. 49–59. DOI: 10.18720/MCE.91.5
6. Yu, B., Kodur, V.K.R. Fire behavior of concrete T-beams strengthened with nearsurface mounted FRP reinforcement. *Engineering Structures*. 2014. 80(1). Pp. 350–361. DOI: 10.1016/j.engstruct.2014.09.003
7. Triantafillou, T.C., Antonopoulos CP. Design of concrete flexural members strengthened in shear with FRP. *J Compos Constr*. 2000. 4(4). Pp.198–205. DOI: 10.1061/(ASCE)1090-0268(2000)4:4(198)
8. Bousselham, A., Chaallal, O. Shear strengthening reinforced concrete beams with fiber-reinforced polymer: assessment of influencing parameters and required research. *ACI Struct J*. 2004. 101(2). Pp. 219–227. DOI: 10.14359/13019
9. Belarbi, A., Bae, S., Brancaccio, A. Behavior of full-scale RC T-beams strengthened in shear with externally bonded FRP sheets. *Constr Build Mater*. 2012. 32(1). Pp. 27–40. DOI: 10.1016/j.conbuildmat.2010.11.102
10. Khalifa, A., Nanni, A. Improving shear capacity of existing RC T-section beams using CFRP composites. *Cem Concr Compos*. 2000. 22(1). Pp. 165–174. DOI: 10.1016/S0958-9465(99)00051-7
11. Mosallam, A., Banerjee, S. Shear enhancement of reinforced concrete beams strengthened with FRP composite laminates. *Composites: Part B*. 2007. 38(1). Pp. 781–93. DOI: 10.1016/j.compositesb.2006.10.002
12. Ashrafuddin, M., Baluch, M.H., Sharif, A., Al-Sulaimani, G.J., Azad, A.K., Khan, A. Peeling and diagonal tension failures in steel plated R/C beams. *Constr Build Mater*. 1999. 13(1). Pp. 459–467. DOI: 10.1016/S0950-0618(99)00044-6
13. Rangan, B.V. Shear design of reinforced concrete beams, slabs and walls. *Cem Concr Compos*. 1998. 20(1). Pp. 455–464. DOI: 10.1016/S0958-9465(98)00027-4
14. Spadea, G., Bencardino, F., Swamy, R.N. Optimizing the performance characteristics of beams strengthened with bonded CFRP laminates. *Mater Struct*. 2000. 33(1). Pp. 1119–1126. DOI: 10.1007/BF02484166
15. Malek, A.M., Saadatmanesh, H. Ultimate shear capacity of reinforced concrete beams strengthened with web-bonded fiber-reinforced plastic plates. *ACI Struct J*. 1998. 95(4). Pp. 391–399. DOI: 10.14359/555
16. Triantafillou, T.C. Shear strengthening of reinforced concrete beams using epoxy-bonded FRP composites. *ACI Struct J*. 1998. 95(2). Pp. 107–115. DOI: 10.14359/531
17. Khalifa, A., Nanni, A. Improving shear capacity of existing RC T-section beams using CFRP composites. *J Cem Concr Compos*. 2000. 22(2). Pp.165–174. DOI: 10.1016/S0958-9465(99)00051-7
18. Hutchinson, R.L., Rizkalla, S.H. Shear strengthening of AASHTO bridge girders using carbon fiber reinforced polymer sheets. *ACI Special Publications (SP-188)*. 1999. 188(1). Pp. 945–958. DOI: 10.14359/5692
19. Zhang, Z., Hsu, C.T. Shear strengthening of reinforced concrete beams using carbon-fiber-reinforced polymer laminates. *J Compos Constr*. 2005. 9(2). Pp. 158–169. DOI: 10.1061/(ASCE)1090-0268(2005)9:2(158)
20. Monti, G., Liotta, M.A. Tests and design equations for FRP-strengthening in shear. *Constr Build Mater*. 2007. 21(24). Pp. 799–809. DOI: 10.1016/j.conbuildmat.2006.06.023
21. Shbeeb, N.I., Al-Rousan, R., Issa, M.A., Al-Salman, H. Impact of bonded carbon fibre composite on the shear strength of reinforced concrete beams. *Proceedings of the Institution of Civil Engineers: Structures and Buildings*. 2018. 171(5). Pp. 364–379. DOI: 10.1680/jstbu.16.00145
22. Lu, X.Z., J.G. Teng, L.P., Ye, J.J. Jiang. Bond-slip models for FRP sheets/plates bonded to concrete. *Engineering Structures Journal* 2005. 27 (1). Pp. 920–937. DOI: 10.1016/j.engstruct.2005.01.014
23. Chen, J.F., Teng, J.G. Shear capacity of FRP strengthened RC beams: FRP debonding. *Construction and Building Materials*. 2003b. 17(1). Pp. 27–41. DOI: 10.1016/S0950-0618(02)00091-0
24. Chen, G.M., Teng, J.G., Chen, J.F. Shear strength model for FRP-strengthened RC beams with adverse FRP-steel interaction. *Journal of Composites for Construction, ASCE*. 2013. 17(1). Pp. 50–66. DOI: 10.1061/(ASCE)CC.1943-5614.0000313
25. ACI Committee 440. Design and Construction of Externally Bonded FRP Systems for strengthening Concrete Structures. *ACI440.2R-02. 2002. American Concrete Institute, Farmington Hills, Mich.: 45 p. DOI: 10.1061/40753(171)159. ISBN: 9780870312854

Contacts:

Rajai Al-Rousan, rzalrousan@just.edu.jo



DOI: 10.34910/MCE.105.2

Effect of sawdust ash and laterite on the electrical resistivity of concrete

A.J. Babafemi^{a*}, O.T. Akinola^b, J.T. Kolawole^{a,c}, S.C. Paul^d, M.J. Miah^e

^a Stellenbosch University, Stellenbosch, South Africa,

^b Obafemi Awolowo University, Ile-Ife, Nigeria,

^c School of Architecture, Building and Civil Engineering, Loughborough University, Loughborough, UK

^d International University of Business Agriculture and Technology, Dhaka, Bangladesh

^e University of Asia Pacific, Dhaka, Bangladesh

*E-mail: ajbabafemi@sun.ac.za

Keywords: laterite, sawdust ash, electrical resistivity, durability, water-cement ratio, laterized concrete

Abstract. This study is an experimental research aimed at evaluating the electrical resistivity of concrete containing laterite and sawdust ash (SDA). Laterite was used to partially replace the sand in concrete while SDA partially replaced cement as a supplementary cementitious material. Cylindrical samples of Ø100 by 200 mm were used to evaluate the singular and combined influences of water-binder ratio, SDA and laterite on the electrical resistivity of concrete as a measure of durability. The sawdust ash content of 0, 10, 20 and 30% by weight of cement was considered while an optimum 30 % laterite content was examined and water-binder ratios of 0.35, 0.50 and 0.65. Additionally, some samples were cured in 1 %, 3 % and 5 % of sodium chloride salt (NaCl) to simulate the marine environment. The electrical resistivity test was conducted using the four-electrode method (Wenner's Method) in accordance with ASTM C1202. The results of the investigations revealed that the resistivity of concrete generally increases with age at all replacement levels with optimum performance at a water-binder ratio of 0.50. Also, the results show that an increase in the sawdust ash content reduces the resistivity of concrete while the addition of laterite at 30% increases the electrical resistivity of concrete at increased water content. Chloride ion exposure generally reduces the ER of concrete while laterite reduces the impact of the chloride ion.

1. Introduction

Concrete is a widely used construction material in the construction industry, hence making it one of the intensely researched materials in civil engineering [1]. However, concrete is a porous material, and the durability of concrete hangs on the properties of its microstructure such as the pore network, size, and interconnections. A finer pore network with less connectivity leads to lower penetrability. On the other hand, a porous microstructure with more degree of interconnections results in higher penetrability and reduced durability in general [2].

According to Baroghel-Bouny et al. [3], the long-term durability of reinforced concrete (RC) structures is a major concern for safety, economic and environmental reasons. There is an increasing number of RC structures and components of infrastructure that are not durable and are failing to realise their design service life [4]. Extensive experience has confirmed that the lack of concrete durability could often be related to a lack of proper quality control and problems during RC structure construction. Therefore, to ensure better construction quality and durability, there has been an increasing focus on the development of performance-based quality control techniques for concrete durability [5], [6]. One of the Non-Destructive

Babafemi, A.J., Akinola, O.T., Kolawole, J.T., Paul, S.C., Miah, M.J. Effect of sawdust ash and laterite on the electrical resistivity of concrete. Magazine of Civil Engineering. 2021. 105(5). Article No. 10502. DOI: 10.34910/MCE.105.2

© Babafemi, A.J., Akinola, O.T., Kolawole, J.T., Paul, S.C., Miah, M.J., 2021. Published by Peter the Great St.Petersburg Polytechnic University



This work is licensed under a CC BY-NC 4.0

Test (NDT) commonly suggested in performance-based quality control programme is electrical resistivity [7], [8].

Electrical resistivity (ER) is a non-destructive assessment technology that is related to how easily ions can move inside the concrete, that is, it is a measure of the diffusion of ions in the concrete through the pore solution. Hope et al. [9] and Hunkeler [10] posited that the electrical resistivity of a concrete sample is related to several factors which include paste microstructure, moisture content and temperature, and it is also affected by the presence of contaminants like chloride and sulphate ions [11]. The presence of chloride ion in concrete's pore liquid can induce corrosion of reinforcing bars [12] which can originate from sea water or marine atmosphere [13]. This has made some studies [13]–[15] to suggest the use of ER to measure chloride diffusion in concrete. As proposed by Tuutti [16], electrical resistivity can be principally classified into two stages of durability which are before and after steel corrosion. Thus, it can be used as the barometer of durability during latent period relating to microstructure of concrete as well as corrosion progress period [9], [17], [18] where the corrosion contaminant affects ion diffusion. These can be idealised in the laboratory with long term water curing and chloride ion exposure after initial 28 days water curing.

The rate of corrosion of steel reinforcement embedded in concrete is governed by the magnitude of the ionic corrosion current which flows in the concrete between the anodic and cathodic areas on the reinforcement. The magnitude of this current is dependent on the potential difference between the anode and the cathode, and the electrical resistance of the concrete. The electrical resistivity measurements can help to quantify these but can be significantly affected by the porosity of concrete [19]. A porous concrete would permit more space for ionic movement which can make way for chemical agents to penetrate concrete. Densifying the microstructure of concrete would reduce pores, thereby limiting ionic movements. Efforts to densify the microstructure of concrete, leading to improved durability has led to the use of supplementary cementitious materials (SCMs) and natural fillers in concrete production [20], [21].

By now, SCMs have proven to be effective in meeting most of the requirements for durable concrete and blended cements are now used in many parts of the world [20]. However, to achieve workability in most blended cement concrete, the water to binder ratio would be increased where a superplasticizer is not available. The increase in the water to binder ratio will reduce the strength of the blended cement concrete since concrete strength is related to this ratio. One such material that has the potential, on a large scale to be used as SCM is sawdust ash (SDA). Many researchers have particularly found SDA a suitable agricultural by-product for use in formulating binary blended cements with ordinary Portland cement (OPC) [21], [22]. As the call for the use of alternative materials which the environment can afford continues to rise, laterite has a potential to serve as a cheap filler or sand replacement in concrete that can improve concrete's resistance to corrosion. In the tropics such as Nigeria, laterite is available in abundance almost from any borrow pit [23]. Laterized concrete is concrete containing some percentages of laterite as replacement for sand and some studies have successfully shown that laterized concrete can achieve similar mechanical properties and sulphate attack resistance with normal concrete [24]–[27]. This experimental study on electrical resistivity of laterized concrete attempts to advance this frontier of research.

Even though many works have shown that electrical resistivity of conventional concrete is affected by factors such as moisture content, sample geometry, chloride ion and temperature of the sample [28]–[32], such investigation is yet to be performed on laterized concrete. Hence, this study also investigates some ER influencing factors such as water-binder ratio, chloride ion exposure and its concentration; these were coupled with the effects of SDA at varying contents as a SCM, yielding a total of about 24 mixes. Four forms of concrete were formulated: normal concrete, SDA blended cement concrete, laterized concrete, and SDA blended cement laterized concrete.

2. Materials and Methods

2.1. Materials

Ordinary Portland cement (CEM II 42.5 N), sand, granite chippings, laterite, sawdust ash, portable water and superplasticizer were the materials used to prepare the test specimens. The coarse aggregate, granite had a maximum size of 19 mm. The grading curve of the sand, granite and laterite is shown in Figure 1; this test was performed according to BS EN 933-1 [33]. Table 1 shows the physical properties of the sand, laterite and granite. Standards procedures have been followed to obtain the physical properties of the materials and binders.

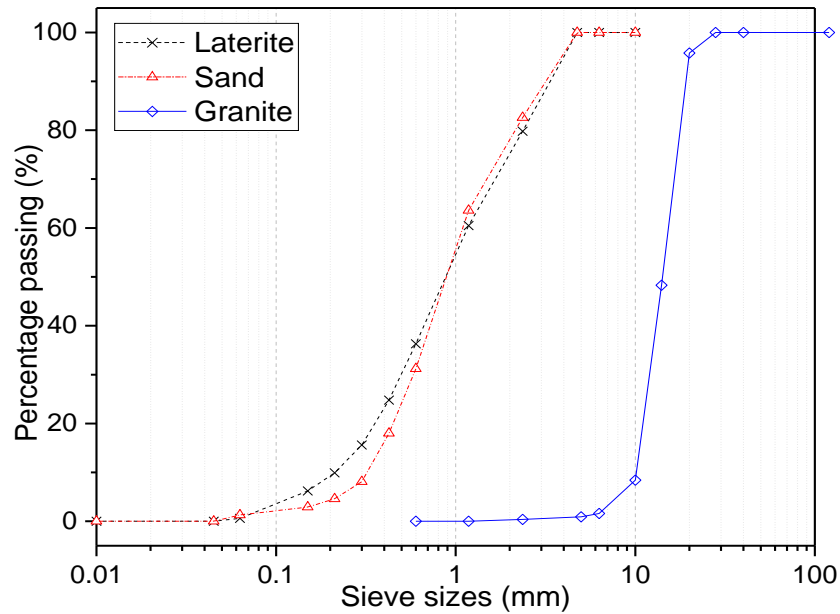


Figure 1. Grading curve of sand, laterite and granite.

Table 1. Physical properties of sand, laterite and granite.

Properties	Laterite	Sand	Granite
Fineness modulus	3.03	3.12	6.95
Coefficient of uniformity (C_u)	5.57	3.47	1.55
Coefficient of curvature (C_c)	1.00	1.00	1.00
Specific gravity	2.53	2.62	2.80
Water absorption (%)	7.33	5.17	0.88
Liquid limit (%)	37.0	-	-
Plastic limit (%)	17.0	-	-
Plasticity index (%)	20.0	-	-

The sawdust was collected from a sawmill and thereafter burnt in the open-air to reduce the bulk of the sawdust. It was then transferred to a temperature-controlled kiln for calcination at 650 °C, the resulting ash was sieved for use as SDA. It should be noted that the sawdust was fillings from different woods in the Sawmill. Table 2 shows the physical and chemical properties of the cement and the SDA. X-ray fluorescent (XRF) analyzer was used in determining the oxide composition of the SDA according to the requirements of BS ISO 29581-2 [34]; the mineralogy of the SDA and laterite was determined by X-ray diffraction according to BS EN 13925-2 [35] while their morphology was investigated by scanning electronic microscopy (SEM+EDX) in accordance to BS ISO 16700 [36]. The SDA particles that passed through sieve aperture 75 μ m was used to replace the OPC at 0, 10, 20 and 30%.

The fineness of the OPC was obtained by the percentage of mass retained on 75 μ m sieves as 20.96% while 20.86% was obtained for SDA. This shows that the OPC is almost of the same fineness as SDA. According to ASTM C618 [37], a limit of 34% is set which is met by the materials. The specific gravity of cement is higher than of SDA (3.14 and 2.08, respectively). The lower values obtained for the specific gravity of the SDA implies that a larger quantity of SDA will be required for batching in relation to OPC.

Table 2. Properties of cement and sawdust ash.

Properties/constituents	OPC	SDA
Fineness (% residue on 75 μ m sieve)	20.96	20.86
Consistency (%)	28	52
Initial setting time (min)	110	-
Final setting Time (min)	210	-
Soundness (mm)	0.00	-1.00
Specific gravity	3.14	2.08

Properties/constituents	OPC	SDA
SiO ₂	16.82	66.96
Al ₂ O ₃	4.35	5.29
Fe ₂ O ₃	2.43	2.65
CaO	60.39	9.53
MgO	1.43	5.48
SO ₃	1.64	0.68
K ₂ O	0.16	0.15
Na ₂ O	0.02	0.06
MnO	0.04	0.01
P ₂ O ₅	0.21	0.48
TiO ₂	0.24	0.00
LOI	9.84	4.85
Free Lime	0.36	0.00
SiO ₂ + Al ₂ O ₃ + Fe ₂ O ₃	23.60	74.94
C ₃ S	85.25	
C ₂ S	16.15	
C ₃ A	7.42	
C ₄ AF	7.39	

2.2. Concrete mixture of SDA blended cement laterized concrete

Twenty-four different mix proportions involving cement, SDA and lateritic soil were prepared as shown in Table 3. The cement was replaced with SDA at 0, 10, 20 and 30% while the laterite was kept constant at 30% as a replacement for sand. The water-to-binder ratios (w/b) of 0.35, 0.50 and 0.65 were used.

The concrete ingredients were batched by weight and mixed manually on a neat impermeable platform with a predetermined amount of water. The cement and SDA were first thoroughly mixed manually to obtain a uniform mixture. The blended cement was then spread over the already mixed aggregate and remixed before water was added to the dry mix. Afterwards, the required dosage of superplasticizer (Mapefluid – N200) was added to obtain a medium slump, Class S2 (50 – 90 mm) for all mixes. The concrete was then thoroughly mixed for additional two minutes. Mixing was concluded when the concrete showed a uniform blend. Slump test was thereafter carried out to determine the workability of each mix. The tests were conducted out by the requirements of BS EN 12350-2 [38].

Table 3. Mix proportion for each replacement levels.

w/b ratio	Replacement levels (%) OPC:SDA:LAT*	Labels	Cement (kg/m ³)	SDA (kg/m ³)	Sand (kg/m ³)	Laterite (kg/m ³)	Granite (kg/m ³)	Water (kg/m ³)	SP* (kg/m ³)
0.65	100:0:0	1C	350	0	900	0	1200	227.5	3.80
	90:10:0	1CS1	315	35	900	0	1200	227.5	4.20
	80:20:0	1CS2	280	70	900	0	1200	227.5	6.30
	70:30:0	1CS3	245	105	900	0	1200	227.5	5.60
	100:0:30	1CL	350	0	630	270	1200	227.5	5.20
	90:10:30	1CLS1	315	35	630	270	1200	227.5	9.70
	80:20:30	1CLS2	280	70	630	270	1200	227.5	16.2
	70:30:30	1CLS3	245	105	630	270	1200	227.5	8.35
0.5	100:0:0	2C	350	0	900	0	1200	175.0	4.87
	90:10:0	2CS1	315	35	900	0	1200	175.0	5.63
	80:20:0	2CS2	280	70	900	0	1200	175.0	6.95
	70:30:0	2CS3	245	105	900	0	1200	175.0	6.05
	100:0:30	2CL	350	0	630	270	1200	175.0	9.97

w/b ratio	Replacement levels (%) OPC:SDA:LAT*	Labels	Cement (kg/m ³)	SDA (kg/m ³)	Sand (kg/m ³)	Laterite (kg/m ³)	Granite (kg/m ³)	Water (kg/m ³)	SP* (kg/m ³)
0.35	90:10:30	2CLS1	315	35	630	270	1200	175.0	6.40
	80:20:30	2CLS2	280	70	630	270	1200	175.0	8.97
	70:30:30	2CLS3	245	105	630	270	1200	175.0	9.82
	100:0:0	3C	350	0	900	0	1200	122.5	5.05
	90:10:0	3CS1	315	35	900	0	1200	122.5	6.43
	80:20:0	3CS2	280	70	900	0	1200	122.5	8.23
	70:30:0	3CS3	245	105	900	0	1200	122.5	9.27
	100:0:30	3CL	350	0	630	270	1200	122.5	6.15
	90:10:30	3CLS1	315	35	630	270	1200	122.5	7.50
	80:20:30	3CLS2	280	70	630	270	1200	122.5	8.45
	70:30:30	3CLS3	245	105	630	270	1200	122.5	11.59

* OPC – Ordinary Portland cement, SDA – saw dust ash, LAT – Laterite, SP – Superplasticizer

2.3. Sample preparation

Cylindrical moulds of Ø100×200 mm was used for casting the test specimen. The moulds were thoroughly cleaned and coated with mould oil before casting to ensure easy de-moulding. The casting was done in accordance with ASTM C192/C192M [39]. After casting, sackcloth was placed over the moulds to avoid evaporation of mix water from the concrete cylinder samples.

De-moulding of the specimens took place after 24 hours of casting, and then was kept in an area free from vibration, dehydration and direct rays of sunlight and other sources of heat. After 28 days of water curing, specimens were transferred to various concentrations of sodium chloride (NaCl) for a maximum period of 60 days. Control specimens were also cured in the water alongside those cured in NaCl for a maximum of 88 days, NaCl concentrations of 1%, 3%, and 5% were used for the investigation. This represents the extreme forms of concrete exposure of typical ocean salt concentration with an average of 3.5% [40] that can penetrate/diffuse into the concrete as contaminants. 1% and 5% concentrations were also selected to represent possible lower and higher concentrations that can occur due to probable variation of salt concentration in the ocean.

2.4. Experimental tests

Electrical resistivity (ER) of the concrete specimens after various curing ages was determined. The test was carried out using the four-electrode method (Wenner's Method) in accordance with AASHTO T 358 [41]. Studies such as Azarsa and Gupta [42] and Lencioni and Lima [43] rated Wenner's method an easily deployable approach to determining electrical resistivity and better than the two-point method. 360 cylindrical specimens were used to determine the effect of SDA and water/cement ratio on the electrical resistivity of lateritized concrete at curing ages of 7, 14, 28, 58 and 88 days in water; 216 cylinder specimens were also used to determine the effect of 1, 3 and 5% NaCl concentration on the electrical resistivity of blended cement lateritized concrete at 30 and 60 days after water curing for 28 days. Four data points were taken per sample and at least three samples were tested for the ER, and the average reported. The schematic diagram of the test equipment is shown in Figure 2. For qualitative purposes AASHTO T 358 [41] classifies the ER values into high (< 12 kΩ.cm), moderate (12–21 kΩ.cm), low (21–37 kΩ.cm), very low (37–254 kΩ.cm) and negligible (> 254 kΩ.cm) potentials for chloride ion penetration based on established correlations. According to AASHTO T 358 [41], curing in lime solution reduces the ER by 10% and should be factored into the ER values. In the case of this study, no correction factors were applied on the ER of the specimens cured in NaCl since they were initially cured in water for 28 days.

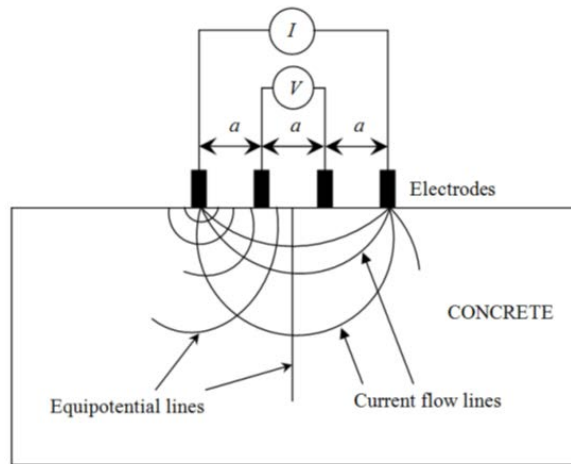


Figure 2. Schematic representation for measurement of electrical resistivity.

3. Results and Discussion

3.1. Mineralogy and morphology of the SDA and laterite

Figure 3 shows the mineralogy of both the saw dust ash (SDA) and laterite. The peaks in the XRD results depict crystalline phases with position and intensity proportional to crystalline compounds [44]. The intensity peaks in Figure 3 shows that the laterite has more crystalline structures than the SDA. This is in order of their use since amorphous compounds (less crystalline) is more reactive with hydrated lime ($\text{Ca}(\text{OH})_2$) as a supplementary cementitious material (SCM) while the more stable crystalline nature of the laterite suits its use as a filler and replacement of sand.

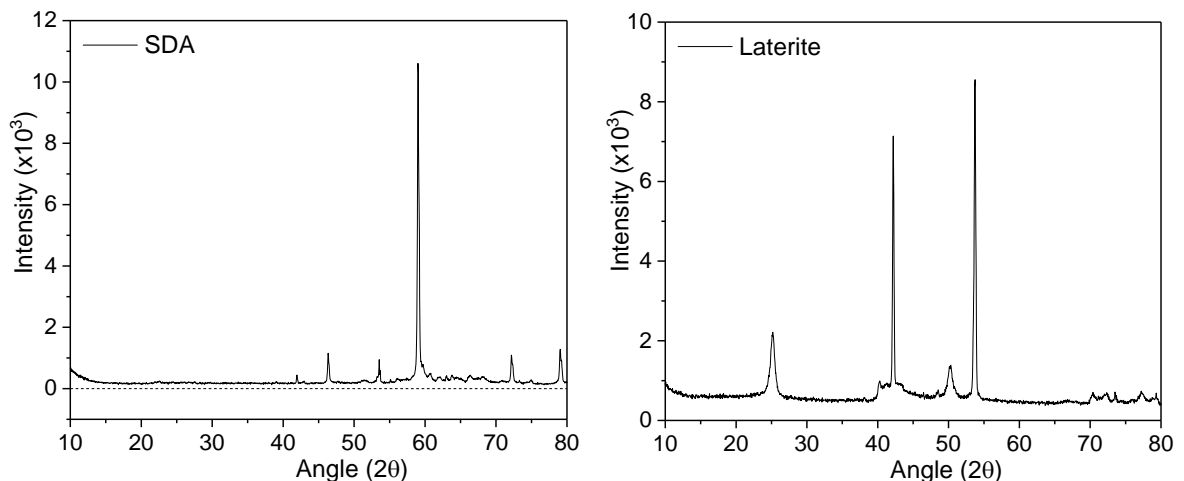


Figure 3. XRD pattern of (a) saw dust ash (SDA) and (b) laterite.

Figure 4 shows the morphology of the SDA and laterite. The images were obtained using a Zeiss MERLIN high-resolution Scanning Electron Microscopy (SEM). The samples were scanned on a coated carbon tape. The results show that the SDA particles tend to be flat with more regularity and less sphericity while the laterite is fairly flat but more rounded. This shape is envisaged to require more water for lubrication, hence workability, as compared to more rounded shapes. This was observed in the next section on the concrete's workability. Since both Figure 4a and b are of the same magnification (200 nm), it can be said that the SDA particles are more bigger than that of the laterite, though the laterite particles seem to agglomerate into bigger particles (lumps). The shape and form of SDA is probably due to its burning that turns it into ash as compared to laterite in its natural form. The energy dispersive X-ray analysis (EDX) shown in Figure 5 helps to quantify the elemental analysis of the material which is shown in Table 4. The richness of the laterite in silica and alumina explains the additional crystalline phases detected as peaks in Figure 3. That is, laterite is known to have phases of quartz (crystalline SiO_2), gibbsite $[\text{Al}(\text{OH})_3]$, kaolinite $[\text{Al}_2\text{Si}_2\text{O}_5(\text{OH})_4]$ and hematite (Fe_2O_3) [45], [46] which coincides with the detected substantial elemental content (Si, Al, Fe) of the laterite in Table 4.

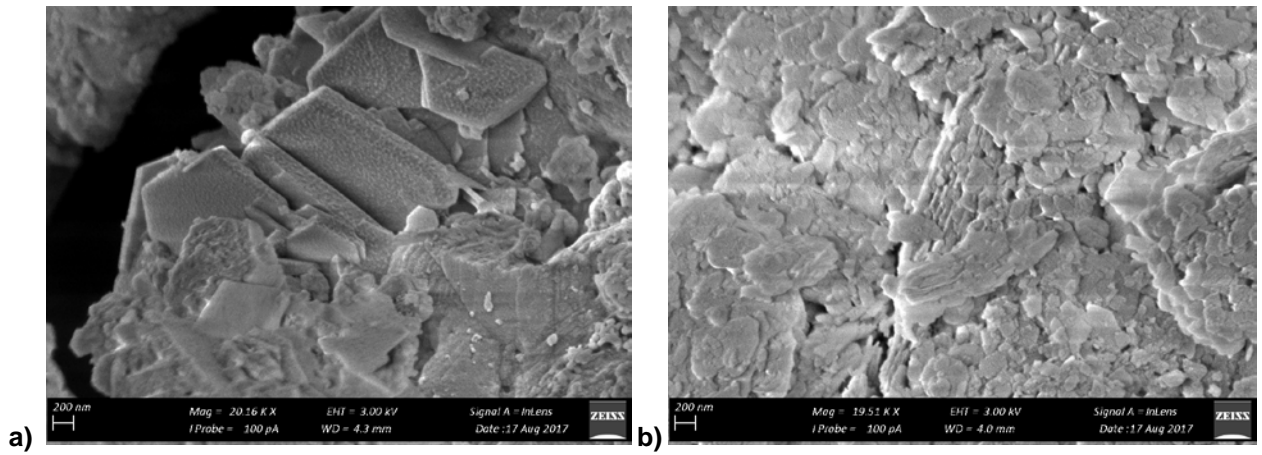


Figure 4. SEM images of (a) saw dust ash and (b) laterite at 200 nm magnification.

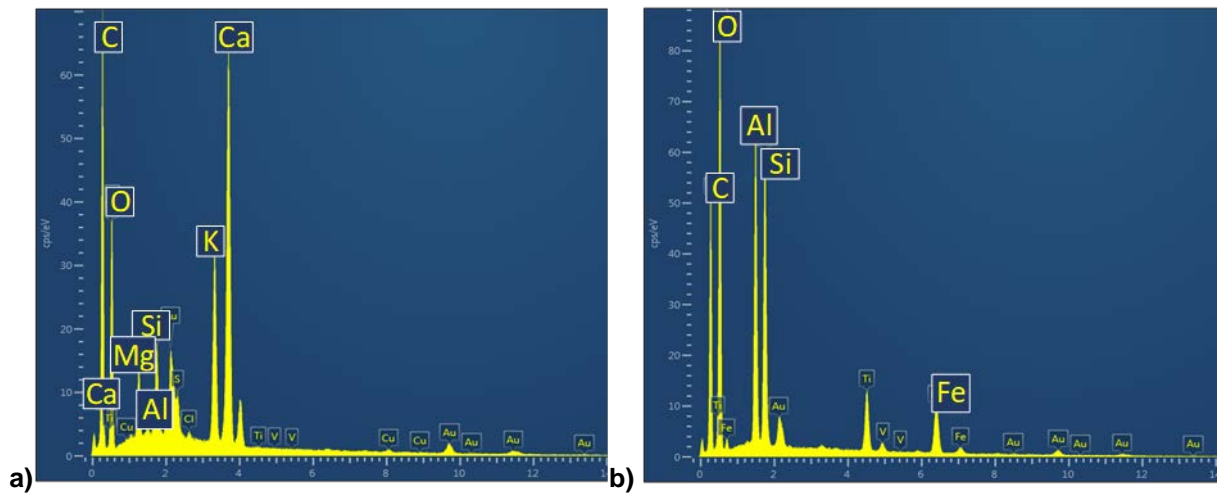


Figure 5. EDX microanalysis of the (a) saw dust ash and (b) laterite.

Table 4. Elemental composition of the SDA and laterite.

	O	Mg	Al	Si	P	S	Cl	K	Ca	Ti	Fe	Cu
Laterite	65.88	0	14.81	14.86	0	0	0.03	0.03	0	0.55	3.55	0.28
SDA	64.83	2.68	0.77	2.61	0.70	0.96	0.30	7.79	18.34	0.06	0.40	0.59

3.2. Workability of the concrete

The slump of every wet concrete mix was carried out as a measure of the workability, and the result is shown in Figure 6. The labels on top of the columns represent the ratio of the superplasticizer (SP) of each mix as a ratio of the control mix; this ratio is normalized by the value of the slump. The result reveals that as the percentage of SDA content increases, the superplasticizer required for mixing to achieve a slump of Class S2 also increases at all w/b ratio. All slump values were within the range of 55–65 mm, this was done to ensure that the concrete's compaction does not influence the microstructure differently; hence, allowing for ER results limited to the concrete's material variation. With the addition of laterite at a constant amount of 30% to all these mixes, the demand for the superplasticizer increases to keep the mix at a medium workability. It can be said that the addition of SDA to laterized concrete makes it stiffer than just adding SDA to normal concrete. For example, addition of 30% SDA to normal concrete required 1.2 times more SP at 0.5 w/b ratio while addition of 30% SDA to laterized concrete required 2 times more SP. This trend is similar at all SDA contents and w/b ratios. It can, therefore, be concluded that the SDA blended cement laterized concrete becomes stiffer and less workable as the content of the SDA increases and much more with the addition of laterite. The flat nature of the SDA and laterite particles from the SEM images in Section 3.1 explains the observed reduction of workability (and increased superplasticizer requirement) due to their inclusion in concrete because more water is needed to lubricate their particles than rounder particles.

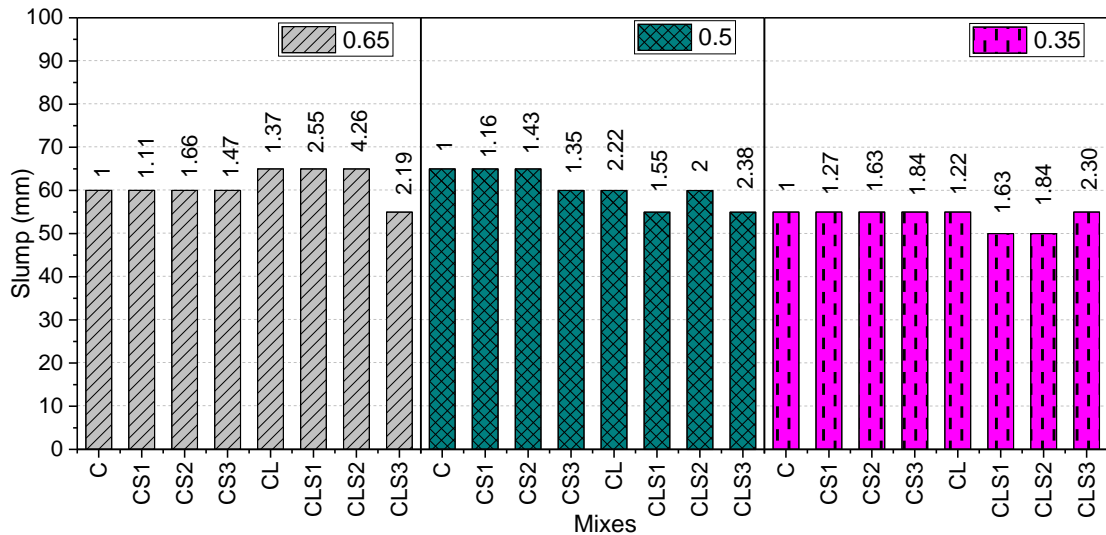


Figure 6. Slump values of SDA blended cement laterized concrete.

3.3. Electrical resistivity (ER) of the concrete

3.3.1. Effect of water-binder ratio: normal and laterized concrete

The effect of the water-binder ratio on the electrical resistivity (ER) of the normal concrete (Mix C) and laterized concrete (Mix CL), at curing ages of 7, 14, 28, 58 and 88 days is shown in Figure 7. The results presented are the average values of three samples taken when the concrete is in the moist state (30 minutes after removal from the curing tank). The specimens were surface dried before the readings were taken. From the result, it is evident that the resistivity of the concrete is a function of age; it increases with curing age irrespective of the w/b ratio and material content. The increase in resistivity with age is due to further hydration as a function of age which improves microstructure against the movement of ions through the pore structure. It should be noted that this was also observed for other mixes (containing SDA with/without laterite) with the curing age. The increase in resistivity of concrete with curing age has been confirmed by previous researchers [47], [48]. However, unlike this study, some studies [47], [49] showed that the ER stabilized at about 14 days at 0.5 w-b ratio.

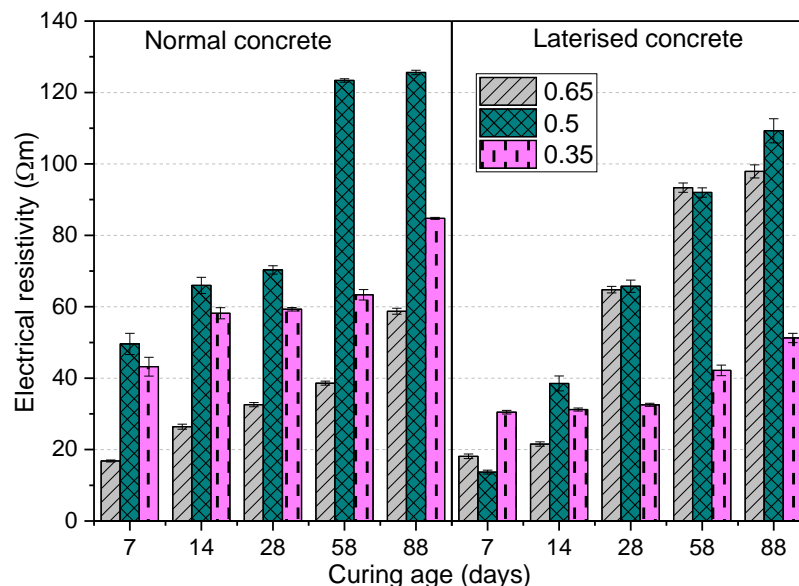


Figure 7. Electrical resistivity of the control concrete at different w/b ratio and curing age.

From the study of Dong *et al.* [50] and Su *et al.* [51], ER resistivity is supposed to increase as w/c ratio increases; this is similar for this study except for 0.5 w/b. According to Neville [52], moist concrete acts as an electrolyte, hence, lower resistivity at higher w/b ratio. It will be observed that at all ages, the resistivity of the normal concrete was higher at a w/c of 0.50 compared to those of 0.35; this difference becomes pronounced as the curing age increased, especially above 28 days. Though considerable effort was made to ensure similar workability of the fresh concrete, the results of Figure 6 revealed that the control mix is stiffest at w/b of 0.35 (slump – 55 mm) followed by that of 0.65 (slump – 60 mm) and 0.5 (slump – 65 mm).

which could influence the efficacy of the equal amount of compaction applied; hence, the pore structure (voids and its interconnectivity) and measured ER. That is, assuming equally applied compaction, 0.5 w/b has a higher chance to achieve denser microstructure for less voids and interconnectivity due to its less slump; hence, having higher ER. In the same vein, the laterized concrete also shows that w/b ratio of 0.65 and 0.5 improved the resistivity more than that of 0.35 and these improvements increases with the curing age. Possible reason for this is the increased water content that is absorbable by the laterite for microstructure densification, this is explained further in the next section.

Water-to-binder ratio as a measure of water content is a crucial factor which determines concrete resistivity because it controls the performance of the concrete. Not only does the w/b ratio has a significant effect on strength and durability of the concrete, but also plays an important role in the microstructure of the cement paste, as well as the ionic concentration of the pore solution. Therefore, an increase in w/b ratio can be concluded to cause a higher porosity and coarser pore structure of the concrete; hence, lower electrical resistivity [53]–[55]. Furthermore, a stiffer concrete can reduce the efficacy of compaction, causing lower ER (due to higher porosity and coarser pore structure). Though the AASHTO T 358 code [41] stated that the classification highlighted in Section 2.4 must be used with caution, all the mixes can be said to have high potential for chloride ion penetration. The use of laterite did not cause any significant change in the classification for chloride ion penetration; as found later, this is also the case for the SDA. Therefore, the effects of the laterite and/or SDA lies in the variation of the numeric results of the ER.

3.3.2. Effect of laterite on ER of normal concrete

As previously stated, laterite at optimum replacement level of 30% [56], [57] was introduced into the concrete mix to form what has been termed laterized concrete. The result of the impact of the laterite on the electrical resistivity of concrete mixes (Mixes CL) at the various w/b ratios and curing ages is shown in Figure 8. The general trend is that the addition of laterite in the concrete reduces the resistivity. It can, however, be observed from the figure that the higher the w/b ratio, the lesser the detrimental influence of the laterite on the concrete's resistivity. In fact, at 28 days curing age and later ages, the laterite increased the ER of concrete at w/b of 0.65 by 99%, 141% and 67%, respectively. This could be due to the fact that laterite as part of the fine aggregate absorbs more water (Table 1) to densify the microstructure and inhibit ion movement, especially along the interfacial transition zone (ITZ) [58], [59]; this absorption will be, expectedly, more pronounced at higher w/b ratio such as 0.65 and 0.5 as noted in the previous section. The recent study of Yaragal *et al.* [28] achieved similar ITZs for laterized and normal concretes at a w-b ratio of 0.5; in this case, the laterite was pre-wetted which can negatively impact the ITZ development of the laterized concrete. Furthermore, it implies that, similar to the effects of w/b ratio in the previous section, increased curing magnifies the effects of the laterite on the ER.

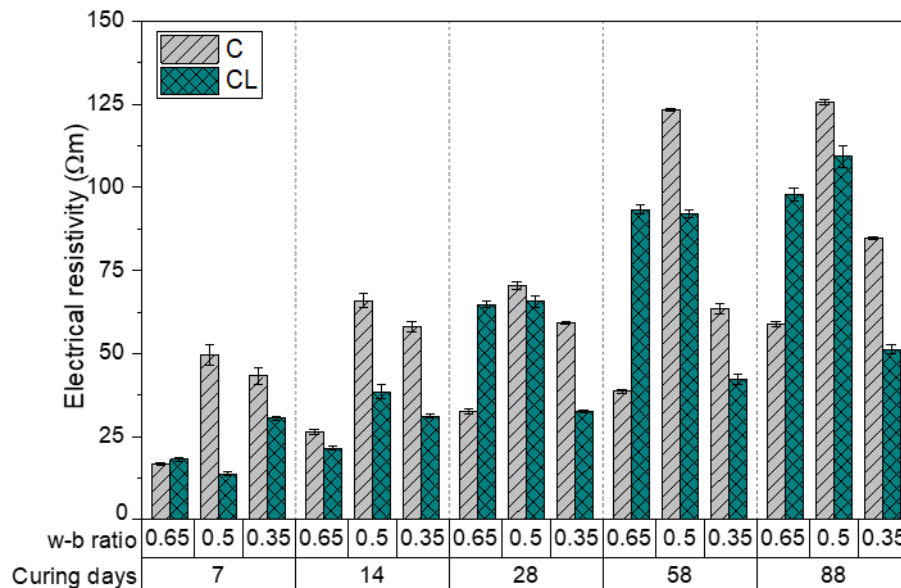


Figure 8. Effect of laterite on the electrical resistivity of concrete at various curing ages.

3.3.3. Effect of saw dust ash (SDA) on ER of normal concrete

The results shown in Figure 9 represent the impact of SDA content at various water-binder ratio and curing ages on the electrical resistivity of concrete. Similar to the normal concrete, concrete mixes containing SDA (Mixes CS1, CS2 and CS3) reveal that increased w/b ratio reduces the ER, the optimum being 0.35. This is dissimilar to the results of Rupnow *et al.* [60] containing slag SCM which showed increased ER values from w-b ratio of 0.35 to 0.65, which could be due to less reactivity of SDA as explained

later. More importantly, w/b ratio of 0.65 and 0.35 tends to dampen the effects of the SDA on the ER of the concrete while 0.5 w/b ratio tends to magnify the influence of the SDA. That is, there is lesser difference between the ERs of the mixes at both 0.65 and 0.35 w/b ratio. For example, at 28 days curing, the difference between the ERs of Mixes C/CS2 and CS1/CS3 at 0.35 w/b ratio are 16% and 8%, respectively, while it was 61% and 55%, respectively, at 0.5 w/b ratio. Again, at the different replacement levels of cement with SDA, the resistivity of concrete mixes increases with curing ages due to further hydration. This behaviour could be due to some pozzolanic action induced by the higher content of SiO_2 , Al_2O_3 and Fe_2O_3 (fallen into Class N raw and calcined natural pozzolans recommended in ASTM C618, see Table 2) in SDA, which increases the amount of secondary CSH, and at the same time continuous formation of hydration product with time (i.e., lower un-hydrated binders). It is noted that the higher content of SDA decreases the ER values; even at later ages of 58 and 88 days when blended cement concrete is expected to have improved properties [61]. This could be attributed to the higher percentage of MgO (5.48%), which could induce higher expansion (soundness, see Table 2), resulting in higher cracking and lower ER. Unlike rice husk ash with a higher reactivity as a pozzolan in concrete [62], SDA has been shown to have a rather reduced reactivity compared to control samples even at later ages [63], [64]. Figure 9 also reveals that the addition of SDA impacts more negatively on the resistivity of concrete than those of laterite. For example, at 28 days curing, laterite (Mix CL – 30% content) impacted the concrete by +50%, -7% and -45% at 0.65, 0.5 and 0.35 w/b ratio, respectively, while the SDA (Mix CS3 – 30% content) impacted the concrete by -42%, -73% and -24%, respectively.

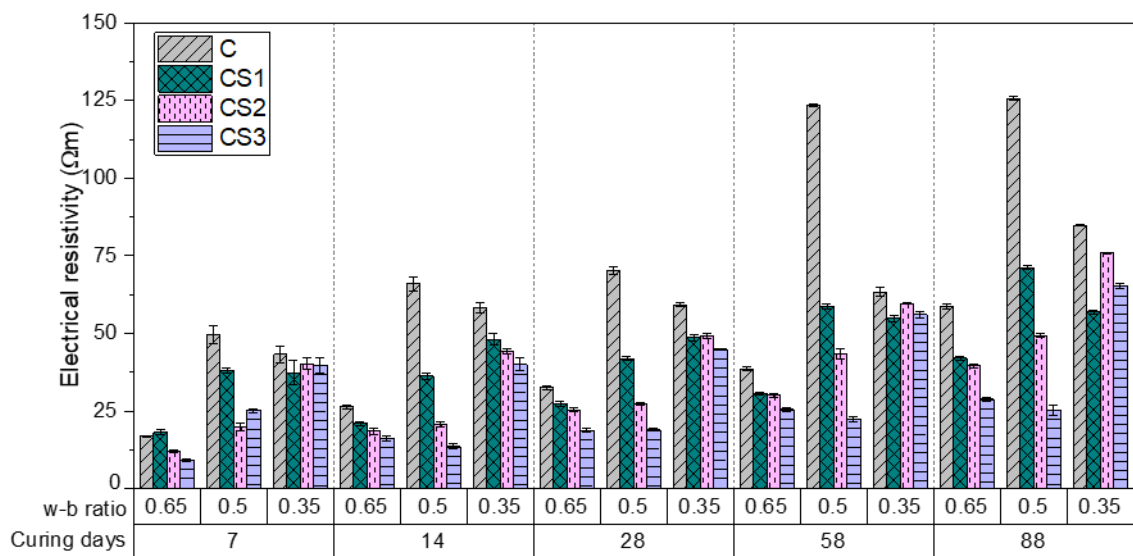


Figure 9. Effect of saw dust ash on the electrical resistivity of concrete at various curing ages.

3.3.4. Effect of saw dust ash (SDA) on ER of laterized concrete

Figure 10 shows the influence of SDA blended cement on the electrical resistivity of laterized concrete. The intention of the figure is to depict the effects of adding both laterite and SDA in concrete. The effects can be proposed to be in two parts: early age (7 and 14 days) and later age (28, 58 and 88 days) at all w/b ratios. At early age, the influence of SDA on laterized concrete tends to be minimal while at later age it tends to be pronounced. For example, at 7 days curing and 0.65 w/b ratio, 30% SDA content (Mix CLS3) impacted the ER of laterized concrete by -27% while it impacted the ER by -72% at 88 days curing. That is, similar to the effect of SDA on ER of normal concrete in the previous section, increased curing tends to magnify the effects of SDA on the ER of laterized concrete. At lower w-b ratio of 0.35, the ER increased for the laterized concrete blended with 10% and 30% SDA at later age while the ER decreased at higher w-b ratios. This behaviour could be due to some pozzolanic action (as explained earlier) which densifies the concrete matrix especially at later ages where the SDA influence became pronounced. The variation in this study has been confirmed by Singh and Singh [65] that showed that the ER of concrete is dependent on the binder combination and nature of aggregates. Singh and Singh [65] made use of silica fume/metakaolin as SCMs and reused concrete aggregates as substitute for river sand.

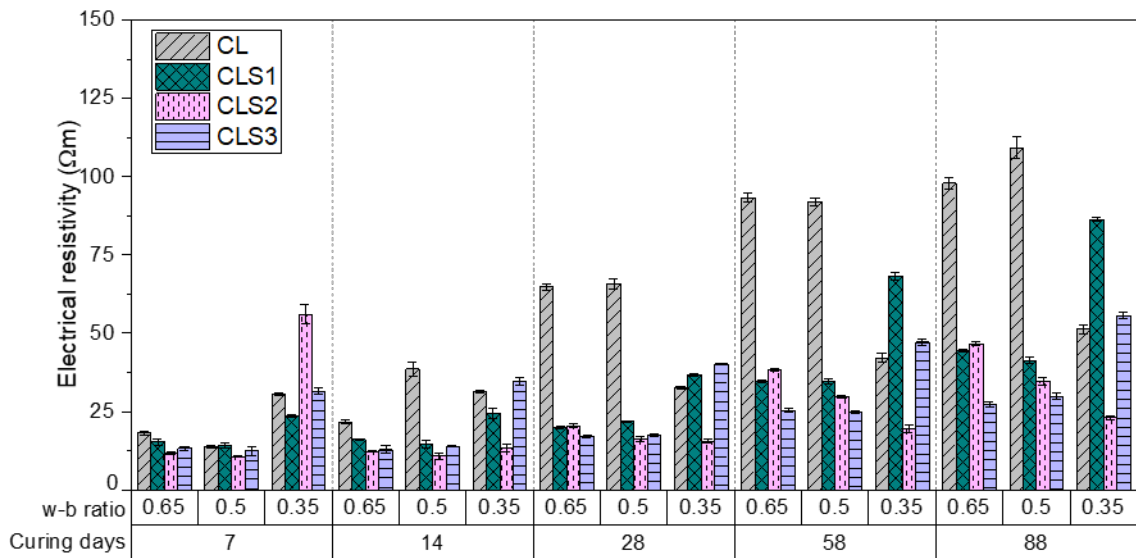


Figure 10. Effect of SDA on the electrical resistivity of laterized concrete at various curing ages.

3.3.5. Electrical resistivity of concrete containing SDA and laterite exposed to chloride ion

This section examines the electrical resistivity (ER) of SDA blended cement laterized concrete exposed to chloride solution. Chloride ion in concrete's pore solution is expected to increase the easy passage of electricity. Hence, a reduction in the ER is expected for the concrete cured in NaCl. It should be noted that the samples were initially cured in water for 28 days before exposure to NaCl for 30 and 60 days. Similar to Section 3.3, this section attempts to delineate the effects of w-b ratio, laterite and SDA, singularly and jointly, on the electrical resistivity.

Figure 11 shows the ER of Mix C and CL in 1, 3 and 5% NaCl at 0.65, 0.5 and 0.35 w-b ratio exposed to NaCl for 30 and 60 days. This figure delineates the effects of laterite, w-b ratio, NaCl concentration, and exposure time. The more the exposure period and chloride ion concentration, the less the ER of the samples; this is also evident in Figure 12 and Figure 13 that depict the effects of SDA (combined with that of w-b ratio) on normal and laterized concrete, respectively. This is because more exposure time and chloride ions would allow for additional penetration of the chloride ions that can create more routes for the passage of electric current. The inclusion of laterite in concrete tends to reduce the ER of the concrete, however, laterite greatly improved the ER at 0.65 w-b ratio. For example, at 30/60 days exposure, the laterite averagely increased the ER by 230%/61% at 0.65 w-b ratio while it reduced the ER by 34 %/31 % at 0.5 w-b ratio and 13 %/31 % at 0.35 w-b ratio, respectively. This is similar to the water curing in Section 3.3.2 where increased water content is envisaged to improve the effectiveness of laterite in mitigating durability problems. The trend in the example sentence also revealed that continued exposure to chloride ion seems to drastically reduce the effectiveness of the laterite at the increased water content. Similar to the results for water curing, 0.5 w-b ratio yielded the highest resistivity in chloride ion.

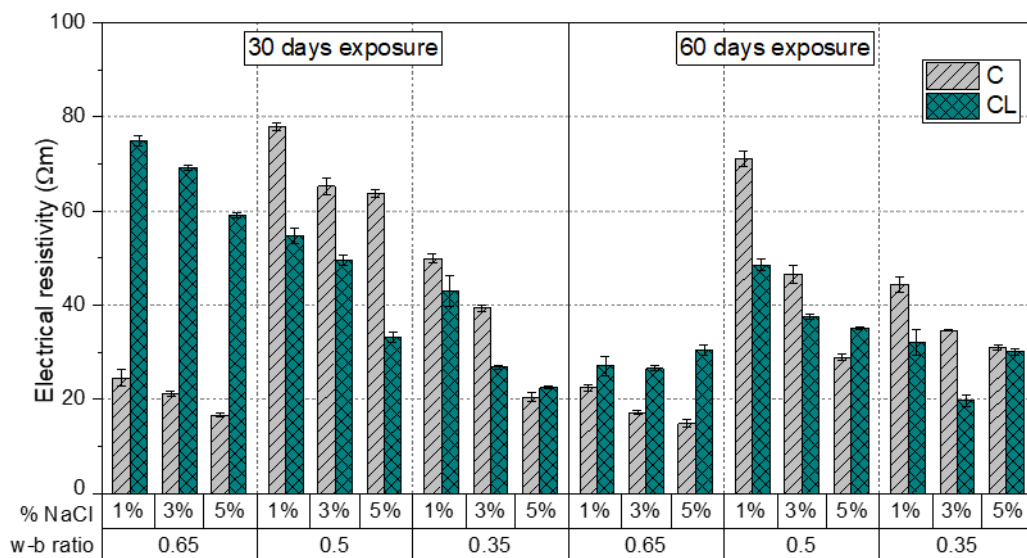


Figure 11. Impact of chloride ion exposure on the ER of normal and laterized concrete.

Figure 12 depicts the influence of SDA on the ER of concrete in the presence of chloride ion. Similar to water curing, lower w-b ratio tends to improve the effectiveness of the SDA in concrete in NaCl solution. This effectiveness being magnified due to the NaCl solution, especially at 0.35 w-b ratio. At 30/60 days of NaCl exposure at 0.35 w-b ratio, 30% inclusion of SDA in normal concrete impacted the ER by an average of +71 %/+17 %, respectively, while water cured samples had -13%/-23% decrease due to 30% SDA.

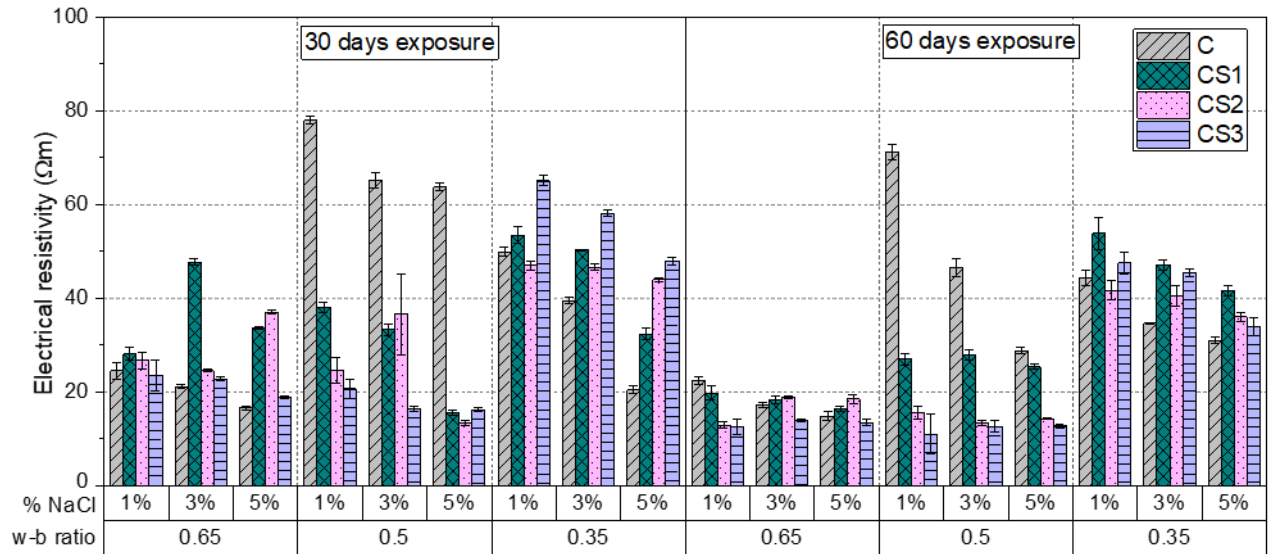


Figure 12. Effects of chloride ion exposure on the ER of normal and SDA blended cement concrete.

The impact of SDA in improving ER of concrete (Figure 13) tends to be dampened due to the presence of laterite, especially at the lower 0.35 w-b ratio identified (see previous paragraph) for SDA utmost efficiency in normal concrete. From Figure 13, 30% inclusion of SDA in laterized concrete at 0.35 w-b ratio and 30/60 days exposure impacted the ER by an average of +31%/+2% respectively which is quite low to that of normal concrete (+71%/+17%). Similar to the SDA in normal concrete, the presence of chloride ion in laterized concrete tends to improve the effectiveness of the SDA.

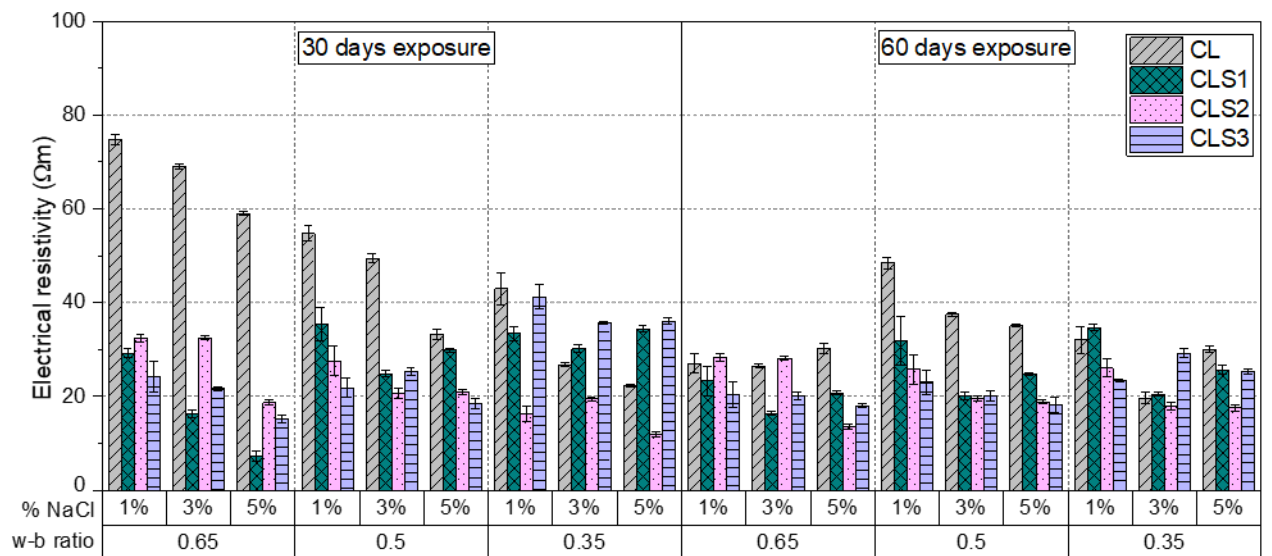


Figure 13. Effects of chloride ion exposure on the ER of normal and SDA blended cement concrete.

3.3.6. Statistical analysis of the effects of w/b ratio, SDA and laterite on the ER of concrete

The essence of the statistical analysis is to examine the kind of relationship and extent of influence of the considered parameters influencing the electrical resistivity (ER) of concrete. These parameters include w-b ratio, SDA, laterite, curing age, and chloride ion. An analysis of variance (ANOVA) showed that significant differences exist within and between the considered parameters (see Tables 5-7), implying that statistical inferences can be made to reinforce inferences made earlier from the experimental results.

Table 5. Univariate ANOVA results for blended cement normal concrete.

Dependent Variable: Resistivity					
Source	Type III Sum of Squares	<i>df</i>	Mean Square	<i>F</i>	Sig.
Corrected Model	1003767252.861 ^a	59	17013004.286	481.467	.000
Intercept	2122246356.806	1	2122246356.806	60059.449	.000
SDA	240117320.994	3	80039106.998	2265.102	.000
w-b ratio	13252728.711	2	6626364.356	187.526	.000
Curing	327062851.222	4	81765712.806	2313.965	.000
SDA * w-b ratio	148135513.822	6	24689252.304	698.704	.000
SDA * curing	124052965.533	12	10337747.128	292.558	.000
w-b ratio * curing	32224314.178	8	4028039.272	113.993	.000
SDA * w-b ratio * curing	118921558.400	24	4955064.933	140.228	.000
Error	4240291.333	120	35335.761		
Total	3130253901.000	180			
Corrected Total	1008007544.194	179			

R Squared = 0.996, adjusted R Squared = 0.99, significance level $p=0.05$

Table 6. Univariate ANOVA results for blended cement laterized concrete.

Dependent Variable: Resistivity					
Source	Type III Sum of Squares	<i>df</i>	Mean Square	<i>F</i>	Sig.
Corrected Model	2040372430.122 ^a	119	17145986.808	434.915	.000
Intercept	5320664977.878	1	5320664977.878	134960.762	.000
w-b ratio	160075425.506	2	80037712.753	2030.188	.000
Mix (SDA, laterite)	540706908.389	7	77243844.056	1959.321	.000
Curing	550901403.761	4	137725350.940	3493.458	.000
w-b ratio * mix	403022369.828	14	28787312.131	730.202	.000
w-b ratio * curing	25300341.772	8	3162542.722	80.219	.000
mix * curing	174279559.972	28	6224269.999	157.881	.000
w-b ratio * mix * curing	186086420.894	56	3322971.802	84.288	.000
Error	9461710.000	240	39423.792		
Total	7370499118.000	360			
Corrected Total	2049834140.122	359			

a. R Squared = 0.995, adjusted R Squared = 0.993, significance level $p=0.05$

Table 7. Univariate ANOVA results for blended cement laterized concrete exposed to chloride ions.

Dependent Variable: Resistivity					
Source	Type III Sum of Squares	<i>df</i>	Mean Square	<i>F</i>	Sig.
Corrected Model	2471098784.998 ^a	191	12937689.974	385.934	.000
Intercept	7322788246.671	1	7322788246.671	218440.493	.000
w-b ratio	121762700.847	2	60881350.424	1816.105	.000
Mix (SDA, laterite)	472689447.984	7	67527063.998	2014.348	.000
Chloride	606444066.769	3	202148022.256	6030.123	.000
Curing	13989781.752	1	13989781.752	417.318	.000
w-b ratio * mix	666290802.208	14	47592200.158	1419.687	.000

Dependent Variable: Resistivity					
Source	Type III Sum of Squares	df	Mean Square	F	Sig.
w-b ratio * chloride	20576840.736	6	3429473.456	102.302	.000
w-b ratio * curing	6483224.222	2	3241612.111	96.698	.000
mix * chloride	204215511.523	21	9724548.168	290.086	.000
mix * curing	15837016.679	7	2262430.954	67.489	.000
chloride * curing	74549371.880	3	24849790.627	741.275	.000
w-b ratio * mix * chloride	155038680.764	42	3691397.161	110.115	.000
w-b ratio * mix * curing	53167007.389	14	3797643.385	113.285	.000
w-b ratio * chloride * curing	1949610.083	6	324935.014	9.693	.000
mix * chloride * curing	18734507.078	21	892119.385	26.612	.000
w-b ratio * mix * chloride * curing	39370215.083	42	937386.073	27.962	.000
Error	12872845.333	384	33523.035		
Total	9806759877.000	576			
Corrected Total	2483971630.332	575			

R Squared = 0.995, adjusted R Squared = 0.992, significance level $p=0.05$

Table 8 shows the correlation analysis which depicts the magnitude of influence of each material component on the workability. The italicized values show significant correlation. The Pearson correlation coefficients help to establish the relationship between the variables (such as slump versus SDA/laterite content, w-b ratio, SP content), that is, the strength of association between them in pairs. The laterite tends to negatively impact the slump more than the SDA and w-b ratio. This can imply that the laterite has more affinity for water than the SDA while the superplasticizer tends to positively improve the workability more than the water content. Furthermore, correlation analysis was carried between the electrical resistivity and the considered parameters (Table 9). The number of samples (N) represent specimens tested with unique values/result used in the correlation analysis. Table 9 reveals that curing age (out of all the parameters) have the highest impact on the ER except when it is exposed to chloride ion where the concentration of the ion influences more than the exposure time. Generally, SDA and laterite inclusion negatively affects the ER while the w-b ratio seems to positively influence the ER. It should, however, be noted that this positive influence is only significant for concrete containing both SDA and laterite (including exposure to chloride ion).

Table 8. Pearson correlation analysis of the parameter influencing the workability.

	SDA content	laterite content	w-b ratio	SP* content
Slump	-0.304	-0.576	+0.315	+0.651

* SP – superplasticizer, number of samples (N) = 24, significance level $p=0.05$

Table 9. Pearson correlation analysis of the parameter influencing the electrical resistivity.

		Mixes				
		SDA content	laterite content	w-b ratio	curing age	% NaCl
Laterized concrete	ER	–	-0.124	+0.037	+0.707	–
SDA blended concrete	ER	-0.421	–	+0.097	+0.548	–
SDA blended laterized concrete	ER		-0.364	+0.276	+0.505	–
SDA blended laterized concrete in NaCl	ER		-0.277	+0.220	-0.075	-0.457

* SP – superplasticizer; number of samples (N) = 90, 180, 360, 576 respectively; significance level $p=0.05$

Various Duncan multi range test results are shown in Table 10 to observe the average ER within each considered parameter. This statistics helps to reinforce the general inductions (from the previous sections) that increased curing improved the ER of the concrete, increased w-b ratio decreases the ER, increased SDA content reduces the ER; and that in the presence of chloride ion, laterite improves the ER of concrete while the further inclusion of SDA reduces the positive impact of the laterite. Furthermore, increased concentration of chloride ion reduces the ER of concrete.

Table 10. Duncan multi range test results.

Water curing				Chloride ion exposure					
Curing age		Water-binder ratio		SDA content		SDA and laterite		NaCl concentration	
N = 18		N = 30		N = 45		N = 72		N = 144	
Mean	Age	Mean	w-b	Mean	% SDA	Mean	Mixes	Mean	% NaCl
87.91	88 days	75.40	0.35	53.50	0%	50.2	CL	52.65	0%
75.47	58 days	49.64	0.5	33.05	10%	49.33	C	34.13	1%
54.20	28 days	46.88	0.65	26.88	20%	31.88	CS	30.13	3%
40.31	14 days			23.89	30%	30.00	CLS	25.68	5%
28.65	7 days								

4. Conclusion

The goal of this study is to examine the electrical resistivity (ER) of concrete. The concrete was modified with laterite as partial replacement of sand and saw dust ash (SDA) as a supplementary cementitious material (SCM). Effects of other factors such as w-b ratio, curing age, chloride ion exposure and concentrations. The following conclusions can be made from the results.

- Increased curing, hence, hydration increases the ER of concrete. The influence of w-b ratio on normal concrete, SDA blended cement concrete, laterized concrete and SDA blended cement laterized concrete were varied. A w-b ratio of 0.5 seemed favourable for normal and laterized concrete while 0.35 seemed the optimum for SDA blended cement concrete and SDA blended cement laterized concrete.
- Inclusion of laterite in concrete can improve the ER at higher water content. SDA has little or no potential to improve the ER of concrete at early age but can yield similar results at later age and reduced water content. However, inclusion of both laterite and SDA in concrete can potentially improve the ER at lower water content.
- The use of laterite in normal or blended cement concrete seems to stabilise the concrete against chloride ion exposure, especially at increased water content. That is, the laterite yielded better ER than the control in NaCl solution.
- Statistical analysis showed that, generally, the laterite tends to have more affinity for water than the SDA; increased curing increases ER, water content reduces ER, SDA reduces ER, chloride ion reduces ER while the laterite improves ER in the presence of chloride ion.

References

1. Das, S., Clements, W., Raju, G. Non-Destructive Electrical Methods to Determine the Quality of Concrete. Athens Journal of Technology & Engineering. 2014. 1(4). Pp. 241–252. DOI:10.30958/ajte.1-4-1.
2. Hamed, A., Aly, N., Gomez-Heras, M., de Buergo, M.A. New experimental method to study the combined effect of temperature and salt weathering. Geological Society Special Publication. 2016. 416(1). Pp. 229–237. DOI:10.1144/SP416.18.
3. Baroghel-Bouny, V., Kinomura, K., Thiery, M., Moscardelli, S. Easy assessment of durability indicators for service life prediction or quality control of concretes with high volumes of supplementary cementitious materials. Cement and Concrete Composites. 2011. 33(8). Pp. 832–847. DOI:10.1016/j.cemconcomp.2011.04.007.
4. Alexander, M.G., Ballim, Y., Stanish, K. A framework for use of durability indexes in performance-based design and specifications for reinforced concrete structures. Materials and Structures/Materiaux et Constructions. 2008. 41(5). Pp. 921–936. DOI: 10.1617/s11527-007-9295-0.
5. Gjrv, O.E. Durability design and construction quality of concrete structures. Proceedings of 4th International Conference on Concrete under Severe Conditions-Environment and Loading. 2004. 1. Pp. 44–55.
6. Silva, B.J., Jalali, S., Ferreira, R.M. Estimating electrical resistivity based on early age measurements. Proceedings of the International RILEM Workshop Performance Based Evaluation and Indicators for Concrete Durability. 2006. Pp. 67–74.
7. Ferreira, R.M., Jalali, S. NDT measurements for the prediction of 28-day compressive strength. NDT and E International. 2010. 43(2). Pp. 55–61. DOI:10.1016/j.ndteint.2009.09.003.
8. Wilson, J.G., Whittington, H.W., Forde, M.C. Physical interpretation of microcomputer-controlled automatic electrical resistivity measurements on concrete. NDT International. 1985. 18(2). Pp. 79–84. DOI:10.1016/0308-9126(85)90101-4.
9. Hope, B.B., Ip, A.K., Manning, D.G. Corrosion and electrical impedance in concrete. Cement and Concrete Research. 1985. 15(3). Pp. 525–534. DOI:10.1016/0008-8846(85)90127-9.
10. Hunkeler, F. The resistivity of pore water solution - A decisive parameter of rebar corrosion and repair methods. Construction and Building Materials. 1996. 10(5 SPEC. ISS.). Pp. 381–389. DOI:10.1016/0950-0618(95)00029-1.
11. Saleem, M., Shameem, M., Hussain, S.E., Maslehuddin, M. Effect of moisture, chloride and sulphate contamination on the electrical resistivity of Portland cement concrete. Construction and Building Materials. 1996. 10(3). Pp. 209–214. DOI:10.1016/0950-0618(95)00078-X.
12. Banea, P.I. The study of electrical resistivity of mature concrete. Delft University, Netherlands, 2015.

13. Balestra, C.E.T., Reichert, T.A., Pansera, W.A., Savaris, G. Evaluation of chloride ion penetration through concrete surface electrical resistivity of field naturally degraded structures present in marine environment. *Construction and Building Materials*. 2020. 230. Pp. 116979. DOI: 10.1016/j.conbuildmat.2019.116979.
14. Fares, M., Villain, G., Bonnet, S., Palma Lopes, S., Thauvin, B., Thiery, M. Determining chloride content profiles in concrete using an electrical resistivity tomography device. *Cement and Concrete Composites*. 2018. 94. Pp. 315–326. DOI: 10.1016/j.cemconcomp.2018.08.001.
15. Sengul, O. Use of electrical resistivity as an indicator for durability. *Construction and Building Materials*. 2014. 73. Pp. 434–441. DOI: 10.1016/j.conbuildmat.2014.09.077.
16. Tuutti, K. Corrosion of steel in concrete. Lund University, 1982.
17. Buenfeld, N.R., Newman, J.B., Page, C.L. The resistivity of mortars immersed in sea-water. *Cement and Concrete Research*. 1986. 16(4). Pp. 511–524. DOI: 10.1016/0008-8846(86)90089-X.
18. Simon, T., Vass, V. The electrical resistivity of concrete. *Concrete Structures*. 2012. 13. Pp. 61–64.
19. He, R., Ma, H., Hafiz, R.B., Fu, C., Jin, X., He, J. Determining porosity and pore network connectivity of cement-based materials by a modified non-contact electrical resistivity measurement: Experiment and theory. *Materials and Design*. 2018. 156. Pp. 82–92. DOI: 10.1016/j.matdes.2018.06.045.
20. Bakar, B.H., Putra Jaya, R., Hamidi, A. Malaysian Rice Husk Ash – Improving the Durability and Corrosion Resistance of Concrete: Pre-review. *Concrete Research Letters*. 2010. 1.
21. Elinwa, A.U., Abdulkadir, S. Sawdust Ash as an Inhibitor for Reinforcement Corrosion in Concrete. *MOJ Civil Engineering*. 2016. 1(3). DOI: 10.15406/mojce.2016.01.00015.
22. Elinwa, A.U., Ejeh, S.P., Mamuda, A.M. Assessing of the fresh concrete properties of self-compacting concrete containing sawdust ash. *Construction and Building Materials*. 2008. 22(6). Pp. 1178–1182. DOI: 10.1016/j.conbuildmat.2007.02.004.
23. Negussie, T. Structural use of scoria concrete. *African Journal of Science and Technology. Series A, Technology*. 1990. 8(1). Pp. 44–49.
24. Rydychowska, D.T. The effect of aggregate variation on the compressive strength of laterite concrete. *Cement and Concrete Research*. 1986. 16(2). Pp. 135–142. DOI: 10.1016/0008-8846(86)90129-8.
25. Muthusamy, K., Kamaruzzaman, N.W., Zubir, M.A., Hussin, M.W., Sam, A.R.M., Budiea, A. Long Term Investigation on Sulphate Resistance of Concrete Containing Laterite Aggregate. *Procedia Engineering*. 2015. 125. Pp. 811–817. DOI: 10.1016/j.proeng.2015.11.145.
26. Awoyera, P.O., Akinmusuru, J.O., Ndambuki, J.M. Green concrete production with ceramic wastes and laterite. *Construction and Building Materials*. 2016. 117. Pp. 29–36. DOI: 10.1016/j.conbuildmat.2016.04.108.
27. Yaragal, S.C., Gowda, S.N.B., Rajasekaran, C. Characterization and performance of processed lateritic fine aggregates in cement mortars and concretes. *Construction and Building Materials*. 2019. 200. Pp. 10–25. DOI: 10.1016/j.conbuildmat.2018.12.072.
28. Hansson, I.L.H., Hansson, C.M. Electrical resistivity measurements of Portland cement based materials. *Cement and Concrete Research*. 1983. 13(5). Pp. 675–683. DOI: 10.1016/0008-8846(83)90057-1.
29. Bütetführ, M., Fischer, C., Gehlen, C., Menzel, K., Nürnberger, U. On-site investigations on concrete resistivity – a parameter of durability calculation of reinforced concrete structures. *Materials and Corrosion*. 2006. 57(12). Pp. 932–939. DOI: 10.1002/maco.200604019.
30. Andrade, C., D'Andrea, R. Electrical resistivity as microstructural parameter for the modelling of service life of reinforced concrete structures. *2nd International Symposium on Service Life Design for Infrastructure*. 2010. Pp. 379–388.
31. Chang, C., Song, G., Gao, D., Mo, Y.L. Temperature and mixing effects on electrical resistivity of carbon fiber enhanced concrete. *Smart Materials and Structures*. 2013. 22(3). DOI: 10.1088/0964-1726/22/3/035021.
32. Chen, C.T., Chang, J.J., Yeih, W.C. The effects of specimen parameters on the resistivity of concrete. *Construction and Building Materials*. 2014. 71. Pp. 35–43. DOI: 10.1016/j.conbuildmat.2014.08.009.
33. BS EN 933-1. Tests for geometrical properties of aggregates. Determination of particle size distribution. Sieving method 2012.
34. BS ISO 29581-2. Cement : test methods. Part 2, Chemical analysis by X-ray fluorescence. British Standards Institution. London, UK, 2010.
35. BS EN 13925-2. Non-destructive testing. X-ray diffraction from polycrystalline and amorphous materials. Procedures. British Standard Institute. London, UK, 2003.
36. BS ISO 16700. Microbeam analysis. Scanning electron microscopy. Guidelines for calibrating image magnification. British Standard Institute. London, UK, 2016.
37. ASTM C618. Standard Specification for Coal Fly Ash and Raw or Calcined Natural Pozzolan for Use in Concrete. ASTM International. West Conshohocken, PA, 2012.
38. BS EN 12350-2. Testing fresh concrete. Slump-test. British Standards Institution, BSI. London, UK, 2009.
39. ASTM C192/C192M. Standard practice for making and curing concrete test specimens in the laboratory. ASTM International. West Conshohocken, PA, 2018.
40. USGS. Why is the Ocean Salty? 2019URL: https://www.usgs.gov/special-topic/water-science-school/science/why-ocean-salty?qt-science_center_objects=0#qt-science_center_objects (date of application: 6.01.2020).
41. AASHTO T 358. Standard Method of Test for Surface Resistivity Indication of Concrete's Ability to Resist Chloride Ion Penetration California, 2015.
42. Azarsa, P., Gupta, R. Electrical Resistivity of Concrete for Durability Evaluation: A Review. *Advances in Materials Science and Engineering*. 2017. 2017. DOI: 10.1155/2017/8453095.
43. Lencioni, J.W., de Lima, M.D., Lima, M. A Study of the Parameters that Affect the Measurements of Superficial Electrical Resistivity of Concrete. *Nondestructive Testing of Materials and Structures*. 6. Springer. Dordrecht, 2013. Pp. 271–276.
44. Yaseri, S., Hajiaghahi, G., Mohammadi, F., Mahdikhani, M., Farokhzad, R. The role of synthesis parameters on the workability, setting and strength properties of binary binder based geopolymer paste. *Construction and Building Materials*. 2017. 157. Pp. 534–545. DOI: 10.1016/j.conbuildmat.2017.09.102.
45. Kolawole, J.T., Olalusi, O.B., Orimogunje, A.J. Adhesive bond potential of compressed stabilised earth brick. *Structures*. 2020. 23. Pp. 812–820. DOI: 10.1016/j.istruc.2019.12.024.

46. Kamtchueng, B.T., Onana, V.L., Fantong, W.Y., Ueda, A., Ntuala, R.F., Wongolo, M.H., Ndong, G.B., Ze, A.N., Kamgang, V.K., Ondoa, J.M. Geotechnical, chemical and mineralogical evaluation of lateritic soils in humid tropical area (Mfou, Central-Cameroon): Implications for road construction. *International Journal of Geo-Engineering*. 2015. 6(1). Pp. 1–21. DOI: 10.1186/s40703-014-0001-0.
47. Coppio, G.J.L., de Lima, M.G., Lencioni, J.W., Cividanes, L.S., Dyer, P.P.O.L., Silva, S.A. Surface electrical resistivity and compressive strength of concrete with the use of waste foundry sand as aggregate. *Construction and Building Materials*. 2019. 212. Pp. 514–521. DOI: 10.1016/j.conbuildmat.2019.03.297.
48. Zhao, R., Weng, Y., Tuan, C.Y., Xu, A. The influence of water/cement ratio and air entrainment on the electric resistivity of ionically conductive mortar. *Materials*. 2019. 12(7). DOI: 10.3390/ma12071125.
49. Garzon, A.J., Sanchez, J., Andrade, C., Rebollo, N., Menéndez, E., Fullea, J. Modification of four-point method to measure the concrete electrical resistivity in presence of reinforcing bars. *Cement and Concrete Composites*. 2014. 53. Pp. 249–257. DOI: 10.1016/j.cemconcomp.2014.07.013.
50. Dong, B., Zhang, J., Wang, Y., Fang, G., Liu, Y., Xing, F. Evolutionary trace for early hydration of cement paste using electrical resistivity method. *Construction and Building Materials*. 2016. 119. Pp. 16–20. DOI: 10.1016/j.conbuildmat.2016.03.127.
51. Su, J.K., Yang, C.C., Wu, W.B., Huang, R. Effect of moisture content on concrete resistivity measurement. *Journal of the Chinese Institute of Engineers, Transactions of the Chinese Institute of Engineers, Series A/Chung-kuo Kung Ch'eng Hsueh K'an*. 2002. 25(1). Pp. 117–122. DOI:10.1080/02533839.2002.9670686.
URL: <https://www.tandfonline.com/doi/abs/10.1080/02533839.2002.9670686> (date of application: 30.09.2020).
52. Neville, A.M. *Properties of concrete*. Second. Prentice Hall. Upper Saddle River, 2011.
53. Owens, G. *Fundamentals of concrete*. Third. Cement and Concrete Institute, 2013.
54. Polder, R.B. Test methods for onsite measurement of resistivity of concrete - a RILEM TC-154 technical recommendation. *Construction and Building Materials*. 2001. 15(2–3). Pp. 125–131. DOI:10.1016/S0950-0618(00)00061-1.
55. Villagrán-Zaccardi, Y.A., Di Maio, Á.A. Electrical resistivity measurement of unsaturated concrete samples. *Magazine of Concrete Research*. 2014. 66(10). Pp. 484–491. DOI: 10.1680/macr.13.00207.
56. Muthusamy, K., Kamaruzaman, N. Assessment of Malaysian Laterite Aggregate in Concrete. *International Journal of Civil & Environmental Engineering*. 2012. 12(4). Pp. 83–86.
57. Godavarthy, S., Ratnam, M.K.M., Prasad, A.C.S., Raju, U.R. A Study on Strength and Durability Characteristics of Concrete with Partial Replacement of Fine aggregate by Laterite Sand. *International Journal for Innovative Research in Science and Technology*. 2015. 2(3). URL: <http://ijrst.org/Article.php?manuscript=IJIRSTV2I3034> (date of application: 30.12.2019).
58. Lo, T.Y., Cui, H.Z. Effect of porous lightweight aggregate on strength of concrete. *Materials Letters*. 2004. 58(6). Pp. 916–919. DOI: 10.1016/j.matlet.2003.07.036.
59. Wasserman, R., Bentur, A. Interfacial interactions in lightweight aggregate concretes and their influence on the concrete strength. *Cement and Concrete Composites*. 1996. 18(1). Pp. 67–76. DOI: 10.1016/0958-9465(96)00002-9.
60. Rupnow, T.D., Icenogle, P.J., Rupnow, T.D., Icenogle, P.J. Evaluation of Surface Resistivity Measurements as an Alternative to the Rapid Chloride Permeability Test for Quality Assurance and Acceptance 2 3 Submission Louisiana, 2011.
61. Ajayi, E.O., Babafemi, A.J. Effects of Pulverized Burnt Clay Waste Fineness on the Compressive Strength and Durability Properties of Blended Cement Concrete. *Engineering Journal*. 2018. 22(2). Pp. 83–99. DOI: 10.4186/ej.2018.22.2.83
62. Gastaldini, A.L.G., Isaia, G.C., Hoppe, T.F., Missau, F., Saciloto, A.P. Influence of the use of rice husk ash on the electrical resistivity of concrete: A technical and economic feasibility study. *Construction and Building Materials*. 2009. 23(11). Pp. 3411–3419. DOI: 10.1016/j.conbuildmat.2009.06.039.
63. Udoeyo, F.F., Dashibil, P.U. Sawdust Ash as Concrete Material. *Journal of Materials in Civil Engineering*. 2002. 14(2). Pp. 173–176. DOI: 10.1061/(ASCE)0899-1561(2002)14:2(173).
64. Raheem, A.A., Ige, A.I. Chemical composition and physicochemical characteristics of sawdust ash blended cement. *Journal of Building Engineering*. 2019. 21. Pp. 404–408. DOI: 10.1016/j.job.2018.10.014.
65. Singh, N., Singh, S.P. Electrical resistivity of self-consolidating concretes prepared with reused concrete aggregates and blended cements. *Journal of Building Engineering*. 2019. 25. DOI: 10.1016/j.job.2019.100780.

Contacts:

Adewumi John Babafemi, ajbabafemi@sun.ac.za

Olayemi Temilorun Akinola, akinolaolayemi@gmail.com

John Temitope Kolawole, j.t.kolawole@lboro.ac.uk

Suvash Chandra Paul, suvashpl@iubat.edu

Md Jihad Miah, jihad.miah@uap-bd.edu



DOI: 10.34910/MCE.105.3

Self-healing bacterial mortar with calcium lactate and improved properties

V.V. Galishnikova^a , S.H. Elroba^{*b} , M. Nassar^c , A. Sakna^d 

^a National Research Moscow State Civil Engineering University, Moscow, Russia

^b Peoples' Friendship University of Russia, Moscow, Russia

^c Renders Engineering Consultants, Dubai

^d Egyptian Russian University, Badr City, Egypt

*E-mail: ERU.SHERIF@yahoo.com

Keywords: crack, self healing, Bacterial Mortar, Bio-cement, mechanical properties, Permeability, Scanning Electron Microscopy, calcite precipitation

Abstract. The advancing technologies of self-healing concrete focus on reversing and repairing the micro-cracks that form in concrete at early ages, increasing the durability of the structure. The utilization of the metabolic properties of bacteria in bacteria-based self-healing mortar has yielded promising results in the reduction of cracks. Two species of bacteria *Bacillus sphaericus* (BS), *Bacillus pasteurii* (BP) were used in this study and patched at a ratio of cement weight in addition to Calcium Lactate being added as nutrition of bacteria. Setting time test was performed to measure the effect of bacteria on fresh mortar properties. The bacterial mixtures were compared to control mix to study their behavior under the influence of permeability test, compressive strength test, flexural strength test, sulfate resistance test and acid resistance test. Also, the restoration of bacterial mixes was tested. Furthermore, advanced technique were employed to evaluate the influence of bacteria addition, e.g. Scanning Electron Microscope (SEM). The cell concentration of *Bacillus sphaericus* (BS) and *Bacillus pasteurii* (BP) of all bacterial mortar mixes were counted. The bacteria nutrition acts as accelerator of cement pastes for initial setting time for all bacterial mortar compared to control mortar, while acts as a retarder of cement pastes for final setting time for all bacterial mortar compared to the control samples. Rate of water Absorption decreased with time and became nearly impermeable for BS60 and BP60 at the age of 120 days. Compressive strength of BS60 at 120 days age increased by 124 % compared to the control specimens. Flexural strength value of BS30 at the age of 120 days increased by 168 % compared to control mortar. Results showed that BP60 had a high ability to resist salts and acids. SEM proved that the bacterial mortar had less voids than that of control mortar. Microbial Induced Calcite Precipitation (MICP) is responsible for filling up the pores in mortar and hence decreased the rate of water absorption and the capillary permeability coefficient, while increasing the compressive and flexural strength for bacterial mortar.

1. Introduction

The past decade, researchers around the globe have addressed the problem of micro cracks forming in concrete and studied its effect on the future durability and service life of structural elements. Cracks at early ages in concrete are usually the result of rapid temperature changes causing shrinkage stresses during the setting process for concrete, in addition to the loading of reinforced elements [1]. Even though the formation of micro-cracks is not an immediate threat to the integrity and strength of the element, it usually leads to permeability and durability issues, especially in humid or wet environments. Formation of micro-cracks usually result in the exposure of the embedded steel rebar to external conditions, thus, resulting in corrosion and needing costly maintenance and repair procedures [2]. Epoxies and other

Galishnikova, V.V., Elroba, S.H., Nassar, M., Sakna, A. Self-healing bacterial mortar with calcium lactate and improved properties. Magazine of Civil Engineering. 2021. 105(5). Article No. 10503. DOI: 10.34910/MCE.105.3

© Galishnikova, V.V., Elroba, S.H., Nassar, M., Sakna, A., 2021. Published by Peter the Great St.Petersburg Polytechnic University



This work is licensed under a CC BY-NC 4.0

synthetic materials have been previously used to remediate these cracks but alternatives for them are being considered because of their incompatibility with cementitious materials in addition to their higher costs.

Mineral formations such as limestone in concrete can be of use and favorable to the concrete's durability. As they are concrete-compatible materials, they work on closing up and sealing the cracks, making the concrete less permeable and protecting the steel rebar from compounds such as chlorides and other corrosion-inducing chemicals that would otherwise reach the rebar through the cracks. Over the past decade various researchers experimented with various concepts of self-healing using a biological base. Albeit each species of bacteria experimented on has different metabolic process, they all share the same principal: an encased specie of bacteria is added to the fresh concrete mix and when cracks occur in the hardened concrete the changing environmental conditions works on activating the bacteria which precipitates calcium carbonate and closes the crack [3–7]. The metabolic process for the bacteria creates limestone depositions, thus, recovering the functional properties of concrete as the aim of this research. The properties regained with the healing of cracks in concrete include reduced permeability, strength or aesthetics. The 'self-healing agent' needed to enhance the healing ability for concrete is encased bacteria in addition to the required mineral and chemical compounds which are added to the concrete mixture. This increased healing ability would reduce the cost of repairs, but it would also enhance the longevity of the structure. Multiple species of bacteria were used to produce calcium carbonate and other inorganic minerals [8]. This process, being a biological process, depends on specific environmental conditions, therefore, the bacteria can make use of certain metabolic pathways in order to change the environmental conditions to facilitate the production of inorganic materials.

Previous research has been done on adding certain bacteria that would result in the desired mineral disposition on concrete with recycled aggregate and has shown an improvement in the crack width and depth in addition to the increase in compressive and flexural tensile strengths [9], [10]. Other researchers has studied the effect of bacteria spores encapsulated in hydrogel on cement mortar cracks and has shown the ability to heal cracks up to 0.5 mm in width [11]. As for the problem with the increased water absorption of cementitious materials due to the formation of micro-cracks, a research in 2008 has shown that the self-healing effect of bacteria can reduce the water absorption by 60–90% thus reducing chloride migration by up to 40 % [12]. In addition, a more recent 2018 study has been performed on *S. Pasteurii* bacteria in addition to calcium chloride and urea-calcium lactate as nutrition for the bacteria and it showed that the self-healing properties of the bacteria has improved the compressive strength by 60 % at 28 days of age and reduced the water absorption by up to 55 % in cement mortar specimen [13]. It was also revealed that the maximum crack healing occurs at the maximum bacterial concentration [14], [15].

This process, in addition to recovering the original performance of concrete by repairing its cracks [16], [17], it is also more compatible and environmentally friendly than the traditional repair materials [18]. The goal of this study is to demonstrate bacteria's potential in enhancing and affecting the mechanical properties of concrete. Setting time test was performed to measure the effect of bacteria on fresh mortar properties. The bacterial mixtures were compared to control mix to study their behavior under the influence of permeability test, compressive strength test, flexural strength test, sulfate resistance test and acid resistance test. Also, the restoration of bacterial mixes was tested. Rate of Water Absorption test and compressive strength test were performed at the ages of 3, 7, 28, 90 and 120 days. Flexural Strength test was performed at the ages of 28, 90 and 120 days. Sulfate Resistance Test and acid Resistance test were performed at the ages of 28 and 90 to determinate the rate of water absorption and the capillary permeability coefficient. Also sulfate resistance test and acid resistance test were performed at the ages of 28, 90 and 180 days to determinate compressive strength. In addition to the mechanical and physical, advanced technique was employed to evaluate the influence of bacteria addition, e.g. Scanning Electron Microscope (SEM).

2. Methods

2.1. Materials

2.1.1 Cement

The properties of mortar are dependent on the ratios and qualities of its constituent. Since cement is the main binding component of mortar and is usually the key cost item, its selection and proper use is crucial in obtaining the most economic mortar mixture with the desired properties. Ordinary Portland (Type 1) grade 42.5 N confirming to the ASTM Standard Specifications was used [19].

2.1.2. Fine aggregate

The fine aggregate used was natural sand. The sand was clean free from impurities. Medium well-graded sand of fineness modulus 2.2mm was used for mortar.

The main physical and mechanical properties of the used sand were measured according to ASTM concrete aggregate specifications [20].

2.1.3. Water

Clean tap drinking water was used for mixing and curing in this work, tap water that used was free from impurities [21].

2.1.4. Bacteria

Two types of bacteria were used in this work (*Bacillus Pasteurii* DSM 33, *Bacillus Sphaericus* DSM 396). The pH for these bacteria is usually neutral and germinates at a pH of 7.0 [22]. The percentages of added bacteria were 0.6 % and 0.3 % by the weight of cement.

Both bacteria were cultured in "Luria-Bertani" (LB) broth medium containing, g/L (12g Yeast Extract, 12g peptone and 6g sodium chloride) [23]. The pH was adjusted to 7.0 and cultures were aerobically incubated in 2L Erlenmeyer flasks using a rotary shaking incubator at 150 rpm for 7 days at 30 °C. Growth and sporulation yield of bacteria was regularly checked and quantified using microscopic analysis and pour-plate count method.

2.1.5. Calcium lactate

Calcium lactate is also known as calcium salt pent hydrate and the chemical formula is $(Ca(C_3H_5O_3)_2)$. This calcium lactate powder is produced by reacting lactic acid with calcium-based water-soluble compounds such as calcium carbonate or calcium hydroxide.

2.2. Mortar mixes

The dry mortar mixture was weighed and mixed using concrete mixer machine for ten minutes. The water was poured afterwards, and mixing process lasted for another ten minutes. Mortar proportions were chosen according to Ferro cement Model Code [24]. Sand/cement ratio was 1:3 by weight. Water/cement ratio was 0.45. Specimens were prepared for mortar mix with (bacterial mortar) addition of calcite-producing *Bacillus pasteurii* or *Bacillus sphaericus*. Control mortar mix was prepared as well to study the effect of bacteria addition.

Bacteria were added to mortar with two ratios (0.6 % and 0.3 % of cement weight). Calcium Lactate was added as nutrition to bacteria by 0.3 % and 0.15 % of cement weight. Experimental mortar mixes proportions are shown in Table 1. The mortar was cast in moulds for different tests. Test specimens were remolded after 24 hours and kept in a wet case. The specimens were kept moist till testing time.

Table 1. Experimental mortar mixes proportions with bacteria and calcium lactate.

Mix	Samples	Sand/ Cement	Water/ Cement	Bacteria /Cement	Calcium Lactate/ Cement
1.	Control			0.0	0.0
2.	<i>B. sphaericus</i> (BS50)			0.6 %	0.3 %
3.	<i>B. sphaericus</i> (BS25)	3:1	0.45	0.3 %	0.15 %
4.	<i>B. pasteurii</i> (BP50)			0.6 %	0.3 %
5.	<i>B. pasteurii</i> (BP25)			0.3 %	0.15 %

2.3. Specimen preparation and testing

2.3.1. Preparation of bacteria

Both bacteria were cultured in liquid media containing (1000.0 ml distilled water, 5.0 g Peptone, 3.0 g yeast extract, 15.0 g Agar) [25]. Adjust pH to 7.0. For *Bacillus* strains the addition of 10.0 mg $MnSO_4 \times H_2O$ is recommended for sporulation, In addition to the above-mentioned 24 g/l Urea only should be added to bacteria of *Bacillus Pasteurii* during preparation. Media is added in to conical flask. It is then made air tight by sealing the flask with a paper and a rubber band. The solution is then sterilized using a flame burner for 10-20 minutes. Now the solution should be free from any contaminants and the solution is a clear orange color before the addition of the bacteria [26].

Later the flasks are opened up and an exactly 1 ml of the bacterium is added to the sterilized flask and is kept in a shaker at a speed of 150–200 rpm overnight at 30 °C. After 24 hours the bacterial solution was found to be whitish yellow turbid solution. Bacterial cultures were incubated for 7 days to ensure sporulation then put it within falcon tube 50mm inside centrifugation at 10000 rpm for 10 minutes. Finally,

the cell pellets were re-suspended in sterile solution of 0.9% NaCl to harvest the vegetative cells and spores. Optical density of the bacterial cultures and pure plate count method were used to prepare culture suspensions with a final cell density of 10^9 CFU/mL, then used in two concentrations including, 0.6 % and 0.3 % of the cement weight, respectively.

2.4. Mortar tests

2.4.1. Bacterial count

After cement mortar preparation and solidification both control and treated cement mortar samples were collected for bacterial counts after 3, 7, 14, 28, 60, 90 and 120 days. Ten gram of each sample was added to 90 mL of sterile 0.9 % NaCl solution and left over night to release the bacterial cells and spores from the cement mortar [27], then serial dilutions of each sample were done by the addition of 1 mL of sample suspensions to 9 mL of sterile 0.9 % NaCl solution, afterwards 1 mL of the final dilution was added to petri dish containing about 20 mL of solid LB medium dispensed over each plate in triplicates for each dilution as shown in Figure 1. Finally, the plates were incubated at 30 °C for 6 days and the CFU/mL in each plate [27] was counted during the time course for *Bacillus sphaericus* (BS) and *Bacillus pasteurii* (BP).

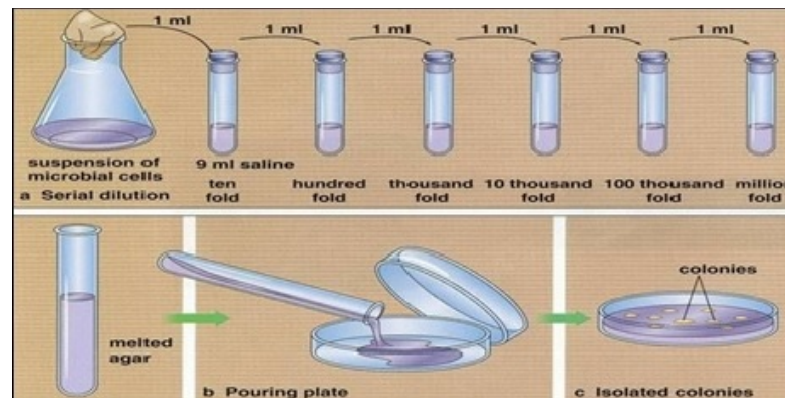


Figure 1. Serial dilution method for bacterial count [29].

2.4.2. Fresh mortar properties

Initial and final setting time tests were carried out by Vicat's apparatus for cement paste [19].

The cement was used without any addition. Standard water/cement ratio was experimented on cement only prior to setting time tests [29].

Another four cement pastes were mixed using the same water ratio with the addition of bacteria and calcium lactate as shown in Table 1 to investigate the effect of bacteria on setting time.

2.5. Hardened mortar properties

2.5.1. Physical properties

2.5.1.1. The rate of water absorption

Speed of water absorption is a measure of the capillary forces caused by the porosity of the structure, thus, forcing liquids to flow into the body of the structure. In this experiment, the flow of water into the body of the samples increased due to the water absorption at times when only one face of the sample was exposed to water [30]. Mortar samples were oven dried at 70 °C for 24 hours and then cooled after 3, 7, 28, 90 and 120 after allowing their moisture to slowly evaporate using the moist curing method. The flow of water in one direction was confirmed by covering the sides of the mortar specimen in silicone pastes. The top and bottom of the samples were insulated using plastic sheets fixed using plastic bands. The initial masses of the samples were recorded after which they were kept partially immersed to a depth of 10 cm in water. The new readings for masses were taken after 2 hours from first contact with water, the samples were removed, and excess water was blotted off using paper towel and then weighed [31]. The gain in mass (Δm , kg/s) at time t (s), exposed area of the specimen (a , m^2), and density of water (d), were used to obtain the rate of water absorption (I , $m/s^{1/2}$) as per the equation [31], [32]:

$$I = \frac{\Delta m}{(a.d)} \quad (1)$$

2.5.1.2 Capillary permeability coefficient

For capillary water absorption tests, specimens were taken from the water curing pan at age of 3, 7, 28, 90 and 120 days, and kept in the drying oven for 24 hours at 70 °C. Afterwards, specimens are taken

out of the oven to be cooled down and immersed in water making sure that only 0.5 cm of the cut surface is submerged in water. Other surfaces were sealed with impermeable tape to prevent exposure to water. After the first 24 hours, the specimens were taken out of the water, dried, weighed, and finally the capillary permeability coefficient was calculated from the following formula [33]:

$$K = \frac{Q^2}{(A^2 \times t)} \quad (2)$$

where Q is the amount of water absorbed (cm³)

K is capillary permeability coefficient (cm²/s)

A is the area of the specimen in contact with water (cm²)

t is the time elapsed (s)

2.5.2. Mechanical properties

2.5.2.1. Compressive strength test

The compression test was conducted for the prepared mortar cubes. Test specimens with dimensions of 70×70×70 mm were used. All specimens were given 24 hours to harden and to be cured. Three specimens were used for each age. After the study period of 3, 7, 28, 90 and 120 days, all the specimens were tested up to determine the failure load in a compression stress apparatus of 3000 kN capacity [4].

2.5.2.2. Restoration of bacteria

Samples were loaded after 14 days from casting date with half of failure load at 7 days. Samples were kept moisturized. Then, samples were put to the test to determine the compressive strength at (28 and 90 days). All specimens were tested for its maximum load in the compression testing machine for each age. Average for three tested specimens for each age was taken.

2.5.2.3. Flexural strength test

Test specimens with dimensions of (160×40×40 mm) were casted. The flexural specimens were subjected to three point loading test. The flexural strength was determined for 28, 90 and 120 days, using a flexural testing machine with a capacity of 15 ton to determine the maximum load before failure.

Average of three tested specimens for each age was taken. The flexural strength is calculated using the formula given below [34], [35]:

$$\text{Flexural strength} = \frac{3PL}{2 \times d_1 \times d_2^2}$$

where P is the maximum applied load to the specimen (N);

d_1 is the width of the specimen (mm);

d_2 is the depth of specimen (mm).

2.6.3. Durability of cement mortar

2.6.3.1. Sulfate resistance test

In this test samples were taken after a month from the date of casting and immersed in sodium sulfate solution with 5 % concentration [36]. Samples were tested to determine the rate of water absorption and capillary permeability coefficient at (28 and 90 days). Two samples of each age were prepared for each test separately.

Other samples were tested to determine the compressive strength at (28, 90 and 180 days). Three samples of each age were prepared for each test separately.

Average of two tested specimens for each age were taken to determinate the rate of water absorption and capillary permeability coefficient, while average of three tested specimens for each age were taken to determinate the compressive strength. Before the measurements, the specimens were removed from sodium sulfate solution then wiped and cleaned.

2.6.3.2. Acid resistance test

In this test samples were taken after a month from the date of casting and immersed in sulfuric acid solution with 1.5 % concentration [37]. Samples were tested to determine the rate of water absorption and

capillary permeability coefficient at (28 and 90 days). Two samples of each age were prepared for each test separately. Other samples were tested to determine the compressive strength at (28, 90 and 180 days). Three samples of each age were prepared for each test separately. Average of two tested specimens for each age were taken to determinate the rate of water absorption and capillary permeability coefficient, while average of three tested specimens for each age were taken to determinate the compressive strength. Before the measurements, the specimens were removed from sulfuric acid solution then wiped and cleaned.

2.6.4. Advanced techniques of self-healing investigation

2.6.4.1. Stopping of the hydration

The stopping of hydration was accomplished by using alcohol-acetone method at age of 120 days of curing then inspected using Scanning Electron Microscopy (SEM). The stopping solution was prepared as (1:1 v/v) of methyl alcohol and acetone. About 10 g was taken from the sample, ground and stirred with 100 ml of stopping solution, then filtered through sintered glass funnel (G4), washed with the same solution three times and finally with Ether. Each sample was dried at 90 °C for 24 hours and then kept in air-tight bottles inside desiccators till the time of testing.

2.6.4.2. Scanning electron microscopy (SEM)

The scanning electron microphotographs were taken with an Energy Dispersive X-ray Analyzer (EDAX). The device is used to scan the microstructures on the surface of a sample using a tightly focused electron beam to produce an image from the interaction of the beam with the microstructures on the surface of the specimen interactions detected by a wide array of sensors. There are a wide range of detectors from secondary electron detectors to give surface information to backscattered detectors for compositional information that work in high or low vacuum modes. Also, it is used to examine the microstructure of the fractured composites with accelerating voltage 30 K.V., magnification 14x up to 106 and resolution for Gun.1n. These samples that were used to conduct SEM observation are first dried at 70 °C until the constant weight is reached, then bonded on the sample holders with conducting glue carbon [38]. The morphology of the mortar specimens after 120 days curing were observed using Inspect S Scanning Electron. Four magnifications of 150, 1500, 5000 and 7500 were selected for the imaging [39].

3. Results and Discussion

3.1. Bacterial count

The statistical analyses of the given data using one-way ANOVA with post-hoc Tukey HSD Test with Scheffé, Bonferroni and Holm multiple comparison, indicated that, there was no significant difference in the bacterial count between *B. Pasteurii* and *B. Sphaericus* during the time course as shown in Figure 2. It is concluded that no significant effects between *B. Pasteurii* and *B. Sphaericus* on bacterial counts during the time course.

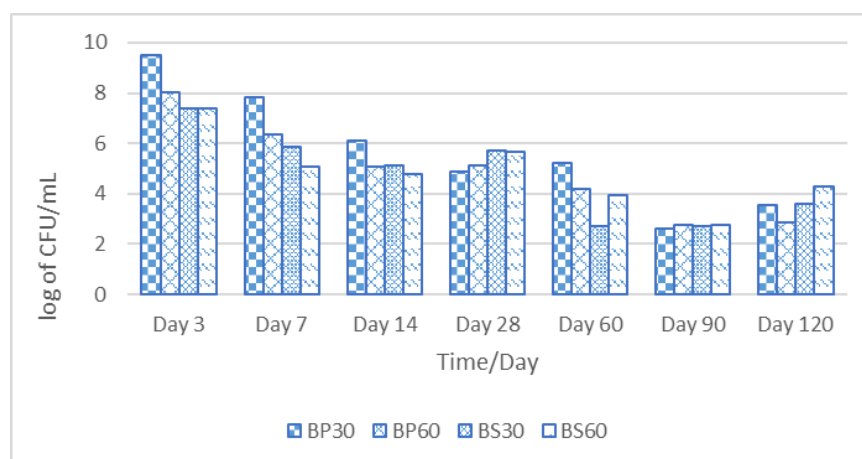


Figure 2. Log of bacterial count CFU/mL of each bacterium (BP = *Bacillus Pasteurii*, BS = *Bacillus Sphaericus*) in 0.25 and 0.5 % concentration, respectively for 3, 7, 14, 28, 60, 90 and 120 days. (Blank = LB Agar Medium without Any Samples, Control = Is Untreated Concrete Sample).

On the other hand, the bacterial count decreased during the time course and this can be suggested as a result of depletion of the nutritional elements found in the mortar. Also, both species follow the same growth trend and were adapted in the same rate with the new environmental conditions inside the mortar.

3.2. Fresh mortar properties

Results showed that initial setting time decreased in all bacterial pastes compared to control paste. Initial setting time of all bacterial pastes were more than 60 minutes (within limit time). The final setting time increased in all bacterial pastes compared to control paste. This may be due to nutrients of bacteria added or to the media of bacteria. Final setting time for all pastes was less than 10 hours. (Within limit). The obtained results from the initial and final setting times of bacterial and control pastes are shown in Figure 3. This means that adding bacteria and calcium lactate to cement paste play an important role in accelerating the initial setting time and relating the final setting time compared to control paste. Initial setting time and final setting time for all pastes were with in limit according to ASTM Specifications [19].

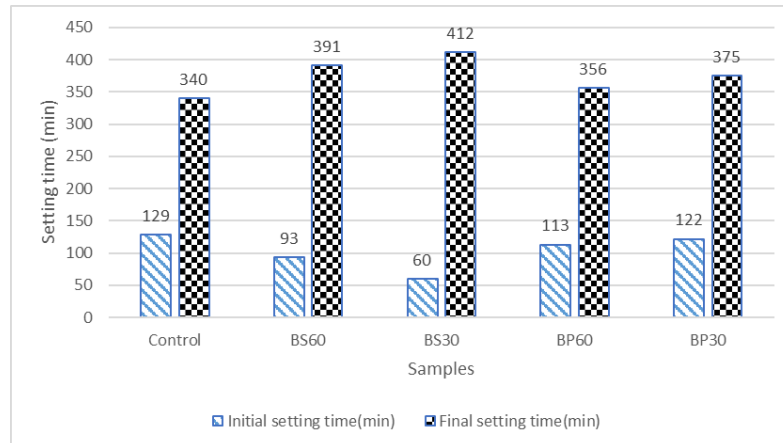


Figure 3. Initial and final setting times of bacterial and control cement paste.

3.3. Hardened mortar properties

3.3.1. Physical properties

3.3.1.1. The rate of water absorption

The influence of bacteria and calcium lactate on the water absorption of mortar after 2 hours was investigated. It was observed that with the inclusion of bacteria, the rate of water absorption of mortar decreased as shown in Figure 4.

At age of 3, 7 and 28 days, it was observed that the rate of water absorption of all bacterial specimens have smaller gain of water absorption than that of control mixture which aligns with what previous literature indicated [9], [12], [13]. At age of 90 days, the relation between rate of water absorption and time after 2 hours showed that BS30 has higher gain of water than that of control mixture. All other bacterial specimens except for BS30 have smaller gain of water than that of control mixture. At the age of 120 days, it was observed that rate of water absorption of all bacterial specimens after 2 hours have smaller gain of water absorption than that of control mixture and became semi-impermeable for BS60 and BP60.

Microbial Induced Calcite Precipitation (MICP) is responsible for filling up the pores in mortar and hence decreasing water absorption of bacterial mortar specimens.

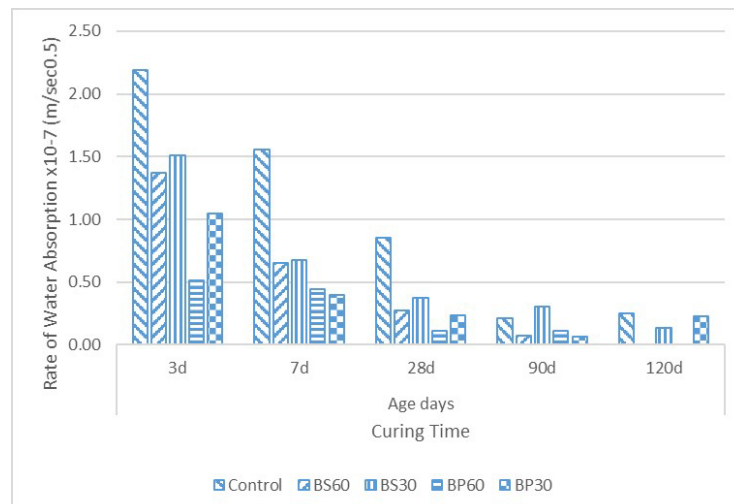


Figure 4. Rate of water absorption (l) for bacterial and control mortar after 2 hours.

3.3.1.2. Capillary permeability coefficient

The influence of bacteria and calcium lactate on permeability of mortar was investigated after 24 hours. At the age of 3, 7, and 28 days capillary permeability coefficient for all bacterial mortar specimens decreased compared to control mortar. At the age of 90 days, capillary permeability coefficient for all bacterial mortar specimens decreased except BS30. At the age 120 days capillary permeability coefficient for all bacterial mortar specimens decreased and became a semi-permeable for BS60 and BP60, as shown in Figure 5. This proves that metabolic activities by bacteria lead to the precipitation of calcium carbonate, which in turn decreases capillary permeability coefficient.

This is in line to previous work that showed a drastic decrease in the relative capillary index by similar amounts indicating a drastic decrease in water absorption [5].

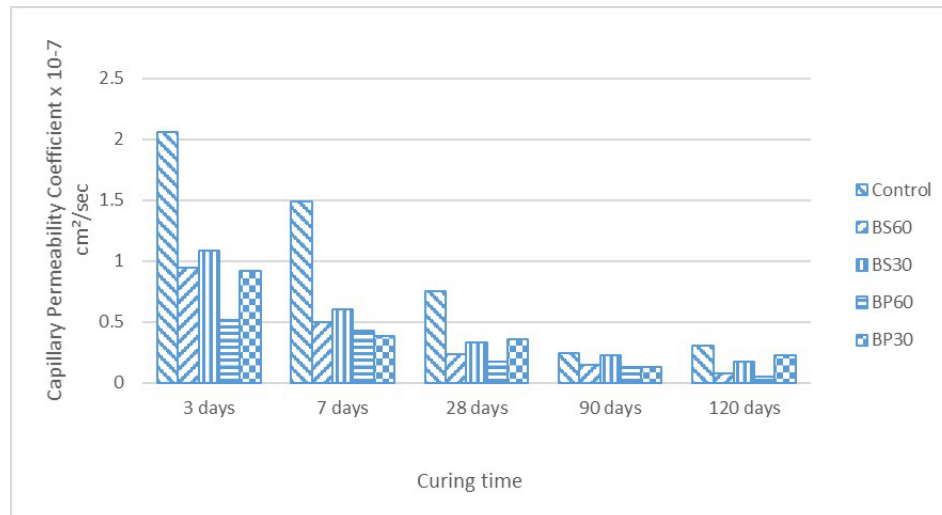


Figure 5. Capillary permeability coefficient (K) for bacterial and control mortar after 24 hours.

3.3.2 Mechanical properties

3.3.2.1 Compressive strength test

The results from the compressive strength test have shown an increase in strength for the bacterial mortar when compared to control mortar. It was noticed that compressive strength values of BS60 were greater than that of compressive strength values of BS30 and control mortar as illustrated in Figure 6. Also, compressive strength values of BP30 were higher than that of compressive strength values of BP60 and control mortar as illustrated in Figure 7.

At the same ratio of bacteria, it was noticed that compressive strength values of BP60 were higher than compressive strength values of BS60 at the age of 3, 7 and 28. At the age of 90 and 120 days, it was noticed that compressive strength values of BS60 became higher than compressive strength values of BP60 as shown in Figure 8. Compressive strength values of BP30 recorded increment in all ages compared to BS30 as illustrated in Figure 9.

Figure 10 showed a significant increase in strength of control and bacterial mortar over time. At the age of 3 days, the compressive strength value of BS60, BS30, BP60 and BP30 were 120 %, 117 %, 134.6 % and 129.1 % of compressive strength of control mortar, respectively. At the age of 7 days, the compressive strength value of BS60, BS30, BP60 and BP30 were 118.4 %, 130.20 %, 123.39 % and 150.0 % of compressive strength of control mortar, respectively. At the age of 28 days, the compressive strength value of BS60, BS30, BP60 and BP30 were 112.30 %, 109.20 %, 115.61 % and 124.88 % of compressive strength of control mortar, respectively. At the age of 90 days, the compressive strength value of BS60, BS30, BP60 and BP30 were 116.51 %, 108.24 %, 113.92 % and 110.76 % of compressive strength of control mortar, respectively. Noting that the increase in compressive strength in bacterial mortar at the ages of 28 and 90 days is remarkably lower than previously mentioned in the literature, having scored an increase of almost 50 % [12], [13].

At the age of 120 days, the compressive strength value of BS60, BS30, BP60 and BP30 were 124.70 %, 112.57 %, 115.79 % and 114.74 % of compressive strength of control mortar, respectively. BS60 had maximum increment in compressive strength. This proved significant activity of bacteria until age of 120 days. Calcite Precipitation Induced by bacteria is responsible for filling up the pores in mortar and hence increasing bonds in the micro structure which resist loads significantly and hence compressive

strength was increased compared to of control mortar. After 120 days, bacterial mortar proves to have higher compressive strength.

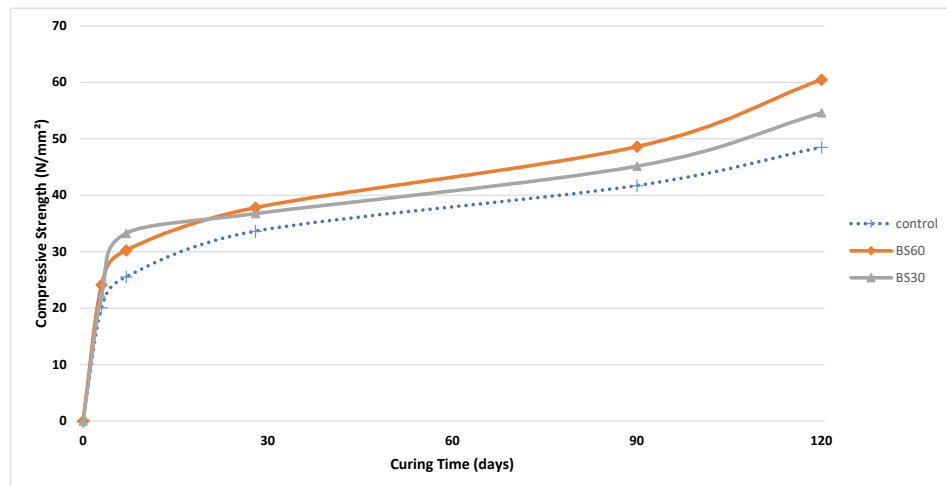


Figure 6. Compressive strength for bacterial mortar specimens (BS60, BS30) and control mortar specimens.

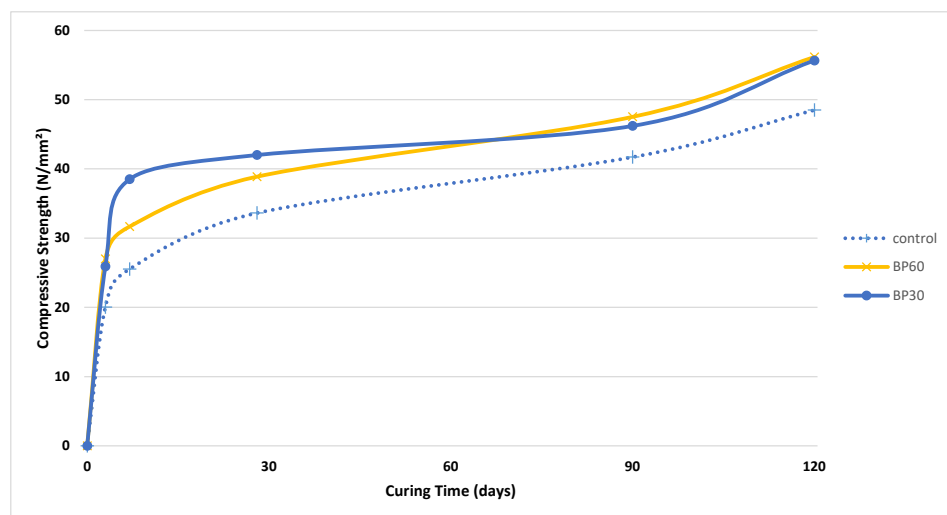


Figure 7. Compressive strength for bacterial mortar specimens (BP60, BP30) and control mortar specimens.

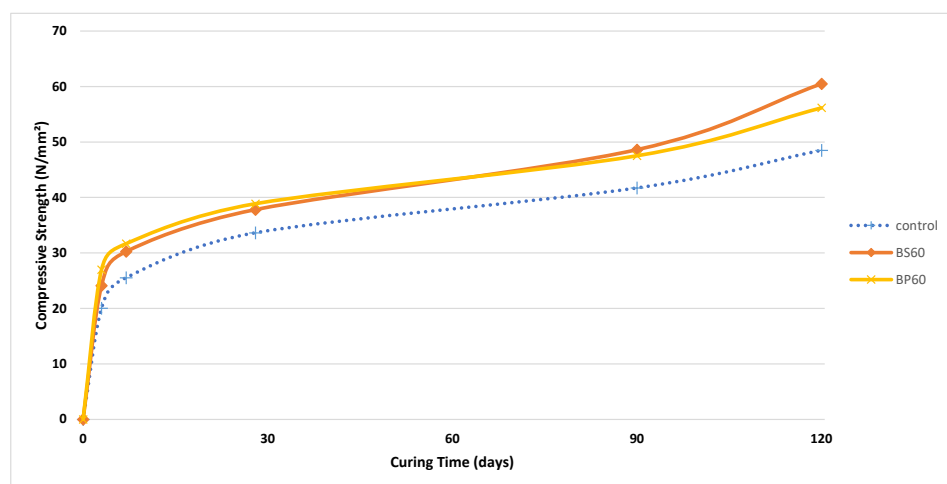


Figure 8. Compressive strength for bacterial mortar specimens (BS60, BP60).

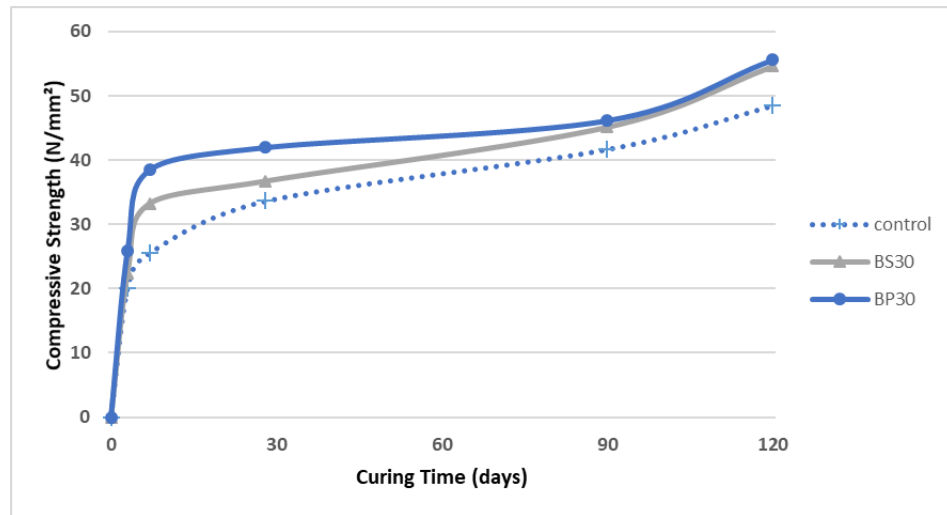


Figure 9. Compressive strength for bacterial mortar specimens (BS30, BP30).

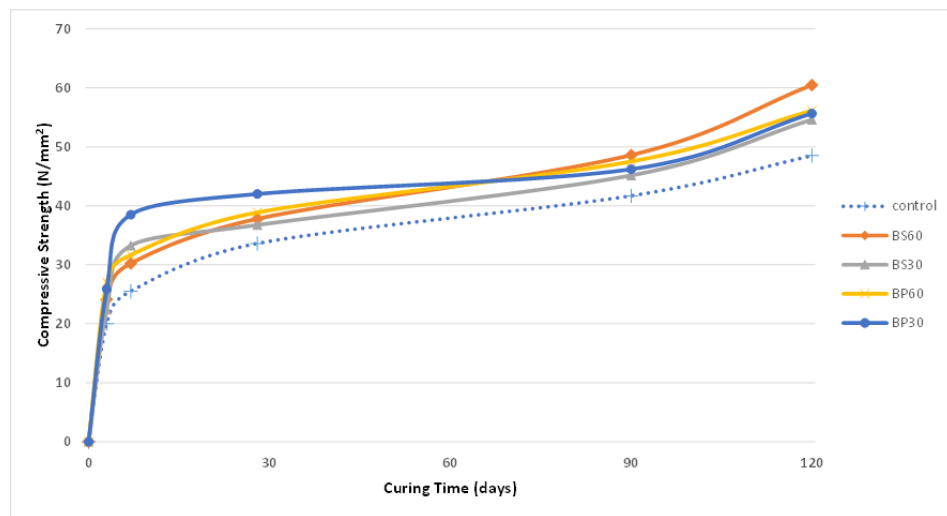


Figure 10. Compressive strength for bacterial and control mortar specimens.

3.3.2.2 Restoration of bacteria

Samples were loaded after 14 days from casting date with 60 % of failure load at 7 days and reloaded at 28 and 90 days. Results of compressive strength test has shown an increase in the strength for all bacterial mortar when compared to its original samples at the age of 28 and for BS30 and BP30 at the age of 90 days as illustrated in Figure 11.

Reloaded samples were compared to original samples. At the age of 28 days, the compressive strength value of Control, BS60, BS30, BP60 and BP30 were 98.06 %, 108.83 %, 121.58 %, 115.49 % and 105.2 % compared to compressive strength of its original state which was determined in compressive strength test. At the age of 90 days, the compressive strength value of Control, BS60, BS30, BP60 and BP30 were 64.87 %, 89.68 %, 103.54 %, 89.92 % and 111.17 % compared to compressive strength of its original state which was determined in compressive strength test. Increasing in compressive strength value of all bacterial mortar at the age of 28 and for BS30 and BP30 at the age of 90 days and decreasing in compressive strength values of control mortar specimen at the age of 28 and 90 days, this means that self-healing in mortar occurred as illustrated in Figures 11, 12.

Increasing in compressive strength value for all bacterial mortar at the age of 28 and for BS30 and BP30 at the age of 90 days and decreasing in compressive strength values of control mortar specimen at the age of 28 and 90 days.

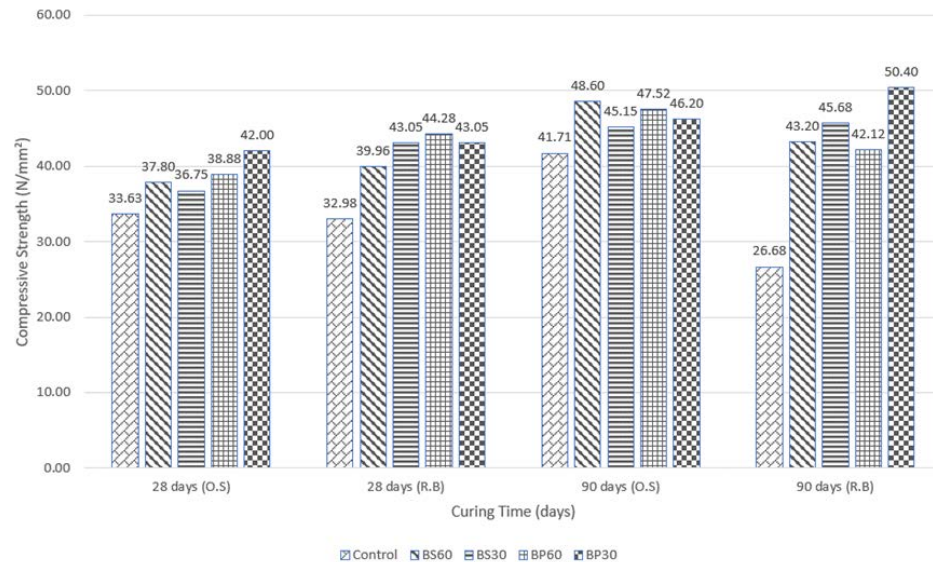


Figure 11. Compressive strength (restoration of bacteria) (R.B) vs. (original samples) (O.S).

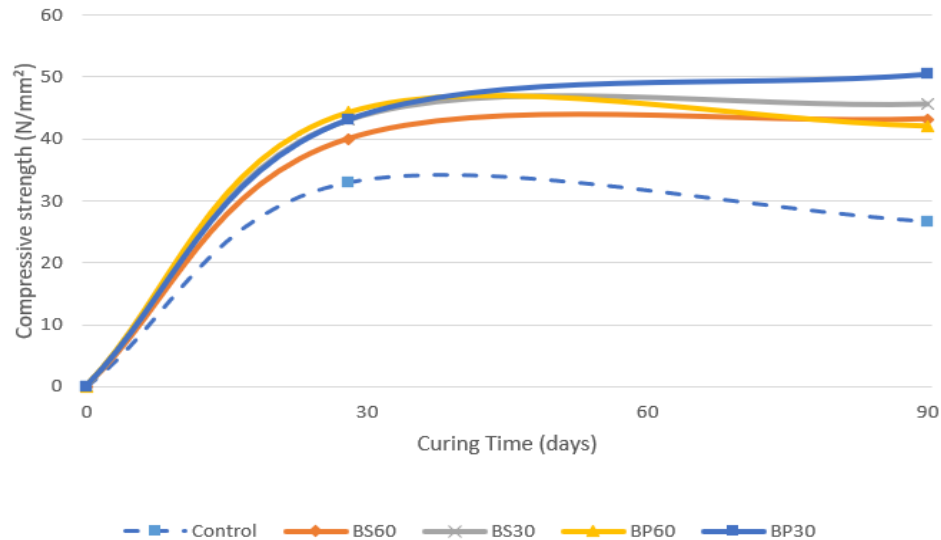


Figure 12. Compressive strength (restoration of bacteria) for bacterial and control mortar specimens.

This means that bacteria of *Bacillus Sphaericus* and *Bacillus Pasteurii* (BS30 and BP30) have the ability to restore the mortar mechanical properties to its original state. Also it is stronger than that of its original state before cracking.

3.3.2.3 Flexural Strength Test

Bacterial and control mortar were tested. It was noticed that flexural strength value of BS60 was higher than that of flexural strength value of BS30 at age of 28 and 90 but it decreased at the age of 120 days as illustrated in Figure 13. Flexural strength value of BP60 was higher than that of flexural strength value of BP30 at age of 28 but it decreased at the age of 90 and 120 days as illustrated in Figure 14.

At the same ratio of Bacteria, it was noticed that flexural strength value of BS60 was higher than that of flexural strength value of BP60 at age of 28, 90 and 120 days as illustrated in Figure 15 and flexural strength value of BP30 recorded increment at age of 28, 90 days but it decreased at age of 120 days compared to BS30 as illustrated in Figure 16.

Results of flexural strength test revealed that there is an increase in the strength for the bacterial mortar when compared to the control mortar as illustrated in Figure 17. At the age of 28 days, the flexural strength value of BS60, BS30, BP60 and BP30 were 127.22 %, 115.37 %, 119.15 % and 119.49 % of flexural strength of control mortar, respectively. At the age of 90 days, the flexural strength value of BS60, BS30, BP60 and BP30 were 132.01 %, 117.51 %, 113.15 % and 121.36 % of flexural strength of control mortar, respectively. At the age of 120 days the flexural strength value of BS60, BS30, BP60 and BP30 were 159.89 %, 167.66 %, 118.06 % and 124.39 % of flexural strength of control mortar, respectively.

Microbial Induced Calcite Precipitation (MICP) is responsible for filling up the pores in mortar and hence increased the flexural strength as observed in previous research [9], [13]. Generally, bacterial mortar proved to have a higher flexural strength.

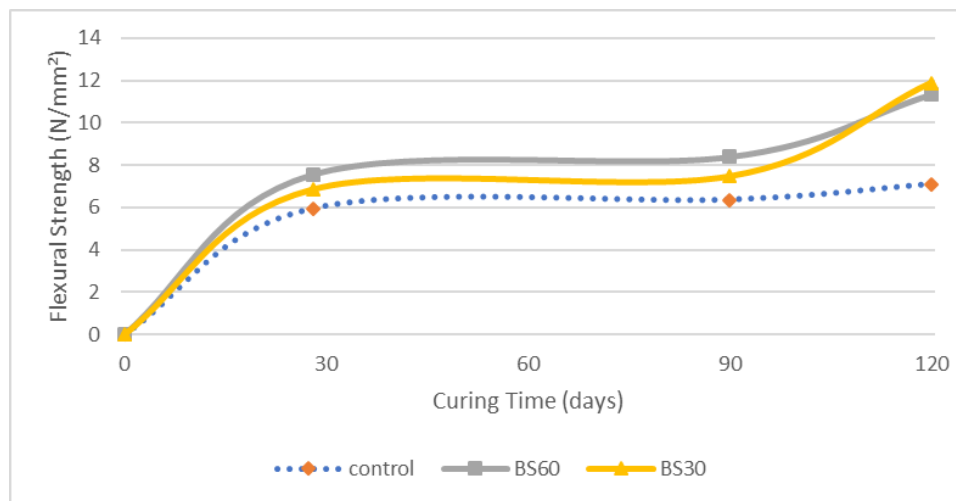


Figure 13. Flexural strength for bacterial mortar specimens (BS60, BS30) and control mortar specimens.

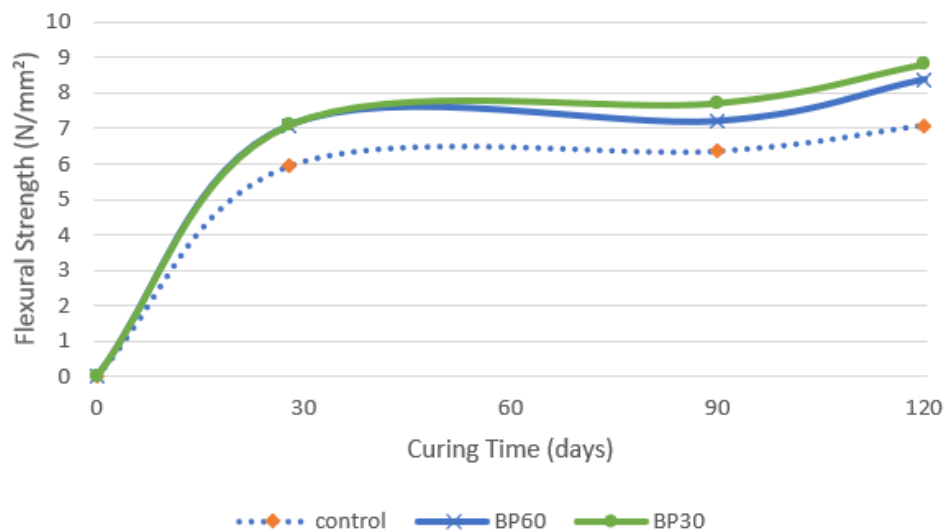


Figure 14. Flexural strength for Bacterial Mortar Specimens (BP60, BP30) and Control Mortar Specimens.

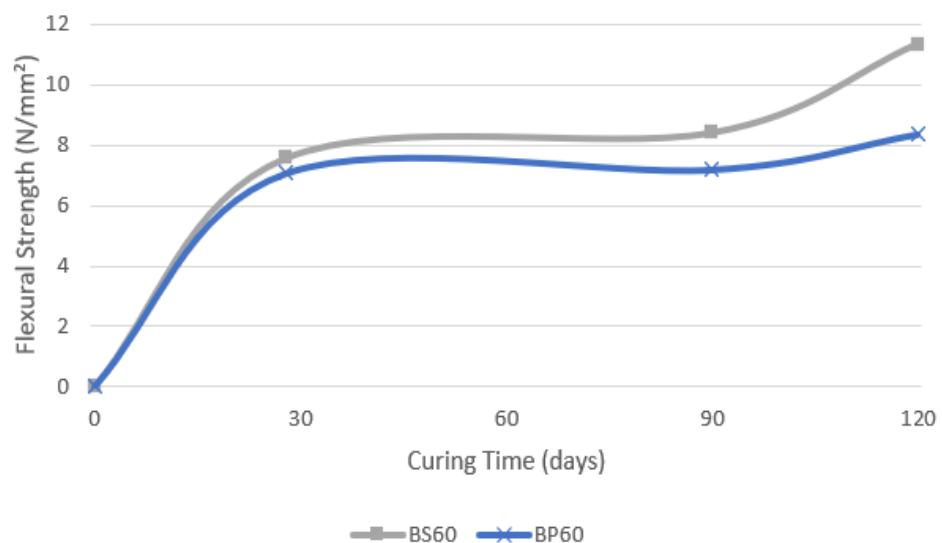


Figure 15. Flexural strength for Bacterial Mortar Specimens (BS60, BP60).

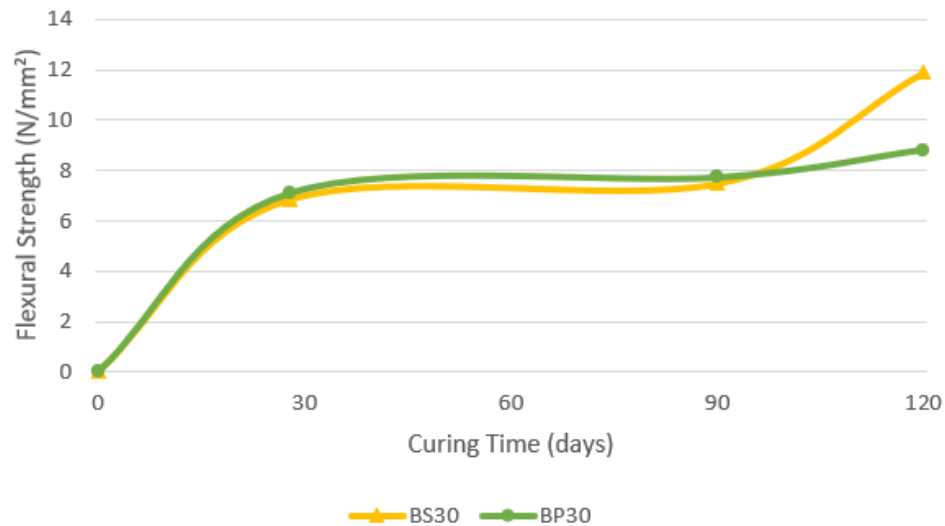


Figure 16. Flexural strength for Bacterial Mortar Specimens (BS30, BP30).

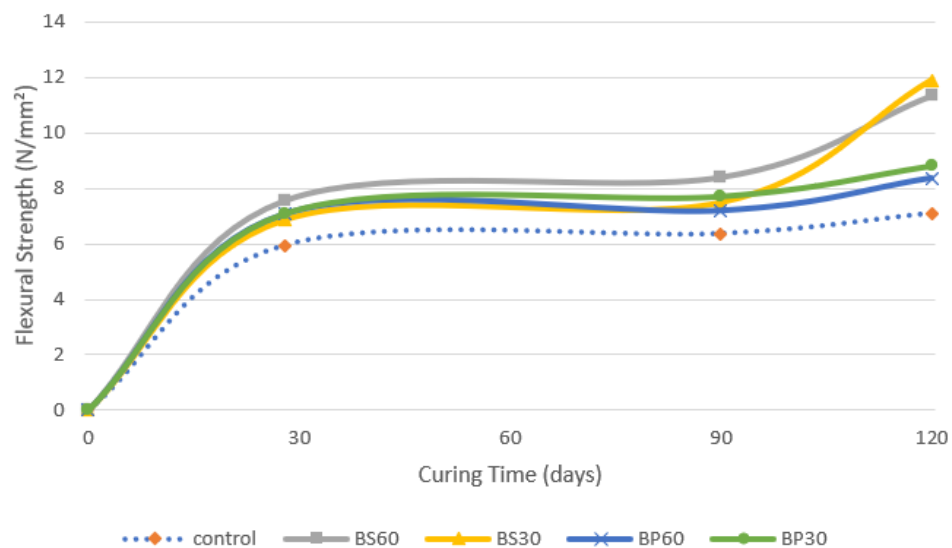


Figure 17. Flexural strength for Bacterial and Control Mortar Specimens.

3.3.3 Durability of Cement Mortar

3.3.3.1 Sulfate Resistance Test

Results of compressive strength test revealed that there was an increase in the strength for the bacterial mortar when compared to the control mortar as illustrated in Figure 18. At the age of 28 days all bacterial mortar increased except BP60 was 98.49 % of compressive strength of control mortar. Also, compressive strength value of BS60, BS30 and BP30 were 134.18 %, 111 % and 113.8 % of compressive strength of control mortar, respectively. At the age of 90 days, all specimens increased for BS60, BS30, BP60 and BP30 and became 139.18 %, 118.1 %, 111.34 % and 118.08 %, respectively.

At the age of 180 days all bacterial mortar increased except BS30 and BP60 were 100.22 % and 96.91 % of compressive strength of control mortar. Also, compressive strength value of BS60 and BP30 were 115.46 %, 116.26 % and of compressive strength of control mortar, respectively.

This means that the compressive strength for bacterial mortar specimens increases in the case of exposure to salts at the age of 28, 90 and 180 days except BS30 at the age of 180 days and BP60 at all ages compared to control mortar at the same ages. Also compressive strength value of control and all bacterial mortar increased with time during exposure to salts compared to them initial statues after immersion in sulphuric acid 98 %.

Comparison between exposed and non-exposed in compressive strength were taken at the age of 28 and 90 days.

At the age of 28 days, compressive strength value of Control, BS60, BS30, BP60 and BP30 were 109.11 %, 145.03 %, 120 %, 103.5 % and 107.63 %, respectively compared to exposed and its non-exposed at the age of 28 days as illustrated in Figure 19.

At the age of 90 days, compressive strength value of Control, BS60, BS30, BP60 and BP30 were 99.26 %, 132 %, 117.21 %, 108 % and 114.55 %, respectively compared to exposed and its non-exposed as illustrated in Figure 20. This showed that BS60 had maximum increment in compressive strength after immersion in sodium sulphate compared to its non-exposed specimens at the age of 28 and 90 days.

On the other side, results showed that the effect of bacteria on the water absorption of mortar after 2hours was investigated. At the age of 28 days, the rate of water absorption for all bacterial mortar specimens decreased compared to control mortar. At the age of 90 days, the rate of water absorption increased for all bacterial mortar specimens except for BP60 increased than of the rate of water absorption for control mortar as illustrated in Figure 21. This means that BP60 had the ability to resist salts absorption.

Figure 22 shows capillary permeability coefficient for control and bacterial mortar specimens after immersion in sodium sulfate. At the age of 28 days, the capillary permeability coefficient for all bacterial mortar specimens decreased compared to control mortar. At the age of 90 days, the capillary permeability coefficient increased for all bacterial mortar specimens except for BP60 decreased than of the capillary permeability coefficient for control mortar. This means that BP60 had the ability to resist salts absorption.

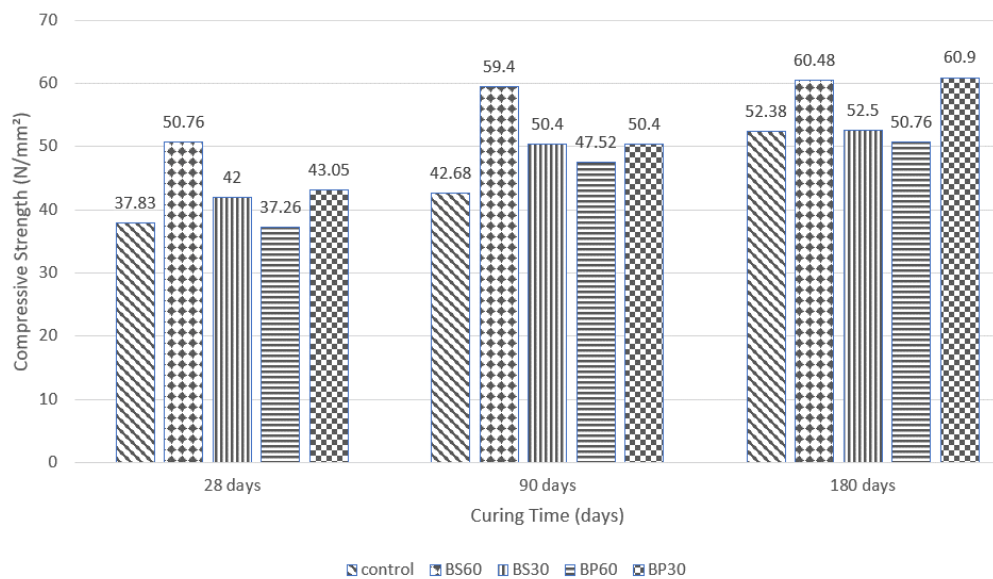


Figure 18. Compressive strength for Bacterial and Control Mortar Specimens after immersion in sodium sulfate.

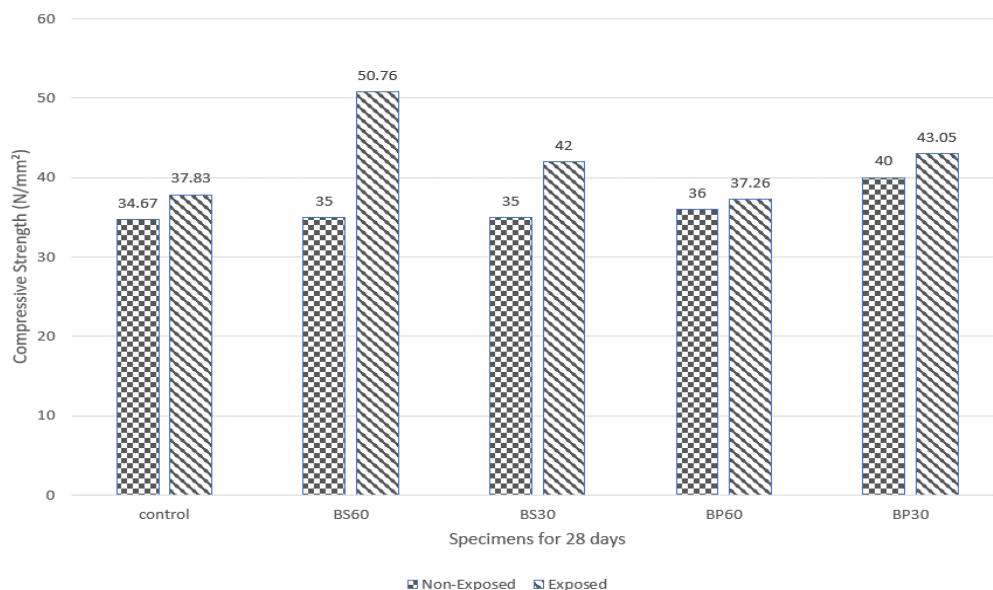


Figure 19. Compressive strength for exposed and non-exposed specimens after immersion in sodium sulfate for (28 days).

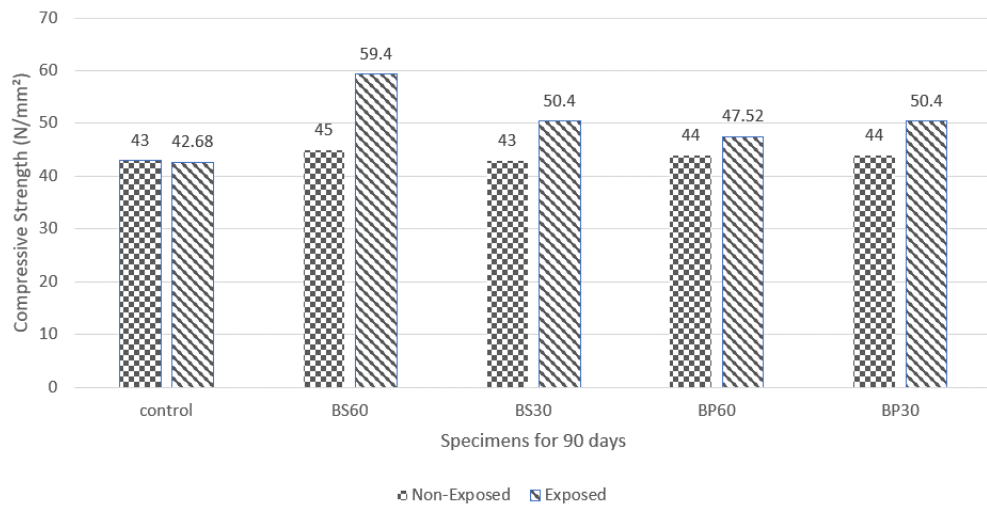


Figure 20. Compressive Strength for exposed and non-exposed specimens after immersion in sodium sulfate for (90 days).

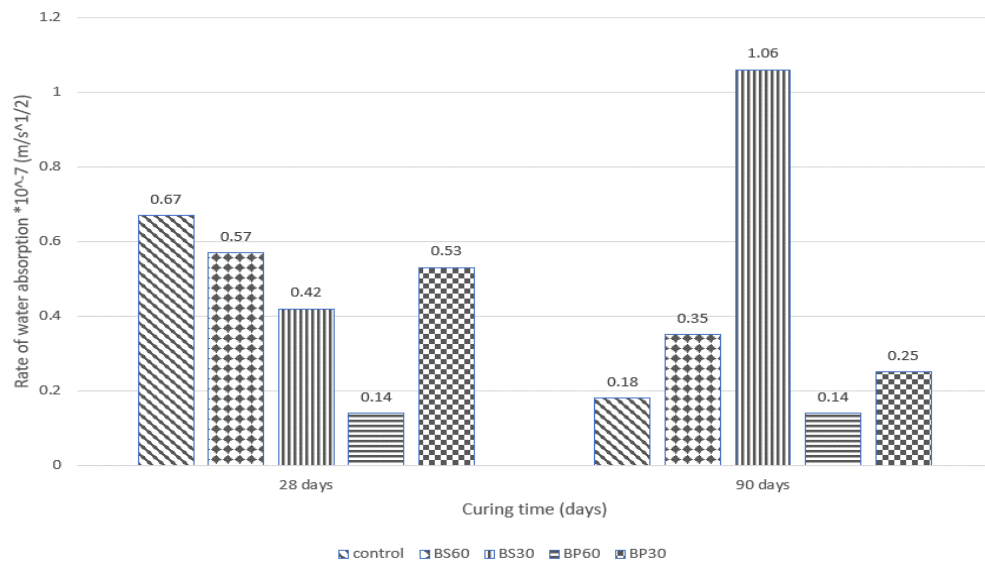


Figure 21. Rate of Water Absorption (I) for Bacterial and Control Mortar Specimens after immersion in sodium sulfate.

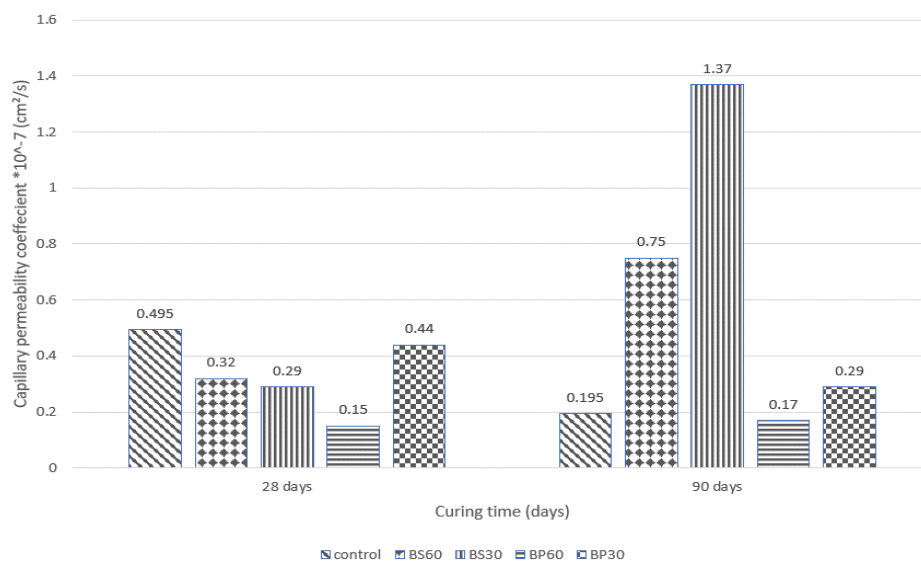


Figure 22. Capillary permeability coefficient (K) for Bacterial and Control Mortar Specimens after immersion in sodium sulfate.

3.3.3.2 Acid Resistance Test

Results of compressive strength test revealed that there was an improvement with time in the strength for the bacterial mortar when compared to the control mortar as illustrated in Figure 23. At the age of 28 days all bacterial mortar decreased except BS60 was 124.92 % compared to compressive strength of control mortar. Also, at the age of 90 days, compressive strength for all bacterial mortar decreased except BS60 was 121.24 % compared to compressive strength of control mortar.

At the age of 180 days the compressive strength value of BS60, BS30, BP60 and BP30 were 121.46 %, 114.8 %, 109.65 and 121.37 % compared to compressive strength of control mortar, respectively.

This means that the compressive strength for bacterial mortar specimens decreases at the early ages (28 and 90 days) in the case of exposure to acids except BS60, but there are improvements in compressive strength with time for all bacterial mortar specimens compared to compressive strength of control mortar. Also compressive strength value of control and all bacterial mortar decreased with time during exposure to salts compared to them initial statues after immersion in sulphuric acid 98 %.

Comparison between exposed and non-exposed in compressive strength were taken at the age of 28 and 90 days.

At the age of 28 days, compressive strength value of Control, BS60, BS30, BP60 and BP30 were 114.71 %, 141.94 %, 105 %, 57 % and 94.50 %, respectively compared to exposed and its non-exposed at the age of 28 days as illustrated in Figure 24. At the age of 90 days, compressive strength value of Control, BS60, BS30, BP60 and BP30 were 101.51 %, 117.6 %, 97.67 %, 78.55 % and 100.23 %, respectively compared to exposed and its non-exposed as illustrated in Figure 25. This showed that BS60 had maximum increment in compressive strength after immersion in sulphuric acid 98 % compared to its non-exposed specimens at the age of 28 and 90 days.

On the other side, results showed that the effect of bacteria on the water absorption of mortar after 2 hours was investigated. At the age of 28 days, the rate of water absorption for all bacterial mortar specimens decreased compared to control mortar. At the age of 90 days, the rate of water absorption increased for all bacterial mortar specimens except for BP60 equaled the rate of water absorption for control mortar as illustrated in Figure 26. This means that BP60 had the ability to resist acids attacking.

Figure 27 shows capillary permeability coefficient for control and bacterial mortar specimens after immersion in sulphuric acid 98%. At the age of 28 days, the capillary permeability coefficient for all bacterial mortar specimens decreased compared to control mortar. At the age of 90 days, the capillary permeability coefficient increased for all bacterial mortar specimens except for BP60 decreased than of the capillary permeability coefficient for control mortar and BP30 equaled the capillary permeability coefficient for control mortar. This means that BP60 and BP30 had the ability to resist acids attacking.

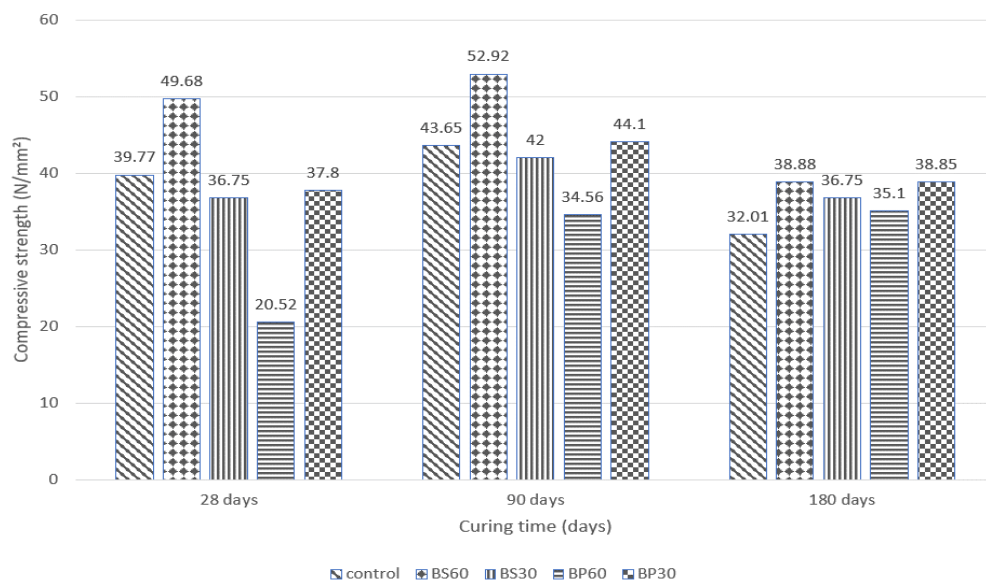


Figure 23. Compressive Strength for Bacterial and Control Mortar Specimens after immersion in sulphuric acid 98 %.

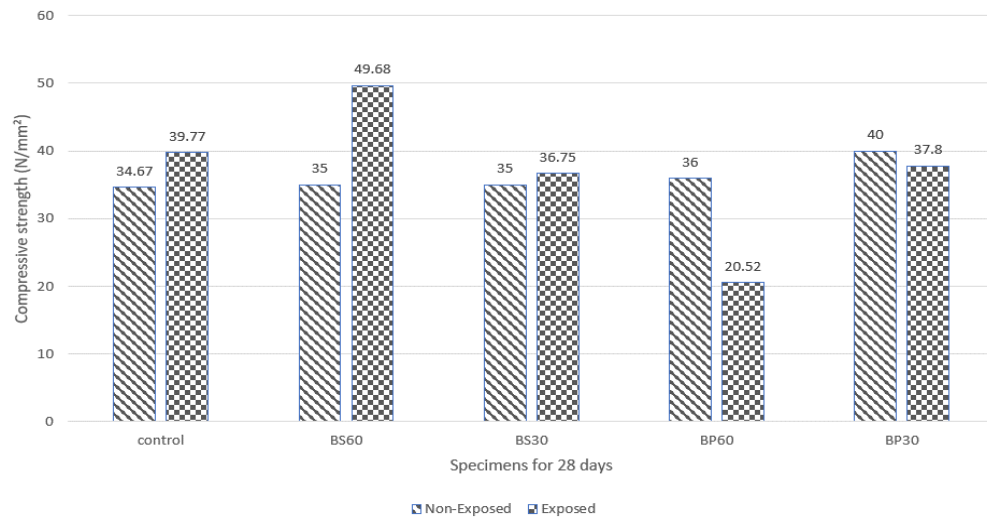


Figure 24. Compressive Strength for exposed and non-exposed specimens after immersion in sulphuric acid 98 % for (28 days).

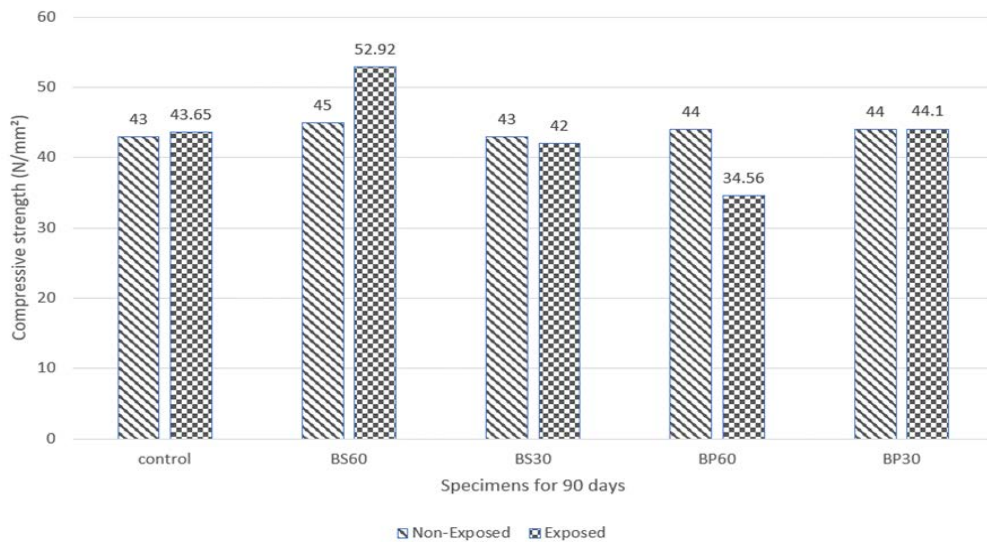


Figure 25. Compressive strength for exposed and non-exposed specimens after immersion in sulphuric acid 98 % for (90 days).

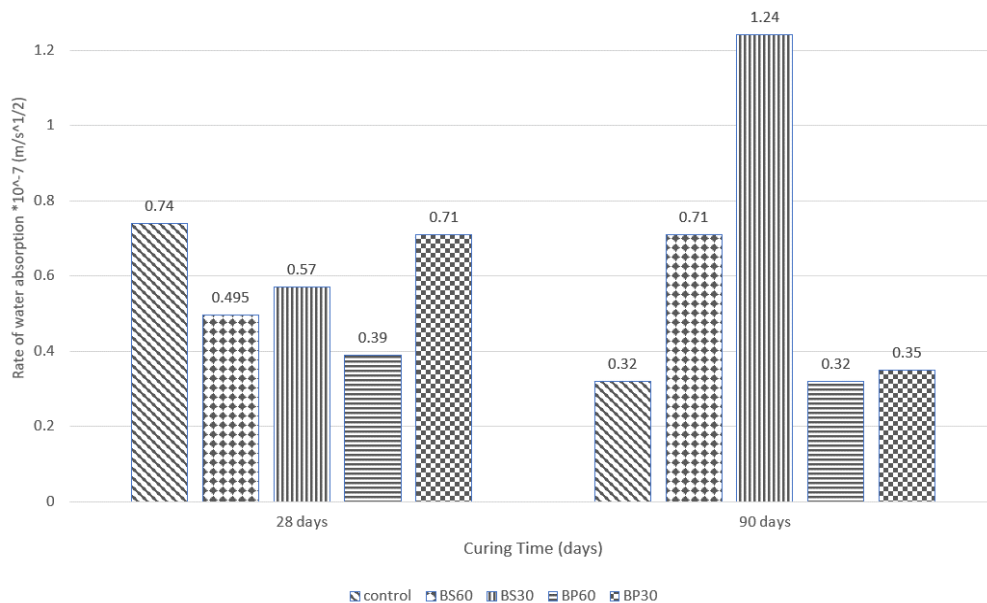


Figure 26. Rate of Water Absorption (l) for Bacterial and Control Mortar Specimens after immersion in sulphuric acid 98 %.

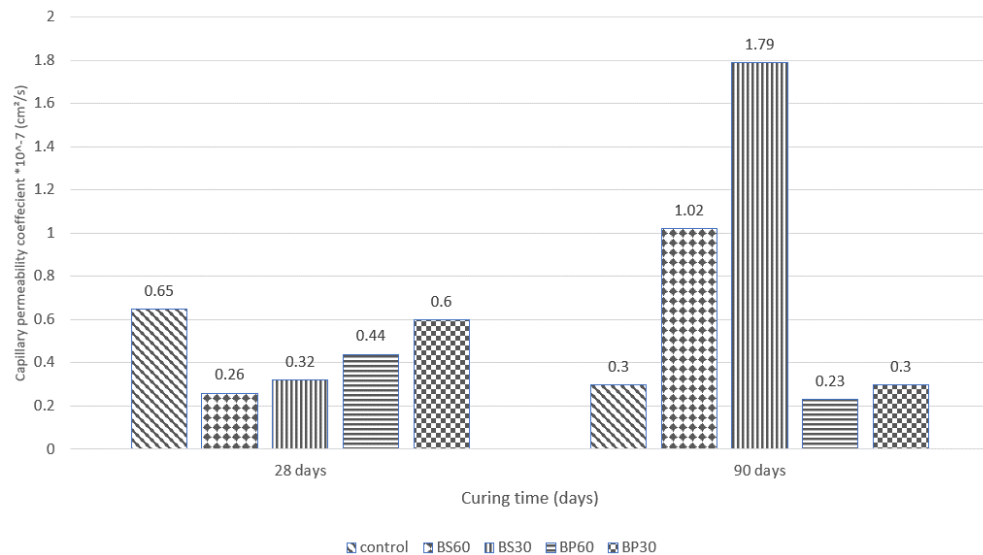


Figure 27. Capillary Permeability Coefficient (K) for Bacterial and Control Mortar Specimens after immersion in sulphuric acid 98 %.

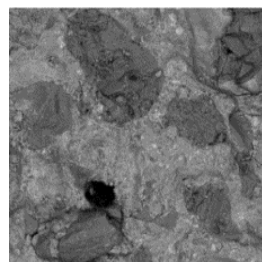
3.3.4 Advanced Techniques of Self-Healing Investigation

3.3.4.1 Scanning Electron Microscopy (SEM)

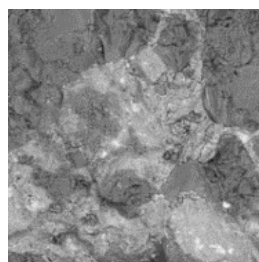
The SEM micrographs were carried out after 120 days of curing with the magnification of 150, 500, 1500, 5000 and 7500. Figures 28–32 showed SEM pictures for Control (no additions of bacteria) and Bacterial mortar specimens, it is showed that calcite crystals are precipitated by bacterial cells, leading to fill pores. This indicates that the bacterial cells act as nucleating sites for precipitation of calcium carbonate.

The three mortar specimens were compared using SEM pictures at the same magnifying.

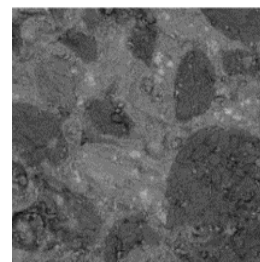
Figure 28 at magnifying X150 showed control mortar specimens had many voids compared with BS50, BS25, BP50 and BP25 mortar specimens. Figure 29–32 at magnifying X500, X1500, X5000 and X7500 showed that there are depositions of calcite within voids of bacterial mortar specimens. Calcite crystals are precipitated by bacterial cells leading to fill pores and making good bonds within bacterial mortar specimens. Calcium carbonate precipitation was clear and their shape is random similar to the figures and images shown in previous works [9]. The figures below show bacterial depositions and crystal formations identical to that previously found in literature concerning bacterial mortar [5], [17].



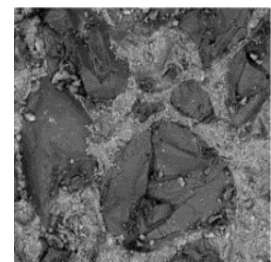
a. Control (X150)



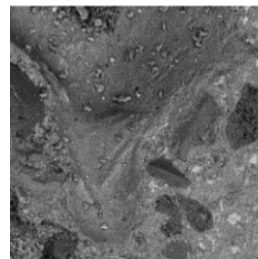
b. BS60 (X150)



c. BS30 (X150)



d. BP60 (X150)



e. BP30 (X150)

Figure 28. SEM Photographs of Control and Bacterial Mortar Samples (*B.Sphaericus* and *B.Pasteurii*) (150X) after 120 days of Curing.

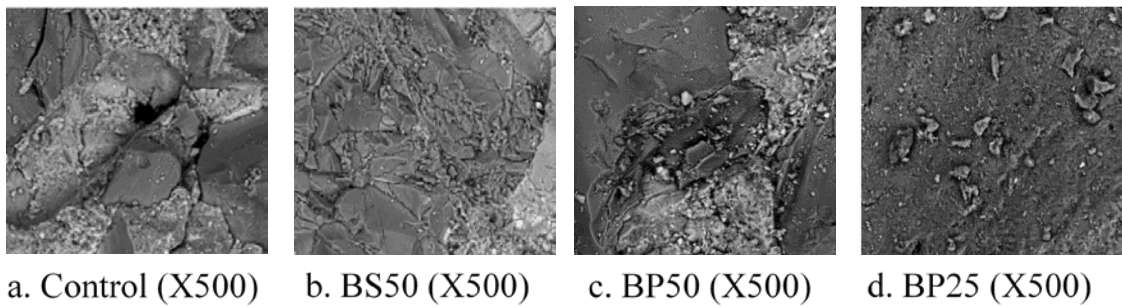


Figure 29. SEM Photographs of Control and Bacterial Mortar Samples (B.Sphaericus and B.Pasteurii) (500X) after 120 days of Curing.

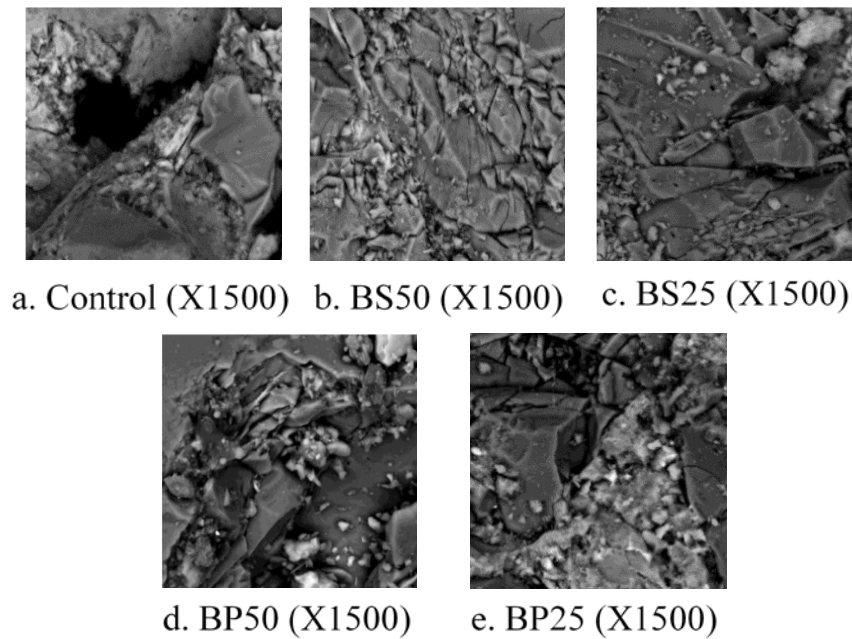


Figure 30. SEM Photographs of Control and Bacterial Mortar Samples (B.Sphaericus and B.Pasteurii) (1500X) after 120 days of Curing.

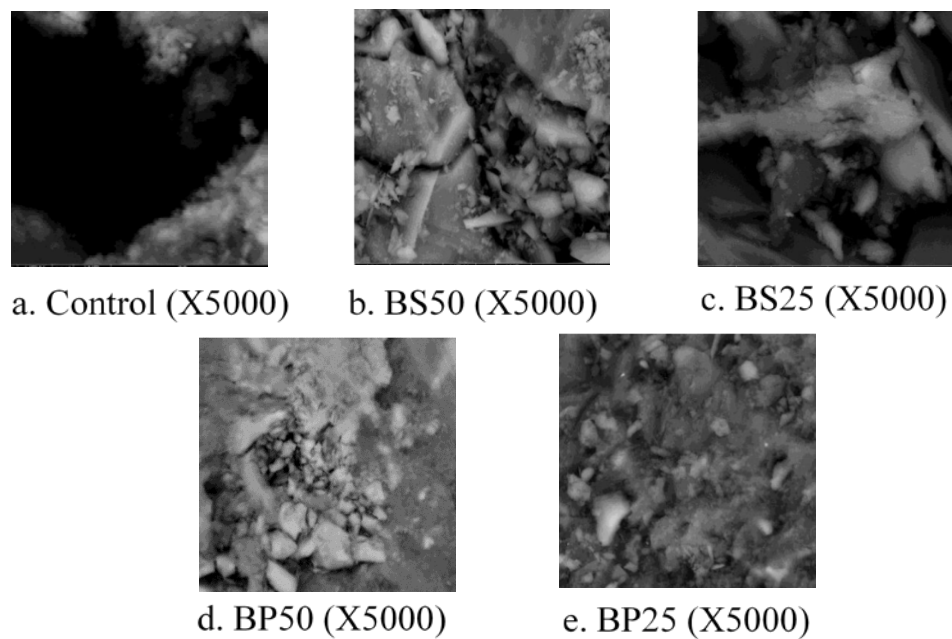


Figure 31. SEM Photographs of Control and Bacterial Mortar Samples (B.Sphaericus and B.Pasteurii) (5000X) after 120 days of Curing.

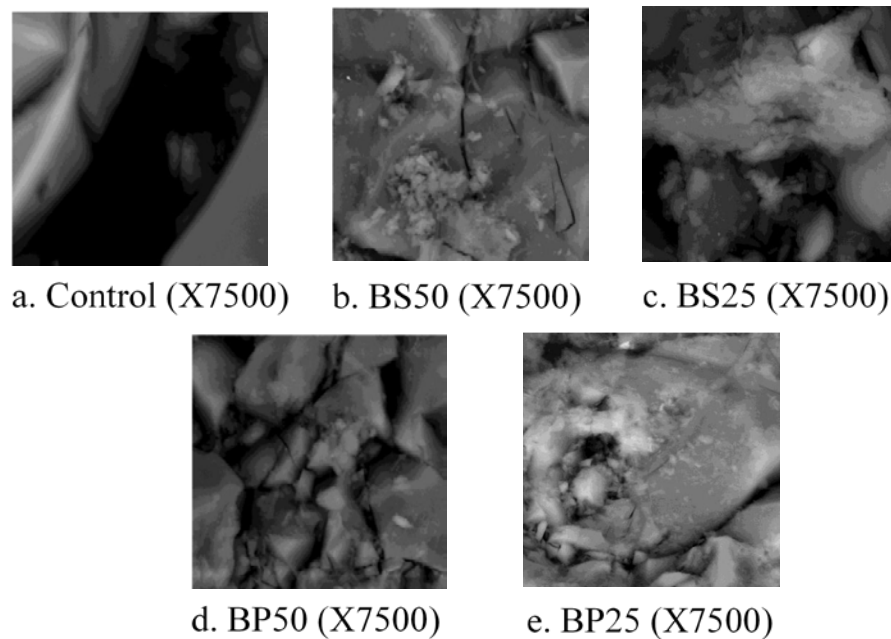


Figure 32. SEM Photographs of Control and Bacterial Mortar Samples (B.Sphaericus and B.Pasteurii) (7500X) after 120 days of Curing.

4. Conclusions

Several conclusions could be derived from the results obtained in this investigation as follows:

1. No significant variation between the two bacterial species (*Bacillus sphaericus*, *Bacillus pasteurii*) in cell count during the time course which indicate that both species can adapt in the same rate with the new environmental conditions inside the concrete.
2. The bacteria nutrition acts as an accelerator for cement pastes for initial setting time for all bacterial mortar compared to control mortar, while acts as a retarder of cement pastes for final setting time for all bacterial mortar. Initial and final setting for all mortar were within limit according to ASTM specifications.
3. The rate of water absorption of all bacterial specimens after 2 hours have smaller gain of water absorption than that of control mixture and became semi-impermeable for BS60 and BP60 after 120 days which aligns with previous results that showed a decrease in water absorption and reduced chloride migration.
4. Significant activity of bacterial mortar, biochemically induced calcium carbonate precipitation is responsible for filling up the pores in mortar which in turn decreases rate of water absorption of bacterial mortar and decreases capillary permeability coefficient as shown in previous literature.
5. Compressive strength for all bacterial mortar increased compared to the control specimens compressive strength. Compressive strength of BS60 at 120 days age increased by 124.7 % compared to the control specimens.
6. *Bacillus sphaericus*, *Bacillus pasteurii* with the ratio (0.6 % and 0.3 %) showed high restoration of compressive strength when loaded with 60 % of ultimate load of 7 days at the age of 14 days.
7. Compressive strength for reloaded samples after 28days from curing improved by 108.83 %, 121.58 %, 115.49 % and 105.2 % from compressive strength of original samples for BS60, BS30, BP60 and BP30, respectively.
8. Also *Bacillus Sphaericus*, *Bacillus Pasteurii* with the ratio (0.30 %) showed high restoration of compressive strength when loaded with 60 % of ultimate load of 7 days at the age of 14days. Compressive strength for reloaded samples after 90days from curing improved by 103.54 % and 111.17 % from compressive strength of original samples for BS30 and BP30, respectively.
9. Flexural strength value of BS30 at the age of 120 days increased by 167.66 % compared to flexural strength of control mortar.
10. Increase in compressive strength and flexural strength are mainly due to the closing of pores inside of the cement mortar due to the bacteria disposing calcite precipitation.

11. Results showed that BP60 had a high ability to resist salts and acids.

12. The SEM micrograph of bacterial mortar shows less voids compared to control mortar. The bacterial cells precipitate calcium carbonate.

Therefore, the calcium-producing microbes are responsible for filling the pores in the cement mortar, thus reducing the rate of water absorption and the permeability of the capillary, while the compressive strength and flexural strength of the bacterial cement mortar have increased, as well as the ability of some types of bacterial cement mortar to resist salts and acids. Thus, improving the properties of cement mortar containing bacteria and calcium lactate as a nutrient for bacteria.

References

1. Meissner, H.S. Cracking in Concrete Due to Expansive Reaction Between Aggregate and High-Alkali Cement as Evidenced in Parker Dam. *ACI Journal Proceedings*. 1941. 37. Pp. 549–568. DOI: 10.14359/8570
2. Rapoport, J., Aldea, C.M., Shah, S.P., Ankenman, B., Karr, A. Permeability of cracked steel fiber-reinforced concrete. *Journal of Materials in Civil Engineering*. 2002. 14(4). Pp. 355–358. DOI: 10.1061/(ASCE)0899-1561(2002)14:4(355)
3. Hughes, B.P., Ghunaim, F. An experimental study of early thermal cracking in reinforced concrete. *Magazine of Concrete Research*. 1982. 34(118). Pp. 18–24. DOI: 10.1680/mac.1982.34.118.18
4. Andalib, R., Abd Majid, M.Z., Hussin, M.W., Ponraj, M., Keyvanfar, A., Mirza, J., Lee, H.-S. Optimum concentration of *Bacillus megaterium* for strengthening structural concrete. *Construction and Building Materials*. 2016. 118. Pp. 180–193. DOI: 10.1016/j.conbuildmat.2016.04.142
5. De Muynck, W., Cox, K., Belie, N. De, Verstraete, W. Bacterial carbonate precipitation as an alternative surface treatment for concrete. *Construction and Building Materials*. 2008. 22(5). Pp. 875–885. DOI: 10.1016/j.conbuildmat.2006.12.011
6. Luo, M., Qian, C., Li, R. Factors affecting crack repairing capacity of bacteria-based self-healing concrete. *Construction and Building Materials*. 2015. 87. Pp. 1–7. DOI: 10.1016/j.conbuildmat.2015.03.117
7. Siddique, R., Nanda, V., Kunal, Kadri, E.H., Iqbal Khan, M., Singh, M., Rajor, A. Influence of bacteria on compressive strength and permeation properties of concrete made with cement baghouse filter dust. 1062016
8. De Muynck, W., De Belie, N., Verstraete, W. Microbial carbonate precipitation in construction materials: A review. *Ecological Engineering*. 2010. 36(2). Pp. 118–136. DOI: 10.1016/j.ecoleng.2009.02.006
9. Jang, I., Son, D., Kim, W., Park, W., Yi, C. Effects of spray-dried co-cultured bacteria on cement mortar. *Construction and Building Materials*. 2020. 243. DOI: 10.1016/j.conbuildmat.2020.118206
10. Annamalai, S.K., Arunachalam, K.D., Sathyanarayanan, K.S. Production and characterization of Bio Caulk by *Bacillus pasteurii* and its remediation properties with carbon nano tubes on concrete fractures and fissures. 47(11)2012.
11. Wang, J.Y., Snoeck, D., Van Vlierberghe, S., Verstraete, W., De Belie, N. Application of hydrogel encapsulated carbonate precipitating bacteria for approaching a realistic self-healing in concrete. 682014
12. De Muynck, W., Debrouwer, D., De Belie, N., Verstraete, W. Bacterial carbonate precipitation improves the durability of cementitious materials. *Cement and Concrete Research*. 2008. 38(7). Pp. 1005–1014. DOI: 10.1016/j.cemconres.2008.03.005
13. Tayebani, B., Mostofinejad, D. Self-healing bacterial mortar with improved chloride permeability and electrical resistance. *Construction and Building Materials*. 2019. 208. Pp. 75–86. DOI: 10.1016/j.conbuildmat.2019.02.172
14. Rong, H., Wei, G., Ma, G., Zhang, Y., Zheng, X., Zhang, L., Xu, R. Influence of bacterial concentration on crack self-healing of cement-based materials. *Construction and Building Materials*. 2020. 244. Pp. 118372. DOI: 10.1016/j.conbuildmat.2020.118372
15. Vaezi, M., Zareei, S.A., Jahadi, M. Recycled microbial mortar: Effects of bacterial concentration and calcium lactate content. *Construction and Building Materials*. 2020. 234. Pp. 117349. DOI: 10.1016/j.conbuildmat.2019.117349
16. Vijay, K., Murmu, M., Deo, S. V. Bacteria based self healing concrete – A review. *Construction and Building Materials*. 2017. 152(1). Pp. 1008–1014. DOI: 10.1016/j.conbuildmat.2017.07.040
17. Siddique, R., Chahal, N.K. Effect of ureolytic bacteria on concrete properties. *Construction and Building Materials*. 2011. 25(10). Pp. 3791–3801. DOI: 10.1016/j.conbuildmat.2011.04.010
18. Rooij, M. De. *Self-Healing Phenomena in Cement-Based Materials*. 11. Springer Netherlands. Dordrecht, 2013.
19. ASTM. C150-Standard Specification for Portland Cement. 2015. Pp. 1–10. DOI: 10.1520/C0150
20. ASTM C33/C33M. Standard specification for concrete aggregates. ASTM Int., 2016. DOI: 10.1520/C0033
21. ASTM. Standard Specification for Mixing Water Used in the Production of Hydraulic Cement Concrete. Practice. 2000. Vol. 93. No. Reapproved. Pp. 2–6.
22. Paine, K. Bacteria-Based Self-Healing of Concrete: Effects of Environment, Exposure and Crack Size. *Proceedings of the RILEM Conference on Microorganisms-Cementitious Materials Interactions*. 2016. 1. Pp. 1–15.
23. Mamiatis, T., Fritsch, E.F., Sambrook, J., Engel, J. *Molecular cloning-A laboratory manual*. New York: Cold Spring Harbor Laboratory. 1982, 545 S., 42 \$. *Acta Biotechnologica*. 1985. 5(1). Pp. 104–104. DOI: 10.1002/abio.370050118
24. International Ferrocement Society (IFS), I.C. 10. (2001). *Ferrocement model code : building code recommendations for the ferrocement* (IFS 10-01) Thailand, 2001.
25. Wendling, C.C., Wegner, K.M. Relative contribution of reproductive investment, thermal stress and *Vibrio* infection to summer mortality phenomena in Pacific oysters. *Aquaculture*. 2013. 412–413. Pp. 88–96. DOI: 10.1016/j.aquaculture.2013.07.009
26. Achal, V., Mukherjee, A., Reddy, M.S. Microbial Concrete: Way to Enhance the Durability of Building Structures. *Journal of Materials in Civil Engineering*. 2011. 23(6). Pp. 730–734. DOI: 10.1061/(ASCE)MT.1943-5533.0000159
27. Afifi, H.A.M., Geweely, N.S., Galal, H.S., Abdelrahim, S.A., Al-Qudsi, F.M.S. Antimicrobial activity of gold nanoparticles (AuNPs) on deterioration of archeological gilded painted cartonnage, late period, Saqqara, Egypt. *Geomicrobiology Journal*. 2015. 0451(March 2016). Pp. 00–00. DOI: 10.1080/01490451.2015.1074323
28. Krivoshein, Y. *Handbook on Microbiology: Laboratory Diagnosis of Infectious Diseases*. Moscow : Mir publ, 1989. Moscow, 1989.

29. ASTM C403. ASTM C 403. Standard Test Method for Time of Setting of Concrete Mixtures by Penetration Resistance. ASTM C 403-95, Annual Book of ASTM Standards, American Society for Testing and Materials, Pennsylvania, 1998. ASTM. 2005. Pp. 1–7. DOI: 10.1520/C0403
30. Givi, A.N., Abdul Rashid, S., Aziz, F.N.A., Mohd Salleh, M.A. Particle size effect on the permeability properties of nano-SiO₂ blended Portland cement concrete. *Journal of Composite Materials*. 2011. 45(11). Pp. 1173–1180. DOI: 10.1177/0021998310378908
31. Naji Givi, A., Abdul Rashid, S., Aziz, F.N.A., Salleh, M.A.M. The effects of lime solution on the properties of SiO₂ nanoparticles binary blended concrete. *Composites Part B: Engineering*. 2011. 42(3). Pp. 562–569. DOI:10.1016/j.compositesb.2010.10.002.
32. ASTM. Standard Test Method for Measurement of Rate of Absorption of Water by Hydraulic-Cement Concretes ASTM C 1585:2007. American Society for Testing and Materials. 2007. Pp. 1–6.
33. Jonkers, H.M., Thijssen, A., Muyzer, G., Copuroglu, O., Schlangen, E. Application of bacteria as self-healing agent for the development of sustainable concrete. *Ecological Engineering*. 2010. 36(2). Pp. 230–235. DOI:10.1016/j.ecoleng.2008.12.036
34. ISO 679-1989: Method of Testing Cement.
35. ASTM C 348-86: Flexural Strength of Hydraulic Cement Mortars.
36. ASTM C1012/C1012M-15. Standard test method for length change of hydraulic-cement mortars exposed to a sulfate solution. ASTM International, West Conshohocken, PA. 2015. 11. Pp. 5–9. DOI:10.1520/C1012.
37. Concretes, P. Standard Test Methods for Chemical Resistance of Mortars , Grouts , and Monolithic. 1998.
38. Yunsheng, Z., Wei, S., Zongjin, L., Xiangming, Z., Eddie, Chungkong, C. Impact properties of geopolymer based extrudates incorporated with fly ash and PVA short fiber. *Construction and Building Materials*. 2008. 22(3). Pp. 370–383. DOI: 10.1016/j.conbuildmat.2006.08.006.
39. Jonkers, H.M.M., Palin, D., Flink, P.J., Thijssen, A. Microbially mediated carbonation of marine alkaline minerals: Potential for concrete crack healing. ICSHM 2013: Proceedings of the 4th International Conference on Self-Healing Materials, Ghent, Belgium, 16-20 June 2013. 2013. Pp. 610–614. DOI: 3078d20c-2173-4c13-a4d7-106207c78577

Contacts:

Vera Galishnikova, GalishnikovaVV@mgsu.ru

Sherif Elroba, ERU.SHERIF@yahoo.com

Mohamed Nassar, nasefmohamedo@gmail.com

Ahmed Sakna, ahmadsakna96@gmail.com



DOI: 10.34910/MCE.105.4

Impact resistance of steel fiber-reinforced self-compacting concrete

S.R. Abid* , S.H. Ali , H.A. Goaiz , T.S. Al-Gasham , A.L. Kadhim 

Wasit University, El-Kut, Iraq

*E-mail: sallal@uowasit.edu.iq

Keywords: concrete, steel fibers, self-compacting concrete, fiber-reinforced concrete, impact

Abstract. Among the adopted test methods to evaluate the impact resistance of materials and structural members is the drop-weight impact test. The ACI 544-2R repeated drop-weight impact testing technique was used in this research to evaluate the impact resistance of Self-Compacting Concrete (SCC) reinforced with micro-steel fibers. SCC concrete sample were made with two concrete grades and four fiber volumetric contents of 0, 0.5, 0.75 and 1.0 %. Another investigated parameter is the shape of the test specimen, where disk specimens (150 mm diameter and 65 mm thickness), 70 mm cubes and 70×70×260 mm beams were tested. The experimental results showed continuous improvement of impact resistance of SCC as the fiber content increased with percentage improvements ranging from 110 to 1200 % compared to the plain SCC. The failure impact resistance of the high strength SCC was higher than that of normal strength SCC regardless of specimen type and fiber content. The test results also showed that the impact resistance of disk specimens were clearly higher than those of cubes and beams and has more uniform variation with fiber content.

1. Introduction

Self-Compacting Concrete (SCC) can be described as a special type of flowable concrete that is consolidated due to its own weight without any signs of undesirable segregation or bleeding. Such property can save both time and cost by eliminating the effort required for external vibration. Moreover, it reduces the site noise leading to a better work environment. The flowability of concrete can also lead to better surfacing of the structural elements resulting in enhanced durability [1]. According to EFNARC [2] and ACI 273R [1], a concrete should pass the required limitations of the tests of three properties to be considered as a successful SCC. Filling ability, passing ability through steel reinforcement and segregation resistance during casting are the desired properties of SCC. Several tests were developed by researches and adopted by different standards to examine the required properties. Like the ordinary concrete, SCC is relatively a brittle material that shows weak behavior under tensile loads. This brittleness also leads to low dynamic response and impact resistance. Steel and synthetic fibers can be added to SCC to make it more ductile, which enhances the structural behavior both under static and dynamic loads. However, such fibers significantly reduce the flowability of SCC mixtures, which imposes the use of more liquidity and viscosity enhancement agents. The effect of different types and sizes of steel fibers on the fresh properties and mechanical properties of Steel Fiber-Reinforced Self-Compacting Concrete (SFRSCC) were investigated by many previous researchers [3–7] who revealed the adverse effect of steel fiber on workability and fresh properties of concrete.

One of the loads that concrete structures are possible to suffer is the short duration dynamic load. Such load can be imposed by accidental impacts of moving objects, projectiles, or even wind gusts [8–11]. The influence of using steel fiber with different types of concretes on the impact resistance was investigated by many studies using different testing techniques. The most widely used of impact loading tests are the

Abid, S.R., Ali, S.H., Goaiz, H.A., Al-Gasham, T.S., Kadhim, A.L. Impact resistance of steel fiber-reinforced self-compacting concrete. Magazine of Civil Engineering. 2021. 105(5). Article No. 10504. DOI: 10.34910/MCE.105.4

© Abid, S.R., Ali, S.H., Goaiz, H.A., Al-Gasham, T.S., Kadhim, A.L., 2021. Published by Peter the Great St.Petersburg Polytechnic University



This work is licensed under a CC BY-NC 4.0

Charpy pendulum test and the drop weight test. In addition, other test methods like the projectile impact and explosive tests were also considered to evaluate the impact resistance of concrete. Among these tests, the repeated drop weight impact test is considered as a simple and low-cost alternative for this purpose. This test is recommended by ACI 544-2R [12], which uses the recorded number of impact blows till cracking and failure as measurements of the impact resistance of the tested specimen. This test was used by many previous studies to evaluate the impact resistance of concretes incorporating steel or other types of synthetic fibers [8, 13–23]. Other studies utilized the procedure of ACI 544-2R [12] to conduct repeated flexural impact tests on concrete beams [24–29]. In these studies, the drop weight, drop height, the geometry of the test specimen and the flexural span differed from study to another.

Few studies were found in the literature on the repeated impact resistance of SFRSCC [30–36]. Using the ACI 544-2R [12] drop-weight impact method, Khalil et al. [30] studied the impact performance of rubberized SCC containing different contents of crumb rubber, while Ismail and Hassan [31] investigated the impact resistance of steel fiber-reinforced rubberized SCC. Khalil et al. [30] and Ismail and Hassan [31] used different replacement levels of the fine aggregate by crumb rubber and steel fiber volume fractions up to 1 %. Hooked end steel fibers were used with fiber lengths of 35 and 60 mm. The test results revealed that both crumb rubber and steel fiber enhance the impact resistance. Another study by AbdelAleem et al. [32] conducted experimental impact tests to investigate the impact resistance of rubberized SCC containing flexible and rigid synthetic fibers. Two test procedures were utilized in the study, the ACI 544-2R drop-weight impact method and the flexural impact test. Ding et al. [33] also used the ACI 544-2R drop-weight impact method and the flexural impact test to study the combined effect of steel bars and fibers on the impact resistance of SCC. Polypropylene and steel fibers were used with lengths of 30 and 35 mm, respectively. The test results showed that the combined effect of steel bars and fibers are superior to the superposition of their individual effects by approximately 30 to 200 %. Mastali et al. [34–36] used the ACI 544-2R [12] method to evaluate the impact resistance of SCC incorporating different types of recycled fibers (glass and carbon fibers).

The previous studies were found in the literature on the impact resistance of steel fiber reinforced concretes or on SCC incorporating synthetic and steel fibers using the ACI 544-2R drop-weight impact method. However, no study was found on the impact resistance of normal and high strength SCC incorporating micro steel fibers. Thus, an experimental program was directed in this study to examine the impact resistance of SFRSCC using the repeated drop-weight impact loading test. In addition, the effect of the specimen shape on the test measurements was also investigated using three different types of test specimens.

2. Methods

The experimental program of this study was directed to examine the impact resistance of SFRSCC. Mainly, two basic SCC mixtures were designed to obtain a nominal compressive strength of 30 MPa as normal strength SCC (NS-SCC) and 50 MPa as high strength SCC (HS-SCC). For each of which, four fiber volumetric contents of 0 %, 0.5 %, 0.75 % and 1.0 % of micro-steel fibers were adopted. For each SCC grade, the zero-fiber specimens were prepared for comparison purposes. The shape of the test specimen was also one of the main investigated parameters in this study. In addition to the impact resistance, the compressive strength was obtained using 70 mm concrete cubes, while the modulus of rupture was obtained using the four-point bending test on 70×70×260 mm beams with a span of 210 mm and shear spans of 70 mm. To evaluate the fresh properties of the SCC mixtures, three fresh concrete properties were tested. For the slump flow, the T50 tests as per the requirements of ASTM C1611 [37] was followed. For the penetration ability, the rapid penetration test procedure recommended by ASTM C1712 [38] was adopted. Also, the slump flow and the T50 tests are recommended by EFNARC [2] to evaluate the acceptability of the SCC. The accepted values of the three tests are shown in Table 1 according to the requirements of ASTM and EFNARC standards.

Table 1. Accepted values of slump flow, T50 and rapid penetration tests.

Test	Limitations		ASTM Standard
	EFNARC	ASTM	
Slump flow (mm)	650–800	480–680* Or 530–740**	ASTM C1611
T50 (sec)	2–5		
Rapid Penetration (mm)		0–10 † 10–25 ††	ASTM C1712

* Single-operator precision; ** Double-operator precision; † Resistance to segregation; †† Moderately resistance to segregation

The impact tests were carried out using the repeated drop-weight test recommended by ACI 544-2R [12]. This testing technique uses the number of impact blows absorbed by the test specimen as an index for impact resistance. Based on the recommendations of ACI 544-2R [12], a drop weight of approximately 4.5 kg should fall freely from a drop height of approximately 450 mm on a steel ball of 63 mm diameter placed on the center of the surface of the test specimen. The impact loading is repeated until a visible crack is shown along the full diameter length of the top surface. During the test, the specimen is restricted in place using four steel lugs and two elastomer pieces on a stiff steel base. After cracking, the elastomers are removed and the impact test continues until failure. The number of blows required to cause the specimen to crack and fracture is then recorded. Fig. 1 shows the details of the testing apparatus.

In this study, the impact load was 4.5 kg and was dropped from a height of 700 mm. The drop height was increased from 450 mm to 700 mm in order to reduce the number of blows in each test due to the high strength characteristic of the SCC used in this study. The test specimen is a concrete disk having a diameter of 150 mm and a thickness of approximately 65 mm. However, as the shape of the specimen is one of the studied variables in this research, different shapes of specimens were tested under repeated impact loading. In addition to the disks, cube specimens of 70 mm side length and beam specimens of 70×70×260 mm were used to evaluate the impact resistance. To evaluate the shape effect, the thickness of all specimens was kept approximately equal which were 65 mm for the disks and 70 mm for the other specimens.

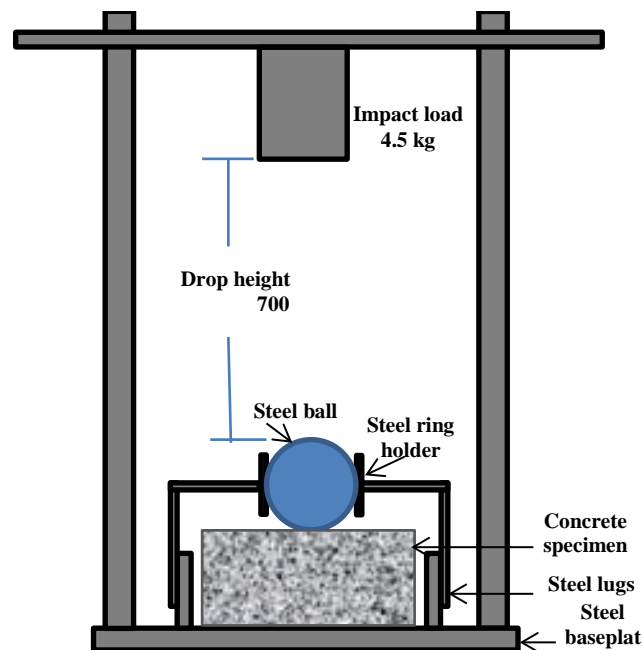
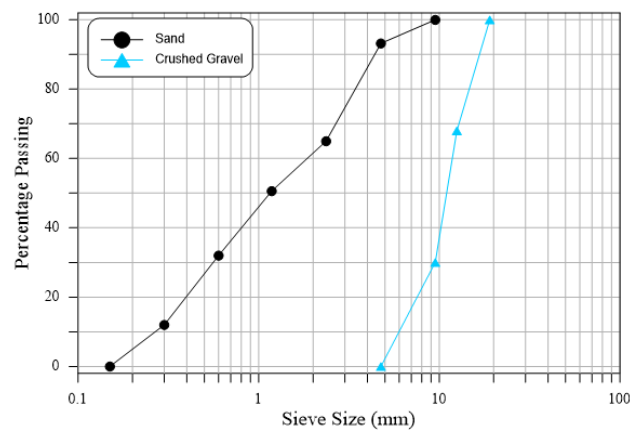


Figure 1. Apparatus of the repeated drop-weight impact test.

As mentioned above, two concrete design grades of 30 MPa (NS-SCC) and 50 MPa (HS-SCC) were adopted with four different fiber contents. Thus, a total of eight SCC mixes were adopted with weight proportions as listed in Table 2. The cement used in all mixtures was type R42.5 Portland cement, while the aggregate of the mixtures were crushed gravel and sand with grading, as shown in Fig. 2. The silica fume was used only with the high strength mixes as shown in Table 2 and 67 kg/m³ of limestone powder was used with all SCC mixes. Cooper-coated straight micro steel fiber were used in this study with diameter and length of 0.2 mm and 15 mm and a tensile strength of 2600 MPa according to properties provided by the manufacturer. Also, the production of the SCC cannot be achieved without using of a high range water reducing agent (super plasticizer), for this reason Sika ViscoCrete-5930 was used in this study. To evaluate the impact resistance of the SCC mixes, six cubes, twelve beams, and six disks were cast from each concrete mix. Four cubes were also cast and tested to evaluate the compressive strength and eight beams were cast and tested to evaluate the modulus of rupture. Thus, a total number of 80 cubes, 160 beams, and 48 disks were cast and tested in this study. All specimens were cured in temperature-controlled water tanks for 28 days at a temperature of approximately 23 °C until testing date. Fig. 3 shows one SCC batch of specimens before and after demolding.

Table 2. Mix proportions per cubic meter of the SCC mixtures.

Mix	Design Grade (MPa)	Fiber volume Content (%)	Cement (kg/m ³)	Sand (kg/m ³)	Gravel (kg/m ³)	Silica fume (kg/m ³)	Water (kg/m ³)	Water/Binder (W/B)	Superplasticizer S.P. (kg/m ³)
M1	30	0	392	1039	574	—	181.3	0.395	9.3
M2	30	0.5	412	1063	503	—	190	0.397	13
M3	30	0.75	412	1063	503	—	190	0.397	13
M4	30	1.0	417	1052	468	—	204	0.42	14.3
M5	50	0	525	907	518	67	190	0.288	17
M6	50	0.5	525	907	518	67	209	0.317	17
M7	50	0.75	525	931	486	67	209	0.317	17
M8	50	1.0	525	931	486	67	209	0.317	17

**Figure 2. Sieve analysis of sand and crushed gravel.****(a)****(b)****Figure 3. A batch of cast disk, cube and beam specimens for one mixture (a) molding (b) demolded.**

3. Results and Discussion

3.1. Fresh properties of SCC

The fresh properties are the slump flow, T_{50} and rapid penetration tests. The test results of all mixtures showed good SCC behavior. The slump flow was within the limitations of EFNARC [2], where the slump flow records of the eight mixtures were in the range of 615 to 755 mm. On the other hand, the T_{50} records ranged from 2.5 to 4.9 seconds for all mixtures except one mixture, this means that these records are within the limitations of EFNARC [2]. For the HS-SCC with fiber content of 0.5, the T_{50} was 6 seconds, which is quite acceptable as it is quite close to the limitation, especially as the other fresh properties of this mixture were within the limitations. The records of the rapid penetration test of all mixtures were less than 9 mm, which reveals a good resistance to segregation, according to ASTM C1712 [38].

3.2. Compressive and flexural strength

The test results of 70 mm cube compressive strength of the eight mixes at the age of 28 days are shown in Fig. 4a and their corresponding beam flexural strength (modulus of rupture) is shown in Fig. 3b. Fig. 4a shows obviously that the compressive strength of the HS-SCC is higher than that of NS-SCC for all fiber contents. However, it also shows that within each grade of the SCC, the compressive strength was not clearly sensitive to the variation of steel fiber content and this behavior was stated within several previous studies [5, 16, 31, 39]. The compressive strength of NS-SCC was in the range of approximately 51 to 56 MPa, while that of HS-SCC was in the range of 83 to 88 MPa for all fiber contents. Fig. 4b shows that the modulus of rupture increases as the fiber content increases for both concrete grades. The modulus of rupture of NS-SCC increased from 5.57 MPa for plain specimens to 7.93 for 1 % fiber content. Similarly, the modulus of rupture of HS-SCC increased from 6.06 MPa for plain specimens to 8.1 for 1 % fiber content.

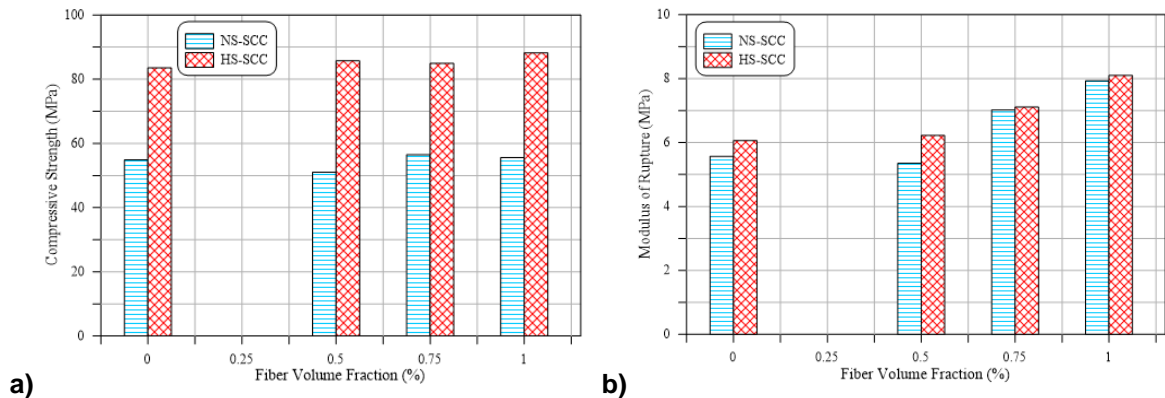


Figure 4. (a) Compressive strength and (b) modulus of rupture of NS-SCC and HS-SCC including different fiber contents.

3.3. Effect of fiber content and concrete strength on impact resistance

Fig. 5 shows the retained number of blows at the first crack stage and failure stage for different fiber contents. The results of disk specimens in Fig. 5a shows that the number of retained impact blows increases with the increase of fiber content for both NS-SCC and HS-SCC. This trend is observed for both the first crack stage and the failure stage. This behavior could be due to the important role of the steel fiber to delay the propagation and distribution of micro-cracks though out the hardened concrete matrix while under stresses. The number of impact blows for NS-SCC disk specimens with fiber contents of 0, 0.5, 0.75 and 1.0 % were 42, 106, 177 and 245 blows at the first crack stage, respectively. For HS-SCC disk specimens, the numbers of blows at the first crack stage were 54, 246, 302 and 408 for fiber contents of 0, 0.5, 0.75 and 1.0 %, respectively. The presence of discrete short fibers in the matrix is known to increase the tensile strength, energy absorption of the fibrous concrete and change the failure mode from brittle to more ductile by the potential of crack bridging [40–42], which improves the impact resistance of fibrous specimens showing larger number of impact blows before cracking or failure and more blows after first crack [43–46].

Fig. 5a also shows that for disk specimens, the impact resistance of HS-SCC was superior to that of NS-SCC. This behavior could be attributed to (a) the lower void ratio within the hardened matrix of HS-SCC than one of NS-SCC due to the higher water/cement ratio of NS-SCC, (b) the better aggregate-cement mortar interface of HS-SCC compare to NS-SCC due to the higher cement content of HS-SCC. The number of impact blows at first crack stage (N_I) and at failure stage (N_f) were clearly higher for the HS-SCC than those of NS-SCC for all fiber contents. Comparing the two curves at failure stage, the N_f values for NS-SCC and HS-SCC, respectively, were 43 and 56 for plain SCC, while the N_f values were 120 and 261, 212 and 343 and lastly 293 and 495 for fiber contents of 0.5, 0.75 and 1.0 %, respectively.

Fig. 5b shows N_I and N_f results of the plain and fibrous NS-SCC and HS-SCC cube specimens. It is clear in the figure that both N_I and N_f increase with the increase of steel fiber content, which confirms the results obtained from Fig. 5a for disk specimens. However, the differences in N_I and N_f values between NS-SCC and HS-SCC are not as clear as for disk specimens. The figure shows that N_f records of NS-SCC fibrous cubes are mostly higher than N_I records of HS-SCC. Such a result was not the case in Fig. 5a where HS-SCC was clearly superior to NS-SCC. Although, N_I values of HS-SCC still obviously higher than their corresponding NS-SCC N_I records and similarly N_f records of HS-SCC were higher than those of NS-SCC. N_I records for NS-SCC were 3, 9, 12, and 17 blows for fiber contents of 0, 0.5, 0.75 and 1.0 %, respectively, while their corresponding N_f records were 4, 22, 24 and 39 blows, respectively. On the other

hand, N_I records of HS-SCC were 7, 15, 24 35 blows for fiber contents of 0, 0.5, 0.75 and 1.0 %, respectively, while the corresponding N_f values were 12, 32, 41 and 56, respectively.

The results of the impact beam specimens confirm that regardless of the strength, the inclusion of micro-steel fiber results in higher impact resistance. Fig. 5c shows that the effect of concrete strength was almost negligible at the first crack stage, where poor impact resistance was observed for both NS-SCC and HS-SCC. The recorded N_I values for NS-SCC beams at the first crack stage were 1, 3, 5 and 6, which are very close to the N_I values for HS-SCC were 1, 4, 5 and 7 blows for steel fiber contents of 0, 0.5, 0.75 and 1.0 %, respectively. However, significant differences were recorded between NS-SCC and HS-SCC at the failure stage. The recorded N_f values for NS-SCC beams at first crack stage were 13, 15 and 16, while the N_f values for HS-SCC were 20, 24 and 26 blows for steel fiber contents of 0.5, 0.75 and 1.0 %, respectively.

Fig. 6 shows the improvement percentages in retained number of impact blows due the inclusion of micro-steel fiber compared to plain SCC for both NS-SCC and HS-SCC. The improvement or increase in impact resistance due to fiber inclusion was calculated as a percentage ratio, which equals the difference between number of blows of fibrous specimens (each fiber content) and nonfibrous reference specimens (0 % fiber) divided by the number of blows of nonfibrous reference specimens. For disk specimens, Fig. 6a shows an obvious increase behavior of the percentage increase in impact resistance with all steel fiber content. It is obvious that the percentage improvement of N_I and N_f for both NS-SCC and HS-SCC increases as the fiber content increases.

Another notice is that the percentage increase in N values for HS-SCC was higher than those of NS-SCC at both first crack and failure stages. For example, the percentage increases in impact resistance of 0.75 % steel fiber content were 321, 393, 459 and 512 % for N_I NS-SCC, N_f NS-SCC, N_I HS-SCC and N_f HS-SCC, respectively. Similar trend of results was observed for the other fiber contents as shown in Fig. 6a. The percentage improvement in impact resistance for disk specimens ranged from approximately 150 % to approximately 780 % for all tested specimens.

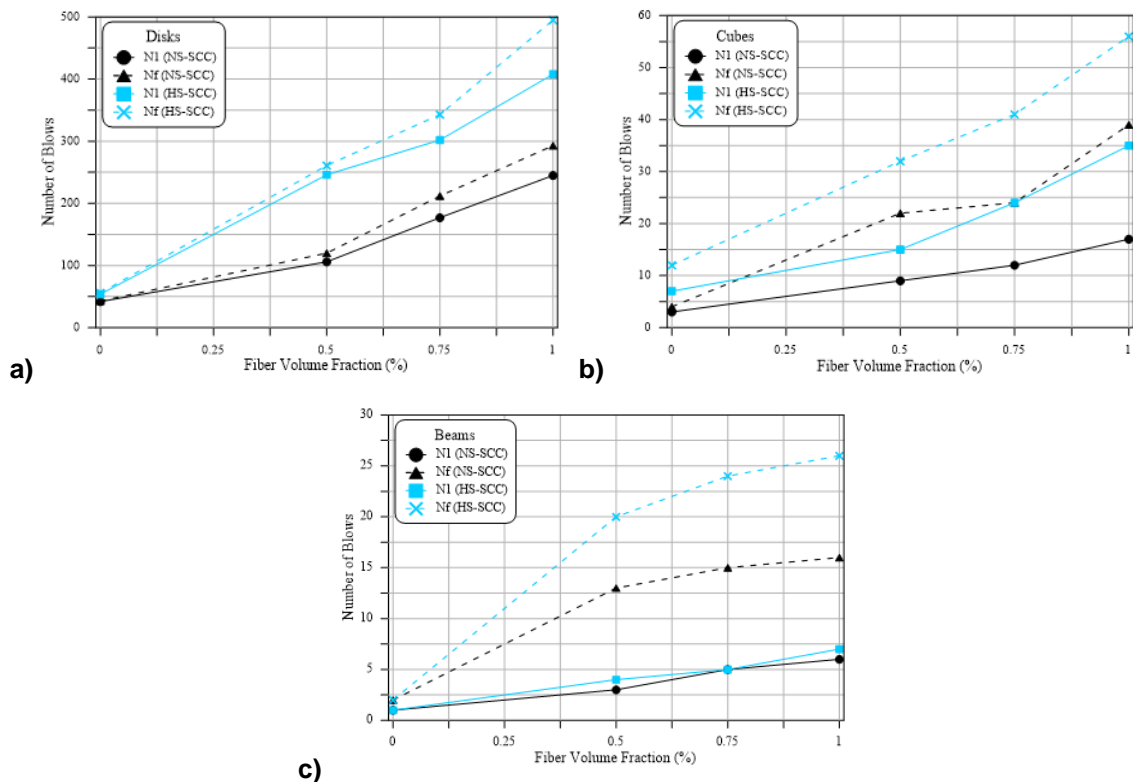


Figure 5 Number of blow at the first crack (N_I) and failure (N_f) stages for (a) disk, (b) cube and (c) beam specimens.

For cube specimens as shown in Fig. 6b, the results trend was different. The cube specimens showed that NS-SCC exhibited higher percentage of developments of impact resistance compared to HS-SCC for all fiber contents. The percentage improvement in N_f values was clearly higher than the N_I values of NS-SCC, while no noticeable improvement was observed for HS-SCC. For a fiber content of 1.0 % for example, the percentage developments in impact resistance of cube specimens were 467, 875, 400 and 366 % for N_I NS-SCC, N_f NS-SCC, N_I HS-SCC and N_f HS-SCC, respectively. In general, the

percentage of developments for cube specimens ranged from 114 % to 875 %, which is very close to the development range obtained by disk specimens. The beam specimens showed that the percentage development of N_f values were higher than the N_I values for both of NS-SCC and HS-SCC. Another notice is that the percentage developments of N_f of HS-SCC were the highest for all fiber contents among the beam specimens and more than those obtained by disk or cube specimens. The percentage of developments in impact resistance of beam specimens were in the range of 200 to 1200 % as shown in Fig. 6c, while the minimum percentage development of N_f for HS-SCC was 900 %.

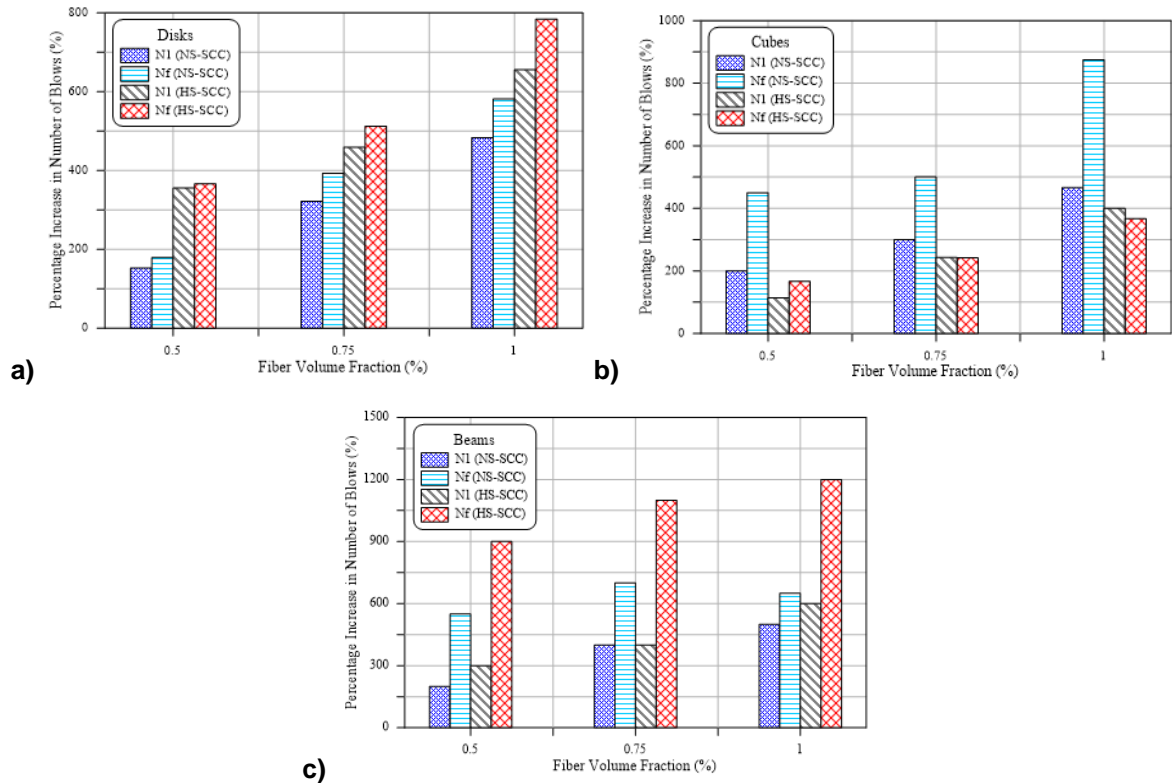


Figure 6. Percentage increase due to fiber addition in number of blows at first crack (N_I) and failure (N_f) stages for (a) disk, (b) cube and (c) beam specimens.

3.4. Effect of specimens shape on the repeated impact test

As mentioned earlier, most of the experimental works on repeated impact tests were either conducted using the ACI 544-2R method, which only uses disc specimens or flexural impact tests on beams. However, few studies used repeated drop-weight impact tests on different configurations of test specimens. Zhu et al. [39] conducted drop-weight impact tests on U-shaped specimens. Zhu et al. [35] used a drop height of 400 mm and a drop weight of less than 1 kg. Wang and Chouh [40] used cylinder test specimens of 100 mm diameter and 200 mm with a drop weight of 40 kg and drop heights ranging from 500 mm to 2000 mm. The current study and as mentioned above (Section 3), in addition to the ACI 544-2R disc specimens, beams and cubes were tested using the testing procedure of ACI 544-2R. The depth of the beam and cube specimens (70 mm) was chosen to be comparable to the depth of the disc specimens (65 mm).

Fig. 7 and 8 compare the impact resistances of the three tested shapes of specimens (disk, cube and beam) for the two grades of SCC in terms of both N_I and N_f values. It is disclosed in the previous section that, in general, disk specimens withstand a much higher number of blows compared to cube or beam specimens. This experimental result is shown clearly in Fig. 7 and 8, where N_I and N_f values of disk specimens are compared with 10 times their corresponding values of cube and beam specimens. The figures show that the N_I and N_f records of disk specimens with the variation of fiber content were more systematic compared to cube or beam specimens. Fig. 7a shows that in the case of N_I values for NS-SCC, the disk records were clearly higher than 10 times those of cube and beam specimens for all fiber contents. However, beam specimens showed the lowest recorded values. The N_I values for disk, cube and beam specimens were 42, 3 and 1, respectively, for plain SCC, while the corresponding N_f values were 43, 4 and 2, respectively, as shown in Fig. 7b. Similarly, the N_I values were 245, 17 and 6, respectively, for fiber content of 1.0 %, while the corresponding N_f values were 293, 39 and 16, respectively. Fig. 7b shows that the variation of N_f values for NS-SCC between the three shapes of specimens is not as uniform as that of

N_I . The cube records multiplied by 10 of fibrous specimens were higher than those of beam specimens and the records of disks, while this was not the case for plain SCC specimens. On the other hand, N_I results of HS-SCC shown in Fig. 8a shows approximately similar uniform trend as that of Fig. 7a, while Fig. 7b of N_f records of HS-SCC shows similar non uniform variation as that of Fig. 7b. Fig. 9 shows the fiber content effect on the difference between N_f and N_I of the three shapes of specimens in the case of NS-SCC and HS-SCC. Fig. 9a and Fig. 9b show that the disk specimens absorbed higher number of impact blows after first crack than cube or beam specimens. Disk specimens also show continuous increase in the number of absorbed blows after first crack as fiber content increases. For cube and beam specimens, the inclusion of fiber was effective in terms of increasing the number of absorbed blows, however, no noticeable effect of fiber content increase from 0.5 % to 1.0 % which is represented by the semi-horizontal lines. The results represented in Fig. 9 confirm the superiority of disk specimens over cube and beam specimens to represent the drop-weight impact test.

To check the reliability of the repeated drop-weight impact test results, linear correlations between N_I and N_f were adopted for each shape of specimens. Fig. 10a, b and c show the linear correlations between N_I and N_f for both NS-SCC and HS-SCC for the disk specimens, cube specimens and beam specimens, respectively. Fig. 10a shows that the linear correlations between N_I and N_f have strong coefficient of determination (R^2) of more than 0.99 for both NS-SCC and HS-SCC. While, the R -squared values of cube specimens were 0.966 and 0.974 for NS-SCC and HS-SCC, respectively and those ones of beam specimens were 0.846 and 0.901 for NS-SCC and HS-SCC, respectively. Note that the high R -squared value reveals the excellent goodness of the linear fit between N_I and N_f of disk specimens. Thus, it is clear that the impact tests of disk specimens showed more consistent results compared to those obtained from cube and beam specimens. Considering the uniformity of the variation trend of the number of retained blows with fiber content, the absorbed blows after first crack with fiber content and the goodness of the relation between N_I and N_f as judgment factors, it is concluded that disk specimen can be considered as a better choice for repeated drop-weight impact test than beam and cube specimens.

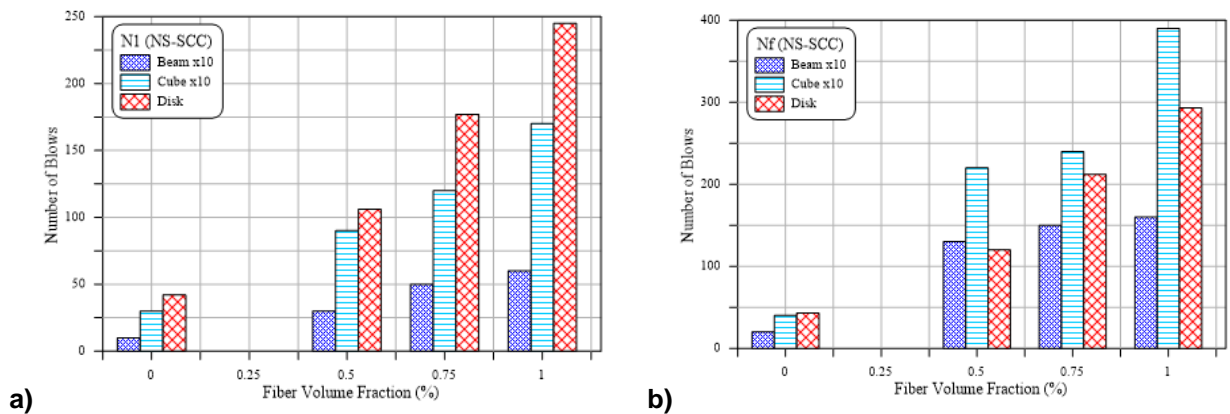


Figure 7. Number of blows for different shape NS-SCC specimens (a) at first crack stage (N_I) and (b) at ultimate failure stage (N_f).

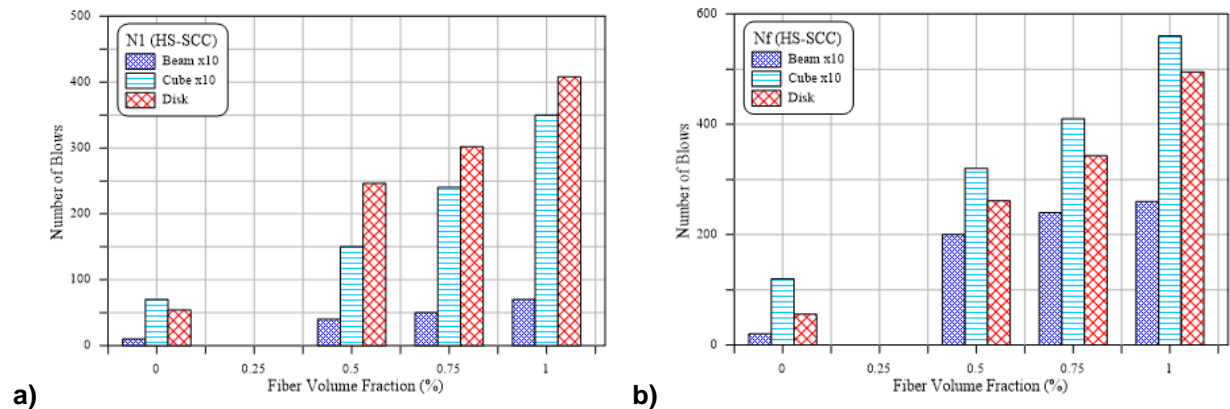


Figure 8. Number of blows for different shape HS-SCC specimens (a) at first crack stage (N_I) and (b) at ultimate failure stage (N_f).

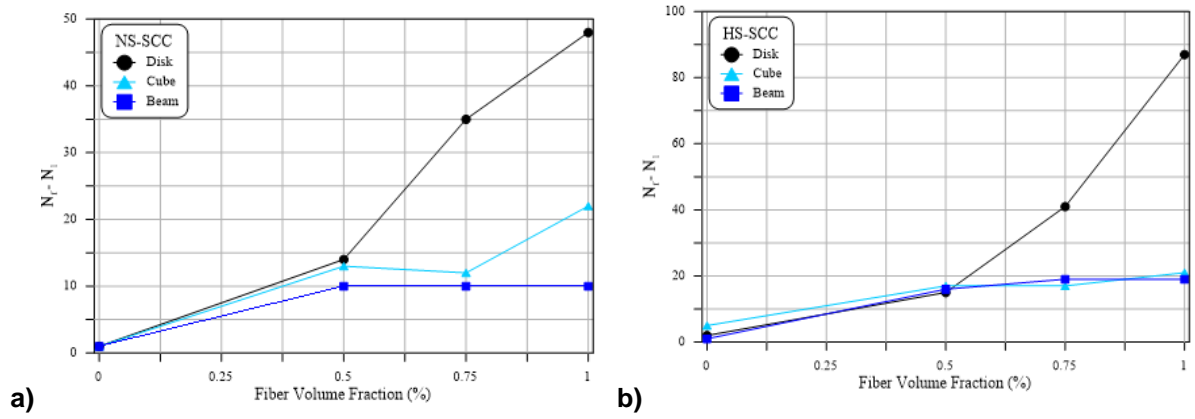


Figure 9. Relation of ($N_f - N_1$) and fiber volume fraction for different specimen shapes for (a) NS-SCC and (b) HS-SCC.

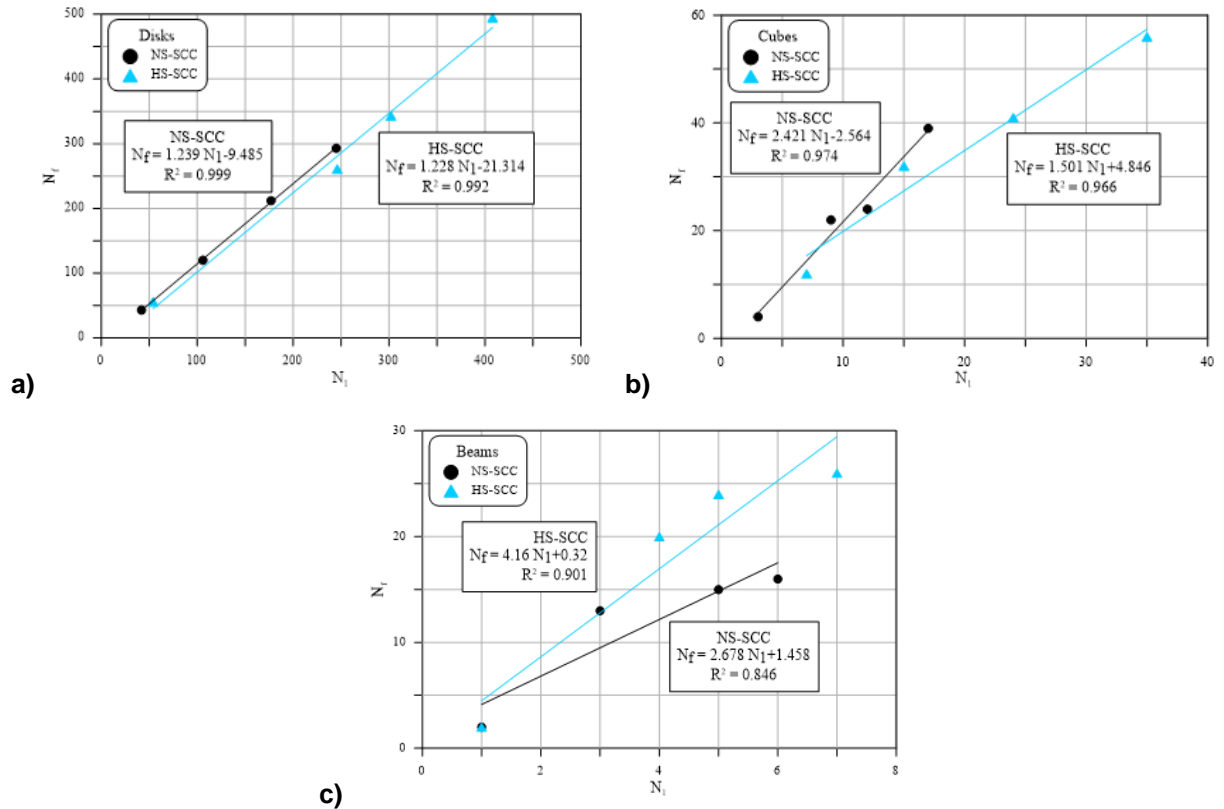


Figure 10. Linear relationships of N_f and N_1 for NS-SCC and HS-SCC for (a) disk, (b) cube and (c) beam specimens.

3.5. Relationship between impact resistance and flexural strength

As presented in section 4.1, the compressive strength was slightly affected by the presence of fibers, while the flexural strength showed a continuous increase with the increase of fiber content. Also, there is no relation can be found in the literature to show the correlation between the impact resistance and the flexural strength. Accordingly, in this study, the flexural strength was chosen to show the relationship between concrete strength and impact absorption capacity of the tested specimens in terms of N_1 and N_f . Such a relation can be used to estimate the impact resistance of fiber-reinforced concrete by conducting a simple test procedure of the flexural test. Due to the limited number of data in this study, test results of other studies were used to create the relationship between the impact resistance and the flexural strength. Most of the available studies in the literature that provide data N_1 , N_f and flexural strength were limited to normal strength concrete and disk shape specimens. For this reason, the test results of HS-SCC, cube specimens and beam specimens of the current study were excluded from the correlation. In addition to the test results of the current study, results of Ismail and Hassan [31], AbdelAleem et al. [32] and Mastali et al. [34] were used to create the correlation as shown in Table 3 and Fig. 11. This figure shows that the relationship between impact resistance and flexural strength can be represented by the simple linear

correlation. The figure also shows that the goodness of the fit slightly varies from N_I and N_f . For N_I , the linear relation shows an R-squared value of approximately 0.856, while this value increases to 0.87 for N_f . Equations 1 and 2 below show the linear correlation between the number of blows (impact resistance) and flexural strength for N_I and N_f , respectively.

$$N_I = 165.2 f_r - 789.1 \quad (R^2 = 0.857) \quad (1)$$

$$N_f = 191.5 f_r - 920.5 \quad (R^2 = 0.874) \quad (2)$$

Table 3. Test results used to create relationship between impact resistance and flexural strength.

Resource of Data	Number of Blows at First crack stage, N_I	Number of Blows at First crack stage, N_f	Flexural Strength, f_r (MPa)
Current Study	105	110	5.4
	145	148	5.6
Ismail and Hassan [31]	38	47	4.88
	56	71	5.36
	76	98	5.98
	141	143	5.7
	185	203	5.7
AbdelAleem et al. [32]	275	315	6.2
	243	273	6
	201	234	5.9
	337	391	6.7
Mastali et al. [34]	434	496	7.46

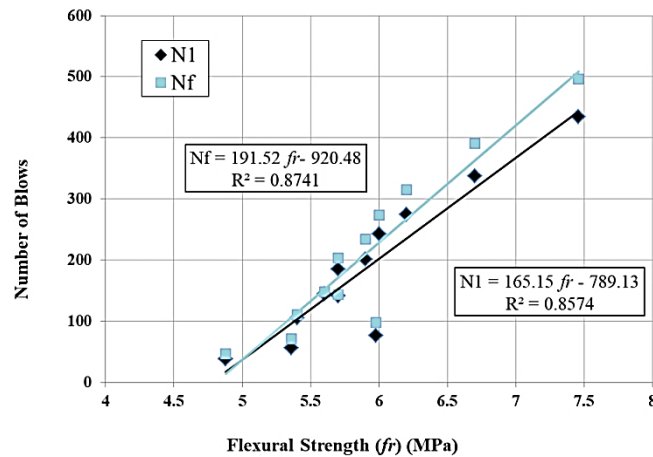


Figure 11. Linear correlations between number of blows and flexural strength for N_I and N_f .

4. Conclusions

In this study, an experimental work was carried out to evaluate the impact resistance of normal strength and high strength self-compacting concretes incorporating micro-steel fibers. The impact resistance was evaluated using the recorded number of repeated impact blows at first crack and failure stages based on the recommendations of ACI 544-2R, using three shapes of specimen disk, cube and beam. Based on the experimental results of this study, it can be concluded:

1. The addition of steel fibers to the SCC enhances its impact resistance significantly, where the retained number of impact blows increased continuously as the fiber volumetric content increased from 0 to 1.0 %. For example, in the case of disk specimens the number of blows at first crack stage N_I was recorded 42, 106, 177 and 245 for NS-SCC with steel volume content of 0 %, 0.5 %, 0.75 % and 1.0 %, respectively. Similar sequence of results was obtained for number of blows at failure stage N_f values.

2. The inclusion of micro-steel fibers led to noticeably high percentage improvement in the impact resistance of both NS-SCC and HS-SCC. The percentage improvement in impact resistance ranged from

more than 110 % to 1200 % for all tested specimens. The highest effect of micro-steel fibers on impact resistance was recorded for beam specimens where the minimum percentage improvement was 900 %.

3. HS-SCC retained significantly higher N_f records than NS-SCC for all types of specimens and at all fiber contents. Similarly, N_I values for HS-SCC were mostly higher than those of NS-SCC. Considering the disk specimen as an example, N_f records for NS-SCC were 43, 120, 212 and 293 blows for fiber volume contents of 0, 0.5, 0.75 and 1.0 %, respectively, while the corresponding values for HS-SCC were 56, 261, 343 and 495 blows, respectively.

4. Disk specimens recommended by ACI 544-2R-2R showed high N_I and N_f values compared to cube and beam specimens. In general, the N_I and N_f records of disc specimens were approximately 10 times those of cube specimens, which were approximately twice those of beam specimens.

5. The disk specimens showed more systematic variation in N_I and N_f values with the variation of fiber content than cube and beam specimens. Similar result were obtained for the relation of the absorbed impact blows after first crack in addition to the correlation between N_I and N_f . Based on the abovementioned parameters, disk specimens can be considered as a better choice for drop-weight loading impact test than beam and cube specimens.

6. A relationship between the impact resistance and the flexural strength of fiber reinforced concrete was created for the first time. This relation can be used to estimate the number of impact blows of FRC by simple test procedure of flexural strength.

References

1. ACI Committee 237. Self-consolidating concrete. (ACI 237R-07). American Concrete Institute, USA. 2007. Pp. 1–30.
2. EFNARC. Specifications and guidelines for self-compacting concrete. EFNARC, UK. 2002. Pp. 1–32.
3. Sahmaran, M., Yurtseven, A., Yaman, O. Workability of hybrid fiber reinforced self-compacting concrete. *Building and Environment*. 2005. 40. Pp. 1672–1677.
4. Aslani, F., Nejadi, S. Self-compacting concrete incorporating steel and polypropylene fibers: compressive and tensile strengths, modulus of elasticity and rupture, compressive stress-strain curve, and energy dissipation under compression. *Composites: Part B*. 2013. 53. Pp. 121–133.
5. Abid, S.R., Hilo, A., Ayoob, N.S., Daek, Y.H. Underwater abrasion of steel fiber-reinforced self-compacting concrete. *Case Studies in Construction Materials*. 2019. e00299.
6. Travush, V.I., Konin, D.V., Krylov, A.S. Strength of reinforced concrete beams of high-performance concrete and fiber reinforced concrete. *Magazine of Civil Engineering*. 2018. 77(1). Pp. 90–100.
7. Ayoob, N.S., Abid, S.R., Hilo, A.N., Daek, T.H. Water-Impact Abrasion of Self-Compacting Concrete. *Magazine of Civil Engineering*. 2020. 4. Pp. 60–69.
8. Nili, M., Afroughsabet, V. Combined effect of silica fume and steel fibers on the impact resistance and mechanical properties of concrete. *International Journal of Impact Energy*. 2010. 37. Pp. 879–886.
9. Haridharan, M.K., Matheswaran, S., Murali, G., Abid, S.R., Fediuk, R., Amran, Y.H., Abdelgader, H.S. Impact response of two-layered grouted aggregate fibrous concrete composite under falling mass impact. *Construction and Building Materials*. 2020. 263. 120628.
10. Salaimanimagudam, M.P., Suribabu, C.R., Murali, G., Abid, S.R. Impact response of hammerhead pier fibrous concrete beams designed with topology optimization. *Periodica Polytechnica Civil Engineering*. 2020. <https://doi.org/10.33-11/PPci.16664>
11. Abirami, T., Loganaganandan, M., Murali, G., Fediuk, R., Sreekrishna, R.V., Vignesh, T., Janupriya, G., Karthikeyan, K. Experimental research on impact response of novel steel fibrous concretes under falling mass impact. *Construction and Building Materials*. 2019. 222. Pp. 447–457.
12. ACI 544-2R. Measurement of properties of fiber reinforced concrete. American Concrete Institute. 1999. USA.
13. Yildirim, S.T., Ekin, C.E., Findik, F. Properties of hybrid fiber reinforced concrete under repeated impact loads. *Russian Journal of Nondestructive Testing*. 2010. 46. Pp. 82–92.
14. Nili, M., Afroughsabet, V. The effects of silica fume and polypropylene fibers on the impact resistance and mechanical properties of concrete. *Construction and Building Materials*. 2010. 24. Pp. 927–933.
15. Murali, G., Abid, S.R., Amran, Y.H.M., Abdelgader, H.S., Fediuk, R., Susrutha, R., Poonguzhali, K. Impact performance of novel multi-layered prepacked aggregate fibrous composites under compression and bending. *Structures*. 2020. 28. Pp. 1502–1515.
16. Nataraja, M.C., Dhang, N., Gupta, A.P. Statistical variations in impact resistance of steel fiber-reinforced concrete subjected to drop weight test. *Cement and Concrete Research*. 1999. 29. Pp. 989–995.
17. Song, P.S., Wu, J.C., Hwang, S., Sheu, B.C. Assessment of statistical variations in impact resistance of high-strength concrete and high-strength steel fiber-reinforced concrete. *Cement and Concrete Research*. 2005. 35. Pp. 393–399.
18. Bard, A., Ashour, A.F., Platten, A.K. Statistical variations in impact resistance of polypropylene fiber-reinforced concrete. *International Journal of Impact Engineering*. 2006. 32. Pp. 1907–1920.
19. Rahmani, T., Kiani, B., Shekarchi, M., Safari, A. Statistical and experimental analysis on the behavior of fiber reinforced concretes subjected to drop weight test. *Construction and Building Materials*. 2012. 37. Pp. 360–369.
20. Abid, S.R., Abdul-Hussein, M.L., Ayoob, N.S., Ali, S.H., Kadhum, A.A. Repeated drop-weight impact tests on self-compacting concrete reinforced with micro-steel fiber. *Heliyon*. 2020. 6. Pp. 1–11.

21. Abid, S.R., Abdul-Hussein, M.L., Ali, S.H., Kazem, A.F. Suggested modified testing techniques to the ACI 544-R repeated drop-weight impact test. *Construction and Building Materials*. 2020. 6. Pp. 1–16.
22. Asrani, N.P., Murali, G., Parthiban, K., Surya, K., Prakash, A., Rathika, K., Chandru, U. A feasibility of enhancing the impact resistance of hybrid fibrous geopolymer composites: Experiments and modelling. *Construction and Building Materials*. 2019. 203. Pp. 56–68.
23. Jabir, H.A., Abid, S.R., Abdul-Hussein, M.L., Ali, S.H. Repeated drop-weight impact tests on RPC containing hybrid fibers. *Applied Mechanics and Materials*. 2020. 897. Pp. 49–55.
24. Mohammadi, Y., Carkon-Azad, R., Singh, S.P., Kaushik, S.K. Impact resistance of steel fibrous concrete containing fibers of mixed aspect ratio. *Construction and Building Materials*. 2009. 23. Pp. 183–189.
25. Rao, M.C., Bhattacharyya, S.K., Barai, S.V. Behaviour of recycled aggregate concrete under drop weight impact load. *Construction and Building Materials*. 2011. 25. Pp. 69–80.
26. Al-Tayeb, M.M., Abu Bakar, B.H., Ismail, H., Akil, H.M. Impact resistance of concrete with partial replacements of sand and cement by waste rubber. *Polymer-Plastics Technology and Engineering*. 2012. 51. Pp. 1230–1236.
27. Dey, V., Bonakdar, A., Mobasher, B. Low-velocity flexural impact response of fiber-reinforced aerated concrete. *Cement & Concrete Composites*. 2014. 49. Pp. 100–110.
28. Zhang, W., Chen, S., Zhang, N., Zhou, Y. Low-velocity flexural impact response of steel fiber reinforced concrete subjected to freeze-thaw cycles in NaCl solution. *Construction and Building Materials*. 2015. 101. Pp. 522–526.
29. Noaman, A.T., Abu Bakar, B.H., Akil, H.M. The effect of combination between crumb rubber and steel fiber on impact energy of concrete beams. *Procedia Engineering*. 2015. 125. Pp. 825–831.
30. Kahlil, E., Abd-Elmohsen, M., Anwar, A.M. Impact resistance of rubberized self-compacted concrete. *Water Science*. 2015. 29. Pp. 45–53.
31. Ismail, M.K., Hassan, A.A. Impact resistance and mechanical properties of self-consolidating rubberized concrete reinforced with steel fibers. *ASCE Journal of Materials in Civil Engineering*. 2017. 29. Pp. 1–14.
32. AbdelAleem, B.H., Ismail, M.K., Hassan, A.A. The combined effect of crumb rubber and synthetic fibers on impact resistance of self-consolidating concrete. *Construction and Building Materials*. 2018. 162. Pp. 816–829.
33. Ding, Y., Li, D., Zhang, Y., Azevedo, C. Experimental investigation on the composite effect of steel rebars and macro fibers on the impact behavior of high performance self-compacting concrete. *Construction and Building Materials*. 2017. 136. Pp. 495–505.
34. Mastali, M., Dalvand, A., Sattarifard, A. The impact resistance and mechanical properties of reinforced self-compacting concrete with recycled glass fiber reinforced polymers. *Journal of Clean Production*. 2016. 124. Pp. 312–324.
35. Mastali, M., Dalvand, A. The impact resistance and mechanical properties of self-compacting concrete reinforced with recycled CFRP pieces. *Composites: Part B*, 2016. 92. Pp. 360–376.
36. Mastali, M., Dalvand, A., Sattarifard, A. The impact resistance and mechanical properties of the reinforced self-compacting concrete incorporating recycled CFRP fiber with different lengths and dosages. *Composites: Part B*. 2017. 112. Pp. 74–92.
37. ASTM C1611. Standard test method for slump flow of self-consolidating concrete. ASTM International, West Conshohocken, USA. 2014.
38. ASTM C1712. Standard test method for rapid assessment of static segregation resistance of self-consolidating concrete using penetration test. ASTM International, West Conshohocken, USA. 2014.
39. Almusallam, T.H., Abadel, A.A., Al-Salloum, Y.A., Siddiqui, N.A., Abbas, H. Effectiveness of hybrid-fibers in improving the impact resistance of RC slabs. *International Journal of Impact Engineering*. 2015. 81. Pp. 61–73.
40. Abbass, A., Abid, S., Özakça, M. Experimental investigation on the effect of steel fibers on the flexural behavior and ductility of high-strength concrete hollow beams. *Advances in Civil Engineering*. 2019. 2019. Pp. 1–13.
41. Arna'ot, F.H., Abbass, A.A., Abualtemen, A.A., Abid, S.R., Özakça, M. Residual strength of high strength concentric column-SFRC flat plate exposed to high temperatures. *Construction and Building Materials*. 2017. 154. Pp. 204–218.
42. Abbass, A.A., Abid, S.R., Arna'ot, F.H., Al-Ameri, R.A., Özakça, M. Flexural response of hollow high strength concrete beams considering different size reductions. *Structures*. 2019. 23. Pp. 69–86.
43. Wang, S., Le, H.T.N., Poh, L.H., Feng, H., Zhang, M-H. Resistance of high-performance fiber-reinforced cement composites against high-velocity projectile impact. *International Journal of Impact Engineering*. 2016. 95. Pp. 89–104.
44. Kantar, E., Yuen, T.Y.P., Kobya, V., Kuang, J.S. Impact dynamics and energy dissipation capacity of fibre-reinforced self-compacting concrete plates. *Construction and Building Materials*. 2017. 138. Pp. 383–397.
45. Luccioni, B., Isla, F., Codina, R., Ambrosini, D., Zerbino, R., Giaccio, G., Torrijos, M.C. Effect of steel fibers on static and blast response of high strength concrete. *International Journal of Impact Engineering*. 2017. 107. Pp. 23–27.
46. Wang, W., Chouw, N. The behaviour of coconut fiber reinforced concrete (CFRC) under impact loading. *Construction and Building Materials*. 2017. 134. Pp. 452–461.

Contacts:

Sallal Abid, sallal@uowasit.edu.iq

Sajjad Ali, sajad_alzuher@yahoo.com

Hussam Goaz, hussam@uowasit.edu.iq

Thaar Al-Gasham, thaar@uowasit.edu.iq

Ahmed Kadhim, alkadhum.wasit@gmail.com



DOI: 10.34910/MCE.105.5

Self-sensing cement composite for traffic monitoring in intelligent transport system

M.T. Bashir^{a,b}, M. Daniyal^c, M. Alzara^b, M. Elkady^b, A. Armghan^b

^a CECOS University of IT and Emerging Sciences, Peshawar, Pakistan

^b Jouf University, Sakaka, Al-Jouf, Saudi Arabia

^c Qurtuba University of Science & Information Technology, Department of Civil Engineering, Dera Ismail Khan, Pakistan

*E-mail: tariqbashir@cecos.edu.pk

Keywords: granulated blast furnace slag (GGBFS), carbon black (CB), cement-based composites, Piezo resistive properties, traffic monitoring.

Abstract. Self-sensing cement-based composite was used to monitor the flow of traffic volume. Composite material was prepared with numerous percentages of carbon black (CB) and activated granulated ground blast furnace slag (GGBFS). This economical and concrete friendly material having piezo resistive properties helped to detect the wheel pressure induced by the vehicles passing over it. Initially, the pressure sensitivity of different mix designs was investigated in the laboratory and the samples having more sensitivity to applied load were used on the real road test for vehicle detection. Mechanical and microstructural properties of hydrated cement composite filled with CB and GGBFS as an active filler were also explored. Scanning electron microscopy/Electron dispersive spectroscopy (SEM/EDS) and X-ray diffraction (XRD) analysis were carried out to characterize the microstructure and hydration product development of different specimens at different curing ages. The tested cement composite gives a remarkable response to both compressive and vehicular loading with excellent mechanical and microstructural properties. The results also showed that the self-sensitive cement composite has a great potential to use as a device for traffic monitoring.

1. Introduction

Vehicle recognition is one of the critical elements in the management and operation of the traffic system all over the world [1, 2]. At present, various detection systems are used to accumulate and process the traffic data. These traffic data include traffic volume, vehicle speed, vehicle length and width, traffic density that are obtained by sensors either buried beneath the road or operational along the roadside. Until now, many types of detectors are used to detect traffic data. Some of these include electronic, magnetic, video, acoustic devices and optical detectors [1, 2].

Among all these sensors, the electronic sensors are preferably used because they have excellent sensing capability, modern-day technology, resistance to all types of weather conditions and are relatively cheaper in costs. Though these type of sensors can accurately measure the traffic flow data like traffic volume, vehicles speed, vehicles occupancy ratio and weight of vehicles but these type of sensors also have some defects on pavement life due their unfavorable compatibility and bond with pavement structure. Advancement in technology, Microsoft computers, and latest communication systems encourage to introduce the latest technologies for traffic monitoring including infrared sensors, microwave radars, and video image processors but these advanced sensors are facing some limitations such as high manufacturing and maintenance cost, poor performance in faulty weather conditions (fog, smoke, rain, and

Bashir, M.T., Daniyal, M., Alzara, A., Elkady, M., Armghan, A. Self-sensing cement composite for traffic monitoring in intelligent transport system. Magazine of Civil Engineering. 2021. 105(5). Article No. 10505. DOI: 10.34910/MCE.105.5

© Bashir, M.T., Daniyal, M., Alzara, M., Elkady, M., Armghan, A., 2021. Published by Peter the Great St.Petersburg Polytechnic University



This work is licensed under a CC BY-NC 4.0

snow) and so on. Moreover, additional structures and time-consuming calibrations are mandatory to install these type of detectors [3, 4].

In the field of Nano-technology, scientists have presented self-sensing cement based sensors maintaining good mechanical and binding properties of cement, that provides a smart way to detect the traffic flow [5]. These types of sensors are fabricated by filling different conductive materials into the cement to enhance the ability to sense the stress or strain [6]. When the cement composite experiences some kind of load, it is deformed, and the contact between conductive material and cement is effected thus affecting the electrical resistivity of the composite [7, 8]. Vehicle detection sensors constructed with smart cement-based mixtures have many advantages over conventional detectors, such as easy installation, easy maintenance, low cost, useful service life, better compatibility with road structure, as they are cement-based materials [9, 10].

In the past few decades, numerous active materials have been presented for piezo resistive cement-based stress sensors [11]. The first reported material was carbon fiber (CF) which was used in cement to enhance the piezo resistive properties. The relationship between applied load and change in electrical resistance of CF based cement composite was clearly and comprehensively described in the article [6]. To proceed this research, new supplements were introduced and studied including carbon fibers (CF) [10, 12–15], steel fibers (SF) [16–18], carbon nanotubes (CNT) [9, 19–21], carbon black (CB) [22–25], graphene [26, 27], hybrid of carbon black and carbon fiber [24, 25], hybrid of carbon fiber and carbon nanotubes [19]. These supplements were introduced to cement because of their electrical conductivity and piezoresistivity [28–30].

Moreover, Gwen et al., in October 2012, investigated that pozzolanic material (fly ash) with a high content of FeO (15.10 %), when mixed with cement up to 40 % of its weight, gave a reversible response to cyclic compressive loading. The workability and economy of cement mortar were also enhanced using magnetic-concentrated fly ash, but a little decrease in compressive and tensile strength was reported due to the high concentration of pozzolanic material [31]. It is noted among all the existing conductive materials, the carbon black when mixed with cement gives mature and even response to compressive loading [22, 32, 33]. Furthermore, carbon black is very cost effective and radially available material throughout the world [24, 34, 35].

2. Materials and Methods

2.1. Materials

The materials used were Portland cement (ASTM C 150), superplasticizer commercially available as acrylic acid ($C_3H_3O_2Zn^+$) was used as water reducing agent, activated (fine up to 99 % having larger surface area) granulated ground blast furnace slag (FeO concentrated) [31], Carbon black with arbanion ions (Type N-550) (Table 1 & 2) and galvanized #6 steel meshes (opening of 4.2 mm) were used as electrodes shown in Fig. 1.

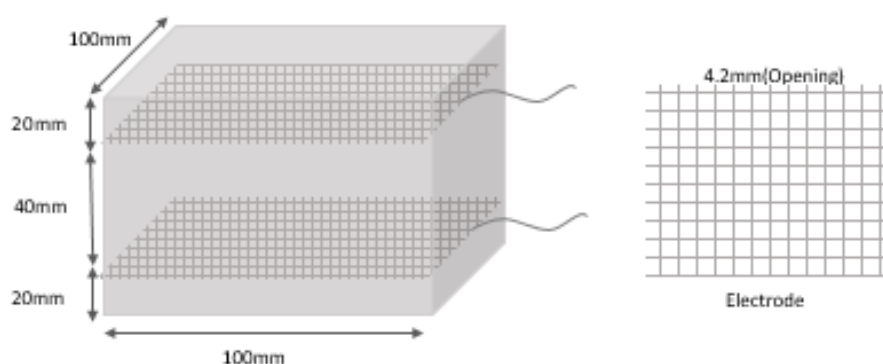


Figure 1. Specimen structure and position of electrodes.

To achieve good sensing and mechanical properties of cement sensor, a new cement composite, hybrid with carbon black (CB) [35] and activated granulated blast furnace slag (pozzolanic material) with 11.9 % FeO content [31] (Table 1) was used as traffic flow detector in this work. Related literature also concludes that GGBFS with an aluminum content of 12 % (Table 2) helps in the development of hydration product (CSH) and leads to compact and crystal microstructure [36–38]. The stress sensing ability of this composite was investigated in the lab as well as on real road test to explore the feasibility of using as a device for traffic flow monitoring.

Table 1. Properties of granulated blast furnace slag.

Item	Unit	Specification	Results
FeO	%	5-13	10.76
Al ₂ O ₃	%	≤ 18	16.72
SiO ₂	%	≤ 36	30.93
CaO (Ca ⁺)	%	≥ 35	39.51
MnO	%	≤ 1.5	0.35
MgO	%	≤ 12	9.44
S	%	≤ 1.3	0.75
TiO ₂	%	≤ 4	3.43
Cl	%	≤ 1	0.01
Moisture	%	≤ 0	8.5
Resistivity	Ω-m	—	27
Granulomere (Fineness)	%	≥ 95	99
Insoluble Residue	%	≤ 0.5	0.28
LOI	%	≤ 3	0.2
Strength Grade	Mpa	—	35.5

Table 2. Properties of carbon black.

Items	Unit	Specifications	Results
Carbon particles (C ⁻)	%	90 Min	93
Apparent Specific Volume	cm ³ /g	14~17	16
Iodine Absorption	g/kg	90 Min.	97
HCL Absorption	cm ³ /g	3.9 Min.	4.4
Resistivity	Ω, m	3.5 Max.	1.25
Heating Loss	%	0.5 Max.	0.09
Ash	%	0.4 Max.	0.07
Grit	%	0.07 Max.	0.01
Insoluble residue	%	30~35	32

2.2. Preparation of smart cement-based sensor

Initially, an aqueous solution was made by manual stirring of water containing CB and GGBFS along with superplasticizer namely acrylic acid (C₃H₃O₂Zn⁺) as a water reducing agent. After manual mixing, a probe-type sonicator was used to sonicate the mixture for 15 minutes at a constant nominal frequency of 24 KHz for uniform mixing. A mortar mixer was used for further mixing of the sonicated aqueous solution and other ingredients, i.e. Portland cement, GGBFS, water (0.40 % by weight of binder) for a further 10 minutes. The mixture obtained by mixing machine was then put into the oiled molds with two galvanized mesh electrodes as shown in Fig. 1. Vibrator was used to remove the air voids of the poured mixture. The casted samples were covered with plastic paper to prevent it from the sudden change in atmosphere and then demolded after 24 hours and cured at room temperature for 28 days. Subsequently, the specimens were dried in an oven at 50 °C for five days before testing to eliminate the polarization effect due to residue pore water contents. The mix proportions used in this study are mentioned in Table 3.

Table 3. List of specimens and mix proportion.

Specimen Composition	Notation	W/B	Binders		
			CB	GBFS	C
C+CB+GGBFS	(M1)	0.40	0.50	5.000	94.5
C+CB+GGBFS	(M2)	0.40	1.00	10.00	89.0
C+CB+GGBFS	(M3)	0.40	1.50	15.00	83.5
C+CB+GGBFS	(M4)	0.40	2.00	20.00	78.0
C+CB+GGBFS	(M5)	0.40	2.50	25.00	72.5
C+CB+GGBFS	(M6)	0.40	2.50	30.00	67.5

C: Cement, CB: Carbon Black (wt. % of cement), GBFS: Granulated Blast Furnace Slag (wt. % of cement), W/B: water to binder ratio.

2.3. Compressive strength test

Three specimens (50×50×50 mm³) for each mix proportion were fabricated to investigate the developed compressive strength at 3, 7, 14, 28 days according to standard test method for compressive strength of hydraulic cement using 2 in or 50 mm cube (ASTM C109). Equation-1 can calculate the compressive strength values.

$$\sigma_c = \frac{P}{A} \quad (1)$$

where

σ_c refers to the average compressive strength of three samples (MPa);

P refers to the maximum load applied (N);

A refers to the area of the specimen (mm²).

2.4. Tensile strength test

To calculate the tensile strength of cement based sensor, three bar-shaped samples of size (40×40×160 mm³) for each mix design, after being cured at 3, 7, 14 & 28 days were carried out for tensile strength according to ASTM C348. Tensile strength was calculated by Equation-2.

$$\sigma_t = \frac{3FS}{2wh2} \quad (2)$$

where

σ_t refers to the average tensile strength (MPa);

F refers to an applied force by a universal testing machine (N);

S refers to span (mm);

w refers to the width (mm);

h refers to depth (mm).

2.5. Analytical characterizations

Previous studies on utilization of GBFS concluded that higher replacements of this pozzolanic material by cement restart the hydration products at early stages but increased curing age, the hydration production can be comparable to Portland cement [36–38] at curing age of 28 days. In this research work, the development of crystalline (hydrated) and amorphous phases (anhydrate) in cement sensor filled with CB and GBFS, powder X-ray diffraction technique was adopted. The samples were crushed and milled into powder (< 300 µm) at curing age of 28 for XRD testing. Before testing of samples at different curing ages, the further hydration of cement sensor was stopped by washing and repeated immersing in isopropanol for 1 hour. X-ray diffractometer scans the samples between 2θ values of 10° to 60°, and the required data were collected. X'pert high score (version 3) software was used to analyze the received data employing XRD.

The microstructure of cement sensors was observed by employing SEM along with energy EDS (to observe the hydration at a specific point). Isopropanol was used to stop further hydration of samples and dried in the oven at 40 °C. After that, the samples were introduced to the machine (JEOL, EDS DETECTOR manufactured by Japan) for SEM/EDS observations.

2.6. Piezoresistivity of cement-based sensors

The laboratory test setup to assess the piezoresistive properties of (28 days cured and dried at 50 °C in the oven for 5 days) smart cement based sensors is described in Fig. 2. All the sensors with different mix designs were tested in the laboratory to check their sensitivity to applied stresses. Electrodes buried in the specimens were energized by UNI-T 30-volt DC supply. Uniaxial repeated compressive loads of 20 kN and 15 kN were applied by universal testing machine. Change in resistance due to applied load was recorded simultaneously by the data acquisition device.

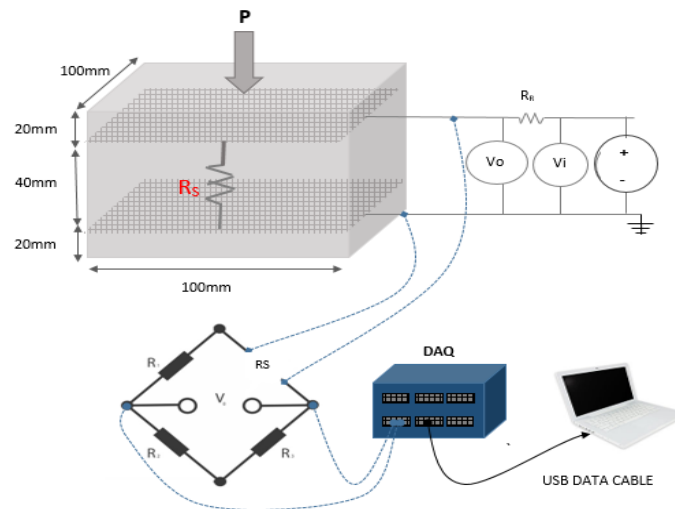
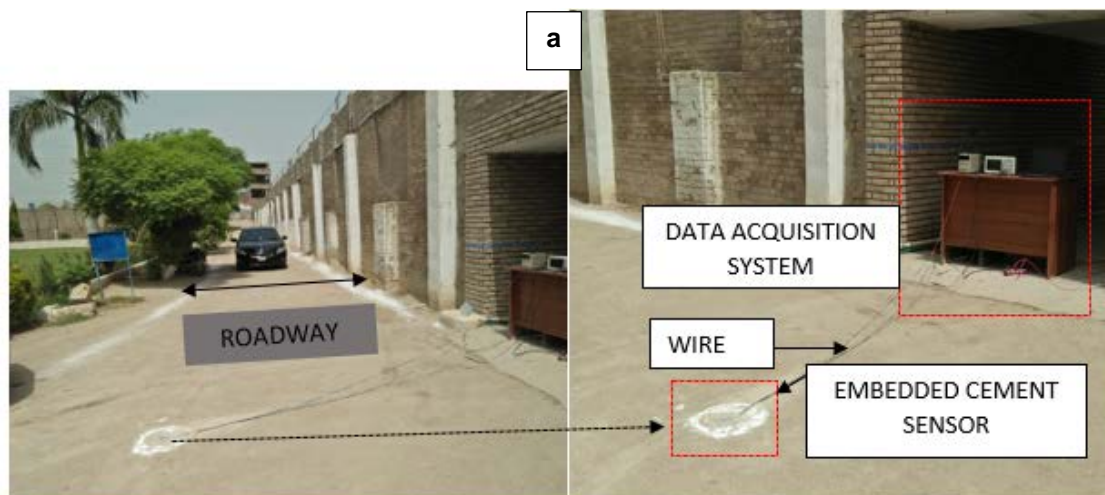


Figure 2. Setup adopted to check the sensitivity of cement sensor to loading.

2.7. Road test

Road test of smart cement sensor was performed in an open environment to observe the feasibility of using it as a device for vehicle detection. A trench was made in pavement and sensor was buried. Cement paste was used to fix the sensor at its place as the vehicles have to pass over it for testing. Vehicles with different axle loads and speed were driven to pass over self-sensing cement sensor in order to investigate its designed sensibility (Fig. 3a and Fig. 3b).



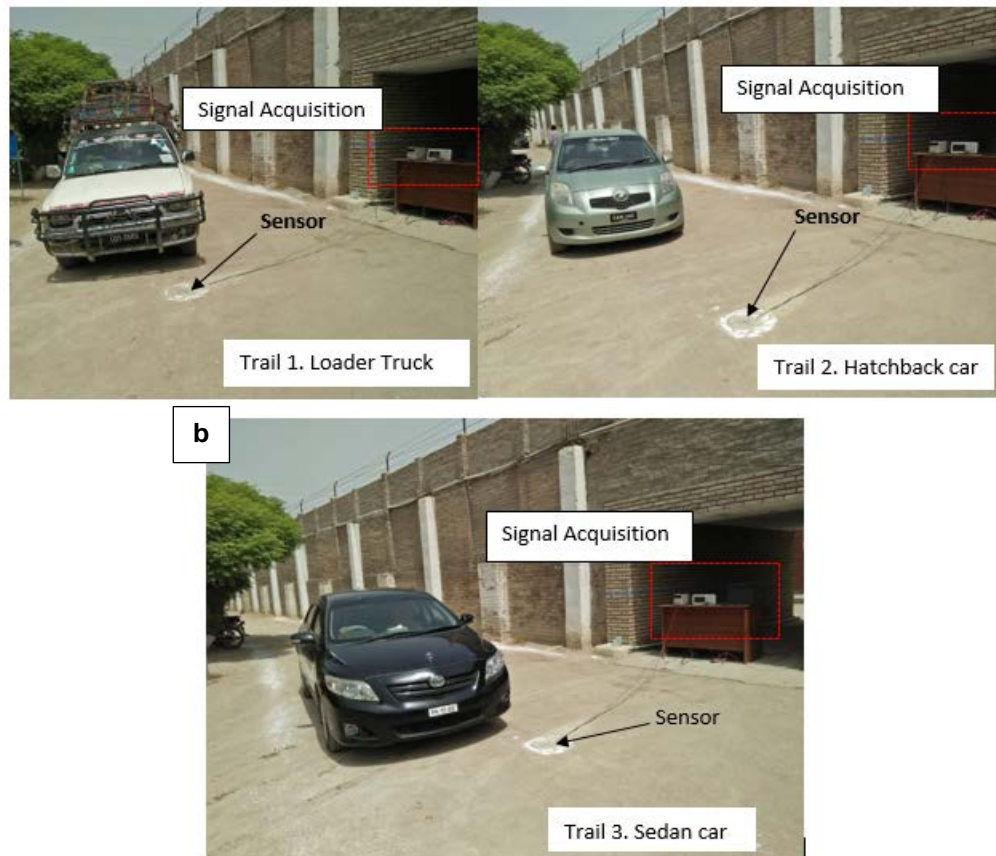


Figure 3. Road Testing (a). Position of embedded sensor and assembly of the data acquisition system, (b). Outdoor testing to check the response of sensor under vehicular loading).

Table 4. List of vehicles passed over cement sensor.

Sr.#	Vehicle type	Weight as per documents (Kg)
01	Hatchback car	1350
02	Sedan car	1600
03	Loader truck	2200

Change in electrical resistivity of cement sensor due to externally applied load denotes the sensing property of self-sensing material and according to Ohm's law (Eq. 3).

$$f_s \times \frac{L}{A} = R_s \quad (3)$$

where R_s , A , and L refer to the electrical resistivity of the sensor when it was attached to DC power supply, the cross-sectional area of the sensor and the space between two electrodes, respectively.

After passing vehicle over the sensor, the resistance of the sensor will change, and Eq. 3 can be written as Eq. 4.

$$\frac{df_s}{f_s} = \frac{dR_s}{R_s} - \frac{(1 + 2\mu)dL}{L} \quad (4)$$

The deformation of the sensor under compressive load is minimal so change in L (dL) can be neglected [39], and Eq. 4 can be modified as Eq. 5.

$$\frac{dR_s}{R_s} = \frac{df_s}{f_s} \quad (5)$$

It can be observed from Eq. (5) that the change in electrical resistance of the sensors is the same as that of electrical resistivity. Furthermore, Fig. 4 shows a circuit diagram of cement sensor connected in series with constant reference resistance and applied voltage along with the data acquisition process.

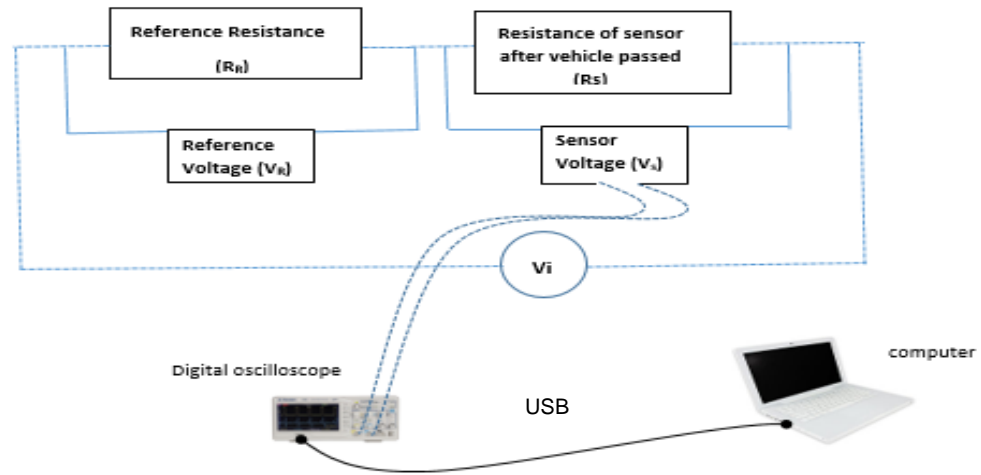


Figure 4. Experimental setup for road testing.

$$\frac{V_s}{R_s} = \frac{V_i - V_s}{RR} \quad (6)$$

Where R_s is the resistance of sensor after the vehicle passes over it and R_R is the reference resistance of sensor before vehicle passing. V_i and V_s are the voltages before and after the application of car load respectively. Eq. (4) can further be written as

$$\frac{V_s}{V_i - V_s} \times RR = R_s \quad (7)$$

The car load made the change in resistance and applied of the sensor which can be expressed as

$$R_s + dR_s = \frac{(V_s + dV_s)}{V_i - (V_s + dV_s)} \times RR \quad (8)$$

Where dV_s change in voltage, and it is much smaller than $(V_i - V_s)$. Thus, Eq. (7) and (8) can be combined and written as

$$\frac{dR_s}{R_s} \cong \frac{dV_s}{V_s} \quad (9)$$

Eq. (9) clearly shows that change in resistance of cement sensor caused by vehicular loading is approximately equaled to change in applied voltage which is taken as an indication of passing vehicles over the smart cement-based sensor. Digital storage oscilloscope made by UNI-T (UTD20000/3000) was used for real time sampling with the frequency of 250 hz.

3. Results and Discussion

3.1. Compressive strength

The effect of partial replacement of GGBFS and CB by cement on compressive strength is shown in Fig. 5. It can be observed from compressive strength development chart (developed at 3, 7, 14, 28 days) that cement composite named as M4 composed of 2 % CB and 20 % GGBFS shows higher strength at 28 days than other mixes. It is due to the pozzolanic reaction of GGBFS combined with the optimum amount of CB (1 %) to form calcium silicate hydrate (CSH). It can also be noted that the amount of GGBFS and CB beyond M4 causes a slight decrease in compressive strength due to higher accumulation of both the filler in cement composite [36].

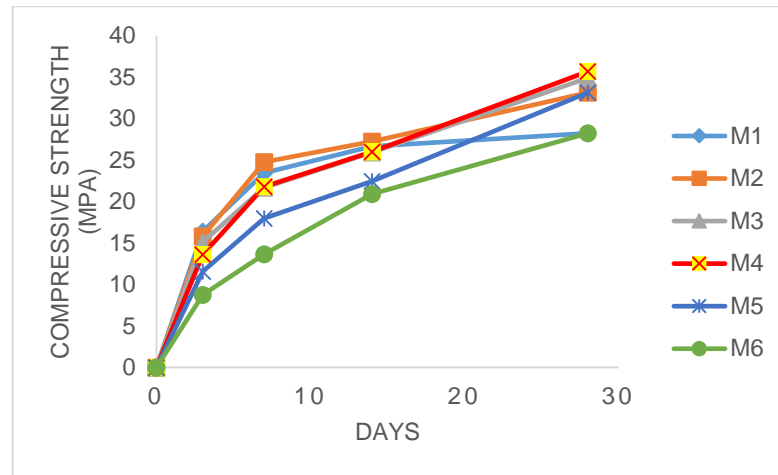


Figure 5. Development compressive strength of cement sensor.

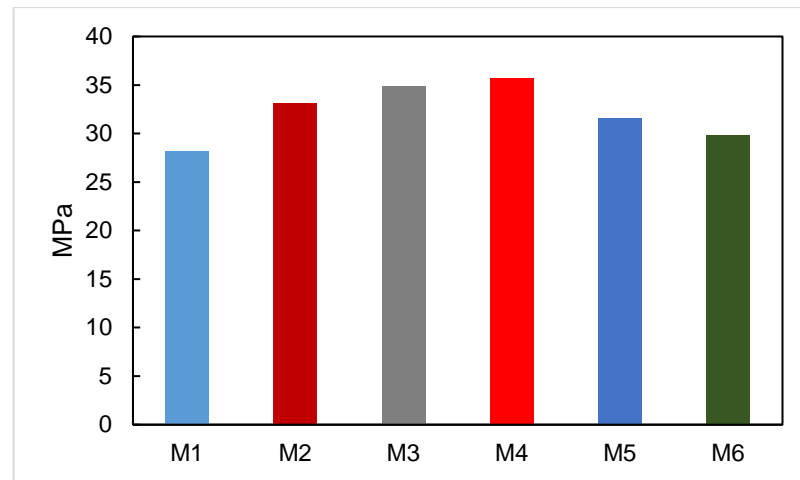


Figure 6. 28 days compressive strength chart.

3.2. Tensile strength

The tensile strength of mortars combined with CB and GGBFS at 3, 7, 14 & 28 days is shown in Fig. 7. A slight increase in tensile strength can be observed for M3 mix as compared to other mixes, but no major change in tensile strength was seen by adding GGBFS and CB. The minor increase in the flexural strength is supposed to be not only from pozzolanic material filling the pores of hydration but also from the tubes linking effect providing support to the matrix which contributes better opposition to stretching effect produced by application of load. It is also noted that the good results will largely depend on proper dispersion of filling material as they would be expected to perform much better regarding the tensile strength of cement-based self-sensing material [15]. In this work, no substantial change in tensile strength is observed compared to plane cement paste.

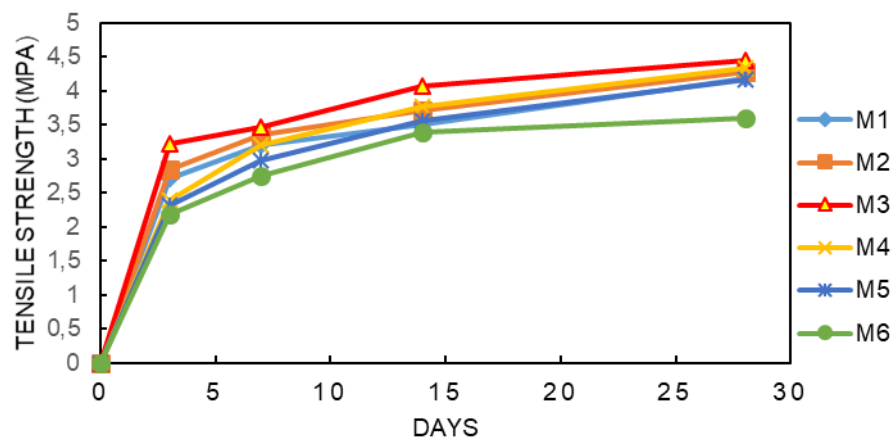


Figure 7. Development tensile strength of cement sensor.

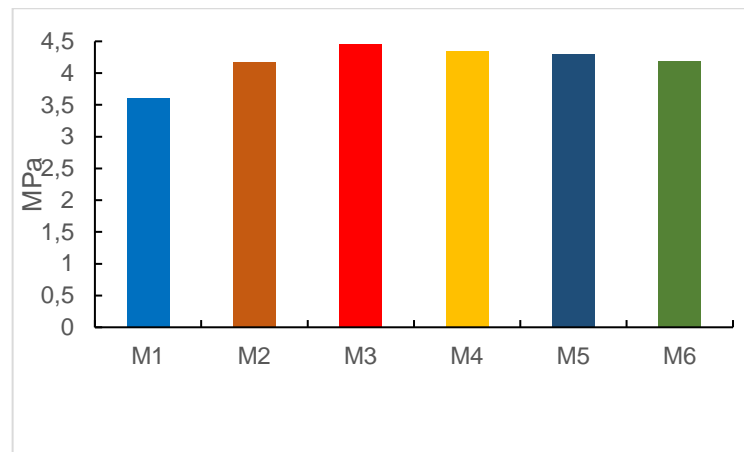


Figure 8. 28 days' tensile strength chart.

3.3. Microstructure

3.3.1 X-ray diffraction (XRD)

Fig. 9 demonstrates the results of XRD analysis of different samples at 3, 7, 14 and 28 days curing. Calcium hydroxide (CH), calcium silicate hydrate (CSH), ettringite, calcium, and quartz are the major hydration products detected by X-ray diffractometer and analyzed by X'pert high score (version 3) software. CH and CSH are the hydration product of alite (C_3S) and belite (C_2S), ettringite is formed by hydration of tri-calcium aluminate (C_3A) and quartz by impurities present in binder during the hydration process or curing [40, 41]. It can be noted from Fig. 9(a) and (b) that M1 and M2 show relatively analogous XRD pattern. Approximately identical peaks were observed while comparing the 28 days' results of M3, M4, and M5, M6 that can be observed in Fig. 9(c) to (f).

The peak intensities of all the hydration products at all curing ages in M1 and M2 show no major changes except a decrease in the peak of alite at 2θ value of 33.7° and increase in peak of CH at 2θ value of 29.2° and 46.2° at 28 days curing which is clearly a sign of development of hydration products. Moreover, it was also noted that the peak of ettringite at 14.7° disappears at 28 days curing age which indicates that hydration of tri-calcium aluminate (C_3A) is almost completed.

Moreover, at the increase in the filling material into cement, a little change was noted while comparing the XRD of M3 and M4 with M1 and M2. The peak of calcium hydroxide obtained at 2θ value of 19.45° and 46.2° shows no significance at curing age of 3 days because a comparatively high dose of blast furnace slag retards the hydration process at an early age [40]. Furthermore, the peak of ettringite at 2θ value of 14.7° a small peak was noted at 28 days curing age which indicates the slow hydration rate of tri-calcium aluminate (C_3A) due to high accommodation of pozzolanic fillers but interestingly 28 days' hydration of all the mixes (M1, M2, M3, M4) was approximately identical to each other as all the hydration products were detected by X-ray diffractometer.

In the mix designs named as M5 and M6, high replacement of GGBFS by cement alters the hydration process at an early age as shown in Fig. 9(e) & (f). By comparing the XRD patterns of M5 and M6 with previous mix designs, a significant change in hydration was noted. While analyzing the patterns of both M5 and M6, no strong peaks of CH and CSH were noted at 2θ value of 19.45° , 29.3° , 46.2° and 30.89° respectively at curing age of 3, 7 and 14 days and much amorphous phase was developed between 15° to 54° . This is due to fact that, the GGBFS particles surrounds the cement components especially C_3S , C_2S and C_3A that slows down the formation process of CH (Portlandite), CSH and ettringite at early age (3, 7 & 14 days) and leads to amorphous phase (non-crystalline phase) in cement mix filled with carbon black (CB) and granulated ground blast furnace slag (GGBFS). On the other hand, samples with 28 days hydration could be comparable (negotiable decrease) to other mixes with relatively low GGBFS as all the hydration products were detected at that curing age.

The contribution of CB to hydration was almost negligible. This is due to the fact that CB is not a mechanical activator (pozzolanic material) and it was filled in cement as a conductive material to increase to the sensitivity of cement mix to load/stress; thus a little contribution of CB to hydration of cement could be neglected.

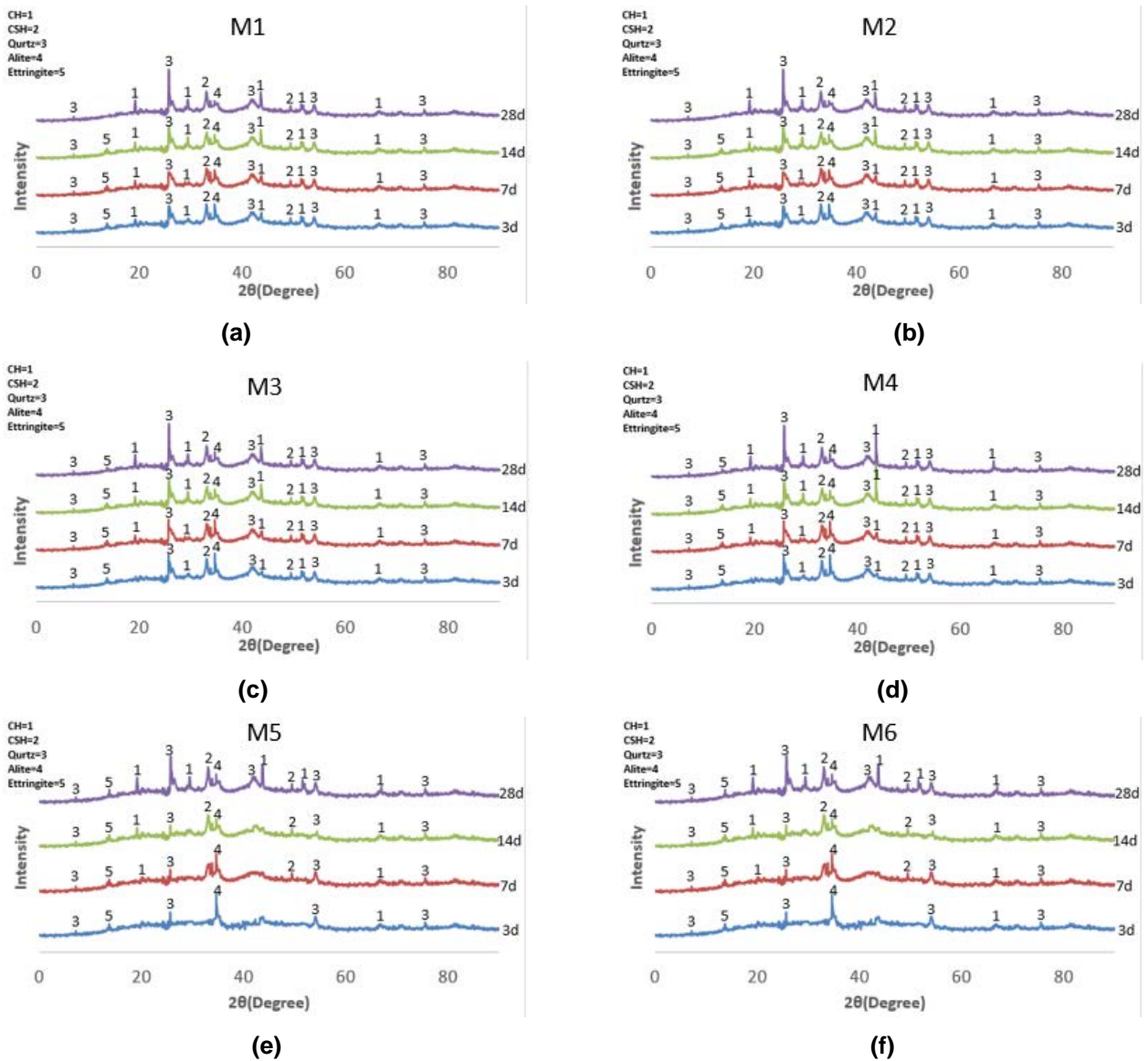


Figure 9. XRD analysis of mix designs at mentioned curing ages.

3.3.2. SEM / EDS

The SEM and EDS were used altogether to detect the microstructure and chemical composition of hydration products of cement paste filled with blast furnace slag and carbon black as pozzolanic conductive materials. The obtained results are shown in Fig. 10 (a) to (c).

It can be observed at 50 μm scale with a very high resolution of $\times 270$, that the paste containing a higher amount of GBFS and CB (M4 and M6) shows dense microstructure as compared to paste with a low amount of both fillers (M1). The filling material specially GBFS ideally covered the pores space between unreacted cement particles and presents a compact and homogenous material because of its excellent pozzolanic reaction with cement. The EDS result of all the three samples show no major difference in the formation of C-S-H gel. The EDS analysis of M1 obtained around unreacted cement shows a Ca/Si ratio of 1.99 which is very much close Ca/Si ratio of plane cement, i.e. 2.02 which indicates the typical C-S-H gel formed by the cement hydration at curing age of 28 days [42, 43]. The EDS of M4 and M6 indicates little decrease in the Ca/Si ratio of 1.81 and 1.68, respectively. This is because of higher accommodation of GBFS and CB in cement which slows down the formation of C-S-H gel and left unreacted particles at 28 days curing age. By analyzing the overall SEM / EDS, the cement paste filled with GBFS and CB as filing material shows excellent and compact microstructure with the excellent chemical composition of hydration product.

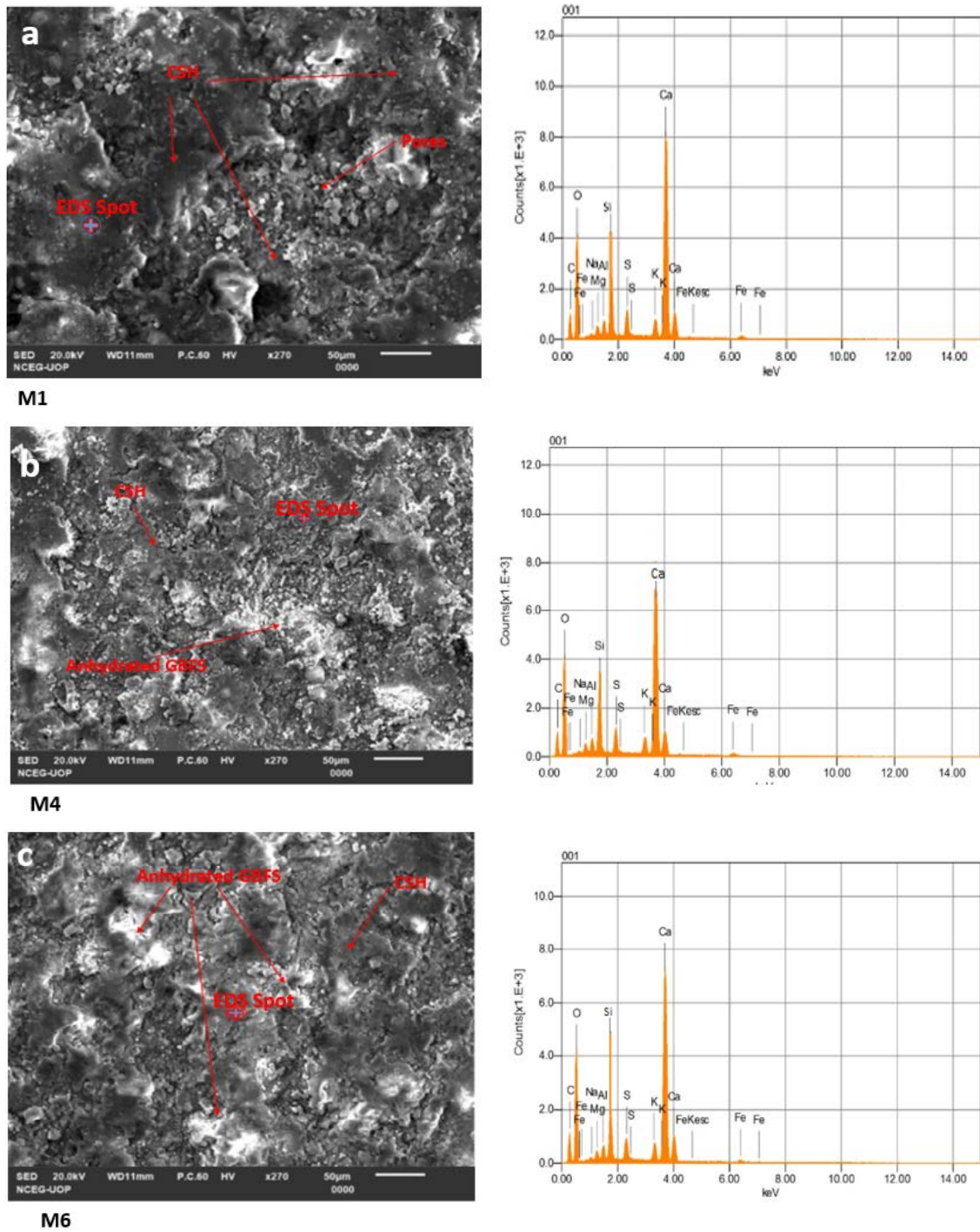


Figure 10. SEM/EDS of mix design M1, M4, and M6.

3.3.3. Piezo-resistive response of self-sensing cement sensor

To find the piezoresistive response of cement sensors, change in electrical resistance was measured in correspondence to applied compressive loads at curing age of 28 days. Cement samples filled with different amount of CB & GGBFS as conductive fillers were put to cyclic compressive loads and the response measured was even and reversible. The results of piezoresistive testing is shown in Fig. 11. It is noted after testing that cement sensor filled with 2.5 % CB and 30 % GGBFS (M6) shows higher sensitivity to applied loading as the relative change in electrical resistivity dp/ρ_o (%) reaches about 7.5 % under the compressive load of 15 KN shown in Fig. 7. Thus it can be concluded that CB combined with GGBFS as hybrid filler have great sensing capability when added to cement.

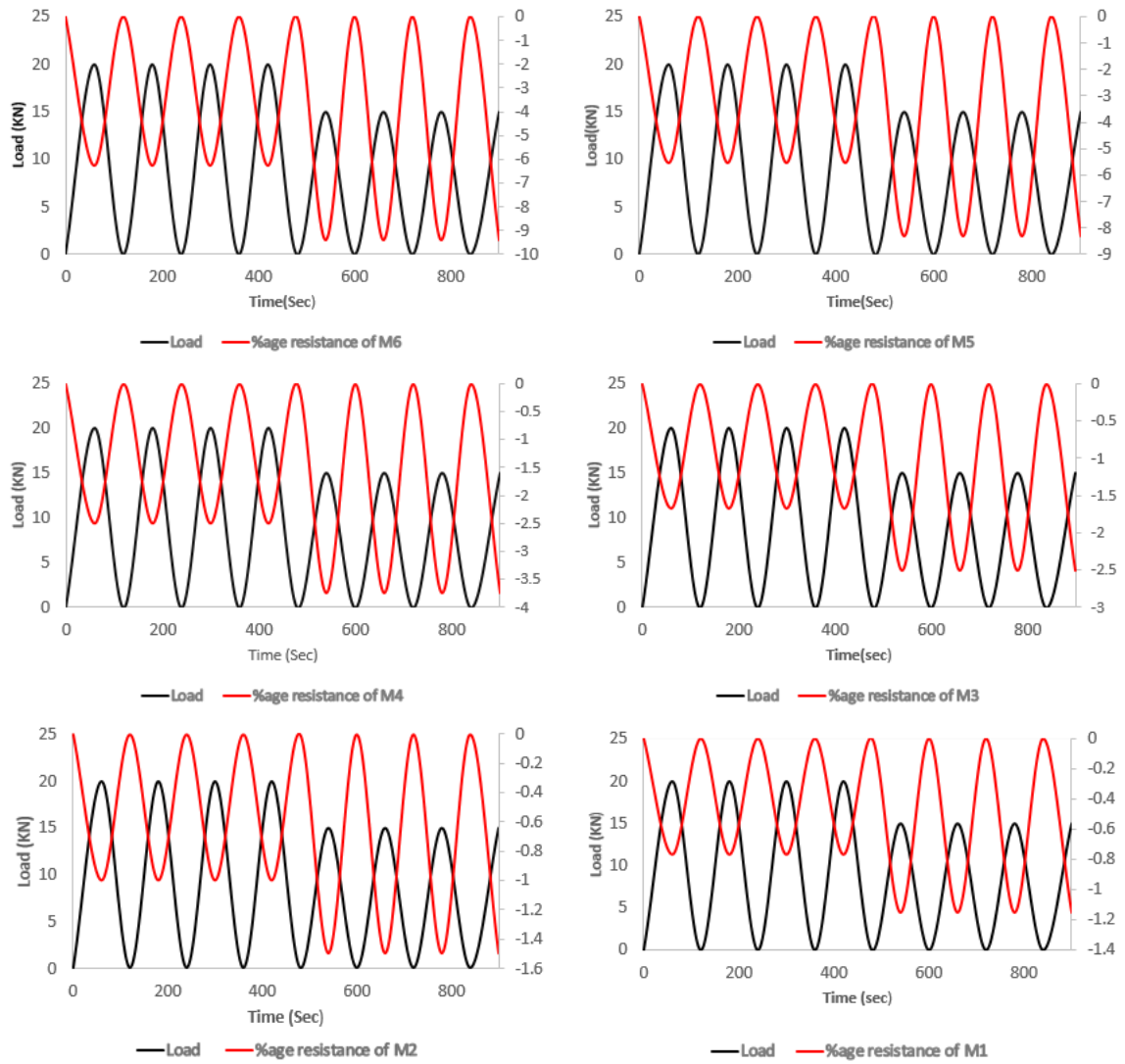


Figure 11. Application of load and a corresponding change in resistance of cement-based sensors filled with different percentages of CB and GGBFS.

Table 5. Maximum percentage resistance of smart sensors in laboratory.

M1 (%)	M2 (%)	M3 (%)	M4 (%)	M5 (%)	M6 (%)
0.933	1.5	2.5	3.75	8.33	9.36

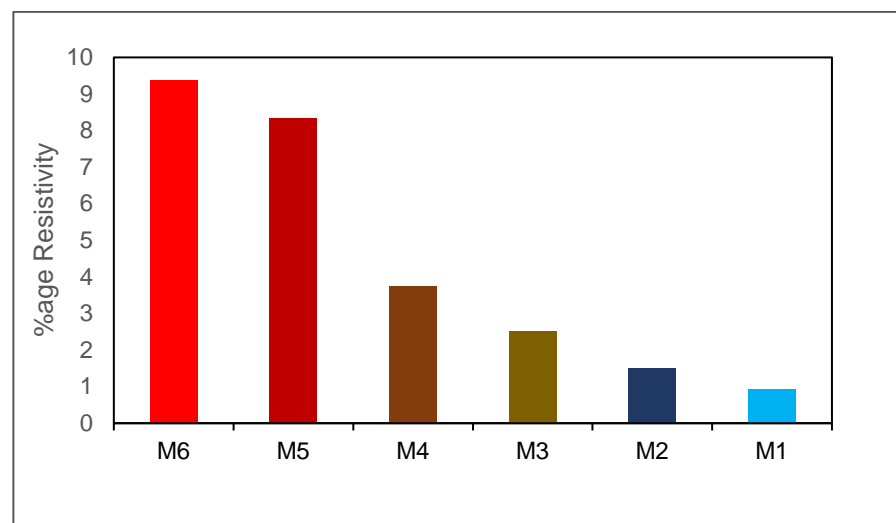
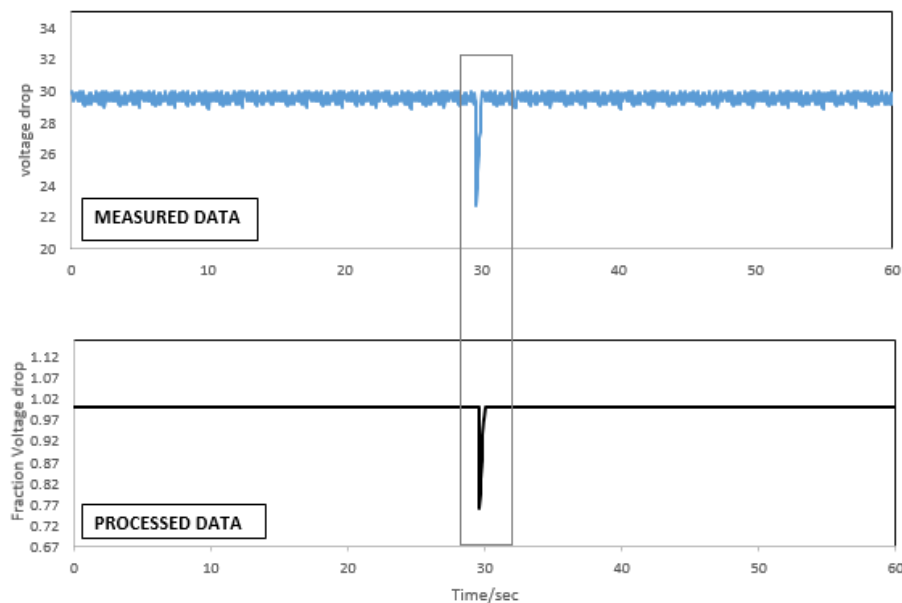


Figure 12. Max percentage resistivity of each sample.

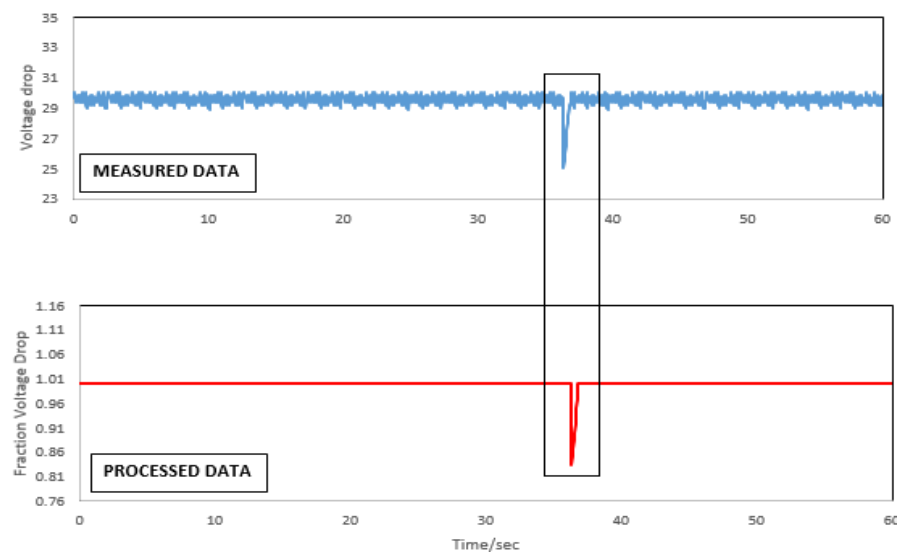
3.3.4. Vehicle detection by cement sensor

Laboratory tests on piezoresistive cement sensors were performed in order to observe their sensitivity and feasibility to use it on the road for vehicle detection. Sensor (M6) which shows maximum sensitivity (i.e., % age change in resistance was maximum to other cement sensors) shown in Fig. 11 (% age resistance of M6) and 12 was adopted for road testing. Different type of vehicles was passed over underneath sensor and the voltage time history record was collected. Sudden change in voltage signals is shown in Fig. 13. Results showed that voltage drop signal was different for a different vehicle which means that the sensor is sensitive to vehicular weight, but the limitation was that one could not measure the exact weight of the vehicle as the position of tyres on cement sensor was different at every trial when a vehicle passes over it. Voltage drop was not uniform even for the same vehicle as axel weight transferred to cement sensor by passing vehicle was not uniform because the contact area between the tyre and cement sensor was not uniform at every trial. Thus, results could be acceptable for vehicle detection, traffic density and vehicle speed as only peak values are required to assess these parameters. Subsequently, this outcome indicates that smart self-sensing cement sensor is feasible to use for detection of passing vehicle as it shows an excellent response in outdoor testing.

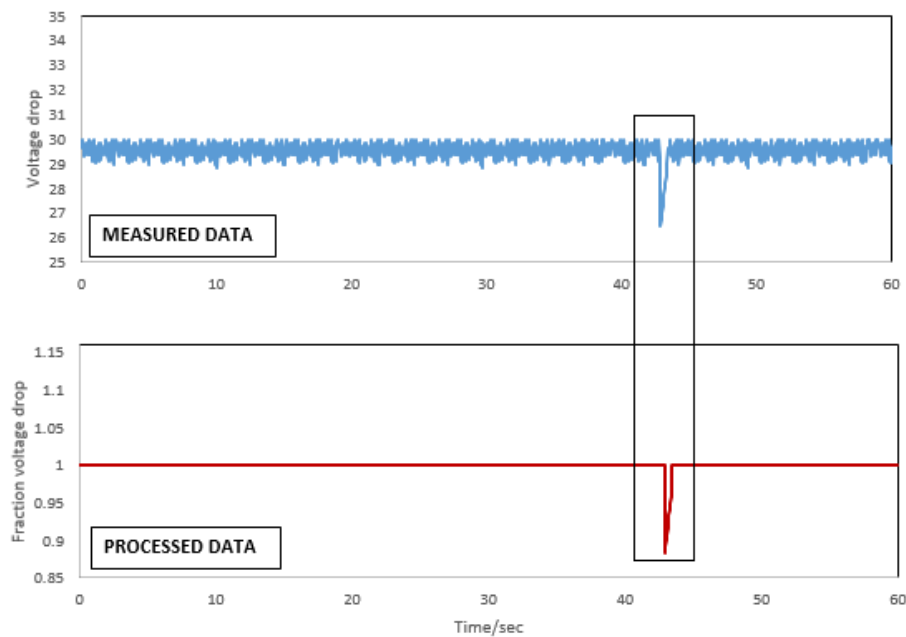
Moreover, it was observed that the change in environmental temperature and polarization effect (pore water particles activation due to applied voltage) had an impact on baseline voltage (applied voltage), but the change was continuous and gradual, which did not disturb required results.



(a). Hatchback passes over cement sensor



(b). Sedan passes over cement sensor



(c). Loader single cabin truck passes over the vehicle

Figure 13. Peak values enclosed in the box shows the passing of different vehicle.

4. Conclusion

Self-sensing CB and GGBFS based cement sensors were fabricated for traffic monitoring. The response was studied for the electrical resistance/electrical voltage of this composite to a repeated compressive load and the vehicular load. The following conclusions are the drawn by the research:

1. The use of GGBFS combined with CB improves both compressive and tensile strength of cement paste due to the pozzolanic reaction and filler effect of GGBFS. Although, CB is a conductive material and does not have pozzolanic properties as compared to GGBFS, but the physical presence of CB resulted in further increase in compressive and tensile strength of cement composite. The optimum improvement for compressive strength is observed at M4 (1 % of CB and 10 % of GGBFS by weight of cement) due to physical filling effect of weak spot and better development of hydration products (CSH and CH) in cement sample but higher percentages of these fillers in cement lead to reduction in compressive strength at early stages because of the existence of extra quantity of filler required for improvement in strength. The improvement in tensile strength can be observed up to 1 % in M3 compared to plane cement paste. It must be noted that tensile strength would largely depend on the dispersion of both the fillers especially GGBFS.
2. The incorporation of GGBFS in cement enhance the hydration products formation compared to plane cement paste [36] at the same curing age but negotiable defect noted was that high (30 %) replacement of GGBFS by cement, retardation/slowdown of hydration process was noted at early age curing, but the later hydration shows no major difference in hydration.
3. SEM/EDS data show that use of GBFS as a pozzolanic filler improves the microstructure of cement paste along with good chemical composition, but it slows down the early age hydration to some extent.
4. Laboratory test to investigate the sensing capability of the cement sensor indicates that there is a corresponding excellent relation between applied compressive load and electrical resistivity and can be used on the road for vehicle detection.
5. The real road test cement sensor also provides an outstanding response to vehicular loading by showing an abrupt/sudden change in baseline voltage.

In conclusion, the findings in lab and road tests indicate that the designed cement sensor has great potential to use as a device for traffic monitoring such as vehicle detection. Moreover, self-sensing cement composite has many advantages including good compatibility with pavement structure, long service life, easy installation and low maintenance cost along with excellent mechanical and microstructural properties.

5. Acknowledgements

The authors acknowledge the technical support given by the Jouf University, Saudi Arabia and Qurtuba University of Science and IT, Dera Ismail Khan, Pakistan, and also acknowledge Dr. Muhammad Waseem (Center of Excellence in Geology, University of Peshawar), Mr. Raheel Khan (Lecturer, EED, QUIST), Mr. Sohail Khalid (EED, QUIST) for providing complimentary technical support in dealing with Telescopic Microscopy (TM) and Probe Sonicator.

References

- Chong, K.P., Carino, N.J., Washer, G. Health monitoring of civil infrastructures. Proc. SPIE 4337, Health Monitoring and Management of Civil Infrastructure Systems. 2001. URL: <https://doi.org/10.1117/12.435595> (date of application: 23.11.2019).
- Faouzi, N.E., El Klein, L.A. Data Fusion for ITS: Techniques and Research Needs. Transportation Research Procedia. 2016. Pp. 495–512. DOI: 10.1016/j.trpro.2016.06.042
- Lawrence, A. Klein, Mills, M.K., Gibson, D.R.P. Traffic Detector Handbook: 3rd edn. US Department of Transportation. VA, (October) 2006. 1–16 p.
- Jelušić, N., Anžek, M., Mandzuka, S. Evaluation of sensor technologies for intelligent transport systems 16th ITS World Congress. 2009. URL: <https://bib.irb.hr/datoteka/428217.3931.pdf> (date of application 29 July 2019).
- Han, B., Ou, J. Embedded piezoresistive cement-based stress/strain sensor. Sensors and Actuators, A: Physical. 2007. Pp. 294–29. DOI: 10.1016/j.sna.2007.05.011
- Shi, Z.Q., Chung, D.D.L. Carbon fiber-reinforced concrete for traffic monitoring and weighing in motion. Cement and Concrete Research. 1999. 29(3). Pp. 435–439. DOI: 10.1016/S0008-8846(98)00204-X
- Chen, B., Liu, J. Damage in carbon fiber-reinforced concrete, monitored by both electrical resistance measurement and acoustic emission analysis. Construction and Building Materials. 2008. 22(11). Pp. 2196–2201. DOI: 10.1016/j.conbuild-mat.2007.08.004
- Bontea, D.M., Chung, D.D.L., Lee, G.C. Damage in carbon fiber-reinforced concrete, monitored by electrical resistance measurement. Cement and Concrete Research. 2000. 30(4). Pp. 651–659. DOI: 10.1016/S0008-8846(00)00204-0
- Han, B., Yu, X., Kwon, E. A self-sensing carbon nanotube/cement composite for traffic monitoring. Nanotechnology. 2009. 20(44). Pp. 445501. DOI: 10.1088/0957-4484/20/44/445501
- Konsta-Gdoutos, M.S., Aza, C.A. Self sensing carbon nanotube (CNT) and nanofiber (CNF) cementitious composites for real time damage assessment in smart structures. Cement and Concrete Composites. 2014. 53. Pp. 162–169. DOI: 10.1016/j.cemconcomp.2014.07.003
- Chen, P.W., Chung, D.D.L. Carbon fiber reinforced concrete for smart structures capable of non-destructive flaw detection. Smart Materials and Structures. 1993. 2(1). Pp. 22–30. DOI: 10.1088/0964-1726/2/1/004
- Wen, S., Chung, D.D.L. Effects of strain and damage on strain-sensing ability of carbon fiber cement. Journal of Materials in Civil Engineering. 2006. 18(3). Pp. 355–360. DOI: 10.1061/(ASCE)0899-1561(2006)18:3(355)
- Urkhanova, L.A., Buyantuev, S.L., Urkhanova, A.A., Lkhasaranov, S.A., Ardashova, G.R., Fediuk, R.S., Svintsov, A.P., Ivanov, I.A. Mechanical and electrical properties of concrete modified by carbon nanoparticles. Magazine of Civil Engineering. 2019. 92(8). Pp. 163–172. DOI: 10.18720/MCE.92.14
- Han, B., Guan, X., Ou, J. Electrode design, measuring method and data acquisition system of carbon fiber cement paste piezoresistive sensors. Sensors and Actuators, A: Physical. 2007. 135(2). Pp. 360–369. DOI: 10.1016/j.sna.2006.08.003
- Wen, S., Chung, D. Strain-Sensing Characteristics of Carbon Fiber-Reinforced Cement. American Concrete Institute Materials Journal. 2005. 102(4). Pp. 244–248. DOI: 10.14359/14617
- Sun, M.Q., Liew, R.J.Y., Zhang, M.H., Li, W. Development of cement-based strain sensor for health monitoring of ultra high strength concrete. Construction and Building Materials. 2014. 65. Pp. 630–637. DOI: 10.1016/j.conbuildmat.2014.04.105
- Banthia, N., Djeridane, S., Pigeon, M. Electrical resistivity of carbon and steel micro-fiber reinforced cements. Cement and Concrete Research. 1992. 22(5). Pp. 804–814. DOI: 10.1016/0008-8846(92)90104-4
- Teomete, E. Transverse strain sensitivity of steel fiber reinforced cement composites tested by compression and split tensile tests. Construction and Building Materials. 2014. 55. Pp. 136–145. DOI: 10.1016/j.conbuildmat.2014.01.016
- Azhari, F., Banthia, N. Cement-based sensors with carbon fibers and carbon nanotubes for piezoresistive sensing. Cement and Concrete Composites. 2012. 34(7). Pp. 866–873. DOI: 10.1016/j.cemconcomp.2012.04.007
- Li, G.Y., Wang, P.M., Zhao, X. Pressure-sensitive properties and microstructure of carbon nanotube reinforced cement composites. Cement and Concrete Composites. 2007. 29(5). Pp. 377–382. DOI: 10.1016/j.cemconcomp.2006.12.011
- D'Alessandro, A., Rallini, M., Ubertini, F., Materazzi, A.L., Kenny, J.M. Investigations on scalable fabrication procedures for self-sensing carbon nanotube cement-matrix composites for SHM applications. Cement and Concrete Composites. 2016. 65. Pp. 200–213. DOI: 10.1016/j.cemconcomp.2015.11.001
- Li, H., Xiao, H. gang, Ou, J. ping. Effect of compressive strain on electrical resistivity of carbon black-filled cement-based composites. Cement and Concrete Composites. 2006. 28(9). Pp. 824–828. DOI: 10.1016/j.cemconcomp.2006.05.004
- Monteiro, A.O., Cachim, P.B., Costa, P.M.F.J. Electrical Properties of Cement-based Composites Containing Carbon Black Particles. Materials Today: Proceedings. 2015. Pp. 193–199. DOI: 10.1016/j.matpr.2015.04.021
- Ding, Y., Chen, Z., Han, Z., Zhang, Y., Pacheco-Torgal, F. Nano-carbon black and carbon fiber as conductive materials for the diagnosing of the damage of concrete beam. Construction and Building Materials. 2013. 43. Pp. 233–241. DOI: 10.1016/j.conbuildmat.2013.02.010
- Wen, S., Chung, D.D.L. Partial replacement of carbon fiber by carbon black in multifunctional cement-matrix composites. Carbon. 2007. 45(3). Pp. 505–513. DOI: 10.1016/j.carbon.2006.10.024
- Rhee, I., Lee, J.S., Kim, Y.A., Kim, J.H., Kim, J.H. Electrically conductive cement mortar: Incorporating rice husk-derived high-surface-area graphene. Construction and Building Materials. 2016. 125. Pp. 632–642. DOI: 10.1016/j.conbuildmat.2016.08.089
- Metaxa, Z.S. Exfoliated graphene nanoplatelet cement-based nanocomposites as piezoresistive sensors: influence of nanoreinforcement lateral size on monitoring capability. Ciencia e Tecnologia dos Materiais. 2016. 28(1). Pp. 73–79. DOI: 10.1016/j.ctmat.2015.12.001

28. Lee, S.J., You, I., Zi, G., Yoo, D.Y. Experimental investigation of the piezoresistive properties of cement composites with hybrid carbon fibers and nanotubes. *Sensors* (Switzerland). 2017. 17(11). P. 2516. DOI: 10.3390/s17112516
29. Han, B.G., Han, B.Z., Ou, J.P. Novel piezoresistive composite with high sensitivity to stress/strain. *Materials Science and Technology*. 2010. 26(7). Pp. 865–870. DOI: 10.1179/026708309X12454008169546
30. Zhang, J., Lu, Y., Lu, Z., Liu, C., Sun, G., Li, Z. A new smart traffic monitoring method using embedded cement-based piezoelectric sensors. *Smart Materials and Structures*. 2015. 24(2). P. 25023. DOI: 10.1088/0964-1726/24/2/025023
31. Jia, X., Zhang, Y., Qian, J. Compression sensibility of magnetic-concentrated fly ash mortar under uniaxial loading. *Journal Wuhan University of Technology, Materials Science Edition*. 2012. 27(5). Pp. 999–1003. DOI: 10.1007/s11595-012-0588-y
32. Monteiro, A.O., Cachim, P.B., Costa, P.M.F.J. Self-sensing piezoresistive cement composite loaded with carbon black particles. *Cement and Concrete Composites*. 2017. 81. Pp. 59–65. DOI:10.1016/j.cemconcomp.2017.04.009
33. Han, B., Zhang, L., Sun, S., Yu, X., Dong, X., Wu, T., Ou, J. Electrostatic self-assembled carbon nanotube/nano carbon black composite fillers reinforced cement-based materials with multifunctionality. *Composites Part A: Applied Science and Manufacturing*, 2015.79. Pp. 103–115. DOI: 10.1016/j.compositesa.2015.09.016
34. Ji, M., Mason, M., Modarelli, D., Parquette, J. Threading carbon nanotubes through a self-assembled nanotube. *Chemical Science*. 2019. 10(34). Pp. 7868–7877. DOI: 10.1039/c9sc02313e
35. Chung, D.D.L. Carbon materials for structural self-sensing, electromagnetic shielding and thermal interfacing. *Carbon*. 2012. 154. Pp. 1079–1086. DOI: 10.1016/j.carbon.2012.01.031
36. Monteiro, A.O., Loreda, A., Costa, P.M.F.J., Oeser, M., Cachim, P.B. A pressure-sensitive carbon black cement composite for traffic monitoring. *Construction and Building Materials*. 2017. 154. Pp. 1079–1086. DOI: 10.1016/j.conbuildmat.2017.08.053
37. Kumar, S., Kumar, R., Bandopadhyay, A., Alex, T.C., Ravi Kumar, B., Das, S.K., Mehrotra, S.P. Mechanical activation of granulated blast furnace slag and its effect on the properties and structure of portland slag cement. *Cement and Concrete Composites*. 2008. 30(8). Pp. 679–685. DOI: 10.1016/j.cemconcomp.2008.05.005
38. Ben Haha, M., Le Saout, G., Winnefeld, F., Lothenbach, B. Influence of activator type on hydration kinetics, hydrate assemblage and microstructural development of alkali activated blast-furnace slags. *Cement and Concrete Research*. 2011. 41(3). Pp. 301–310. DOI: 10.1016/j.cemconres.2010.11.016
39. Liu, G., Florea, M.V.A., Brouwers, H.J.H. The hydration and microstructure characteristics of cement pastes with high volume organic-contaminated waste glass powder. *Construction and Building Materials*. 2018. 87. Pp. 1177–1189. DOI: 10.1016/j.conbuildmat.2018.07.162
40. Han, B., Zhang, K., Yu, X., Kwon, E., Ou, J. Nickel particle-based self-sensing pavement for vehicle detection. *Measurement: Journal of the International Measurement Confederation*. 2011. 44(9). Pp. 1645–1650. DOI: 10.1016/j.measurement.2011.06.014
41. Slavchevaa, G., Khanb, M., Baidzhanovb, D., Shvedovac, M., Imanovb, Y. (2019). Slinkerless slag-silica binder: hydration process and hardening kinetics. *Magazine of Civil Engineering*. 2019. 92(8). Pp. 96–105. DOI: 10.18720/MCE.92.8
42. Rodger, S.A., Groves, G.W. Electron Microscopy Study of Ordinary Portland Cement and Ordinary Portland Cement–Pulverized Fuel Ash Blended Pastes. *Journal of the American Ceramic Society*. 1989. 72(6). Pp. 1037–1039. DOI: 10.1111/j.1151-2916.1989.tb06265.x
43. Richardson, I.G., Groves, G.W. Microstructure and microanalysis of hardened ordinary Portland cement pastes. *Journal of Materials Science*. 1993. 28(1). Pp. 265–277. DOI: 10.1007/BF00349061

Contacts:

Muhammad Tariq Bashir, tariqbashir@cecos.edu.pk

Muhammad Daniyal, drmtb@qurtuba.edu.pk

Majed Alzara, arc_majed@hotmail.com

Mahmoud Elkady, m.s.h.kady@gmail.com

Ammar Armghan, aarmghan@ju.edu.sa



DOI: 10.34910/MCE.105.6

Resistance to temperature and humidity changes of construction plywood and thermal-insulation boards

A.A. Fedotov , T.N. Vahnina, I.V. Susoeva* 

Kostroma State University, Kostroma, Russia

*E-mail: i.susoeva@yandex.ru

Keywords: wood composites, phenol-formaldehyde binder, modification, structure, temperature, humidity, strength

Abstract. Plywood and thermal-insulation boards with phenol-formaldehyde binder (PF), like other composites for construction purposes, must have long-term strength with changing temperature and humidity. The insufficient degree of curing of the phenol-formaldehyde binder reduces the hydrolytic stability of the material. The aim of the study is to increase the long-term strength of materials when exposed to changes in temperature and humidity by improving the structure formation of composites with the introduction of modifying additives in the binder. In the work, the method of cyclic testing of materials “soaking – freezing – thawing – drying” was used. After each cycle, the strength of the samples was determined. Nine modifying additives to the phenol-formaldehyde binder were used – hydrogen peroxide, metal salts, sulfosalicylic acid, dimethylglyoxime. The proportion of additives varied from 0.5 to 1.5 %. Graphic dependences of changes in the strength of PF plywood and thermal-insulation boards from plant waste after cyclic tests are given. Materials on a modified binder have long-term resistance to variable temperature and humidity effects. Plywood on a phenol-formaldehyde binder with the addition of 0.5 % sulfosalicylic acid has, after 15 test cycles, a 2.8 times higher residual strength compared to plywood on an unmodified binder. Thermal-insulation composites from plant waste on a modified binder after cyclic tests have a strength of 9 % higher than plates on an unmodified binder.

1. Introduction

In the work, the ability of plywood and thermal-insulation boards with a phenol-formaldehyde binder to maintain long-term strength under temperature-humidity changes was studied. PF plywood and other composites based on lignocellulosic fillers and a thermosetting binder for use in construction should have increased water resistance and long-term performance under conditions of changes in temperature and humidity. Hot cured phenolic adhesives have high water resistance, but it can only be achieved at a sufficiently high pressing temperature. The manufacture of materials at low temperatures does not allow the formation of a hydrolytically stable binder, this leads to a decrease in the strength of the composites.

According to Sameer F. Hamad and colleagues, the necessary degree crosslinking of the phenol-formaldehyde oligomer can be achieved only by prolonged heating at high temperature, which is uneconomical [1].

It is necessary to reduce the pressing temperature to increase the efficiency of the production of plywood and boards on a phenolic binder. However, it is not only reduces the degree cure of the phenol formaldehyde binder. According to H.D. Dibaba, in the process of curing the phenolic binder, the yield of low molecular weight polycondensation products is difficult, which creates a porous structure of the polymer matrix [2].

As a result, the structure of the cured phenolic polymer is weakened [3]. Moisture falling into the adhesive layer at the boundary of the polymer and veneer or fine-grained filler causes moisture stress. When used as building materials, plywood and boards are affected by variable factors: moisture, freezing, heating, etc. The result is a decrease in the strength and water resistance of the material.

Fedotov, A.A., Vahnina, T.N., Susoeva, I.V. Resistance to temperature and humidity changes of construction plywood and thermal-insulation boards. Magazine of Civil Engineering. 2021. 105(5). Article No. 10506. DOI: 10.34910/MCE.105.6

© Fedotov A.A., Vahnina T.N., Susoeva I.V., 2021. Published by Peter the Great St.Petersburg Polytechnic University



This work is licensed under a CC BY-NC 4.0

With regard to PF plywood used as multi-turn formwork, a decrease in the long-term resistance of plywood will lead to non-compliance with the requirements of regulatory documents (Russian standard 34329–2017 Formwork).

The long-term resistance of PF plywood and other building composites based on plant fillers and phenol formaldehyde binder depends on the strength of the binder. Wood and other plant fillers are also affected by the processes of freezing, thawing, and drying [4–8].

During freezing, the volume of water inside the lumen of plant cells increases. Pressure on cell walls can cause microcracks in the material [9, 10].

The need to make a rational scientific and technological decision when choosing factors for the production of plywood and heat-insulating boards with phenol-formaldehyde binders led to the goal of this study. The study aims to ensure the long-term strength of the composites when exposed to changes in temperature and humidity by improving the structure formation of the material with the introduction of modifying additives in the binder.

To predict changes in the strength of wood-adhesive composites for construction purposes, such as plywood and slabs, methods of full-scale tests or accelerated cyclic methods can be used. Field test methods are informative and accurate. However, their disadvantages include a significant time frame for research. The complexity and duration of field tests reduces the efficiency of decision-making on the choice of technological effects on the material. Therefore, in world and domestic research practice, accelerated cyclic tests are more often used, which make it possible to evaluate the performance of the material after temperature and humidity effects.

A significant part of research in the world is aimed at studying the effect of freezing-thawing and freezing cycles on the mechanical properties of wood-plastic composites [11–16].

The effect of freezing and heat treatment cycles on the properties of plywood and other wood composites is not well understood.

A method for assessing the durability of wood-adhesive compositions was developed by V.M. Khrulev and A. S. Freidin. To assess the weather resistance of glued wood and board materials, a cyclic test regime was proposed, which included the presence of samples in water for 5 hours and drying at 70 °C for 24 hours. Russian standard 17580 (as amended in 1972) was developed in the development of studies.

Cyclic methods are applicable to the assessment of structural adhesive joints for wood-based building materials [17, 18]. The results of cyclic tests allow us to evaluate the resistance of the material to changes in temperature and humidity during operation.

2. Methods

Effect of modifying additives to the phenol formaldehyde binder (PF) on the PF-3014 resin (Russian standard 20907–2016) on the strength for shearing plywood FSF was investigated in this work (Table 1). Addition of each modifier ranged from 0.5 to 1.5 % by weight of the binder (in increments of 0.5 %).

Effect of the addition of sulfosalicylic acid to the PF on the strength under static bending of soft thermal-insulating boards of the wet method of production from wood waste and flax spinning waste compared with the dynamics of the change in the value of particle boards (PB) [19] are also presented. Thermal-insulating boards were made with an average density of 275 kg/m³, and the average density of particle board was 800 kg/m³. Samples of thermal-insulating boards were dried at 100 °C to a moisture content of 8±1 %, the particle boards were pressed at a temperature of 170 °C, a specific pressure of 2.6 MPa.

Table 1. Additives used to modify PF in the manufacture of PF plywood.

Modifier view	Chemical formula
Hydrogen peroxide (3 % aqueous solution)	H ₂ O ₂
Zinc sulfate eight-water (aqueous solution)	ZnSO ₄ ·8 H ₂ O
Iron ammonium alum (aqueous solution)	NH ₄ Fe(SO ₄) ₂ ·12H ₂ O
Anhydrous magnesium chloride (aqueous solution)	MgCl ₂
Ferric chloride hexahydrate (aqueous solution)	Fe Cl ₃ ·6 H ₂ O
Aluminum chloride hexahydrate (aqueous solution)	AlCl ₃ ·6 H ₂ O
Dimethylglyoxime (in dry form)	C ₄ H ₈ N ₂ O ₂
Aluminum sulphate eighteen-water (aqueous solution)	Al ₂ (SO ₄) ₃ ·18H ₂ O
Sulfosalicylic acid two-water (aqueous solution)	C ₇ H ₆ O ₆ S·2 H ₂ O

Five-layer plywood was made on the basis of peeled birch veneer with a nominal thickness of 1.5 mm (Russian standard 99–2016). The veneer was pre-dried to a moisture content of $(7\pm1)\%$. After forming the package and applying the binder, hot pressing was performed in a P100–400 laboratory hydraulic press with the following constant factors: pressing temperature – 120 °C; pressing time – 5 min; specific pressing pressure – 1.6 MPa; binder consumption – 100 g/m². Manufactured plywood was cooled for 24 hours, then cut into samples for testing on shear strength.

For testing the strength of the samples used tensile testing machine R-5 (Russian standard 28840). Adaptation to a testing machine with wedge grippers was used to determine the strength of plywood during chipping. The arithmetic average of five duplicate experiments was taken as the test result.

According to the standard method of cyclic testing of material [18] one cycle of temperature and humidity effects on the samples included the following operations:

- the samples were placed in a vessel, loaded and poured for 20 hours with water having a temperature of (20 ± 2) °C, so that they were covered with water by 2 ... 3 cm;
- wet samples extracted from water were transferred to a freezer and kept for 6 hours at a temperature of minus (20 ± 2) °C;
- frozen samples extracted from the freezer were laid out on the rack and left to thaw for 16 hours at an air temperature of (20 ± 2) °C;
- after thawing, the samples were placed in a drying chamber and kept for 6 hours at a temperature of (60 ± 5) °C and air humidity (60 ... 75) %.

Samples of plywood passed 15 test cycles, samples of particle boards and thermal-insulating boards – 10 cycles.

3. Results and Discussion

The results of determining the strength of plywood during chipping after each of the test cycles are presented in Table 2 and in Fig. 1–3. Main results are presented in the figures due to the large volume of tests, in Table 2 shows the values for control samples without modification of the binder and for samples of plywood on a binder modified by the addition of sulfosalicylic acid.

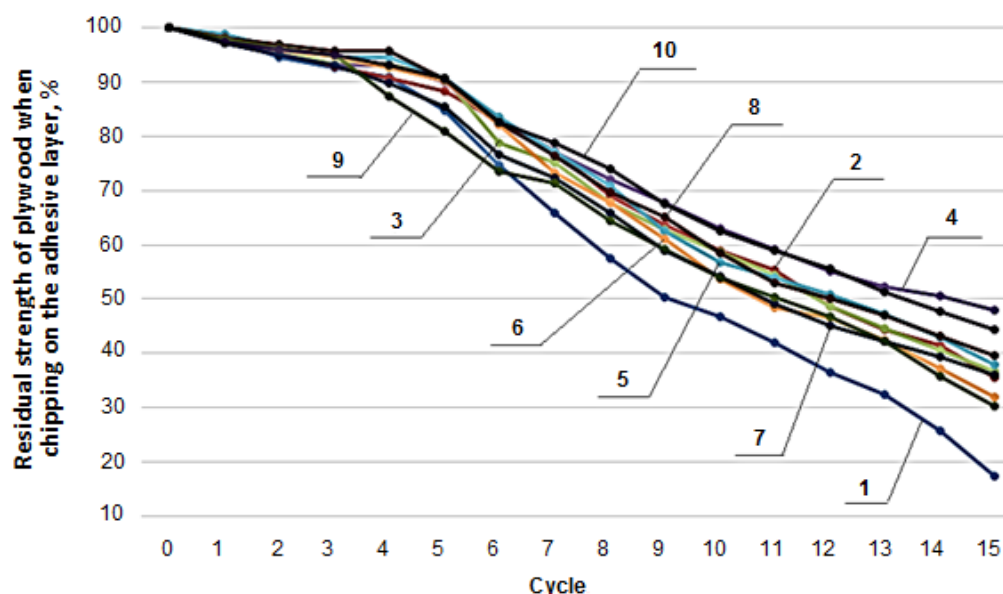


Figure 1. Dependences of residual shear strength, % plywood on a binder with the addition of 0.5 % modifier after cycles of temperature and humidity:

- 1 – control (without modifier); 2 – hydrogen peroxide (3 % aqueous solution); 3 – aluminum chloride hexahydrate (aqueous solution); 4 – sulfosalicylic acid two-water (aqueous solution); 5 – iron chloride III six-water (aqueous solution); 6 – anhydrous magnesium chloride (aqueous solution); 7 – iron ammonium alum (aqueous solution); 8 – zinc sulfate eight-water (aqueous solution); 9 – eighteen-aluminum sulphate (aqueous solution); 10 – dimethylglyoxime (in dry form).**

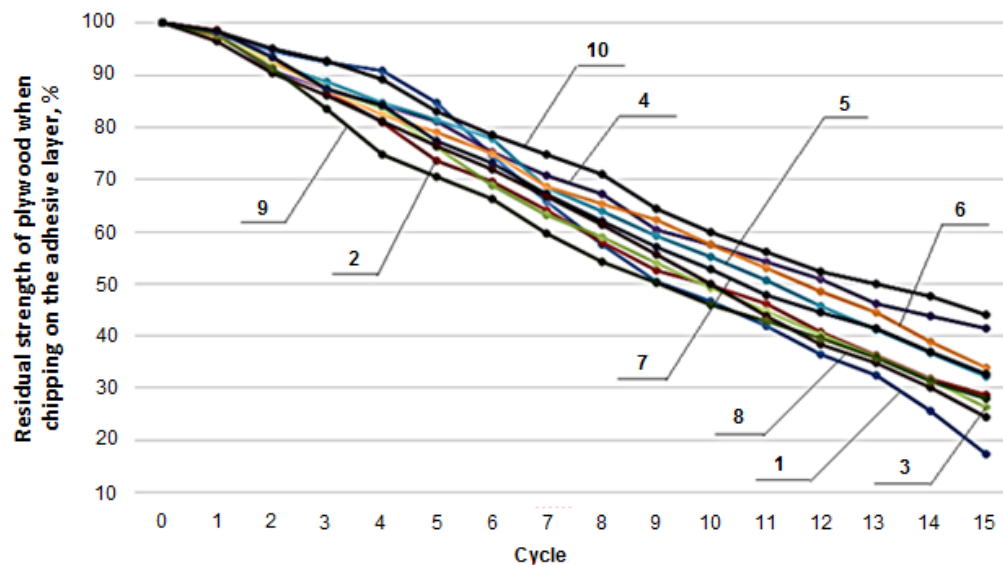


Figure 2. Dependences of residual shear strength, % plywood on a binder with the addition of 1 % modifier after cycles of temperature and humidity:

- 1 – control (without modifier); 2 – hydrogen peroxide (3 % aqueous solution); 3 – aluminum chloride hexahydrate (aqueous solution); 4 – sulfosalicylic acid two-water (aqueous solution); 5 – iron chloride III six-water (aqueous solution); 6 – anhydrous magnesium chloride (aqueous solution); 7 – iron ammonium alum (aqueous solution); 8 – zinc sulfate eight-water (aqueous solution); 9 – eighteen-aluminum sulphate (aqueous solution); 10 – dimethylglyoxime (in dry form).

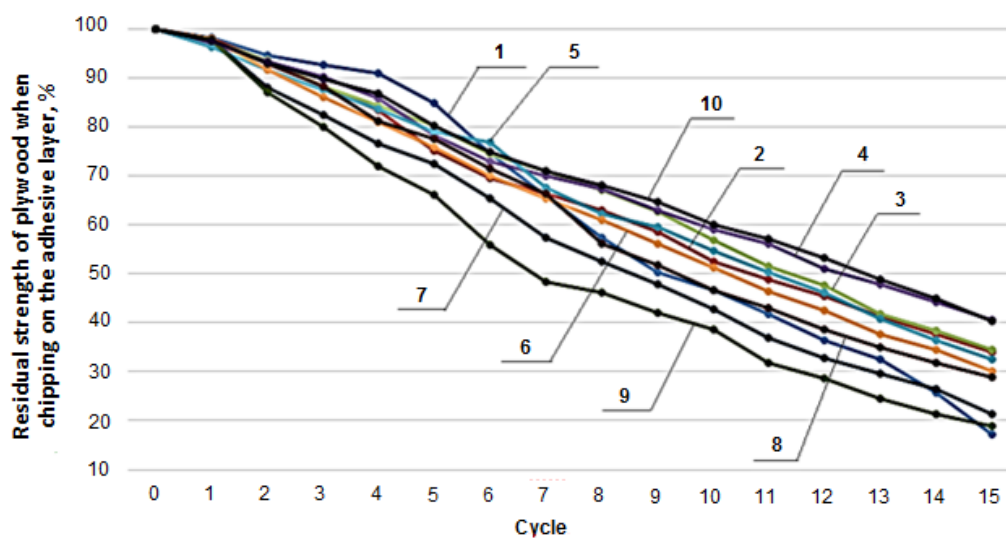


Figure 3. Dependences of residual tensile strength, % plywood on a binder with the addition of 1.5 % modifier after cycles of temperature and humidity:

- 1 – control (without modifier); 2 – hydrogen peroxide (3 % aqueous solution); 3 – aluminum chloride hexahydrate (aqueous solution); 4 – sulfosalicylic acid two-water (aqueous solution); 5 – iron chloride III six-water (aqueous solution); 6 – anhydrous magnesium chloride (aqueous solution); 7 – iron ammonium alum (aqueous solution); 8 – zinc sulfate eight-water (aqueous solution); 9 – eighteen-aluminum sulphate (aqueous solution); 10 – dimethylglyoxime (in dry form).

Table 2. Dynamics of changes in the strength of plywood chipping in cyclic tests (above the line for samples with a modifier, below the line for control).

Cycles	Shear strength, σ_{ss} , MPa	Residual strength, %
Before the test	2.79/2.96	—
0.5 % modifier additive		
1	2.71/2.90	97.25/98.10
2	2.65/2.80	94.98/94.59
3	2.60/2.74	93.19/92.57
4	2.60/2.69	93.19/90.88
5	2.51/2.51	89.96/84.80
6	2.29/2.21	82.08/74.66
7	2.15/1.95	77.06/65.88
8	2.01/1.70	72.04/57.43
9	1.89/1.49	67.74/50.34
10	1.76/1.38	63.08/46.62
11	1.65/1.24	59.14/41.89
12	1.54/1.08	55.20/36.49
13	1.46/0.96	52.33/32.43
14	1.41/0.76	50.54/25.68
15	1.34/0.51	48.03/17.23
1.0 % modifier additive		
1	3.12/2.90	98.06/98.10
2	2.89/2.80	90.88/94.59
3	2.78/2.74	87.42/92.57
4	2.68/2.69	84.28/90.88
5	2.58/2.51	81.13/84.80
6	2.39/2.21	75.16/74.66
7	2.25/1.95	70.75/65.88
8	2.14/1.70	67.30/57.43
9	1.92/1.49	60.38/50.34
10	1.83/1.38	57.55/46.62
11	1.72/1.24	54.09/41.89
12	1.62/1.08	50.94/36.49
13	1.47/0.96	46.23/32.43
14	1.39/0.76	43.71/25.68
15	1.32/0.51	41.51/17.23
1.5 % modifier additive		
1	2.87/2.90	96.83/98.10
2	2.76/2.80	93.24/94.59
3	2.67/2.74	90.20/92.57
4	2.54/2.69	85.81/90.88
5	2.32/2.51	78.38/84.80
6	2.16/2.21	72.97/74.66
7	2.07/1.95	69.93/65.88
8	1.99/1.70	67.23/57.43
9	1.86/1.49	62.84/50.34
10	1.75/1.38	59.12/46.62
11	1.66/1.24	56.08/41.89
12	1.51/1.08	51.01/36.49
13	1.42/0.96	47.97/32.43
14	1.31/0.76	44.26/25.68
15	1.20/0.51	40.54/17.23

Plywood on an unmodified phenol-formaldehyde binder after 15 test cycles has a residual strength of less than 20 %. The reason for this is the low degree of curing of the binder at a pressing temperature of 120 °C and the presence of microvoids in the cured binder. Water penetrates micropores during testing, freezes, evaporates, and causes hydrolytic destruction of the polymer.

One cannot disagree with G.A. Ormondroyd [20], that the adhesives used in the manufacture of wood composites have arguably the most influence on the composites properties. The adhesives influence all aspects of the composites, from their mechanical properties and their ability to perform in wet conditions.

With a share of modifier additives of 0.5 % by weight of the resin, plywood sulfosalicylic acid and dimethylglyoxime give the best resistance to variable temperature and humidity effects (Fig. 1). They create additional crosslinking units in the cured polymer network [21] and provide higher hydrolytic stability of the binder. With a share of modifier additives of 1 % and 1.5 %, sulfosalicylic acid and dimethylglyoxime also give the best results in increasing the residual strength of plywood after cyclic tests (Fig. 2).

Hydrogen peroxide, used by J. Sedliacik and colleagues in the study as a phenolic binder modifier [22], in small amounts (0.5 %), a positive effect on the spreadability of the binder during the veneering of veneer. Up to five test cycles, it positively affects the residual strength of plywood, however, with further temperature and humidity effects, the addition of hydrogen peroxide has a lesser effect on increasing the residual strength of plywood. Addition of hydrogen peroxide in an amount of 1 ... 1.5 % does not significantly affect the increase in the residual strength of plywood during cyclic tests.

Addition of iron, magnesium and aluminum chlorides on average increases the residual strength of plywood after cyclic tests, but their effect is less effective than for the addition of dimethylglyoxime and sulfosalicylic acid.

Despite the fact that aluminum salts are traditionally considered to be phenolic binder modifiers, aluminum sulfate showed the worst results when introduced into the adhesive composition. When the proportion of the additive is 1.5 %, the amount of aluminum sulfate becomes redundant, the residual strength of plywood with this modifier is lower than that of control samples.

The results of tests for static bending after cyclic effects of thermal-insulating boards with the addition of spinning waste of flax fiber and particle boards are presented in Table 3.

Table 3. Dynamics of changes in strength under static bending thermal-insulating boards and particle boards in cyclic tests (above the line for samples with a modifier, below the line for control).

Cycles	Thermal-insulating boards		Particle boards	
	Strength in static bending, σ_i , MPa	Residual strength, %	Strength in static bending, σ_i , MPa	Residual strength, %
Before the test	0.55/0.58		25.5	
1	0.53/0.57	96/98	21.1	82.5
2	0.53/0.56	96/97	18.3	71.5
3	0.52/0.53	94/91	16.0	62.9
4	0.51/0.52	93/90	13.2	51.6
5	0.49/0.51	89/88	10.5	41.0
6	0.47/0.50	85/86	7.9	31.3
7	0.47/0.48	85/84	6.0	23.5
8	0.41/0.43	74/75	4.7	18.5
9	0.32/0.40	58/70	4.3	16.8
10	0.26/0.32	47/56	3.5	13.7

The addition of sulfosalicylic acid in an amount of 0.5 % to the phenol-formaldehyde binder also increases the residual strength of soft thermal-insulating boards from wood waste and flax fiber spinning waste (Table 3). Low-density boards have a low value of strength under static bending, however, in comparison with more durable particle boards, thermal-insulating boards have a higher value of residual strength after cyclic tests. It should be noted that the modification of the phenolic binder with the addition of sulfosalicylic acid increases by 9 % the residual strength of the thermal-insulating boards after 10 test cycles, the residual strength index for these boards is four times higher than that of particle boards with an unmodified phenol-formaldehyde binder.

4. Conclusions

1. Plywood on a phenol formaldehyde binder with the addition of 0.5 % sulfosalicylic acid, manufactured at a pressing temperature that does not provide a high degree of curing of the binder, has

after 15 test cycles 2.8 times higher residual strength compared to plywood on an unmodified binder. This allows us to predict a longer service life of plywood during operation with changes in temperature and humidity.

2. Best results on increasing the residual strength of plywood with changes in temperature and humidity are provided by modifiers sulfosalicylic acid and dimethylglyoxime, added in an amount of 0.5 ... 1.5 % by weight of the phenolic binder.

3. Modification of the binder with sulfosalicylic acid for the production of soft thermal-insulating boards of the wet method production from wood waste and non-returnable waste spinning flax, allows to increase the residual strength of the material by 9 %.

4. Thus, the obtained experimental data make it possible to recommend the addition of dimethylglyoxime or sulfosalicylic acid as modifiers of the phenol formaldehyde binder for lignocellulosic materials, such as plywood and thermal-insulating boards. Modifiers will increase the residual strength of materials used under changing temperature and humidity conditions, and therefore, will increase the life of plywood and boards.

5. Acknowledgement

The study was financially supported by the Russian Federal Property Fund and the Kostroma Oblast Administration as part of a scientific project No. 19-43-440001.

References

1. Hamad, S.F., Farr, N., Fei, T. Optimizing size and distribution of voids in phenolic resins through the choice of catalyst types. *Journal of Applied Polymer Science*. [Online]. System requirements: Adobe Acrobat Reader. URL: <https://doi.org/10.1002/app.48249> (date of application: 10.03. 2020).
2. Henock, D.D. Permeability barriers for composites ageing mechanisms and surface treatment of polymeric matrix composites under cyclic load. *Materials Processing Technology*. [Online]. System requirements: Adobe Acrobat Reader. URL: <http://www.theseus.fi> (date of application: 10.03. 2020).
3. Fedotov, A.A., Vachnina, T.N., Kotikov, S.A. Improving strength indicators of fsf plywood by using modifying additives to binding agent. *Forestry Engineering Journal*. 2020. 1. Pp. 124–135. DOI: 10.34220/issn.2222-7962/2020.1/13. (rus)
4. Ugolev, B.N., Galkin, V.P., Gorbacheva, G.A., Kalinina A.A. Frozen shrinkage of wood. *Proceedings 6th International symposium IUFRO – TUZVO «Wood Structure and Properties'10»*. Zvolen. Slovakia, 2010. Pp. 73–77.
5. Câmpăan, M., Ispas, M., Porojan, M. Considerations on drying frozen spruce wood and effects upon its properties. 2008. *Drying Technology*. 26. Pp. 596–601.
6. Kärenlampi, P.P., Tynjälä, P., Ström, P. Phase transformations of wood cell wall water. *Journal of Wood Science*. 2005. 51. Pp. 118–123.
7. Green, D.W., Evans, J.W., Logan, J.D., Nelson, W.J. Adjusting modulus of elasticity of lumber for changes in temperature. *Forest Products Journal*. 1999. 49 (10). Pp. 82–94.
8. Mishiro, A. Effect of freezing treatments on the bending properties of wood. *Bulletin of Tokyo University*. 1990. 82. Pp. 177–189.
9. Ilic, J. Advantages of pre-freezing for reducing shrinkage-related degrade in eucalyptus: General considerations and review of literature. *Wood Science and Technology*. 1995. 29 (4). Pp. 277–285.
10. Szmuk, M.B., Câmpăan, M., Sandu, A.V. Microstructure modifications induced in spruce wood by freezing. *ProLigno*. 2011b. 7 (4). Pp. 26–31.
11. Pilarski, J.M., Matuana, L.M. Durability of wood flour-plastic composites exposed to accelerated freeze-thaw cycling. Part I. Rigid PVC matrix. *Journal of Vinyl and Additive Technology*. 2005. 11(1). Pp. 1-8. DOI: 10.1002/vnl.20029
12. Wang, W.H., Morrell, J.J. Effects of moisture and temperature cycling on material properties of a wood/plastic composite. *Forest Product Journal*. 2005. 55 (10). Pp. 81–83.
13. Schildmeyer, A.J., Wolcott, M.P., Bender, D.A. Investigation of the temperature-dependent mechanical behavior of a polypropylene-pine composite. *Journal of Materials in Civil Engineering*. 2009. 21 (9). Pp. 460–466. DOI: 10.1061/(ASCE)0899-1561(2009)21:9(460)
14. Nadir, A., Songklod, J., Vallayuth, F., Piyawade, B. Effect of thermal treatment of wood-fiber on properties of flat-pressed wood plastic composites. *Polymer Degradation and Stability*. 2011. 96 (5). Pp. 818–822.
15. Xue, Y., Veazie, D., Glinsey, C., Wright, M., Rowell, R.M. Mechanical Properties of Wood Fiber Composites Under the Influence of Temperature and Humidity. [Online]. System requirements: Adobe Acrobat Reader. URL: <https://www.researchgate.net/publication/237135869> (date of application: 10.03. 2020).
16. Franco, L.A.L., Graça, M.L.A., Silva, F.S. Interlaminar shear strength and fractographic evaluation with varying temperature and moisture content of thermoplastic composites. *Applied Mechanics and Materials*. 2005. 3–4. Pp. 179–184.
17. Russian standard 17580-82. Konstrukcii derevyannye kleenye. Metod opredeleniya stojkosti kleevykh soedinenij k ciklichnym temperaturno-vlazhnostnym vozdejstviyam [State standard specification. Wooden laminated structures. Method to determinate stability of glued joints against cyclic temperature-and humidity influences]. (rus)
18. Russian standard 33121-2014. Konstrukcii derevyannye kleenye. Metody opredeleniya stojkosti kleevykh soedinenij k temperaturno-vlazhnostnym vozdejstviyam [State standard specification. Glued timber structures. Methods for determining the resistance of glue joints to the temperature and humidity effects]. (rus)
19. Susoeva, I.V., Vachnina, T.N., Titunin, A.A., Asatkina, J.A. The performance of composites from vegetable raw materials with changes in temperature and humidity. *Magazine of Civil Engineering*. 2017. 3(71). Pp. 39–50. DOI: 10.18720/MCE.71.5

20. Ormondroyd, G.A. Adhesives for wood composites. [Online]. System requirements: Adobe Acrobat Reader. URL: https://www.researchgate.net/publication/284172771_Adhesives_for_wood_composites (date of application: 10.03. 2020).
21. Vakhnina, T.N., Fedotov, A.A., Titunin, A.A., Susoeva, I.V. Vliyanie modifikatorov na vremya otverzhdeniya fenoloformal'degidnogo svyazuyushchego dlya pressovaniya fanery pri nizkotemperaturnom rezhime [Influence of modifiers on the curing time of the phenol formaldehyde binder for pressing panels at low temperature mode]. Forestry Engineering Journal. 2019. 4. Pp. 99–108. DOI: 10.34220/issn.2222-7962/2019.4/11. (rus)
22. Sedliacik, J., Bekhta, P., Potapova, O. Technology of low-temperature production of plywood bonded with modified phenol–formaldehyde resin. Wood research. 2010. 55(4). Pp. 124–130. <https://www.researchgate.net/publication/267026018>

Contacts:

Alexander Fedotov, aafedotoff@yandex.ru

Tatiana Vahnina, t_vachnina@mail.ru

Irina Susoeva, i.susoeva@yandex.ru



DOI: 10.34910/MCE.105.7

Production of sustainable concrete using sawdust

W.W. El-Nadoury 

Pharos University in Alexandria, Alexandria, Egypt

E-mail: wegdanelnadoury@gmail.com

Keywords: mechanical properties, aggregate, Portland cement, building materials, sustainability, sawdust, cost

Abstract. Rapid progression of construction industry rises the demand on building materials. With focusing on developing cost effective, sustainable and eco-friendly buildings, there is a need to find alternative materials to fulfil the constructions' requirements. This paper presents an experimental study to investigate the applicability of using sawdust and sawdust ash as a green alternative for natural sand and cement respectively in order to lessen both environmental impacts and construction cost. The proposed mixtures incorporate sawdust with 5 %, 10 %, 15 %, 20 %, 25 % and 30 % as partial substitution for each of natural sand and cement. Mechanical properties of proposed mixes were compared to reference mixtures with typical concrete constituents. Physical properties were also investigated. The test results reveal that the optimum percentage of replacement of natural sand for producing sawdust concrete mixture is 10 % to 20 % and the acceptable percent of partial replacement of cement with sawdust ash is up to 15 %.

1. Introduction

Sustainable development is related to balance in maintaining resources, energy and solving environmental problems. It is becoming progressively well-defined that incorporation of sustainable practices and methodologies into civil engineering is crucial for the sustainability of the environment [1]. Concrete is acknowledged for being the basic material used in construction based on its ability to be cast in different geometrical structures, less maintenance requirements, and good durability and mechanical properties. However, different gases, especially CO₂, are discharged tremendously during production of its constituents which is considered a global concern. In addition, it is categorized as an excessive energy ingestion industry. Furthermore, the essential reliant of concrete on the availability of natural resources such as sand, which is utilized as fine aggregate, causes growing scarcity of sand and eco-system disruption. This imposes researchers to yield novel materials from renewable sources to be used in construction to mitigate the effect of building industry on environment.

Natural fibers and industrial and agricultural wastes, with their renewable and sustainable nature, are increasingly applied in construction. Previous research specified that natural fiber provides considerable reduction in weight of structure, improves sound absorbent properties owing to its excessive void ratio, facilitates handling, mixing and placing of mixtures compared to other types of concrete [2–3]. It is also recognized by its low production cost, less health hazards, and accessible processing [2–3].

An equally significant direction is the usage of industrial wastes in producing of building materials with low density, sound and heat conductivity, as well as high physical and mechanical properties. These materials are used in casting cellular concrete for constructing the external and internal walls of buildings [4–5]. Several studies describe the compositions and technology for producing cellular concrete from lightweight geopolymers as an example of industrial wastes [6–13].

The implementation of fillers which can be represented as particles of the dispersed phase change the energy state of the dispersed system [14–18]. The used fillers depend on their chemical activity. Efficient fillers have a multifunctional usefulness in the synthesis of materials through forming a denser packaging

El-Nadoury, W.W. Production of sustainable concrete using sawdust. Magazine of Civil Engineering. 2021. 105(5). Article No. 10507. DOI: 10.34910/MCE.105.7

© El-Nadoury, W.W., 2021. Published by Peter the Great St.Petersburg Polytechnic University



This work is licensed under a CC BY-NC 4.0

of the initial components and changing the chemistry of the binder hardening [19–23]. Granulated blast furnace slag, silica fume, fly ash, and rice husk ash [24–27] are considered suitable alternatives for partial replacement of cement. While recycling concrete, crushed steel, and expanded perlite symbolize good alternatives for aggregates [28–31].

Another direction is the technology of modifying the structure of concrete by introducing into the concrete mixture the porous dispersed components (damping additives). This method of increasing the shock endurance of concretes was researched by R. Oyguc [32], M. Kristoffersen [33], A. Maazoun [34], Z.I. Syed [35], and K. Makita [36]. However, these concretes provide a relatively moderate increase in shock endurance – up to 2–4 times, which is not sufficient for protective structures in conditions of the action of the means of destruction, which create high dynamic loads on the enclosing structures.

The use of fiber-reinforced concrete for the production of enclosing structures of protective structures is promising because it has high impact resistance [37–46]. Dispersed reinforcement allows to substantially increase the whole set of mechanical characteristics of concrete, such as static strength, crack toughness, impact resistance.

Sawdust, collected from grinding, cutting, or pulverizing of hard and soft woods is an example of natural fiber. Sawdust has been used, but not widely, as fine aggregate in casting floors, roofs and walls for more than 50 years. Recently, some researcher investigated the applicability of using wood waste as a replacement for fine aggregate in concrete mixtures [47–51]. Turgut [52] postulated that it can be used efficiently in producing artificial limestone brick. Researchers [53–54] suggested that wood chipping improves the thermal and insulation properties of concrete mixtures and lessen the density of the concrete, however, it attained high water absorption [53]. Coatanlem et al [55]. Boob [56] investigated the effect of replacing 15 % of sand with sawdust in casting blocks for partition walls in multi-storey building using 1:6 cement and sand mix. His results reveals that the compressive strength for these blocks was 4.5 N/mm² which is considered reasonable and economic for this application. Compressive strength, flexural strength, ultrasonic pulse velocity (UPV), unit weight and water absorption of lightweight composite consists of combinations wood sawdust waste and limestone powder wastes were assessed by Turgut and Algin [57]. They found values for tested properties are in accordance to International Standard (IS). On assessing the effect of sawdust on compressive strength at 28 days, Paramaswam et al. [58] argued that for mixtures with cement to sawdust ratio of 1:1, 1:2, and 1:3, the compressive strengths were 31, 8.5, and 5 N/mm² respectively. Jr. [59] and Osei and Jackson [60] found that the strength of sawdust concrete decrease as water-cement ratio is less than 0.45.

The aim of this paper is to demonstrate the potential of using sawdust wastes in order to produce the desired composite and sustainable green construction material. Natural fine aggregate and cement is substituted by sawdust at percentages 5, 10, 15, 20, 25 and 30. Experimental investigations on physical and mechanical properties of concrete made with sawdust were conducted and compared to control mix cast with typical concrete constituents.

2. Methods

The experimental work was premeditated to assess the effect of fractional replacement of natural sand and cement with sawdust and sawdust ash respectively on physical and mechanical properties of concrete. The tested properties include; compressive strength, tensile strength, flexural strength, fineness modulus, specific gravity, moisture content, water absorption, bulk density, and porosity.

2.1. Materials

Ordinary Portland Cement in accordance to ASTM Type I was used throughout the work for mixing concrete complying with specifications in ASTM Standard C150 [61]. Table 1 demonstrates the physical properties of cement. Sand passing through 5.00 mm sieve was used as fine aggregates with specific gravity of 2.67. Machine crushed limestone passing through 20 mm sieve and retained on 4.75 mm sieve were used as coarse aggregates with specific gravity of 2.7. The sawdust was immersed in solution of NaOH with concentration 5 % for two hours to lose some amount of lignin. Then washed several times using fresh water before being oven dried for one night at 100 °C. Sawdust used as fine aggregate was composed of particles that passed through 5.00 mm sieve. While saw dust used as replacement of cement was sieved through sieve 200 after being burned at temperature of 200 °C. Chemical composition of sawdust is given in Table 2. Physical properties of fine and coarse aggregate are demonstrated in Table 3. Sieve analysis for sawdust, prepared in accordance of ASTM C136/C136M-19 [62], is illustrated in Table 4.

2.2. Concrete mix design

Thirteen concrete mixtures were prepared where sawdust was used to replace either sand or cement at percentages of 0 %, 5 %, 10 %, 15 %, 20 %, 25 %, and 30 %. The proportional ratio of cement: fine

aggregate: coarse aggregate was 1:1.5:3 and design was proposed by using ACI 211.1 [63]. The water to cement ratio was set to 0.45 to obtain concrete with grade M-25. The mixture proportions are shown in Table 5. In order to validate that all sawdust concrete mixes attain the required workability, the slump test was performed, the slump test results ranged from 133 mm to 170 mm. Mixtures were then cast in standard moulds required for each test. The concrete mixtures were poured into the mould in three layers followed with compaction in between those layers to assure well compaction, thus avoiding any deficiencies such as honeycombs and air traps. A total 234 specimens were casted. After 24 hours of casting, the specimens were demoulded and moist cured till the day of testing in accordance to ASTM C192 [64].

Table 1. Physical properties of cement.

Characteristics	Value
Specific gravity	3.12
Initial setting time(min.)	28
Final Setting time(min.)	615
Standard consistency	37

Table 2. Chemical composition of sawdust.

Oxides	Percentages
SiO ₂	68.5
Al ₂ O ₃	5
Fe ₂ O ₃	3.3
CaO	10.5
MgO	6.7
MnO	0.01
Na ₂ O	0.07
K ₂ O	0.1
P ₂ O ₅	0.44
SO ₂	0.47

Table 3. Physical Characteristics of sawdust, sand, and coarse aggregate.

Characteristics	Sand	Sawdust	Coarse aggregate
Specific gravity	2.67	2.5	2.7
Fineness	2.31	1.78	----
Moisture content %	3.7	0	0
Bulk density(kg/m ³)	1570	1250	1450
Voids %	41	64	39
Water absorption %	0.47	0.58	8

2.3. Tests on hardened concrete

The effect of replacement of fine aggregate and cement with sawdust with different percentage was assessed by determining specific gravity, water absorption, moisture content, bulk density, compressive, flexural strength, and tensile strength.

2.3.1 Water absorption test

The specimens required for water absorption test were demoulded and immersed in water for 24 hours before being tested according to ASTM C642[65].

2.3.2 Compressive strength test

Six cubes of size 150 mm × 150 mm × 150 mm, uncertainty of reading dimensions = ± 0.05 mm, were prepared from each concrete mixture for investigation of compressive strength. The concrete specimens were cured under normal conditions as per ASTM 192 [64] and were tested using Universal Test Machine at 28 and 90 days. The test method requires rounding to nearest 0.1 N/mm, expanded uncertainty at level of confidence = 1.21 N/mm².

Table 4. Sieve analysis for sawdust and sawdust ash.

Sieve size	% passing of saw dust	% of passing for saw dust ash
Sieve 4	95	100
Sieve 8	89	100
Sieve 16	77	100
Sieve 30	49	100
Sieve 50	18	97
Sieve 100	1.25	92
Sieve 200	0.10	90

Table 5. Proposed mix proportion and slump test results.

Mix No.	% of replacement	Cement	Water	F. Aggregate	C. Aggregate	Sawdust	Slump
FC	0	450	202.5	675	1350	0	150
F1	5	450	202.5	641.25	1350	33.75	142
F2	10	450	202.5	607.5	1350	67.5	141
F3	15	450	202.5	573.75	1350	101.25	140
F4	20	450	202.5	540	1350	135	140
F5	25	450	202.5	506.25	1350	168.75	137
F6	30	450	202.5	472.5	1350	202.5	133
C1	5	427.5	202.5	675	1350	22.5	158
C2	10	405	202.5	675	1350	45	160
C3	15	382.5	202.5	675	1350	67.5	163
C4	20	360	202.5	675	1350	90	167
C4	25	337.5	202.5	675	1350	112.5	168
C6	30	315	202.5	675	1350	135	170

2.3.3 Tensile test

150 × 300 mm cylinder specimens were used to detect the tensile strength. Seventy-eight specimens were cast and cured in water at room temperature in the laboratory for 7 and 28 days. After curing, three specimens for each mixture were tested for tensile strength in accordance to ASTM C496/C496M-17 [66] and the average was recorded.

2.3.4 Flexural Strength

Flexural strength was measured using 100 × 100 × 500 mm beam specimen in the centre of the beam load applied. A total of 78 beams were cast and cured in water for 28 and 90 days. For each mixture, three beams were loaded to failure in accordance to ASTM C78/C78M-18 [67], and the average strength was recorded in each case.

3. Results and Discussion

3.1. Density

The density of concrete dimensioned with the increase in sawdust content. Fig. 1 illustrates the average density of concrete specimens. The density at 28 days for mix with 30 % replacement of sand and cement was less than that of the control mix by 7 % and 5 % respectively. The density of sand and cement is higher than the density of sawdust, therefore a decrease in density is associated with mixtures with sawdust. The range of densities was 2100–2400 kg/m³ for all the replacement values. This revealed that the concrete with sawdust can be considered as normal weight concrete. This is in agreement with results of Layla and Hasan [13] and Mageswari and Vidivelli [14] who suggested that the decrease in density of sawdust concrete is about 4–5 %. However, Abdul et al [19] postulated that the decrease in density can reach 40 % using mixtures with ratio 1:3 cement to sawdust.

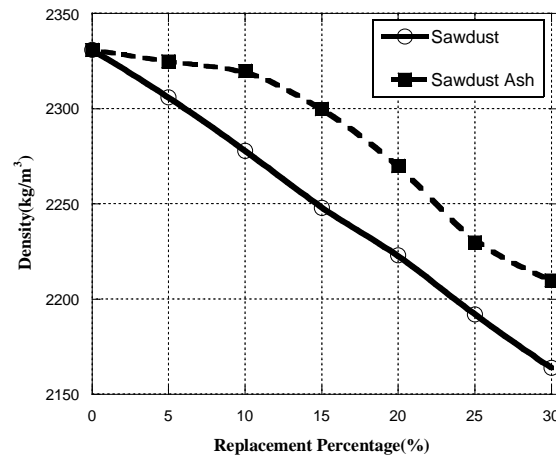


Figure 1. Effect of replacement of sand and cement on density of concrete.

3.2. Water absorption

Water absorption for specimens from different mixtures was calculated. It was deduced that water absorption enlarged with rising content of saw dust. The range of increase in water absorption was from 13 % to 80 higher than that of control mix with the maximum rate of water absorption for concrete mix with 30 % saw dust content, however it is still in the accepted limits. Table 6 represents the percentage of water absorption for different mixtures tested.

Table 6. Percentage of water absorption.

Mix No.	Dry weight of cube(gm)	Wet weight of cube (gm)	Water absorbed	% of water absorption
FC	8360	8460	100	1.19 %
F1	8450	8564	114	1.35 %
F2	8235	8360	125	1.52 %
F3	8225	8361	136	1.65 %
F4	8000	8147	147	1.84 %
F5	7900	8059	159	2.00 %
F6	7880	8052	172	2.18 %
C1	8462	8566	104	1.22 %
C2	8335	8450	115	1.38 %
C3	8225	8351	126	1.53 %
C4	8000	8137	137	1.71 %
C4	7990	8140	150	1.88 %
C6	7970	8132	162	2.03 %

3.3. Compressive strength

The effect of incorporation of sawdust on compressive strength of concrete, as given in literature, was contradicting. Researchers [50] suggested that 30 % replacement of fine aggregate with sawdust increased the compressive strength by 13 %. On the other hand, Layla and Hasan [48] argued that the 25 % of sawdust decreases the compressive strength by 54 %. The results of this work indicated that on testing the effect of replacement of natural sand with sawdust on the compressive strength, it was perceived that the compressive strength was not affected at 5 % replacement. The 10 % sawdust replacement attained the highest compressive strength with nearly 3 % more than that of control mix. At percentage higher than 10 %, the compressive strength decreased with the increase in the percentage of sawdust. However, all specimens surpassed the designed value of concrete grade 25. Accordingly, this certainly ensure that the designed sawdust mix can be effectively used to obtain the required strength. The results are shown in Fig. 2(a). As for the results of partial replacement of cement with sawdust ash, the compressive strength decreased with increasing percentage of replacement. The highest rate of reduction was 10.3 %, see Fig. 2(b). However, the replacement of cement with sawdust ash by percentage up to 15 % decreased the compressive strength by only 5 %. These results confirmed that with proper concrete mix proportion the sawdust can be effectively used as partial replacement of fine aggregate and cement.

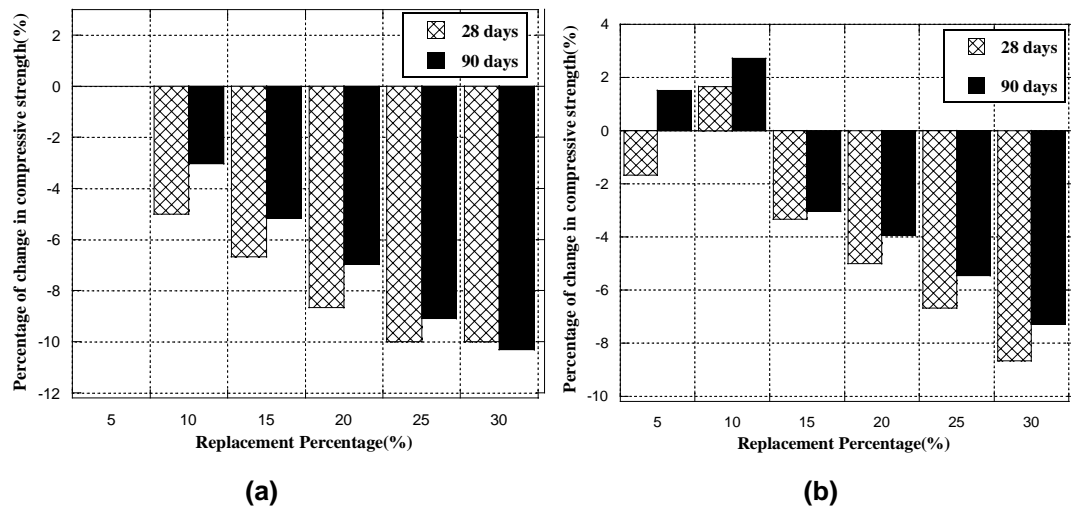


Figure 2. Compressive strength for mixes (a) sawdust replacing sand, (b) sawdust ash replacing cement.

3.4. Tensile Strength

The results at 28 days showed that the replacement of natural sand and cement with sawdust and sawdust ash decreases the tensile strength despite the percent of replacement compared to the control mix. However, at 90 days the results implied that incorporation of sawdust with percentage up to 15 % improves the tensile strength. The extreme degree of enhancement in case of replacing of natural sand was 10 % while in case of replacing cement was 4 %. This is in agreement with previous results in literature [49–50]. Fig. 3 demonstrates the tensile strength for specimens with sawdust and sawdust ash.

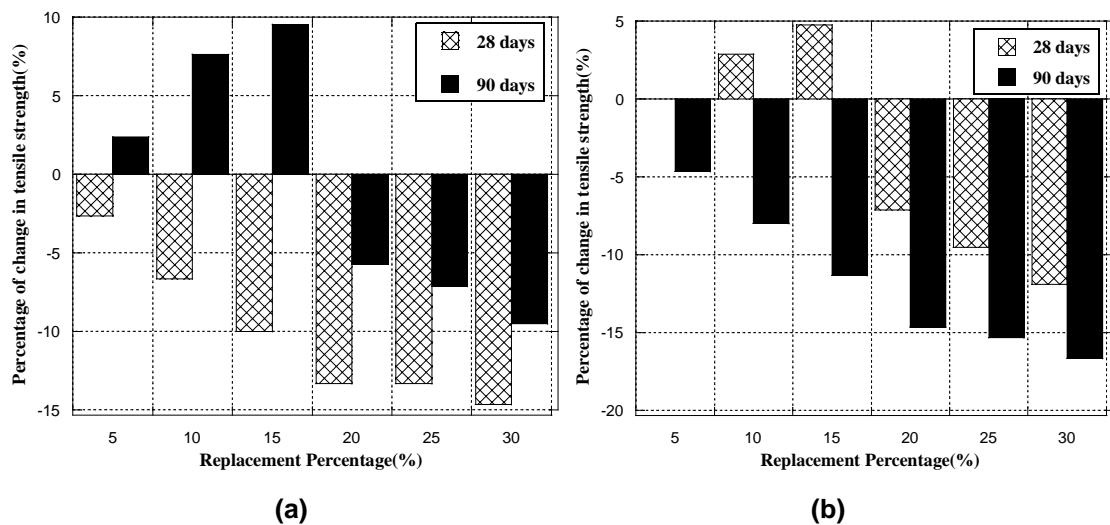


Figure 3. Tensile strength for mixes (a) sawdust replacing sand, (b) sawdust ash replacing cement.

3.5. Flexural Strength

The substitution of natural sand with sawdust has nearly no effect on the flexural tensile strength, the results indicated comparable values to control specimens at all considered levels of replacement. This may be attributed to the fact that the saw dust used served as a source of strengthening in the beam specimens, the results for 28-day and 90 days are shown in Fig. 4. As for substituting cement with sawdust ash, the results signified that up to 20 % of replacements, the sawdust has nearly no effect on the flexural strength. However, beyond 20 % the increase in percentage of replacement decreases the flexural strength. The maximum reduction was 5 % at 30 % of replacement, see Fig. 7. This is in accordance with results obtained by previous researchers [49, 54, 59]. Conversely, Chitra et al [50] overemphasized that 30 % sawdust increased the flexural strength by 8 %.

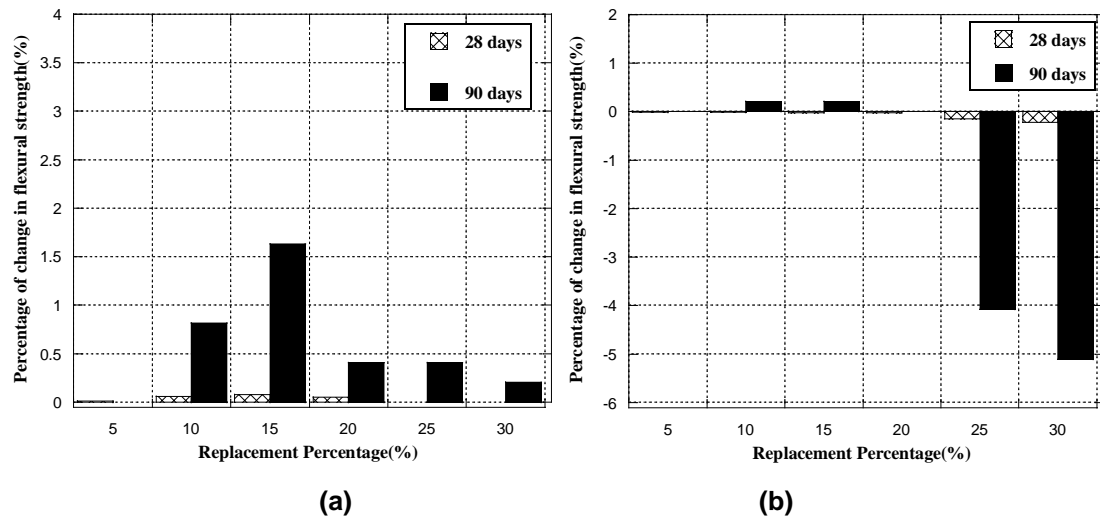


Figure 4. Flexural strength for mixes (a) sawdust replacing sand, (b) sawdust ash replacing cement.

4. Conclusions

Sawdust is a leftover material comes from cutting or sawing of wood. It is available in ample amounts, and it is suitable for use in concrete production. This will go a long way to reduce the quantity of waste in our environment. The fineness modulus, specific gravity, moisture content, uncompacted bulk density and compacted bulk density of concrete with Sawdust ash were found to be 2.2, 2.67, 3.7 %, 1435 kg/m³ and 1436 kg/m³. For a certain mix, the water requirement increases as the SDA content increases. The compressive strength, tensile strength, and flexural strength for all mix increases with age of curing. The optimum replacement level in fine aggregate with SDA is 15 %.

Depending on results of the experimental study the succeeding points were concluded:

- The replacement of sand and cement with sawdust decreases the density of the concrete.
- The replacement of sand and cement with sawdust has opposed effect on workability.
- For a constant mix proportion, the water absorption increases as the sawdust content increases.
- The compressive strength, tensile strength, and flexural strength of the concrete for different mix increases with age of curing.
- The compressive strength of the concrete with 10 % substitution of natural sand increases the compressive strength.
- On testing the flexural strength, the replacement of sand with sawdust improves the strength while the replacement of cement with sawdust ash has negligible effect.
- The optimum replacement percent with sawdust is 15 %.
- Use of sawdust ash and sawdust in concrete has positive effect on economic and environment.

From the above review, the potentials for wood waste to be used as structural concrete constituent for the development of sustainable built environment is not in disbelief. However, more works need to be done, either to approve some perceived behaviour, or cover to areas that are not yet studied as: bending behaviour, stiffness, shear behaviour, and bond characteristics. These are thus recommended for further investigations.

References

1. Suhendro, B. Toward green concrete for better sustainable environment. *Procedia Engineering*. 2014. Vol. 95. Pp. 305–320.
2. Madurwal, M.N., Relegaonkar, R.V., Mandavgane, S.A. (2013). Application of agro- waste for sustainable construction materials: A review. *Construction and Building Materials*. 2013. 38. Pp. 872–878.
3. Olanipekun, E.A. A Comparative Study of Concrete Properties Using Coconut Shell and Palm Kernel Shell as Coarse Aggregates. *Journal of Building and Environment*. 2006. 41(3). Pp. 297–301.
4. Amran, Y.H.M., Farzadnia, N., Ali, A.A.A. Properties and applications of foamed concrete; A review. *Construction and Building Materials*. 2015. No. 101. Pp. 990–1005. DOI: 10.1016/j.conbuildmat.2015.10.112
5. Steshenko, A.B., Kudyakov, A.I. Cement based foam concrete with aluminosilicate microspheres for monolithic construction. *Magazine of Civil Engineering*. 2018. 84(8). Pp. 86–96. DOI: 10.18720/MCE.84.9
6. Wu, H.-C., Sun, P. New building materials from fly ash-based lightweight inorganic polymer. *Construction and Building Materials*. 2007. 21(1). Pp. 211–217. DOI: 10.1016/j.conbuildmat.2005.06.052

7. Zhang, Z., Provis, J.L., Reid, A., Wang, H. Geopolymer foam concrete: An emerging material for sustainable construction. *Construction and Building Materials*. 2014. No. 56. Pp. 113–127. DOI: 10.1016/j.conbuildmat.2014.01.081
8. Hlaváček, P., Šmilauer, V., Škvára, F., Kopecký, L., Šulc, R. Inorganic foams made from alkali-activated fly ash: Mechanical, chemical and physical properties. *Journal of the European Ceramic Society*. 2015. 35(2). Pp. 703–709. DOI: 10.1016/j.jeurceramsoc.2014.08.024
9. Abdollahnejad, Z., Pacheco-Torgal, F., Félix, T., Tahir, W., Barroso Aguiar, J. Mix design, properties and cost analysis of fly ash-based geopolymer foam. *Construction and Building Materials*. 2015. No. 80. Pp. 18–30. DOI: 10.1016/j.conbuild-mat.2015.01.063
10. Al Bakri Abdullah, M.M., Tahir, M.F.M., Hussin, K., Binhussain, M., Sandu, I.G., Yahya, Z., Sandu, A.V. Fly ash based lightweight geopolymer concrete using foaming agent technology. *Revista de Chimie*. 2015. 66(7). Pp. 1001–1003.
11. Arellano Aguilar, R., Burciaga Díaz, O., Escalante García, J.I. Lightweight concretes of activated metakaolin-fly ash binders, with blast furnace slag aggregates. *Construction and Building Materials*. 2010. 24(7). Pp. 1166–1175. DOI: 10.1016/j.conbuild-mat.2009.12.024
12. Badanoiu, A.I., Al Saadi, T.H.A., Stoleriu, S., Voicu, G. Preparation and characterization of foamed geopolymers from waste glass and red mud. *Construction and Building Materials*. 2015. No. 84. Pp. 284–293. DOI: 10.1016/j.conbuildmat.2015.03.004
13. Pimraksa, K., Chindaprasirt, P., Rungchet, A., Sagoe-Crentsil, K., Sato, T. Lightweight geopolymer made of highly porous siliceous materials with various $\text{Na}_2\text{O}/\text{Al}_2\text{O}_3$ and $\text{SiO}_2/\text{Al}_2\text{O}_3$ ratios. *Materials Science and Engineering A*. 2011. 528(21). Pp. 6616–6623. DOI: 10.1016/j.msea.2011.04.044
14. Zharikov, I.S., Laketich, N. Impact of concrete quality works on concrete strength of monolithic constructions. *Construction Materials and Products*. 2018. Vol. 1. No. 1. Pp. 51–58.
15. Zagorodnyuk, L.Kh., Lesovik, V.S., Sumskey, D.A. Thermal insulation solutions of the reduced density. *Construction Materials and Products*. 2018. Vol. 1. No. 1. Pp. 40–50.
16. Klyuev, S.V., Klyuev, A.V., Vatin, N.I. Fine-grained concrete with combined reinforcement by different types of fibers. *MATEC Web of Conferences*. 2018. 245. 03006.
17. Klyuev, S.V., Khezhev, T.A., Pukhareno, Yu.V., Klyuev, A.V. The Fiber-Reinforced Concrete Constructions Experimental Research. *Materials Science Forum*. 2018. Vol. 931. Pp. 598–602.
18. Klyuev, S.V., Khezhev, T.A., Pukhareno, Yu.V., Klyuev, A.V. Fiber Concrete on the Basis of Composite Binder and Technogenic Raw Materials. *Materials Science Forum*. 2018. Vol. 931. Pp. 603–607.
19. Yu, R., Spiesz, P., Brouwers, H.J.H. Development of an ecofriendly Ultra-High Performance Concrete (UHPC) with efficient cement and mineral admixtures uses. *Cement and Concrete Composites*. 2015. Vol. 55. Pp. 383–394.
20. Khezhev, T.A., Zhurto, A.V., Tsipinov, A.S., Klyuev, S.V. Fire resistant fibre reinforced vermiculite concrete with volcanic application. *Magazine of Civil Engineering*. 2018. 80(4). Pp. 181–194. DOI: 10.18720/MCE.80.16
21. Khezhev, T.A., Pukhareno, Yu.V., Khezhev, Kh.A., Klyuev, S.V. Fiber Gypsum Concrete Composites with Using Volcanic Tuff Sawing Waste. *ARP Journal of Engineering and Applied Sciences*. 2018. Vol. 13. No. 8. Pp. 2935–2946.
22. Sivakumar, N., Muthukumar, S., Sivakumar, V., Gowtham, D., Muthuraj, V. Experimental studies on High Strength Concrete by Using Recycled Coarse aggregate. *Research Inventy: International Journal of Engineering and Science*. 2014. Vol. 4. No. 1. Pp. 27–36.
23. Brouwers, H.J.H., Radix, H.J. Self-Compacting Concrete: Theoretical and experimental study. *Cement and Concrete Research*. 2005. Vol. 35. Pp. 2116–2136.
24. Demirboga, R., Gul, R. Production of high strength by use of industrial by-products. *Building environment*. 2006. Vol. 41. Pp. 1124–1127.
25. Detwiler, R.J., Fapohunda, C.A., Natalie, J. Use of supplementary cementing materials to increase the resistance to chloride ion penetration of concrete cured at elevated temperatures. *ACI Materials Journals*. 1994. Vol. 91. No. 1. Pp. 63–66.
26. ZelJKovic, M. Metakaolin effects on concrete durability. MSc. Thesis, University of Toronto, Canada. 2009.
27. Fapohunda, C., Akinbile, B., Shittu, A. Structure and properties of mortar and concrete containing rice husk ash as partial replacement of ordinary Portland cement – A review. *International Journal of Sustainable Built Environment*. 2017. 6. Pp. 675–692. DOI: 10.1016/j.ijsbe.2017.07.004
28. Mcneil, K., Kang, T.H. Recycled concrete aggregates: A review. *International Journal of Concrete Structures and Materials*. 2013. Vol. 7. No. 1. Pp. 61–69. DOI: 10.1007/s40069-013-0032-5
29. Alengaram, U.J., Muhit, B.J., Jumaat, M.Z. Utilization of oil palm kernel shell lightweight aggregate in concrete – A review. *Construction and Building Materials*. 2013. Vol. 38. Pp. 161–172.
30. Fapohunda, C.A., Akinsanya, A.Y., Aderoju, S.O., Shittu, K.A. Suitability of crushed cow bone as partial replacement of fine aggregates for concrete production. *The West Indian Journal of Engineering*. 2016. Vol. 39. No. 1. Pp. 25–31.
31. Fapohunda, C.A., Shittu, K.A., Aderoju, S.O., Akinsanya, A.Y. Strength characteristics of concrete having crushed bone as partial replacement of fine aggregates at different water-cement ratios. *Acta Technica Corniviensis – Bulletin of Engineering*. 2016. Vol. 9. No. 1. Pp. 162–169.
32. Oyguc, R., Oyguc, E., Tonuk, G. Case study on seismic behavior of aseismically designed reinforced concrete frame structures. *Bulletin of Earthquake Engineering*. 2018. No. 16(7). Pp. 3057–3080.
33. Kristoffersen, M., Pettersen, J.E., Aune, V., Børvik, T. Experimental and numerical studies on the structural response of normal strength concrete slabs subjected to blast loading. *Engineering Structures*. 2018. Vol. 174. Pp. 242–255.
34. Maazoun, A., Belkassam, B., Reymen, B., Matthys, S., Vantomme, J., Lecomte, D. Blast response of RC slabs with externally bonded reinforcement: Experimental and analytical verification. *Composite Structures*. 2018. Vol. 200. Pp. 246–257.
35. Syed, Z.I., Raman, S.N., Ngo, T., Mendis, P., Pham, T. The Failure Behaviour of Reinforced Concrete Panels Under Far-field and Near-field Blast Effects. *Structures*. 2018. Vol. 14. Pp. 220–229.
36. Makita, K., Uda, Y., Yoshikado, H., Mori, K., Sato, Y., Kaneko, Y. Drop-Weight Test for RC Frame Made of Polypropylene Fiber-Reinforced Concrete. *Journal of Advanced Concrete Technology*. 2018. Vol. 16(1). Pp. 36–45.
37. Lesovik, V.S. Stroitel'nye materialy. Nastoyashchee i budushchee [Construction Materials. the Present and the Future]. *Vestnik MGSU [Proceedings of Moscow State University of Civil Engineering]*. 2017. Vol. 12. No. 1(100). Pp. 9–16.

38. Lesovik, V.S., Strokova, V.V., Krivenkova, A.N., Hodykin, E.I. Kompozicionnoe vjzhashushee s ispol'zovaniem kremnistyh porod [Composite binder using siliceous rocks]. Vestnik BG TU im. V.G. Shuhova – Bulletin of BSTU na. V.G. Shukhov. 2009. No. 1. Pp. 25–27. (rus)
39. Fediuk, R., Smoliakov, A., Stoyushko, N. Increase in composite binder activity. IOP Conference Series: Materials Science and Engineering. 2016. No. 156(1). Pp. 012042.
40. Fediuk, R.S. Mechanical Activation of Construction Binder Materials by Various Mills. IOP Conference Series: Materials Science and Engineering. 2016. No. 125(1). Pp. 012019.
41. Abrishambaf, A., Pimentel, M., Nunes, S. Influence of fibre orientation on the tensile behaviour of ultra-high performance fibre reinforced cementitious composites. Cement and Concrete Research. 2017. No. 97. Pp. 28–40.
42. Yoo, D.-Y., Banthia, N. Mechanical properties of ultra-high-performance fiber-reinforced concrete: A review. Cement and Concrete Composites. 2016. No. 73. Pp. 267–280.
43. Yoo, D.-Y., Banthia, N., Yoon, Y.-S. Predicting service deflection of ultra-high-performance fiber-reinforced concrete beams reinforced with GFRP bars. Composites Part B: Engineering. 2016. No. 99. Pp. 381–397.
44. Yang, J.-M., Shin, H.-O., Yoo, D.-Y. Benefits of using amorphous metallic fibers in concrete pavement for long-term performance. Archives of Civil and Mechanical Engineering. 2017. No. 17(4). Pp. 750–760.
45. Ranjbar, N., Behnia, A., Alsubari, B., Birgani, P.M., Jumaat, M.Z. Durability and mechanical properties of self-compacting concrete incorporating palm oil fuel ash. Journal of Cleaner Production. 2016. Vol. 112. Pp. 723–730.
46. Ranjba, R.N., Kuenzel, C. Influence of preheating of fly ash precursors to produce geopolymers. Journal of American Ceramic Society. 2017. Vol. 00. Pp. 1–10.
47. Ettu, L.O., Ibearugbulem, O.M., Anya, U.C., Nwachukwu, K.C., Awodiji, C.T.G. Strength of Blended Cement Soilcrete Containing Afikpo Rice Husk Ash and Saw Dust Ash. International Journal of Engineering Research and Development (IJERD). 2013. Vol. 7. Pp. 52–57.
48. Bdeir, L.M.H. Study Some Mechanical Properties of mortar with Sawdust as a Partially Replacement of Sand. Anbar Journal for Engineering Sciences. 2012. Vol. 5. No. 1. Pp. 22–25.
49. Mageswari, M., VidiVELLI, B. The Use of Sawdust Ash as Fine Aggregate Replacement in Concrete. Journal of Environment Research and Development. 2010. 3(3). Pp. 720–726.
50. Osei, D.Y., Jackson, E.N. Compressive Strength of Concrete Using Sawdust as Aggregate. International Journal of Scientific & Engineering Research. 2016. 7. Pp. 1349–1353.
51. Singh, G., Siddique, R. Effect of waste of saw dust as partial replacement of sand on the strength, ultrasonic pulse velocity and permeability of concrete. International Journal of Construction and Building Materials. 2016. Vol. 26. Pp. 416–422.
52. Turgut, P. (2006). Cement composites with limestone dust and different grades of wood sawdust. Building and Environment. 2006. Vol. 42. Pp. 3801–3807.
53. Bouguerra, A., Amiri, O., Ait-Mokhtar, A., Diop, M.B. Water sorptivity and pore structure of wood cementitious composites. Magazine of Concrete Research. 2002. Vol. 54(2). Pp. 103–112. DOI:10.1680/macr.54.2.103.40898
54. Awal, A.A., Mariyana, A., Hossain, M. Some Aspects of Physical and Mechanical Properties of Sawdust Concrete. International Journal of GEOMATE. 2016. 10. Pp. 1918–1923.
55. Coatanlem, P., Jauberthie, R., Rendell, F. Lightweight wood chipping concrete durability. Construction and Building Materials. 2006. Vol. 20. Pp. 776–781.
56. BooB, T.N. Performance of saw-dust in low cost sandcrete blocks. American Journal of Engineering Research (AJER). 2014. Vol. 3. No. 4. Pp. 197–206.
57. Turgut, P., Algin, H.N. Limestone Dust and Wood Sawdust as Brick Material. Building and Environment. 2007. 42. Pp. 3399–3403.
58. Paramaswam, P., Loke, Y.O. Study of Sawdust Concrete. Proceedings of International Conference on Materials of Construction for Developing Countries Bangkok. 1978. Vol. 1. Pp. 169–179.
59. Ganiron Jr, T.U. Testing Water Vapour Permeability of Sawdust and Banana Peels Ply Board as Non-Veneer Panel. International Journal of Construction Engineering and Management. 2013. Vol. 2. No. 2.
60. Osei, D.Y., Jackson, E.N. Compressive Strength of Concrete Using Sawdust as Aggregate. International Journal of Scientific & Engineering Research. 2016. 7. Pp. 1349–1353.
61. ASTM (2012a). "Standard specification for Portland cement." ASTM C150, ASTM International, West Conshohocken, PA.
62. ASTM (2019). "Standard Test Method for Sieve Analysis of Fine and Coarse Aggregates." C136 / C136M – 19, ASTM International, West Conshohocken, PA.
63. ACI Committee 211.1 (1991). Standard Practice for Selecting Proportions for Normal, Heavyweight, and Mass Concrete Standard Practice for Selecting Proportions for Normal, Heavyweight, and Mass Concrete, American Concrete Institute. Detroit, USA, 1991, 25 p.
64. ASTM (2013a). "Standard practice for making and curing concrete test specimens in the laboratory." ASTM C192, ASTM International, West Conshohocken, PA.
65. ASTM (2013). "Standard Test Method for Density, Absorption, and Voids in Hardened Concrete." ASTM C642, ASTM International, West Conshohocken, PA.
66. ASTM (2017). "Standard Test Method for Splitting Tensile Strength of Cylindrical Concrete Specimens." ASTM C496 / C496M, ASTM International, West Conshohocken, PA.
67. ASTM (2018). "Standard Test Method for Flexural Strength of Concrete (Using Simple Beam with Third-Point Loading)." ASTM C78, ASTM International, West Conshohocken, PA.

Contact:

Wegdan El-Nadoury, wegdanelnadoury@gmail.com



DOI: 10.34910/MCE.105.8

Determining the peat soil dynamic properties using geophysical methods

K. Basri^a , A. Zainorabidin^a , H.M. Mohamad^b , B. Musta^b 

^a Universiti Tun Hussein Onn Malaysia, Johor, Malaysia

^b Universiti Malaysia Sabah, Sabah, Malaysia

*E-mail: hf170042@siswa.uthm.edu.my

Keywords: peat, dynamic properties, shear wave velocity, shear modulus, elastic modulus

Abstract. The small strain dynamic properties of peat soil are a fundamental parameter related to the mechanical behaviour of a structure constructed on peat ground. These parameters are used in evaluation of the dynamic behaviour and seismic design in geotechnical structures. Determination of dynamic properties of peat soil is often done using laboratory-based tests that risk overestimation and underestimation due to sample disturbance. Since geophysical methods are proven to be able to obtain small strain dynamic properties with similar magnitude as the laboratory tests, it has become popular and is increasingly used in practice. Two geophysical methods known as multichannel analysis of surface waves (MASW) and seismic refraction were performed in this study to estimate the small strain maximum shear modulus (G_{\max}) and maximum elastic modulus (E_{\max}). The results showed the value of G_{\max} and E_{\max} were ranging from 1.01 to 6.83 MPa and from 3.88 to 10.9 MPa respectively. Correlations were also established to assist in estimating G_{\max} and E_{\max} on peat soil with bulk density. There appears to be a particularly good link between the G_{\max} , E_{\max} and bulk density. Overall, the small strain dynamic properties determined shows significant increment with depth which could be governed primarily by the effective stress. Other parameters such as water content, bulk density, organic content and degree of decomposition also could significantly influence the dynamic properties of peat soil.

1. Introduction

The foundation vibrations analysis and the investigation of geotechnical earthquake engineering problems in civil engineering require the characterization of dynamic properties using geophysical methods. Dynamic soil properties are also important on dynamic structural analysis of the superstructure as the knowledge on the dynamic response of the soil structure is critical. According to L'Heureux and Long [1], the application of dynamic soil properties includes site characterization, seismic hazard analyses, settlement analysis, site response analysis, design application and soil-structure interaction. Geophysical methods are often used in the characterization of the subsurface dynamic soil properties as these methods focused on the very low strain tests that are not large enough to induce significant non-linear and non-elastic stress strain behaviour [2]. Multichannel analysis of surface waves (MASW) and seismic refraction had been increasingly popular among other geophysical methods due to the simplicity and non-destructive nature. MASW and seismic refraction method had been used to determine the soil's compression and shear wave velocities, as well as the soil's elastic and shear moduli which are the key stiffness parameters in the prediction of the response of soil and soil-structure systems to dynamic loading. The determination of stiffness parameters for deformation analyses also is one of the most important aspects of geotechnical engineering [3]. Despite the importance of these parameters, very limited studies are reported especially for soft soil such as peat soil. Most of the studies are laboratory-based test which includes triaxial and resonant column test [4–10]. Studies using geophysical methods are limited to SASW method [11], PS

Basri, K., Zainorabidin, A., Mohamad, H.M., Musta, B. Determining the peat soil dynamic properties using geophysical methods. Magazine of Civil Engineering. 2021. 105(5). Article No. 10508. DOI: 10.34910/MCE.105.8

© Basri, K., Zainorabidin, A., Mohamad, H.M., Musta, B., 2021. Published by Peter the Great St.Petersburg Polytechnic University



This work is licensed under a CC BY-NC 4.0

logging [12], MASW method [13, 14]. However, in recent years, the application of geophysical methods on soft soil such as peat soil has grown rapidly due to the challenges in obtaining high quality samples for laboratory test.

Investigation of peat soil small strain dynamic properties presents geotechnical engineers and researchers with many challenges arising from their problematic behaviour which includes, high compressibility, high organic content, high water content and relatively low shear strength [15]. Laboratory-based method required sampling of peat soil using tube and brought to the laboratory to be tested. This method raised major doubt on the risk of sample disturbance contributed by the peat soil characteristics. The laboratory testing also associated with the inability to reproduce the actual ground conditions (i.e. stress levels), heterogeneity and anisotropy of peat soil [16]. According to Matthews et al. [3], low stiffness values measured in the laboratory were generally attributed to sample disturbance. Thus, compared to laboratory-based tests, field measurement using geophysical methods provide alternative to measure the peat soil in its natural state. According to Seed and Idris [4] and Sauvin et al. [17], field measurement mitigates the effect of sample disturbance caused by boring, tube insertion, extraction, transportation, storage, trimming and reconsolidation.

With the aim of providing helpful information to designers and engineers for practical works on the dynamic properties of peat soil ground, this paper attempted to establish data on the maximum shear modulus (G_{\max}) and maximum elastic modulus (E_{\max}) of peat soil in Klias, Beaufort, Sabah. The shear-wave velocity (V_s) and primary-wave velocity (V_p) used to estimate the G_{\max} and E_{\max} are obtained using geophysical methods.

2. Methods

2.1. Overview of Sabah's peat soil

In Malaysia there are 2.4 million hectares of peat soil which is 7.45 % of Malaysia's total land area. Approximately 116, 965 ha were located in the state of Sabah. The Klias Peninsula and Kinabatangan-Segama Valleys contributed most of the peat areas. Fig. 1 shows the geological map for the location of the study, which is located near the Klias Forrest Reserve, Beaufort. As can be seen on the geological map, the peat deposits are found mainly in lowland area where the conditions are favourable for peat formation. Historically the Klias Peninsula supported 60, 500 ha of peat swamp forest, but in 2003, only 5, 500 ha remained [18]. The Klias forest Reserve contains approximately 3,630 ha of peat swamp forest and the remaining 1, 870 ha in Binsuluk Forest Reserve [19]. The Klias Peninsula peat swamp forest is the largest remaining piece in the Northern end of Borneo Island with peat layer as thick as 14 m [18]. While at Kinabatangan Valley, peatland forest comprise of 17, 155 ha and about 5, 000 ha between Batu Puteh and Bilit [19]. Sabah peatlands are tropical peat peat mainly discovered in a thick waterlogged that made up in decaying plant materials. The peat characteristics provides challenges especially from the engineering perspective as it is made up of mostly by decaying plant materials. Tropical fibrous peat causes the highest settlement followed by hemic and sapric peat when subjected to a load over a period of time [20].

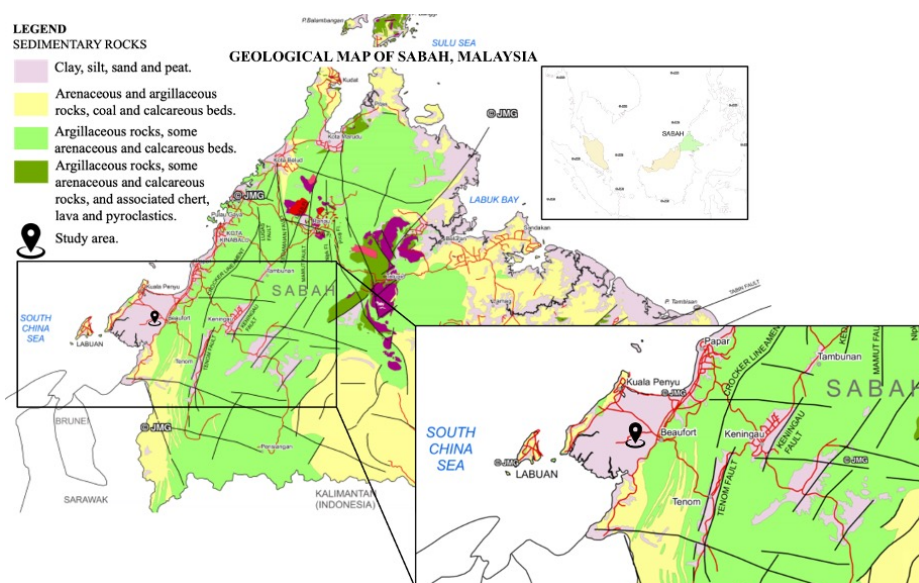


Figure 1. Geological map of the study area.

Table 1 summarizes some of the index properties for peat soil at Beaufort, Sabah. Overall, the peat type in the area are mostly hemic with Von Post classification of H6. However, some area with shallow peat (< 3 m) was categorized as fibric peat with Von Post scale H7. The classification also further supported by the fiber content value range from 61.61 to 79.4 %. As peat is classified into three groups according to their fibre content known as Sapric (< 33 %), Hemic (33–66 %) and Fibric (> 66 %) by US Department of Agriculture (USDA) classification. The water content recorded was among the highest ever recorded with almost 1000 %. The liquid limit and organic content range from 169.0 to 299.5 % and 53.97 to 95.82 % respectively. The peat soil is considered very acidic with pH value range between 4.0 and 4.9.

Table 1. Index properties of Beaufort, Sabah peat soil [21–23].

Properties	Value
Moisture content (%)	448.32 – 985.4
Liquid limit (%)	169.0 – 299.5
Organic content (%)	53.97 – 95.82
Specific gravity	1.25 – 1.44
Fibre content (%)	61.61 – 79.4
pH	4.0 – 4.9
Von post scale	H6 – H7
Peat type	Hemic – Fibric

2.2. Field survey

The study area was located in west Sabah within the Beaufort district that contain large area of peat soil. The location was as shown in Fig. 1. Three stations labelled as S1, S2 and S3 were investigated in the same area. Peat sampler investigation on all three stations revealed that the peat soil depth were 3.5 m, 5.4 m and 6.8 m for S1, S2 and S3 respectively. Thus, all the data obtained were limit to the depth of peat soil recorded as the main focused of this study is to study the peat dynamic properties. Two geophysical methods known as MASW method and seismic refraction were used to obtain the shear-wave velocity (V_s) and primary-wave velocity (V_p). The survey lines of the MASW method and seismic refraction were ensured redundant to allow comparison and correlation between both values. The in-situ V_s measurement was carried out at all stations. While, the V_p measurements were only conducted at S1 and S2. In addition, the peat soil density was collected for every 0.5 meter until peat soil layer ends using the peat sampler at all stations. The maximum shear modulus (G_{\max}) was obtained using Equation 1 from the relationship between V_s and bulk density. The relationship between V_p , V_s and ν was used to compute the maximum elastic modulus (E_{\max}) using Equation 2 and 3.

$$G_{\max} = \rho V_s^2 \quad (1)$$

where ρ is bulk density, V_s is shear-wave velocity and G_{\max} is maximum shear modulus.

$$\nu = 0.5 \left[\frac{\left(\frac{V_p}{V_s} \right)^2 - 2}{\left(\frac{V_p}{V_s} \right)^2 - 1} \right] \quad (2)$$

$$E_{\max} = 2G_{\max}(1 + \nu) \quad (3)$$

where ν is Poisson's ratio, V_p is primary-wave velocity and E_{\max} is maximum elastic modulus.

The MASW method and Seismic Refraction were conducted using ABEM Terraloc Pro II. The survey was planned for the dynamic properties determination with maximum depth (Z_{\max}) less than 10 m. Because the investigation was shallow in depth, a receiver spacing (dx) of 1 m with 24-channel acquisition system was adopted as the configuration seemed optimal to ensure the Z_{\max} (> 10 m). A 14 Hz frequency of receiver sensor was used for both methods. The source offset (X_1) was fixed at half the total spread length

to prevent interference of near-field and far-field effect. As the near-field and far-field effect results in either underestimation or overestimation of measurement [24]. Due to the characteristics of peat soil, which is very soft and high void ratio, weak seismic energy is expected. As mentioned by Said et al. [25], high attenuation in peat soil causes low signal-to-noise (S/N) ratio which lead to difficulties of data interpretation and processing. Thus, 5 stackings were used for every measurement to ensure sufficient seismic energy recorded and high S/N ratio data. Finally, the data obtained was processed using SeisImager and Plotrefa software.

3. Results and Discussion

3.1. Multichannel Analysis of Surface Waves (MASW)

The V_s profiles were determined using the MASW method. Three survey lines were investigated at three different stations marked S1, S2 and S3. The V_s profiles for all three points are shown in Fig. 2. Broadly speaking the V_s profiles can be divided into two layers. The first layer shows the decreasing value from the surface up to 2 meters. While the second layer shows significant increase with depth especially at depth greater than 3 meters. The slight drop in V_s value on the first layer was likely due to the change in decomposition rate of peat soil with depth. Based on the observation made on the peat profile obtained using the peat sampler, the peat soil shows the increasing decomposition rate with depths. As mentioned by Huat et al. [26] and Ulusay et al. [27], peats near the surface are less humified and with increasing of depth it became more humified. Lesser humified peat is more fibrous, and is likely to have greater strength than more humified peat at depth [28]. Thus, greater strength generally means higher stiffness and in turn higher V_s [4]. The slight variation of the V_s value on the first layer also could be contributed by a larger percentage error in timing over short distances or extreme variability of the material [29]. While on the second layer, the significant increase of V_s value with depth was primarily governed by the increase in effective stress. According to L'Heureux and Long [30], there was clear tendency of V_s to increase with effective stress. Comparison between all three stations shows lower V_s value especially on the top 3 meters at S3 compared to S1 and S2. As mentioned earlier, the peat soil depth at S3 was the thickest among all 3 stations which might suggest that thicker peat layer tend to result in lower V_s value near the surface (< 3 m). Overall, the V_s value determined for Klias peat soil range from 34.9 to 35.6 m/s, 34.4 to 49.0 m/s and 33.3 to 66.0 m/s for S1, S2 and S3 respectively.

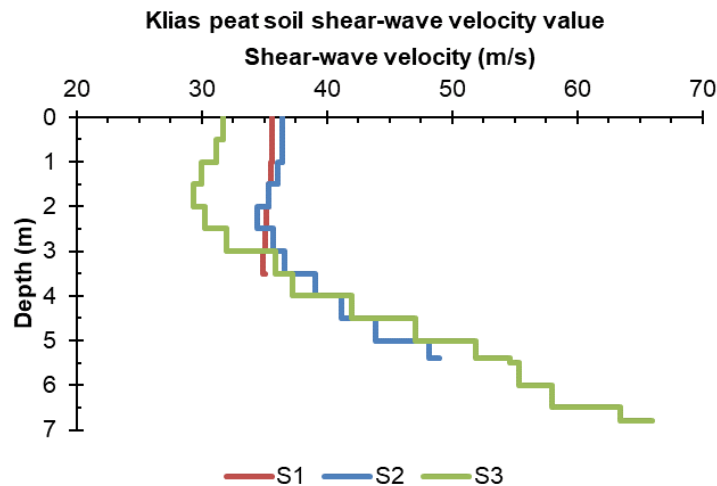


Figure 2. V_s profile of Klias peat soil.

3.2. Seismic refraction

The seismic refraction method is well suited for soil dynamics and earthquake engineering for general site investigation. This method determined the elastic wave velocities of a layered soil profile. The wave velocities and thickness of each layer are determined as long as the wave velocities increase with successively deeper layer. The V_p value was determined using seismic refraction. Two survey lines were investigated at a similar location as the MASW method with the exception of the S3. Fig. 3 shows the results obtained for the V_p value at Klias peat soil. Overall, the V_p value at both locations showed slight increases up to 3 meters depth. At the depth more than 3 meters the value increases more rapidly compared to the previous. The behavior observed was similar to the V_s profiles. The increase was primarily governed by the

increases effective stress and decreasing void ratio [30]. The V_p value for peat obtained range from 316.7 to 335.5 m/s and 357.4 to 497.4 m/s for S1 and S2 simultaneously.

3.3. Comparison between V_s and V_p values

High accuracy determination of V_s and V_p value is important to allow estimation of G_{\max} and E_{\max} value accurately. According L'Heureux et al. [16] to geophysical method profiling has the advantage of to be able to obtain interval velocity accurately. This is important as inaccurate determination of V_s and V_p value will significantly affect the estimation of G_{\max} and E_{\max} value. As mentioned by L'Heureux and long [30], approximately 30 % of G_{\max} and E_{\max} value error will be contributed by 20 % error in V_s and V_p value used. Fig. 4 shows the comparison between the V_s and V_p value of Klias peat soil. From the graph, both V_s and V_p value behave differently at the top 3 meters where the V_s value was found decreasing and increasing simultaneously with depth. While, the V_p value increase slightly with depth and become significant at depth greater than 3 m. According to Foti et al. [31], the compressibility of the pore fluid strongly influenced the propagation of V_p compared to the soil skeleton. While, the propagation of V_s is linked to mass density rather than the pore fluid as it has no shearing resistance. This explained the fluctuating of V_s on the top 3 m as the dry peat soil had a lower mass density compared to saturated peat soil. As for the V_p , the slow increment was governed by the low compressibility of peat soil pore fluid especially for the top 3 m. Approaching the transition of soft clay layer the V_p increases drastically due to the effect of the high compressibility of the pore fluid of soft clay. Generally, the significant increase for both V_s and V_p value at depth greater than 3 m was likely due to the increment of effective stress. This finding suggests that for peat soil, the influence of the effective stress to the V_s and V_p value become significant only at depth greater than 3 meters. Although there was some drift in the results obtained especially for the top 3 m, the difference was extremely small and negligible.

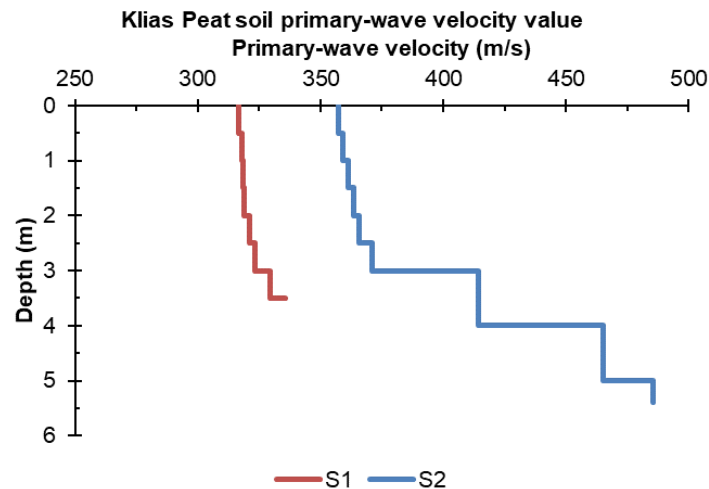


Figure 3. V_p profile of Klias peat soil.

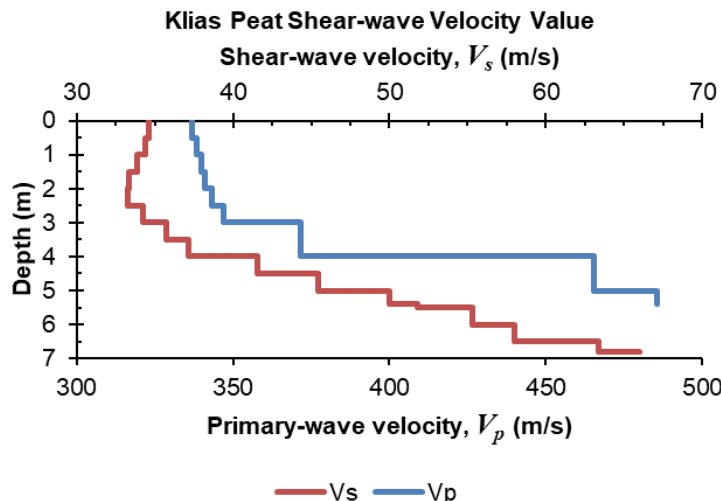


Figure 4. V_s and V_p value of Klias peat soil.

The V_s value obtained on Klias peat soil are plotted against V_p value in Fig. 5. The results show an increase in V_s with increasing V_p . The best fit is given by Eq. 4 with regression coefficient (R^2) of 0.80.

$$V_p = 12.144V_s - 85.281 \quad (4)$$

Equation 4 can also be used to assess V_s from V_p measurements by rewriting the relationship and solving for V_s as follow:

$$V_s = \frac{V_p + 85.281}{12.144} \quad (5)$$

Combining the V_s and V_p value obtained, a relationship between both values was established for estimation of V_s or V_p value when either value was not available. The relationship showed good potential with the R^2 value determined at 0.80.

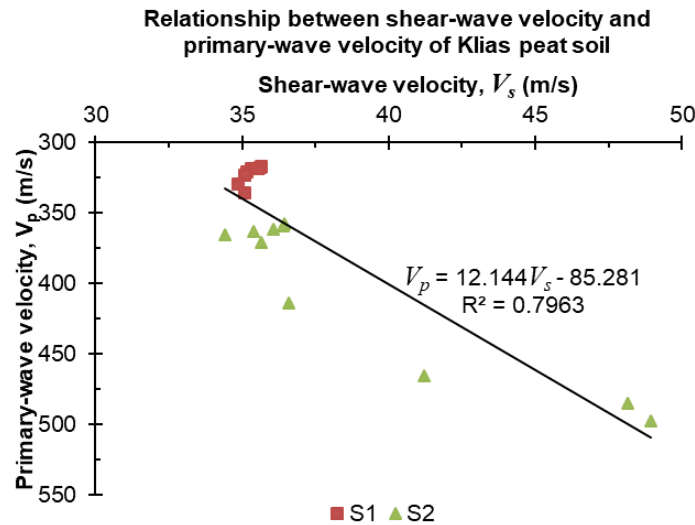


Figure 5. Relationship between V_s and V_p of Klias peat soil.

3.4. Maximum shear modulus (G_{\max}) and maximum elastic modulus (E_{\max})

The relationship between V_s and density was used to compute maximum shear modulus (G_{\max}) as shown in Equation 1. While, the relationship between V_p and V_s was used to obtain the Poisson's ratio (ν) for peat soil which was then used to compute maximum elastic modulus (E_{\max}) using Equation 2 and Equation 3 simultaneously. The density of Klias peat soil range from 1071.7 to 1466.6 kg/m³, 976.3 to 1521.9 kg/m³ and 1005.8 to 1529.4 kg/m³ for S1, S2 and S3 respectively. Fig. 6 and Fig. 7 presents the G_{\max} and E_{\max} value for Klias peat soil. Overall, the G_{\max} and E_{\max} value shows significant increase with depth especially at depth greater than 3 meter which similarly observed on V_s and V_p value. Similar conclusion was made by Abbiss [29] and Donohue et al. [31] which concluded that stiffness modulus tend to increase with depth. Minimum changes on the top 3 meters was likely due to the minimum changes in effective stress contributed by the very high-water table and low bulk density on-site. The water table measured on-site was approximately 0.8 m. According to Huat [33], there may not be a discernible increase of strength within the depth of the peat layer between 0.5 to 4 m due to low bulk density and high water table which implies low effective pressure. Thus, in this case the top 3 m of peat layer has low effective pressure which lead to lower stiffness. While, the significant increase of G_{\max} and E_{\max} value at depth greater than 3 m primarily governed by the increase in effective stress. As mentioned by Matthews et al. [34], stiffness of near-surface materials significantly increases with depth due to increases in effective stress and the degrading effects of weathering and stress relief. The increase in G_{\max} and E_{\max} value could also be attributed by the decrease in organic content. As mentioned by Kishida et al. [35], the decrease in organic content will generally cause the G_{\max} and E_{\max} value to increase. The G_{\max} obtained were ranging from 1.36 to 1.80 MPa, 1.30 to 3.65 MPa and 1.01 to 6.83 MPa for S1, S2 and S3 respectively. The value showed good agreement with previous study which obtained G_{\max} range from 1.5 to 12.3 MPa using laboratory based method [36]. While, the E_{\max} value range from 4.07 to 5.39 MPa and 3.88 to 10.9 MPa for S1 and S2.

Comparison between the in-situ dynamic properties with laboratory-based dynamic properties by previous studies found that the values were in good agreement. Matthews et al. [34] found that the dynamic properties determined using oedometer and triaxial shows good agreement with the geophysical method, and the previous assumption that the value will be differs at least one magnitude seems incorrect. Clayton and Heymann [37] compared the measurement of dynamic properties between triaxial test and geophysical method and found the value to be almost similar. Kishida et al. [38] also found that there is good agreement between the dynamic properties obtained in the laboratory using triaxial and from the field using geophysical method. Thus, the dynamic properties profile established on Klias peat soil using geophysical method could be safely used although comparison with any laboratory-based tests was still not available. The dynamic properties values obtained also was in good agreement with several studies includes Hayashi et al. [36], Zainorabidin and Said [14], Basri et al. [13], Zolkefle et al. [39] and Zainorabidin and Wijeyesekera [40]. This affirmed that the dynamic properties obtained using geophysical methods could be used to determine geotechnical parameters with relatively high accuracy.

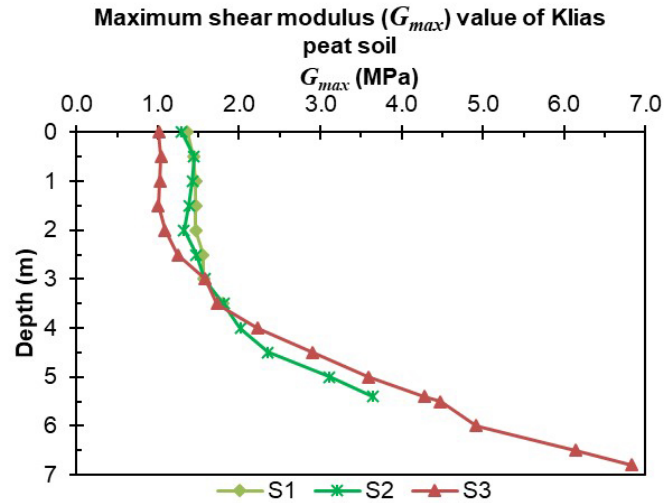


Figure 6. G_{max} value of Klias peat soil.

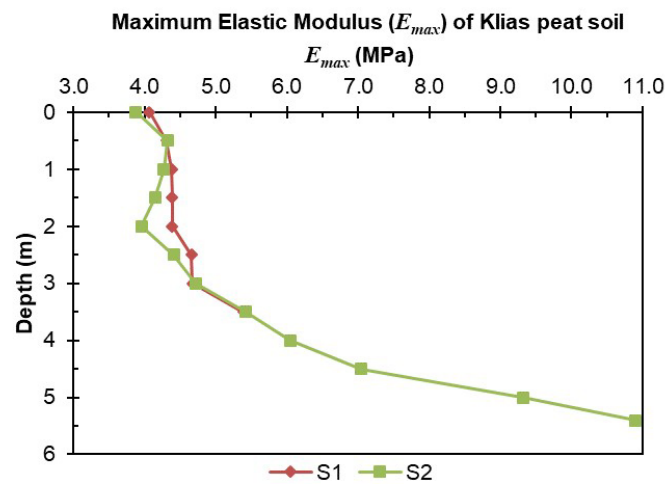


Figure 7. E_{max} value of Klias peat soil.

Fig. 8 and Fig. 9 show the relationship between the G_{max} and E_{max} value with the density value. The relationship was made to allow estimation of either density, G_{max} or E_{max} value when limited data available. Both G_{max} and E_{max} values show an increase with increasing density. The best fit is given by Equation 6 and Equation 7 with regression coefficient (R^2) of 0.83 and 0.72 respectively.

$$\rho = 241.71 \ln(G_{max}) + 1072 \quad (6)$$

$$\rho = 341.57 \ln(E_{max}) + 634.06 \quad (7)$$

Where, ρ is density, G_{max} is maximum shear modulus and E_{max} is maximum elastic modulus.

4. Conclusions

The limited existence of dynamic properties of peat soil especially for Sabah's peat soil and risk of overestimation and underestimation of those values determined using laboratory tests initiated the need of investigation using geophysical methods. Therefore, a study was conducted to determine the V_s and V_p value to be used to estimate the dynamic properties of peat soil. The application of geophysical methods known as MASW method and seismic refraction allowed the determination of these parameters in its natural state and mitigate the risk of sample disturbance. In addition to providing stratigraphic information, V_s and V_p value yield quantitative information that can be used directly for geotechnical applications. The flexible system provides consistent results for characterizing the spatial and vertical variabilities of peat soil (up to about 6.8 m thick). Although there was still very limited data obtained, the data can have an important impact on future development on peat soil ground especially in Sabah. The database obtained was expected to assist geotechnical engineers in understanding peat soil dynamic behaviour. Overall, V_s , V_p , G_{max} and E_{max} shows consistent increase with depth governed primarily by the increment of effective stress. The V_s and V_p value for Klias peat soil range from 33.3 to 66.0 m/s and from 316.7 to 497.4 respectively. The G_{max} obtained were ranging from 1.01 to 6.83 MPa and E_{max} value range from 3.88 to 10.9 MPa. Some empirical correlations between in situ V_s and V_p with the G_{max} , E_{max} and density were also developed. The relationship showed good potential with high regression coefficient value. Note that the relationship presented herein can be used either to evaluate G_{max} and E_{max} , or the way around to evaluate density. The recommendations presented also should be used in conjunction with the engineer's own experiences and engineering judgement.

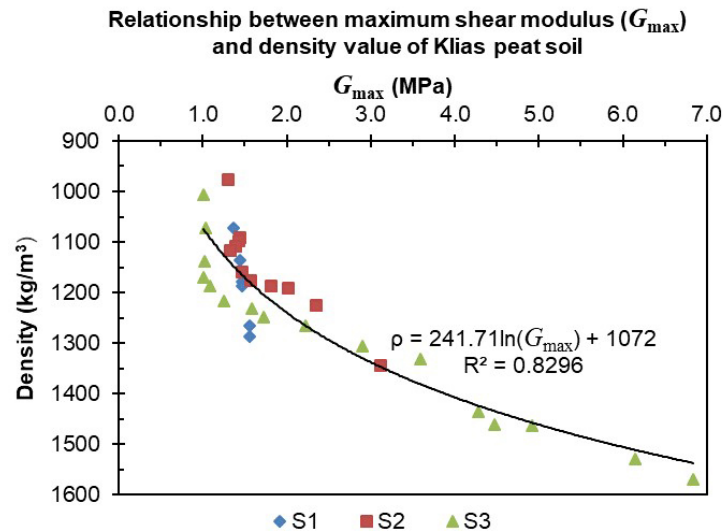


Figure 8. Relationship between G_{max} and density of Klias peat soil.

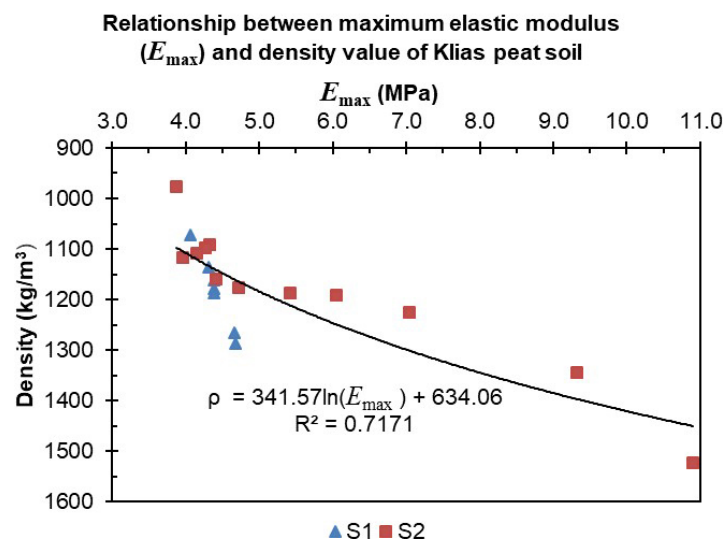


Figure 9. Relationship between E_{max} and density of Klias peat soil.

5. Acknowledgments

The authors would like to thank Universiti Tun Hussein Onn Malaysia, Faculty of Engineering UMS, and Faculty of Science and Natural Resources UMS for allowing the use of research equipment and facilities.

References

1. L'Heureux, J.-S., Long, M. Correlations between shear wave velocity and geotechnical parameters in Norwegian clays. *Proceedings of the 17th Nordic Geotechnical Meeting*. 2016. Pp. 299–308.
 2. Luna, R., Jadi, H. Determination of dynamic soil properties using geophysical methods. *First International Conference on the Application of Geophysical and NDT Methodologies to Transportation Facilities and Infrastructure*. 2000. (December). Pp. 1–15.
 3. Matthews, M.C., Hope, V.S., Clayton, C.R.I. The geotechnical value of ground stiffness determined using seismic methods. *Geological Society Engineering Geology Special Publication*. 1997. 12(1 OP-Geological Society, London, Engineering Geology Special Publications). Pp. 113–123. DOI: 10.1144/GSL.ENG.1997.012.01.10
 4. Seed, H.B. Soil moduli and damping factors for dynamic response analysis. *Journal of Terramechanics*. 1972. 8(3). Pp. 109. DOI: 10.1016/0022-4898(72)90110-3
 5. Boulanger, R.W., Arulnathan, R., Harder, L.F., Torres, R.A., Driller, M.W. Dynamic Properties of Sherman Island Peat. *Journal of Geotechnical and Geoenvironmental Engineering*. 1998. 124(1). Pp. 12–20. DOI: 10.1061/(ASCE)1090-0241(19-98)124:1(12)
 6. Wehling, T.M., Boulanger, R.W., Arulnathan, R., Harder, L.F., Driller, M.W. Nonlinear Dynamic Properties of a Fibrous Organic Soil. *Journal of Geotechnical and Geoenvironmental Engineering*. 2003. 129(10). Pp. 929–939. DOI: 10.1061/(ASCE)1090-0241(2003)129:10(929)
 7. Kramer, S.L. Dynamic response of peats. Final research report. Washington State Transportation Center, Seattle, WA (United States), 1996.
 8. Kramer, S.L. Dynamic Response of Mercer Slough Peat. *Journal of Geotechnical and Geoenvironmental Engineering*. 2000. 90(June). Pp. 504–510.
 9. Kishida, T., Wehling, T.M., Boulanger, R.W., Driller, M.W., Stokoe, K.H. Dynamic Properties of Highly Organic Soils from Montezuma Slough and Clifton Court. *Journal of Geotechnical and Geoenvironmental Engineering*. 2009. 135(4). Pp. 525–532. DOI: 10.1061/(ASCE)1090-0241(2009)135:4(525)
 10. Zolkefle, S.N.A., Zainorabidin, A., Mohamad, H.M. The Characteristics of Pontian Peat Under Dynamic Loading. *InCIEC 2014*. Springer, 2015. Pp. 487–499.
 11. Stokoe, K.H., Wright, S.G., Bay, J.A., Roesset, J.M. Characterization of geotechnical sites by SASW method. *Geophysical characterization of sites*. 1994. Pp. 15–25.
 12. Tokimatsu, K., Sekiguchi, T. Effects of dynamic properties of peat on strong ground motions during 2004 mid Niigata prefecture earthquake. In *Proc., 4th Int. Conf. on Earthquake Geotechnical Engineering*, Thessaloniki. 2007. (1531).
 13. Basri, K., Zainorabidin, A., Masirin, M.I.M., Said, M.J.M., Abdurahman, M.N. Estimation of Shear Wave Velocity Using 1-D Multichannel Analysis of Surface Waves (MASW) and Shear Modulus of Peat. *Malaysian Construction Research Journal*. 2018. 24(1). Pp. 1–10.
 14. Zainorabidin, A., Mad Said, M.J., Jazlan, M., Said, M., Madun, A. Determination of Shear Wave Velocity using Multi-channel Analysis of Surface Wave Method and Shear Modulus Estimation of Peat soil At Western Johore. *Procedia Engineering*. 2015. 125(September). Pp. 2–6. DOI: 10.1016/j.proeng.2015.11.073
 15. Zainorabidin, A., Wijeyesekera, D.C. Geotechnical Challenges with Malaysian Peat. *Proceeding Advances in Computing and Technology*. 2007. Pp. 252–261.
 16. L'Heureux, J.S., Long, M., Vanneste, M., Sauvin, G., Hansen, L., Polom, U., Lecomte, I., Dehls, J., Janbu, N. On the prediction of settlement from high-resolution shear-wave reflection seismic data: The Trondheim harbour case study, mid Norway. *Engineering Geology*. 2013. 167. Pp. 72–83. DOI: 10.1016/j.enggeo.2013.10.006
 17. Sauvin, G., Vanneste, M., Heureux, J.S.L. Impact of data acquisition parameters and processing techniques on S-wave velocity profiles from MASW – Examples from Trondheim, Norway. *Proceedings of the 17th Nordic Geotechnical Meeting*. 2016. Pp. 1297–1306.
 18. Phua, M., Conrad, O., Kamlun, K.U., Fischer, M., Böhner, J. Multitemporal fragmentation analysis of peat swamp forest in the Klias Peninsula, Sabah, Malaysia using GIS and remote sensing techniques. *Hamburger Beiträge zur Physischen Geographie und Landschaftsökologie*. 2008. Pp. 81–90.
 19. Jon, D., Usha, M., Sarala, A., Nyon, Y.C., Gabriel, C. A quick scan of Peatlands in MALAYSIA. *Wetlands International Malaysia*. 2010. 1.
 20. Duraisamy, Y., Huat, B.B.K., Aziz, A.A. Engineering properties and compressibility behavior of tropical peat soil. *American Journal of Applied Sciences*. 2007. 4(10). Pp. 768–773. DOI: 10.3844/ajassp.2007.768.773
 21. Zainorabidin, A., Mohamad, H.M. Engineering Properties of Integrated Tropical Peat Soil in Malaysia. *Electronic Journal of Geotechnical Engineering*. 2017. 22(02). Pp. 457–466.
 22. Zainorabidin, A., Mohamad, H.M. Preliminary peat surveys in ecoregion delineation of North Borneo: Engineering perspective. *Electronic Journal of Geotechnical Engineering*. 2016. 21(12). Pp. 4485–4493.
 23. Zainorabidin, A., Mohamad, H.M. A geotechnical exploration of Sabah peat soil: Engineering classifications and field surveys. *Electronic Journal of Geotechnical Engineering*. 2016. 21(20). Pp. 6671–6687.
 24. Roy, N., Jakka, R.S. Near-field effects on site characterization using MASW technique. *Soil Dynamics and Earthquake Engineering*. 2017. 97. Pp. 289–303. DOI: 10.1016/j.soildyn.2017.02.011
 25. Said, M.J.M., Zainorabidin, A., Madun, A. Data Acquisition Challenges on Peat Soil Using Seismic Refraction. *InCIEC 2014*. Vol. 42. Springer, 2015. Pp. 477–486.
 26. Huat, B.B.K., Kazemian, S., Prasad, A., Barghchi, M. State of an art review of peat: General perspective. *International Journal of the Physical Sciences*. 2011. 6(8). Pp. 1988–1996. DOI: 10.5897/IJPS11.192
 27. Ulusay, R., Tuncay, E., Hasancebi, N. Geo-engineering properties and settlement of peaty soils at an industrial site (Turkey). *Bulletin of Engineering Geology and the Environment*. 2010. 69(3). Pp. 397–410. DOI: 10.1007/s10064-010-0290-2
- Basri, K., Zainorabidin, A., Mohamad, H.M., Musta, B.

28. Macculloch, F. Guidelines for the Risk Management of Peat Slips on the Construction of Low Volume / Low Cost Roads Over Peat. The ROADX II Project. 2006. Pp. 46.
29. Abbiss, C.P. Shear wave measurements of the elasticity of the ground. *Geotechnique*. 1981. 31(1). Pp. 91–104. DOI: 10.1680/geot.1981.31.1.91
30. L'Heureux, J.S., Long, M. Relationship between shear-wave velocity and geotechnical parameters for Norwegian clays. *Journal of Geotechnical and Geoenvironmental Engineering*. 2017. 143(6). Pp. 4017013. DOI: 10.1061/(ASCE)GT.1943-5606.00-01645
31. Foti, S., Lai, C.G., Rix, G.J., Strobbia, C. Surface wave methods for near-surface site characterization. CRC press, 2014.
32. Donohue, S., Long, M., O'Connor, P., Gavin, K. Use of multichannel analysis of surface waves in determining G_{max} for soft clay. *Proceedings 2nd. Int. Conf on Geotechnical Site Characterisation, ISC*. 2004. 2. Pp. 459–466.
33. Kim Huat, B. Deformation and Shear Strength Characteristics of Some Tropical Peat and Organic Soils. *Pertanika Journal of Science & Technology*. 2006. 14(1 & 2). Pp. 61–74.
34. Matthews, M.C., Clayton, C.R.I., Own, Y. The use of field geophysical techniques to determine geotechnical stiffness parameters. *Proceedings of the Institution of Civil Engineers: Geotechnical Engineering*. 2000. 143(1). Pp. 31–42. DOI: 10.1680/geng.2000.143.1.31
35. Kishida, T., Boulanger, R.W., Zehling, T.M., Driller, M.W. Variation of Small Strain Stiffness for Peat and Organic Soil. 8th U.S. National Conference on Earthquake Engineering. 2006. (1057). Pp. 1057–1067.
36. Hayashi, H., Yamanashi, T., Hashimoto, H., Yamaki, M. Shear Modulus and Damping Ratio for Normally Consolidated Peat and Organic Clay in Hokkaido Area. *Geotechnical and Geological Engineering*. 2018. 36(5). Pp. 3159–3171. DOI: 10.1007/s10706-018-0527-6
37. Clayton, C.R.I., Heymann, G. Stiffness of geomaterials at very small strains. *Géotechnique*. 2001. 51(3). Pp. 245–255.
38. Kishida, T., Boulanger, R.W., Abrahamson, N.A., Wehling, T.M., Driller, M.W. Regression Models for Dynamic Properties of Highly Organic Soils. *Journal of Geotechnical and Geoenvironmental Engineering*. 2009. 135(4). Pp. 533–543. DOI: 10.1061/(ASCE)1090-0241(2009)135:4(533)
39. Zolkefle, S.N.A., Zainorabidin, A., Mohamad, H.M. The Characteristics of Pontian Peat Under Dynamic Loading. *InCIEC 2014*. Springer Singapore. Singapore, 2015. Pp. 487–499.
40. Zainorabidin, A., Wijeyesekera, D.C. Shear Modulus and Damping Properties of Peat Soils. *Advances on Computing and Technology 2009*. 2009. Pp. 61–67.

Contacts:

Kasbi Basri, hf170042@siswa.uthm.edu.my

Adnan Zainorabidin, adnanz@uthm.edu.my

Habib Musa Mohamad, habibmusa@ums.edu.my

Baba Musta, babamus@ums.edu.my



DOI: 10.34910/MCE.105.9

Stress condition of brick barrel vaults in view of anisotropic properties

A-Kh.B. Kaldar-ool^a, V.N. Glukhikh^b, E.K. Opbul^b, S.S. Saaya^a

^a *Tuvan State University, Kyzyl, Republic of Tuva, Russia*

^b *St. Petersburg State University of Architecture and Civil Engineering, St. Petersburg, Russia*

*E-mail: oorzhaka-h@mail.ru

Keywords: barrel vaults, brickwork, elasticity modulus, elasticity constants, elasticity parameters, orthotropic-anisotropic material, cylindrical anisotropy

Abstract. The subject of our studies are brickwork barrel vaults used in historic buildings and structures. To keep flat-arched vaults in good working order, it is required to perform appropriate theoretical research aimed at studying their stress condition. It is necessary to find elastic constants in a new coordinate system in complex curved objects consisting of bricks and mortared joints. To determine elastic constants, we used brickwork strength characteristics obtained from experiments on the basis of known formulas, studied the elastic modulus of bricks and mortar, found the elastic modulus of brickwork with the help of rheology method and used the elasticity parameters interconnecting elastic constants of cylindrical anisotropic bodies in the principal anisotropy directions in new coordinate systems. When assessing the load-bearing capacity of flat-arched vaults, it is possible to determine primary stress values using elastic constants in new coordinate systems with the help of the finite elements method using computer software.

1. Introduction

A brickwork barrel vault [1] is considered as an orthotropic anisotropic body with a cylindrical anisotropy [2] to whom the laws of mechanics of anisotropic bodies may be applied.

The studies [3–12] are the best known ones as regards the methods of analyzing arches and vaults of various shapes. Works [13–25] are experimental studies exploring the strength of brickwork vault structures.

At present, physical and mechanical properties of brickwork are determined in compliance with the requirements of State standards and regulations, in particular, Russian Set of Rules SP 15.13330.2012 [26]. They are examined as those of an elastoplastic material.

Being an anisotropic material, brickwork has different compression, tensile, bending and shear strength values depending on the load direction. In this regard, studies of brickwork barrel vaults with the goal of determining their stress conditions in view of anisotropic properties that allow to assess the carrying capacity of a structure are highly topical.

To reach the set goal, we shall use a numerical method based on the Abaqus 6.14 software package [27]. Whereupon elastic constants of the brickwork entered into the initial data field for calculation were determined using an analytical approach with regard for elasticity parameters in a new system of coordinates.

We have set ourselves the following goal:

1. Experimental determination of the brick and mortar types.
2. Known methods of determining the elasticity modulus of the bricks and the mortar.

Kaldar-ool, A-Kh.B., Glukhikh, V.N., Opbul, E.K., Saaya, S.S. Stress Condition of Brick barrel Vaults in View of Anisotropic Properties. Magazine of Civil Engineering. 2021. 105(5). Article No. 10509. DOI: 10.34910/MCE.105.9

© Kaldar-ool, A-Kh.B., Glukhikh, V.N., Opbul, E.K., Saaya, S.S., 2021. Published by Peter the Great St.Petersburg Polytechnic University



This work is licensed under a CC BY-NC 4.0

3. Brickwork elasticity modulus and anisotropic index depending of the principal anisotropy direction.
4. Determining the brickwork elasticity constants depending on the elasticity parameters needed to carry out a numerical calculation.
5. Numerical calculation.

The following are theoretical studies of a brick barrel vault in an existing building based on actual geometrical and strength characteristics. The studies have been carried out experimentally.

2. Methods

To implement the proposed numerical calculation method, apart from the brick and mortar types, we need to determine their elasticity moduli. According to V.N. Glukhikh, the directions (tangential, radial) of the elastic moduli of the brickwork in the main axes of anisotropy are established.

The brickwork strength was determined ultrasonically using the UK-14P instrument [1].

1. Brick strength limit (surface base equal to 100 mm):

$$R_1 = 7.5201 + 0.008 \nu_1 \text{ MPa.} \quad (1)$$

Brickwork mortar strength limit (base equal to 40 mm):

$$R_2 = 7.3975 - 0.0068 \nu_2 \text{ MPa.} \quad (2)$$

Brick elasticity modulus is determined according to [28]:

$$E_0^{brick} = 200 \div 1200 \cdot R_{brick}, \quad (3)$$

where R_{brick} is the brick compression strength limit.

Mortar elasticity modulus is determined according to [29]:

$$E_0^{mortar} = \frac{t_{mortar}}{\lambda_{mortar}}, \quad (4)$$

where t_{mortar} is the thickness of a mortar joint.

λ_{mortar} is compression compliance of a manually laid horizontal mortar joint under short-term loads determined according to the formula:

$$\lambda_{mortar} = 1.5 \cdot 10^{-3} \cdot R_{mortar}^{-\frac{2}{3}} \cdot t_{mortar},$$

R_{mortar} is the mortar strength limit.

We used a phenomenological rheology method in order to find the brickwork elasticity modulus on the main anisotropy axes for a brickwork being under a complex stress [30].

According to [30], one can obtain a realistic picture of the material's behaviour under load by using more complex schemes including both elastic and viscous elements. If we take an elastic material (brick) and a viscous one (mortar) and join them in parallel in the vault head (see Fig. 1, a) and in series near the vault abutments (see Fig. 1, b), we shall obtain rheological models of a Kelvin body and a Maxwell body, respectively [31].

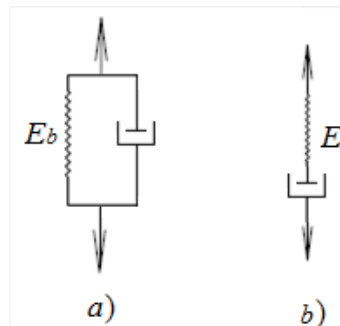


Figure 1. Rheological models.

a – Kelvin body (the elements are joined in parallel);
b – Maxwell body (the elements are joined in series).

When the elements are joined in parallel: $M_{brick} = 102$; $R_{1, medium} = 10.03$.

$$E_r = E_0^{brick} + E_0^{mortar} . \quad (6)$$

When the elements are joined in series:

$$E_t = \frac{E_0^{brick} \cdot E_0^{mortar}}{E_0^{brick} + E_0^{mortar}} , \quad (5)$$

Thus, we have obtained elasticity constants E_r, E_t on the main anisotropy directions.

Theoretical studies V.N. Glukhikh have determined that orthotropic cylindrically anisotropic materials differ in elasticity parameters (B_1, B_2) and can be divided into 2 groups:

- for the first group, the elasticity parameter is characterized by three extremes when axes turn from the radial direction to the tangential one, i.e. from 0° to 90° :

$$B_{(1)} = 3 - k^2 ; \quad (7)$$

- the second group has two extremes:

$$B_{(2)} = \frac{1 + 5k^2}{3} , \quad (8)$$

anisotropic index:

$$k^2 = \frac{E_t}{E_r} . \quad (9)$$

Both parameters are used as multipliers in a fourth-order differential equation in partial derivatives for an orthotropic coordinates; they only depend on relationships between elasticity moduli between the main anisotropy directions.

The graphic illustration of the relationship between elasticity parameters is shown in Fig. 2.

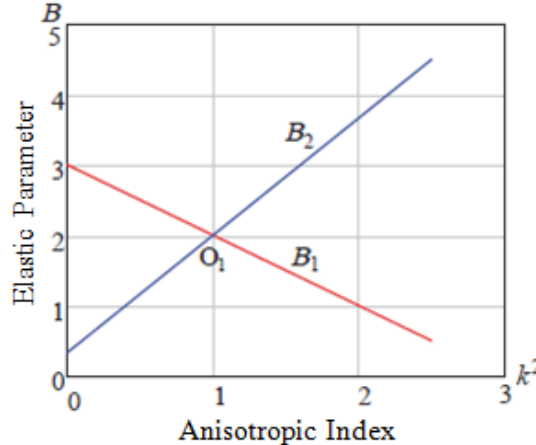


Figure 2. Relationships between an orthotropic body elasticity parameters.

The dependences shown above (see formulas 7 and 8) were deduced mathematically; they interconnect the tension modulus, the shear modulus and the Poisson ratios. This allows to improve the accuracy of determining elasticity constants for anisotropic bodies and to reduce the scope of experimental investigations in accordance with the existing known standards.

In case difficulties arise in determining viscosity constants of, e.g., bricks, mortar joints or brickwork, the result of the calculations may be assessed using the graph shown in Fig. 1 where point O_1 characterizes the isotropic properties of a materials. Both inclined straight lines describe the elasticity properties of anisotropic materials belonging to two groups.

Elasticity constants in a new system of coordinates in view of the first elasticity parameter B_1 (see formulas 7 and 8) of anisotropic bodies will be simplified:

$$\frac{1}{E_x} = \frac{\cos^4 \theta}{E_r} + \frac{\sin^4 \theta}{E_t} + \frac{3 - k^2}{E_t} \cdot \cos^2 \theta \sin^2 \theta ; \quad (10)$$

$$\frac{1}{G_{x'y'}} = \frac{8(k^2 - 1)}{E_t} \cdot \sin^2 \theta \cdot \cos^2 \theta + \frac{1}{G_{rt}}; \quad (11)$$

$$\mu_{x'y'} = -E_{x'} \left[\frac{2(k^2 - 1)}{E_t} \cdot \sin^2 \theta \cdot \cos^2 \theta + \frac{\mu_{rt}}{E_t} \right], \quad (12)$$

where $G_{rt} = \frac{E_t}{3 - k^2 + 2 \cdot \mu_{rt}}$ is the shear modulus.

Elasticity constants in a new system of coordinates in view of the second elasticity parameter B_2 :

$$\frac{1}{E_{x'}} = \frac{\cos^4 \theta}{E_r} + \frac{\sin^4 \theta}{E_t} + \frac{1 + 5k^2}{3E_t} \cdot \sin^2 \theta \cos^2 \theta; \quad (13)$$

$$\frac{1}{G_{x'y'}} = \frac{8 \cdot (1 - k^2)}{3 \cdot E_t} \cdot \sin^2 \theta \cdot \cos^2 \theta + \frac{1}{G_{rt}}; \quad (14)$$

$$\mu_{x'y'} = -E_{x'} \left[\frac{2 \cdot (1 - k^2)}{3 \cdot E_r} \cdot \sin^2 \theta \cdot \cos^2 \theta - \frac{\mu_{rt}}{E_t} \right], \quad (15)$$

where $G_{rt} = \frac{3 \cdot E_t}{1 + 5 \cdot k^2 + 6 \cdot \mu_{rt}}$ is the shear modulus.

Using Abaqus 6.14 software package [27], we have modeled a flat-arched vault having width $b = 1$ m. We have modeled backup in order to take its volume weight into account correctly. The finite element scheme of the vault and the backup is shown in Fig. 3.

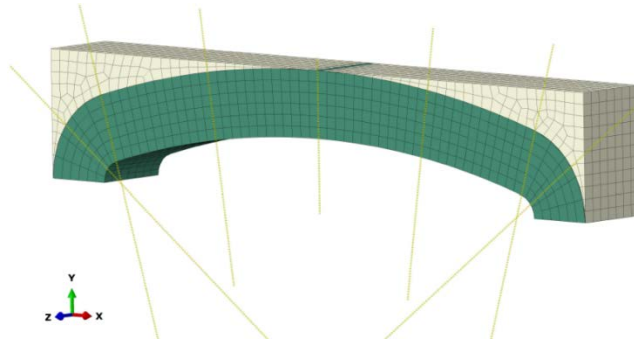


Figure 3. Finite element model.

The vault was modeled as four rigidly connected parts: two parts forming the flat part of the vault and two abutments being small-radius curves. The vault anisotropy scheme was adopted as a cylindrical orthotropic one. The material orientation for the flat and the abutment parts of the vault is shown in Fig. 4.

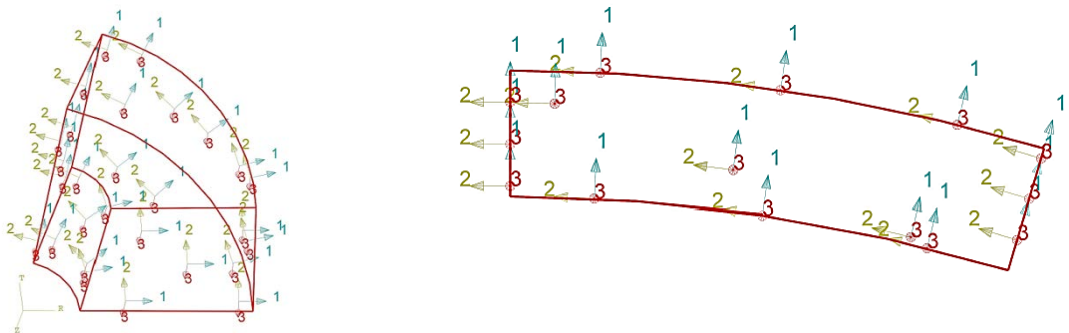


Figure 4. Material orientation for the vault abutment and flat part.

The loads are presented in Fig. 5. Own weight is entered in Abaqus 6.14 by setting gravity on the basis of the brickwork material density. In order to take the reliability coefficient 1.1, the gravity load was increased by this coefficient. The temporary load and the floor load were applied to the horizontal surface

of the backup. Concentrated forces were applied to the backup along the structure central axis at 2 and 3 m distances from the vault head.

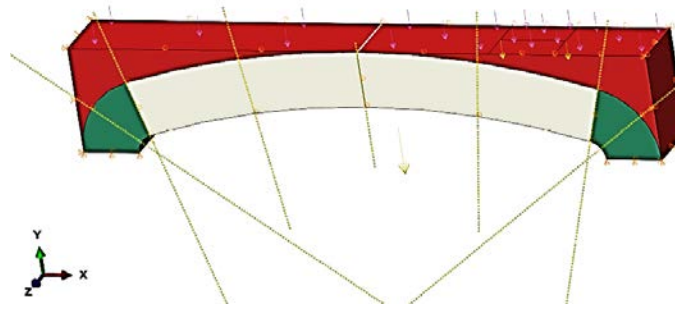


Figure 5. Loads and boundary conditions.

Boundary conditions were set on the basis of the vault design: vertical restraint under the abutments, restraint of the backup end faces along the X axis (see Fig. 5) and restraint of the free sides of the whole structure along the Z axis (in order to take interaction with sister components of the structure into account).

3. Results and Discussion

Table 1. Results of determining brick and mortar strength using the UT nondestructive testing method.

Item No.	t_1 μs	v_1 m/s	R_1 MPa	t_2 μs	v_2 m/s	R_2 MPa	R_i MPa	$p_i = \frac{R_i}{R_{\min}}$	$p_i R_i$	$S_i = R_i - R_{\text{med.}}$
1	32	3125	10	47	851	1.78	1.14	1.00	1.14	-0.053
2	31	3226	10.1	54	741	2.51	1.25	1.10	1.37	0.056
3	36	2778	9.74	51	784	2.22	1.19	1.04	1.24	-0.006
4	29	3448	10.3	48	833	1.90	1.17	1.03	1.21	-0.019
5	30	3333	10.2	53	755	2.42	1.24	1.09	1.35	0.049
6	34	2941	9.87	49	816	2.01	1.17	1.02	1.19	-0.028

$$R_{\text{med.}} = \sum p_i R_i / \sum p_i = 1.19 \text{ MPa.}$$

$$\Delta R = \sqrt{\frac{\sum p_i s_i^2}{(n-1) \sum p_i}} = 0.12 \text{ MPa.}$$

Design brickwork resistance:

$$R = R_{\text{medium}} - \Delta R = 1.07 \text{ MPa or } 10.92 \text{ kg/cm}^2;$$

at average value:

$$1. \text{ brick grade } M_{\text{brick}} = 102; R_{1, \text{medium}} = 10.03 \text{ MPa};$$

$$\text{mortar grade } M_{\text{mortar}} = 22; R_{2, \text{medium}} = 2.14 \text{ MPa.}$$

Using formulas (3, 4), we obtained the brick and mortar elasticity moduli:

$$E_0^{\text{brick}} = 1200 \cdot R_{\text{brick}} = 1200 \cdot 10.3 = 12036 \text{ MPa.}$$

$$\begin{aligned} E_0^{\text{mortar}} &= \frac{t_{\text{mortar}}}{\lambda_{\text{mortar}}} = \frac{t_{\text{mortar}}}{1.5 \cdot 10^{-3} \cdot R_{\text{mortar}}^{-\frac{2}{3}} \cdot t_{\text{mortar}}} = \\ &= 1.5 \cdot 10^3 \cdot R_{\text{mortar}}^{\frac{2}{3}} = 1.5 \cdot 10^3 \cdot 2.14^{\frac{2}{3}} = 2140 \text{ MPa.} \end{aligned}$$

Theoretical brick and mortar elasticity moduli calculated according to formulas (3, 4), e.g., at $k^2 = 0.5$ are presented in Tables 2–5.

Table 2. Theoretical brick elasticity modulus at $B_{(1)} = 3 - k^2$ ($E_0 = 12036$ MPa).

θ°	0°	15°	30°	45°	60°	75°	90°
$k^2 = 0.5$	24072	20190	14810	12036	11330	11700	12036

Table 3. Theoretical brick elasticity modulus at $B_{(2)} = \frac{1+5k^2}{3}$ ($E_0 = 12036$ MPa).

θ°	0°	15°	30°	45°	60°	75°	90°
$k^2 = 0.5$	24072	23480	21400	18050	14810	12730	12036

Brick elasticity modulus anisotropy is shown in Fig. 6.

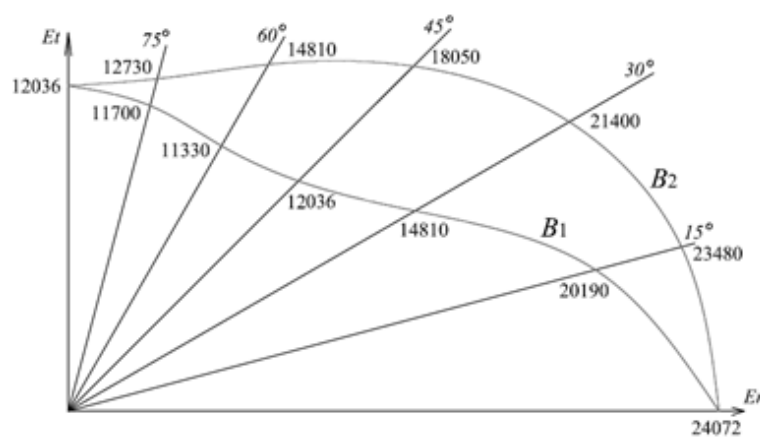


Figure 6. Brick elasticity modulus anisotropy E_x for $E_0 = 12036$ MPa.

Table 4. Theoretical mortar elasticity modulus at $B_{(1)} = 3 - k^2$ ($E_0 = 2140$ MPa).

θ°	0°	15°	30°	45°	60°	75°	90°
$k^2 = 0.5$	4280	3591	2634	2140	2014	2080	2140

Table 5. Theoretical mortar elasticity modulus at $B_{(2)} = \frac{1+5k^2}{3}$ ($E_0 = 2140$ MPa).

θ°	0°	15°	30°	45°	60°	75°	90°
$k^2 = 0.5$	4280	4174	3804	3210	2634	2263	2140

Mortar elasticity modulus anisotropy is shown in Fig. 7.

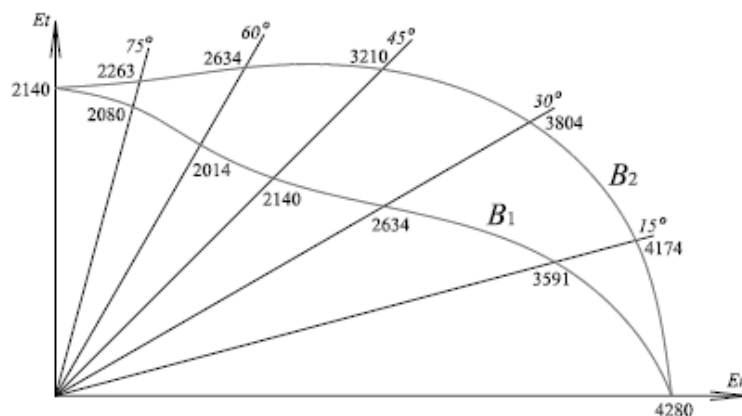


Figure 7. Mortar elasticity modulus anisotropy for $E_0 = 2140$ MPa.

3. Brickwork elasticity modulus in the tangential direction (connection in series):

$$E_t = \frac{E_0^{brick} \cdot E_0^{mortar}}{E_0^{brick} + E_0^{mortar}} = \frac{12036 \cdot 2140}{12036 + 2140} = 1816 \text{ MPa.}$$

Brickwork elasticity modulus in the radial direction (connection in parallel):

$$E_r = E_0^{brick} + E_0^{mortar} = 12036 + 2140 = 14176 \text{ MPa.}$$

Then anisotropic index $k = \sqrt{\frac{E_t}{E_r}} = 0.358$.

The anisotropic index and elasticity parameters calculated by dependencies (see formulas 7, 8) Glukhikh V.N. but with regard for brick and mortar characteristics according to [28, 29] are presented in Table 6.

Table 6. Brickwork anisotropic index and elasticity parameters.

$k^2 = \frac{E_t}{E_r}$	Elasticity Parameters	
	$B_{(1)} = 3 - k^2$	$B_{(2)} = \frac{1 + 5k^2}{3}$
0.128	2.872	0.547

The diagram of anisotropy index – elasticity parameters dependency obtained in work [30] for determining relationships between brickwork elasticity characteristics is shown in Fig. 8.

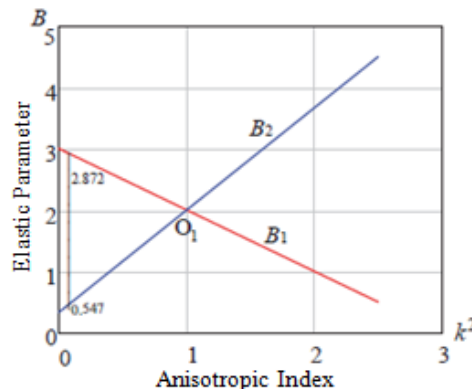


Figure 8. Anisotropy index – brickwork elasticity parameters dependences according to formulas from reference literature.

Therefore, if the barrel vault brick and mortar type are known and with regard for the known formulas (3, 4) according to [28, 29], the brickwork elasticity parameters being the subject of this study are in the field (or within the limit) between the two straight lines (Fig. 8).

The values of theoretical brickwork elasticity moduli are presented in Tables 7, 8.

Table 7. Theoretical brickwork elasticity modulus at $B_{(1)} = 3 - k^2$ ($E_0 = 12036 \text{ MPa}$).

θ°	0°	15°	30°	45°	60°	75°	90°
According to formulas (12, 13) $k^2 = 0.128$	14176	6146	2698	1816	1638	1729	1816

Table 8. Theoretical brickwork elasticity modulus at $B_{(2)} = \frac{1 + 5k^2}{3}$ (MPa).

θ°	0°	15°	30°	45°	60°	75°	90°
According to formulas (12, 13) $k^2 = 0.128$	14176	12092	7660	4337	2698	2006	1816

Brickwork elasticity modulus anisotropy in view of known formulas (10–15) according to [28, 29] is shown in Fig. 9.

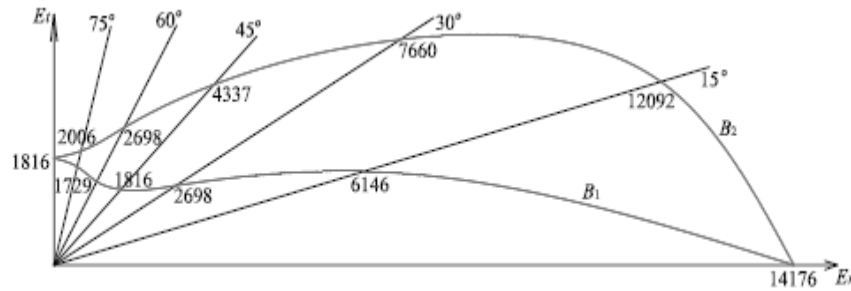


Figure 9. Brickwork elasticity modulus anisotropy (calculated by formulas (3, 4) [31, 32]).

4. Calculation of elasticity constants in a new system of coordinates in view of anisotropy properties in the first group of the elasticity parameter $B_{(1)} = 3 - k^2$, $\theta = 90^\circ$:

$$E_{x'} = \frac{E_r \cdot E_t}{E_t \cdot \cos^4 \theta + E_r \cdot (3 - k^2) \cdot \cos^2 \theta \sin^2 \theta + E_r \cdot \sin^4 \theta} = 1816 \text{ MPa};$$

$$E_{y'} = \frac{E_r \cdot E_t}{E_t \cdot \sin^4 \theta + E_r \cdot (3 - k^2) \cdot \cos^2 \theta \sin^2 \theta + E_r \cdot \cos^4 \theta} = 14176 \text{ MPa};$$

$$G_{rt} = \frac{E_t \cdot G_{rt}}{3 - k^2 + 2 \cdot \mu_{rt}} = 572.528 \text{ MPa},$$

where $\mu_{rt} = 0.15$ is Poisson ratio [32].

$$G_{x'y'} = \frac{E_t \cdot G_{rt}}{G_{rt} \cdot 8 \cdot (k^2 - 1) \cdot \sin^2 \theta \cdot \cos^2 \theta + E_t} = 572.528 \text{ MPa};$$

$$\mu_{x'y'} = -E_{x'} \left[\frac{2(k^2 - 1)}{E_r} \cdot \sin^2 \theta \cdot \cos^2 \theta + \frac{\mu_{rt}}{E_t} \right] = 0.15.$$

Calculation of elasticity constants in a new system of coordinates in view of anisotropy properties in the second group of the elasticity parameter $B_{(2)} = \frac{1 + 5k^2}{3}$, $\theta = 90^\circ$:

$$E_{x'} = \frac{3 \cdot E_r \cdot E_t}{3 \cdot E_t \cdot \cos^4 \theta + E_r \cdot (1 + 5 \cdot k^2) \cdot \cos^2 \theta \sin^2 \theta + 3 \cdot E_r \cdot \sin^4 \theta} = 1816 \text{ MPa};$$

$$E_{y'} = \frac{3 \cdot E_r \cdot E_t}{3 \cdot E_t \cdot \sin^4 \theta + E_r \cdot (1 + 5 \cdot k^2) \cdot \cos^2 \theta \sin^2 \theta + 3 \cdot E_r \cdot \cos^4 \theta} = 14176 \text{ MPa};$$

$$G_{rt} = \frac{E_t \cdot G_{rt}}{1 + 5 \cdot k^2 + 6 \cdot \mu_{rt}} = 2144.44 \text{ MPa};$$

$$G_{x'y'} = \frac{3 \cdot E_t \cdot G_{rt} \cdot 8 \cdot (1 - k^2)}{G_{rt} \cdot 8 \cdot (1 - k^2) \cdot \sin^2 \theta \cdot \cos^2 \theta + 3 \cdot E_t} = 2144.44 \text{ MPa};$$

$$\mu_{x'y'} = -E_{x'} \left[\frac{2 \cdot (1 - k^2)}{3 \cdot E_r} \cdot \sin^2 \theta \cdot \cos^2 \theta - \frac{\mu_{rt}}{E_t} \right] = 0.15.$$

The results are shown in Fig. 10–12 (Option $B_{(1)} = 3 - k^2$ and concentrated loads in $F_{1,2} = 5$ kN).

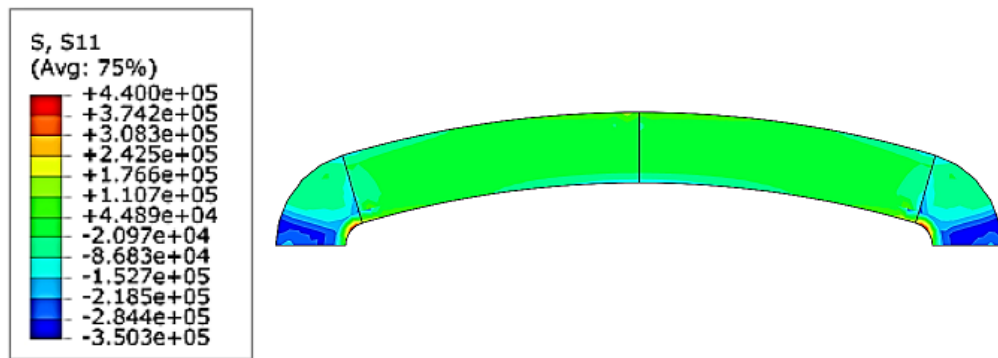


Figure 10. Stress isofields σ_r , Pa.

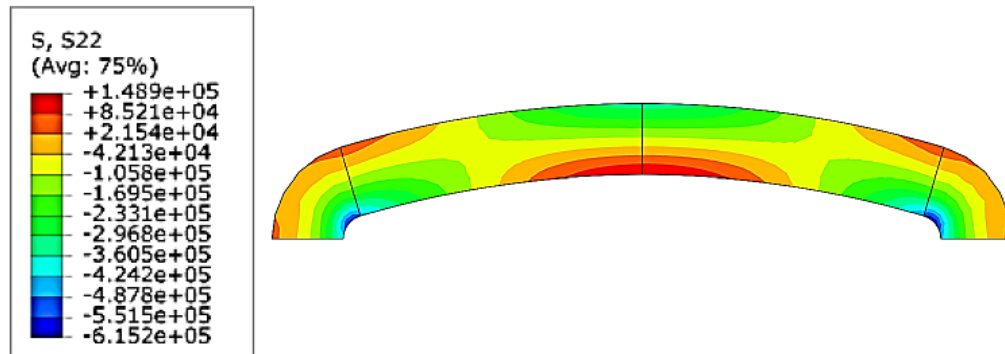


Figure 11. Stress isofields σ_θ , Pa.

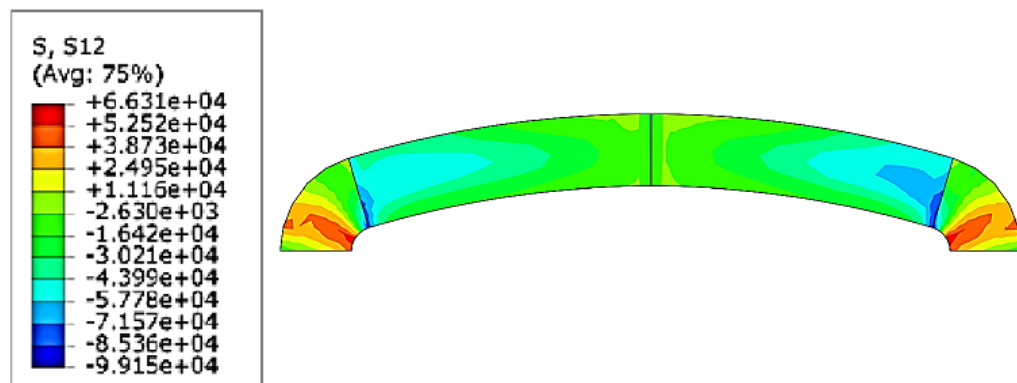


Figure 12. Stress isofields $\tau_{r\theta}$, Pa.

Graphics from the Abacus SW for $B_{(2)} = \frac{1+5k^2}{3}$, $F_{1,2} = 5$ kN (Fig. 13÷15):

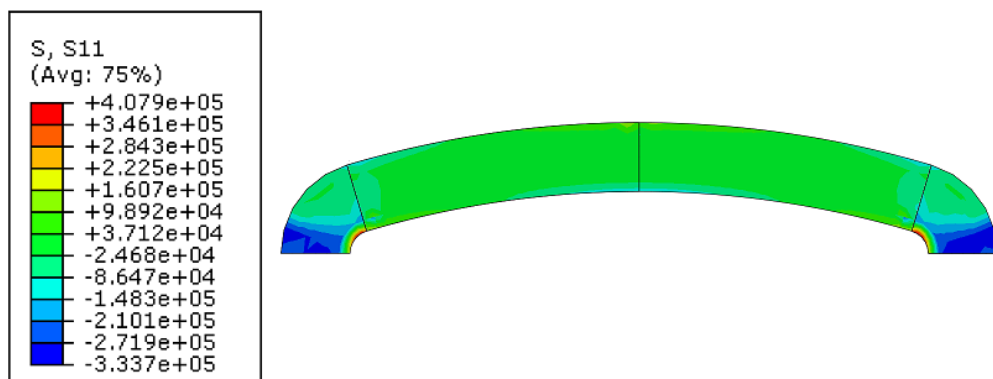


Figure 13. Stress isofields σ_r , Pa.

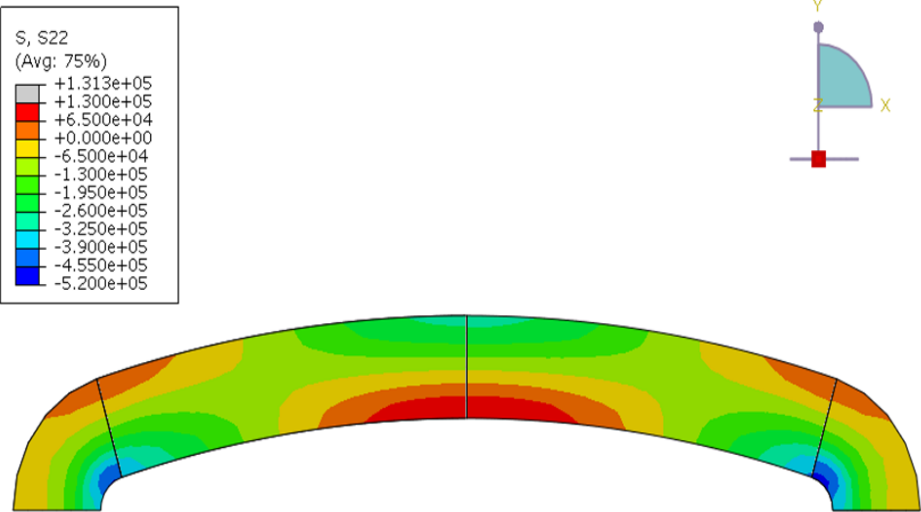


Figure 14. Stress isofields σ_θ , Pa.

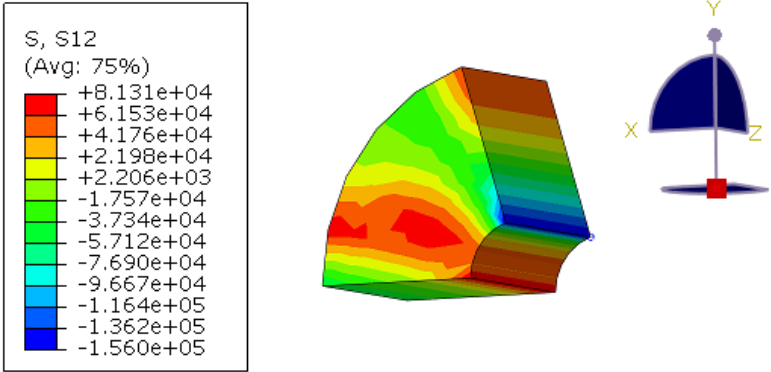


Figure 15. Stress isofields $\tau_{r\theta}$, Pa.

The resulting stress values calculated by two elasticity parameters at the vault head and near the vault abutments are presented in Tables 9–11.

Table 9. Radial stresses σ_r in the vault head ($\varphi = 0^\circ$).

On the external surface, r_d	
$B_{(1)} = 3 - k^2$	$B_{(2)} = \frac{1 + 5k^2}{3}$
σ_r , MPa	σ_r , MPa
−0.045	−0.037

Table 10. Radial stresses σ_r in the vault head ($\varphi = 0^\circ$).

On the internal surface, r_t		On the external surface, r_d	
$B_{(1)} = 3 - k^2$	$B_{(2)} = \frac{1 + 5k^2}{3}$	$B_{(1)} = 3 - k^2$	$B_{(2)} = \frac{1 + 5k^2}{3}$
σ_θ , MPa	σ_θ , MPa	σ_θ , MPa	σ_θ , MPa
0.15	0.13	−0.35	−0.3

Table 11. Tangential σ_θ and shearing $\tau_{r\theta}$ stresses at the intersection of two curves at the abutment.

On the internal surface, r_i		On the middle part, r	
$B_{(1)} = 3 - k^2$	$B_{(2)} = \frac{1 + 5k^2}{3}$	$B_{(1)} = 3 - k^2$	$B_{(2)} = \frac{1 + 5k^2}{3}$
σ_θ , MPa	σ_θ , MPa	$\tau_{r\theta}$, MPa	$\tau_{r\theta}$, MPa
-0.551	-0.475	-0.099	-0.156

Thus, we have performed a numerical analysis of a stress condition using Abaqus 6.14 software package with regard for two elasticity parameters.

Our studies confirm the hypothesis according to which it is required to take into account the properties of materials and the brickwork itself in every specific case in order to improve calculation accuracy.

A well-known work [2] presents curves describing the nature of stress distribution σ_r and σ_θ for an anisotropic circular structure for $k^2 < 1$, $k^2 > 1$, $k^2 = 1$. In the case of materials $E_\theta > E_r$, $k^2 > 1$ stresses decrease as they approach the center, and they become zero at the center. If $E_\theta < E_r$ and $k^2 < 1$, stresses will increase as they approach the center.

It is notable that the relationship between elasticity constants or the so-called anisotropic index (k^2) plays an important role in the analysis of stress strain behavior of orthotropic structures; it is impossible to find out the stress distribution pattern without knowing its numerical value.

According to various sources [28, 29], elasticity constant distribution anisotropic index in cylindrically anisotropic bodies is different. Correspondingly, stress strain behavior will be different in 3 cases under study (bricks, mortar, brickwork). Therefore, a relationship between elasticity constants found out on the basis of experimental strength data in smooth transition from the radial direction to the tangential one is the most suitable one for brickwork.

As it can be seen from the obtained results, the choice of the arch axis outline in the process of survey exercises a significant influence on the obtained arch stress state results.

4. Conclusions

1. This work recommends to take elasticity constant into account for determining the deformation modulus value. We propose a method for determining elasticity constants using elasticity parameters for a barrel vault in the form of a curvilinearly orthotropic anisotropic bar with a cylindrical anisotropy.

2. On the basis of the results of theoretical and experimental studies of well-known Russian scientists, we proposed a diagram connecting elasticity constants for a brickwork barrel vault on the principal anisotropy directions.

3. On the ground of studies performed earlier, we have refined the method of determining elasticity constants on arbitrary directions for a complex brickwork structure as an anisotropic material (bricks and mortar joints).

4. Comparative analysis of the obtained results has proved that the formulas for determining elasticity constants for cylindrically orthotropic anisotropic body can also be used for complex brickwork structures, like flat-arched vaults.

References

1. Kaldar-ool, A-Kh.B., Babanov, V.V., Allahverdiv, B.M., Saaya, S.S. Additional load on barrel vaults of architectural monuments. Magazine of Civil Engineering. 2018. 08(84). Pp. 15–28. DOI: 10.18720/MCE.84.2
2. Lekhnitskiy, S.G. Anisotropic plates. Moscow, 1957. 463 p. (rus)
3. Stefanou, I., Sab, K., Heck, J.V. Three dimensional homogenization of masonry structures with building blocks of finite strength: a closed form strength domain. International Journal of Solids and Structures. 2015. No. 54. Pp. 258–270.
4. Carini, A., Genna, F. Stability and strength of old masonry vaults under compressive longitudinal loads: Engineering analyses of a case study. Engineering Structures. 2012. No. 40. Pp. 218–229.
5. Skripchenko, I.V., Bespalov, V.V., Lukichev, S.Y., Zimin, S.S. Unconventional cases of the stone vaults. Construction of Unique Buildings and Structures. 2017. 2(53). Pp. 87–95.
6. Basilio, I., Fedele, R., Lourenco, P.B., Milani, G. Assessment of curved FRP-reinforced masonry prisms: Experiments and modelling. Construction and Building Materials. 2014. No. 51. Pp. 492–505.

7. Milani, G. Upper bound sequential linear programming mesh adaptation scheme for collapse analysis of masonry vaults. *Advances in Engineering Software*. 2015. No. 79. Pp. 91–110.
8. Milani, G., Tralli, A. A simple meso-macro model based on SQP for the non-linear analysis of masonry double curvature structures. *International Journal of Solids and Structures*. 2012. No. 49. Pp. 808–834.
9. Kamal, O.A., Hamdy, G.A., El-Salakawy, T.S. Nonlinear analysis of historic and contemporary vaulted masonry assemblages. *HBRC Journal*. 2014. 10(3). Pp. 235–246.
10. Lalin, V.V., Dmitriev, A.N., Diakov, S.F. Nonlinear deformation and stability of geometrically exact elastic arches. *Magazine of Civil Engineering*. 2019. 5(89). Pp. 39–51. DOI: 10.18720/MCE.89.4
11. Orlovich, R.B., Nowak, R., Vatin, N.I., Bespalov, V.V. Natural oscillations of a rectangular plates with two adjacent edges clamped. *Magazine of Civil Engineering*. 2018. 82(6). Pp. 95–102. DOI: 10.18720/MCE.82.9
12. Rizzi, E., Rusconia, F., Cocchetti, G. Analytical and numerical DDA analysis on the collapse mode of circular masonry arches. *Engineering Structures*. 2014. No. 60. Pp. 241–257.
13. Thavalingam, A., Bicanic, N., Robinson, J.I., Ponniah, D.A. Computational framework for discontinuous modelling of masonry arch bridges. *Composite & Structures*. 2001. No. 79. Pp. 1821–1830.
14. Pottman, H., Eigensatz, M., Vaxman, A., Wallner, J. Architectural geometry. *Computers & Graphics*. 2015. No. 47. Pp. 145–164.
15. Cancelliere, I., Imbimbo, M., Sacco, E. Experimental tests and numerical modeling of reinforced masonry arches. *Engineering Structures*. 2010. No. 32. Pp. 776–792.
16. Ramaglia, G., Lignola, G.P., Prota, A. Collapse analysis of slender masonry barrel vaults. *Engineering Structures*. 2016. Vol. 117. Pp. 86–100.
17. Castori, G., Borri, A., Corradi, M. Behavior of thin masonry arches repaired using composite materials. *Composites Part B: Engineering*. 2016. Vol. 87. Pp. 311–321.
18. De Santis, S., Tomor, A.K. Laboratory and field studies on the use of acoustic emission for masonry bridges. *NDT & E International*. 2013. No. 55. Pp. 64–74.
19. Aydin, A.C., Özkaya, S.G. The finite element analysis of collapse loads of single-spanned historic masonry arch bridges (Ordu, Sarpdere Bridge). *Engineering Failure Analysis*. 2018. Vol. 84. Pp. 131–138.
20. Felice, G. Assessment of the load carrying capacity of multi span masonry arch bridges using fibre beam elements. *Engineering Structures*. 2009. No. 31. Pp. 1634–1647.
21. Madani, K. A study of fiber deboning in circular composite arches. *Comptes Rendus Mecanique*. 2002. No. 330. Pp. 535–541.
22. Zhang, Y., Macorini L., Izzuddin B.A. Mesoscale partitioned analysis of brick-masonry arches. *Engineering Structures*. 2016. Vol. 124. Pp. 142–166.
23. Diaferio, M., Venerito, M., Vitti, M. Experimental Testing and Numerical Analysis of a Barrel Vault. *Engineering Structures*. 2018. Vol. 15. Pp. 138–151.
24. Zimin, S.S., Bespalov, V.V., Kazimirova, A.S. The computational model stone arch. System requirements: Adobe Acrobat Reader. URL: [http://donnasa.ru/publish_house/journals/vestnik/2015/vestnik_2015-3\(113\).pdf](http://donnasa.ru/publish_house/journals/vestnik/2015/vestnik_2015-3(113).pdf). (accessed: August 01, 2018). (rus)
25. Zimin, S.S., Kokotkova, O.D., Bespalov, V.V. Vault structures of historical buildings. *Construction of Unique Buildings and Structures*. 2015. 2(29). Pp. 57–72. (rus)
26. Russian Set of Rules SP 15.13330.2012. Masonry and reinforced masonry structures. The actual formulation of Construction Norms and Regulations II-22-81*. Moscow: FAU "FCS", 2012. 86 p. (rus)
27. Sidorov, V.N. The finite element method in the calculation of structures: theory, algorithm, examples of calculations in the SIMULIA Abaqus software package. Moscow, 2015. 288 p. (rus)
28. Umanskiy, A.A. Guidance book for designers of industrial, residential and public buildings. Calculation and theoretical reference book. 2nd ed., revsed. Moscow, 1972. 599 p. (rus)
29. Residential Building Design Guide. №3. The design of residential buildings (to SNiP 2.08.01-85) 2.08.01-85). Moscow, 1989. 305 p. (rus)
30. Rjanisyn, A.R. Some problems of the mechanics of systems that deform in time. M-St. Petersburg, 1949. 252 p. (rus)
31. Ugolev, B.N. Deformability and stresses in wood during drying. Moscow, 1971. 174 p. (rus)
32. Yakovlev, K.P. Brief physico-technical reference book. Moscow, 1960. 412 p. (rus)

Contacts:

Anay-Khaak Kaldar-ool, oorzhaka-h@mail.ru

Vladimir Glukhikh, tehme@spbgasu.ru


Eres Opbul, fduecnufce@mail.ru

Svetlana Saaya, sedip@list.ru



DOI: 10.34910/MCE.105.10

Assessment of wave impact on hydraulic structures of the Flood Prevention Facility Complex of St. Petersburg obtained from field observations

A.V. Kozhurova*, A.V. Shipilov 

"B.E. Vedeneev VNIIG", St. Petersburg, Russia

*E-mail: bagmut_alex@list.ru

Keywords: wave, wave height, Gulf of Finland, Monte Carlo method, field observations

Abstract. The article describes an attempt to estimate wave parameters from available data of the average and maximum wave heights impacted to hydraulic structures of the FPFC of St. Petersburg obtained from field observations. The methodology was developed to estimate wave heights of the set repeatability during storms, with application of the Monte Carlo method and method of the inverse transform of Smirnov. Convergence of the empirical and model distributions was checked by using the Kolmogorov-Smirnov criterion. Field data analysis shows some storms that took place within the observed period could be characterized by wave heights (h_1 %) exceeding the designed ones.

1. Introduction

The hydraulic structures of Flood Prevent Facility Complex of Saint-Petersburg (FPFC of St. Petersburg) are exposed to different loads and impacts, in particular from water environment: hydrostatic pressure from depth difference in Gulf of Finland and Neva Bay and hydrodynamic pressure caused by wind and ship waves.

Estimation and prediction of actual impacts on hydraulic structures, especially taking account to the problem of climate change, is an important issue, which makes it possible to obtain information needed to ensure reliable and safe operation of hydraulic structures.

According to Russian building code SP 38.13330 [1], for determining loads and impacts on hydraulic structures: for shore protection structures of I and II classes and protective structures of sloping profile of all classes, design repeatability of wave heights is taken no more than 1 % for corresponding design storm.

To investigate the patterns of occurrence, evolution and propagation of wind wave various methods and equipment are used, which make it possible to measure the basic characteristics of surface waves [2–7]. At the FPFC of St. Petersburg, information on the wave impact on the structures can be obtained from the data recorded by the Flood Threat Prevention System (FTPS). The FTPS was designed for flood forecasting and wave impact measurement is not its main function, but this system is records the following data: date and time, sea level in the Baltic system, average wave height, maximum wave height, average wave period, peak period, the period between the intersections of zero-level realizations, energy period, steepness of waves and inhomogeneity of the wave field. The specified parameters of waves are calculated from waveforms obtained by the sensor and transmitted one time per minute to the FTPS. The sensor is measures water pressure and cannot transmit the parameters of single wave or waveforms to the FTPS. It is located at a depth of about 7 meters in water area near the navigation pass S-1 as shown on Fig. 1. The FTPS also has other sensors near the navigation pass S-2 and sluices V-1 and V-5, but in this article is analyzed only data from sensor near the navigation pass S-1.

Kozhurova, A.V., Shipilov, A.V. Assessment of wave impact on hydraulic structures of the Flood Prevention Facility Complex of St. Petersburg obtained from field observations. Magazine of Civil Engineering. 2021. 105(5). Article No. 10510. DOI: 10.34910/MCE.105.10

© Kozhurova, A.V., Shipilov, A.V., 2021. Published by Peter the Great St.Petersburg Polytechnic University



This work is licensed under a CC BY-NC 4.0



Figure 1. FTPS sensor location scheme.

The relevance of investigation of storm waves is justified by many authors [8–10]. The wave conditions in the Baltic Sea were considered in [11–14]. Theoretical estimates of extreme waves and wave conditions of the Gulf of Finland are presented in [15–16]. It is also noted that the season of the most powerful wave activity of the Baltic Sea is often not interconnected with the period of the strongest winds [17].

This article represents an attempt to estimate wave parameters from available data of the average and maximum wave heights affecting the hydraulic structures of the FPFC of St. Petersburg obtained during field observations, and to determine the calculated wind wave height with repeatability 1 % during the observed storms for their further comparison with the values accepted in project. For this purpose authors fulfilled the analysis of the series of observations recorded by the FTPS gauge located at the structures of navigation pass S-1. The data used in this article were provided by State Owned Enterprise “Directorate of FPFC of the Saint Petersburg Ministry of Construction Industry, Housing and Utilities Sector of Russian Federation” from database of FTPS.

Authors could not find the articles are describing methods of statistical estimation of wave parameters during the storm from the average and maximum wave heights in open publications, and for with purpose a special methodology has been developed.

2. Methods

To determine the wave height of 1 % of repeatability ($h_{1\%}$) during the storm and to compare the actual wave impact on the hydraulic structures with the designed one, it is necessary to have statistical data of wave heights, or a known empirical function of their distribution. Wave characteristics should be recorded using available waveforms and contain a record of at least 100 waves following each other continuously [18]. FTPS sensors calculate the average value of wave heights in the interval of 1 minute, which does not allow explicitly evaluate the law of distribution of wave heights and as a consequence to evaluate their repeatability.

To solve this problem and obtain data needed to analyze the impact of wind waves, a special methodology has been developed, the scheme of which is shown on Fig. 2.

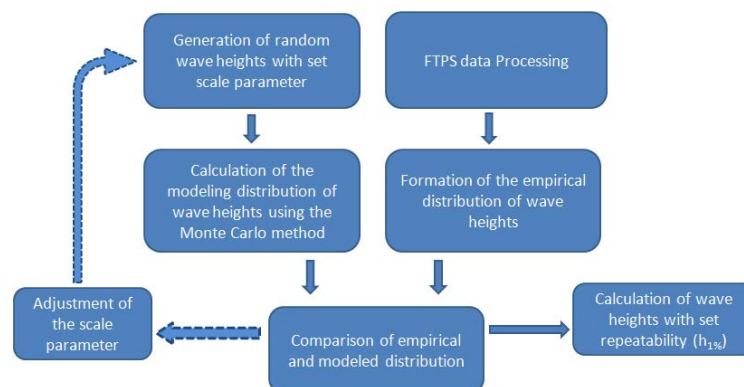


Figure 2. Methodology used to analyze the impact of wind waves.

According to the methodology, the FTPS data were processed with the next forming of the empirical distribution of the averaged wave heights observed during the selected storm.

Next, random wave heights were generated and a model distribution of their averaged values was calculated using the Monte Carlo method, with following assumptions:

- 1) During a storm, the distribution of the height of a single wave obeys the Rayleigh law;
- 2) The scale factor in the Rayleigh distribution during the storm remains unchanged.

To calculate a modeled distribution, a special algorithm has been developed that makes it possible to simulate data obtained by the gauge FTPS during a storm, taking into account the assumptions made above. During the execution of the algorithm, 20 unit waves were generated, which approximately corresponds to an interval of 1 minute for a wave period of 3 seconds, and then their averaging was performed.

The generation of random variables of a given distribution was carried out by the method of inverse transform developed by N.V. Smirnov. Assuming that the height of the wind waves obeys the Rayleigh distribution, the generation of a random variable was performed according to the formula:

$$x_i = a \cdot \sqrt{-2 \cdot \ln r_i} ,$$

where x_i is a random variable having a Rayleigh distribution, r_i is a random variable having a uniform distribution in the range from 0 to 1, a is a scale parameter in the Rayleigh distribution.

By generating and evaluating 100000 averaged quantities, a simulated distribution function was constructed which was compared with the empirical one.

The scale parameter in the Rayleigh distribution (a) was selected so that the distribution obtained by modeling was most consistent with the empirical one. Probability density functions were reduced to one scale for comparison, based on the condition of the probability density function area is equal to the one.

To generate single random wave height, a cryptographically strong pseudorandom number generator was used.

After obtaining good convergence of the empirical and model distributions, their consistent was checked by using the Kolmogorov-Smirnov criterion. For storms with empirical distribution of averaged wave heights consistent with the model one, wave heights $h_{1\%}$ were calculated and the obtained values were compared with the design ones.

During the processing of empirical data taken by the measuring system was excluded data which at least one measure has missed. Measurement errors were also not taken into account in the analysis.

3. Results and Discussion

To estimate the wave heights, the periods of storm impacts has been distinguished.

In regulatory documents, for example, RD 52.10.865-2017 [19], a storm is defined as a period of time with wave heights above a given level. In Russian State Standard GOST R 55615.3-2013 [20] it is described as a condition in the sea, under which the wind speed averaged over 10 minutes is 15 m/sec or more.

In this paper, a storm has been determined as a period of time lasting more than 100 minutes, during which the wind had an average maximum speed, exceeds 15 m/sec within 10-minute period.

According to the methodology described above the data array was processed, from November 22, 2011 to December 31, 2019. In the considered period several months were skipped: in 2016 – a total of 2 months, in 2019 – 6 months.

The time intervals of the storm impacts obtained after processing the observation series of the FTPS gauge located at the structures of navigation pass S-1 are presented in Table 1.

Table 1. Time intervals of storm impacts on the structures during 2011–2019.

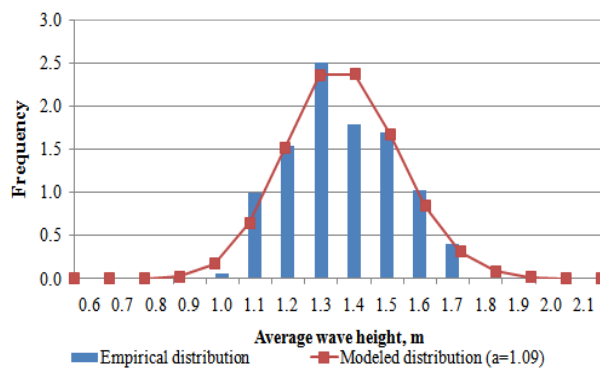
Storm's №	Beginning		End		Interval of observation, min	Wind direction*, degree	Average of maximum wind speed, m/sec
	Date	Time	Date	Time			
1	28.11.2011	00:11	28.11.2011	15:20	909	230-300	21.0
2	26.12.2011	08:29	26.12.2011	19:38	668	239-276	23.0
3	27.12.2011	06:11	27.12.2011	10:56	285	237-287	26.0
4	27.12.2011	12:47	28.12.2011	13:09	1450	259-292	25.0
5	12.05.2012	07:32	12.05.2012	10:56	204	261-270	17.0
6	17.06.2012	19:30	18.06.2012	06:53	506	197-261	16.0
7	19.06.2012	17:56	19.06.2012	19:51	114	237-257	16.0
8	20.06.2012	05:25	20.06.2012	07:36	131	260-268	19.0
9	23.08.2012	16:03	23.08.2012	20:55	289	248-286	18.0
10	06.11.2012	21:26	07.11.2012	02:51	324	253-283	18.0
11	07.11.2012	18:32	07.11.2012	23:15	282	213-292	17.0
12	12.11.2012	17:07	12.11.2012	20:10	183	226-239	17.0
13	12.11.2012	20:42	12.11.2012	23:34	172	255-270	17.0
14	17.07.2013	07:59	17.07.2013	16:29	510	241-259	17.0
15	15.08.2013	13:07	15.08.2013	20:12	425	236-250	20.0
16	15.08.2013	20:36	16.08.2013	00:00	201	258-272	20.0
17	19.10.2013	10:00	19.10.2013	12:44	160	265-283	21.0
18	19.10.2013	15:03	19.10.2013	18:31	201	268-302	17.0
19	17.11.2013	00:55	17.11.2013	08:45	465	233-297	24.0
20	17.11.2013	08:47	17.11.2013	15:24	397	260-285	24.0
21	27.11.2013	20:37	27.11.2013	22:29	100	232-257	18.0
22	28.11.2013	02:03	28.11.2013	07:03	276	259-272	19.0
23	28.11.2013	11:01	28.11.2013	17:41	387	255-286	18.0
24	12.12.2013	22:03	13.12.2013	13:46	943	217-325	26.0
25	22.12.2013	02:25	22.12.2013	04:07	102	235-238	16.0
26	08.03.2014	12:04	08.03.2014	19:50	387	222-248	18.0
27	05.04.2014	09:48	05.04.2014	15:40	347	236-245	20.0
28	05.04.2014	17:48	05.04.2014	22:10	254	246-253	21.0
29	03.12.2014	21:41	03.12.2014	23:48	127	227-234	18.0
30	03.12.2014	23:49	04.12.2014	05:12	323	234-251	18.0
31	13.12.2014	16:45	13.12.2014	19:46	181	251-265	22.0
32	13.12.2014	19:47	13.12.2014	21:47	120	247-267	22.0
33	10.04.2015	01:06	10.04.2015	04:14	188	249-267	16.0
34	10.04.2015	20:24	10.04.2015	22:09	105	242-262	18.0
35	22.04.2015	14:31	22.04.2015	16:48	122	256-265	18.0
36	04.06.2015	06:32	04.06.2015	20:35	810	236-262	18.0
37	11.06.2015	14:01	11.06.2015	16:08	127	256-259	15.0
38	22.07.2015	19:03	22.07.2015	22:43	219	259-275	17.0
39	02.08.2015	03:38	02.08.2015	05:38	113	251-262	15.0
40	06.12.2015	06:07	07.12.2015	03:15	1257	210-270	25.0
41	07.12.2015	04:17	07.12.2015	12:31	486	252-270	19.0
42	07.12.2015	12:32	07.12.2015	20:10	452	266-301	19.0
43	08.12.2015	02:45	08.12.2015	10:17	432	276-288	16.0
44	09.06.2016	06:27	09.06.2016	15:03	515	271-289	20.0
45	05.07.2016	01:35	05.07.2016	14:37	782	262-300	22.0
46	05.07.2016	14:47	06.07.2016	16:41	1494	270-288	22.0
47	02.06.2017	08:15	02.06.2017	14:20	365	279-302	18.0
48	21.06.2017	09:31	21.06.2017	16:58	427	263-292	17.0
49	27.06.2017	10:20	27.06.2017	20:10	571	257-271	17.0
50	18.10.2017	02:41	18.10.2017	04:39	118	252-256	16.0

Storm's №	Beginning		End		Interval of observation, min	Wind direction*, degree	Average of maximum wind speed, m/sec
	Date	Time	Date	Time			
51	13.12.2017	11:13	13.12.2017	13:52	139	250-267	17.0
52	07.01.2018	7:31	07.01.2018	18:45	670	269-291	18.0
53	08.01.2018	0:03	08.01.2018	4:14	249	261-272	18.0
54	08.01.2018	4:15	08.01.2018	7:30	195	270-278	18.0
55	05.06.2018	2:56	05.06.2018	10:42	466	279-318	18.0
56	19.06.2018	20:01	19.06.2018	22:42	142	236-257	21.0
57	20.06.2018	11:25	20.06.2018	19:24	373	250-259	19.0
58	29.06.2018	16:06	29.06.2018	19:11	183	223-279	17.0
59	06.08.2018	13:54	06.08.2018	16:24	149	240-269	16.0
60	21.08.2018	3:44	21.08.2018	5:38	114	273-315	22.0
61	12.09.2018	7:55	12.09.2018	19:23	607	217-245	23.0
62	13.09.2018	12:20	13.09.2018	15:24	184	250-259	19.0
63	17.09.2018	22:27	18.09.2018	2:45	258	261-293	18.0
64	26.09.2018	14:32	27.09.2018	21:42	1760	186-288	22.0
65	22.11.2018	2:12	22.11.2018	4:18	123	264-287	18.0
66	14.09.2019	11:23	14.09.2019	16:24	286	278-291	16.0
67	15.09.2019	20:13	16.09.2019	01:34	319	235-295	20.0
68	16.09.2019	07:43	16.09.2019	13:22	337	253-296	16.0
69	01.10.2019	10:17	01.10.2019	17:19	419	237-265	22.0
70	12.10.2019	14:58	12.10.2019	18:15	194	255-266	19.0
71	12.10.2019	18:50	12.10.2019	22:55	245	272-301	19.0
72	22.10.2019	20:12	23.10.2019	01:58	347	246-259	20.0
73	23.10.2019	01:59	23.10.2019	07:28	329	252-274	20.0
74	25.10.2019	22:57	26.10.2019	12:55	681	231-257	20.0
75	26.10.2019	20:35	26.10.2019	22:19	104	240-268	20.0
76	05.12.2019	18:56	06.12.2019	00:02	306	232-244	19.0
77	06.12.2019	00:03	06.12.2019	04:51	288	228-234	19.0
78	18.12.2019	23:31	19.12.2019	05:41	325	266-301	27.0
79	19.12.2019	07:14	19.12.2019	09:45	150	285-295	16.0
80	30.12.2019	16:16	30.12.2019	18:12	115	247-254	16.0

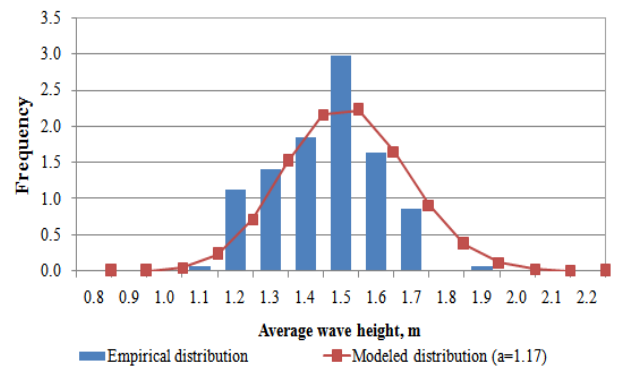
Note: the north direction of the wind is taken as zero, the positive direction of the angle coincides with the clockwise direction.

Based on the accepted conditions for determining the storm, those that were less than 100 minutes were excluded from the found intervals. Also, occurring only storms in the western direction of the wind (direction from 230-315°) were considered, since due to conditions of location of structures in other directions, the wave way length is not enough to form a significant height.

The figures below (Fig. 3) show examples of the modeled and empirical distributions using the above-mentioned methodology.



Storm № 10



Storm № 22

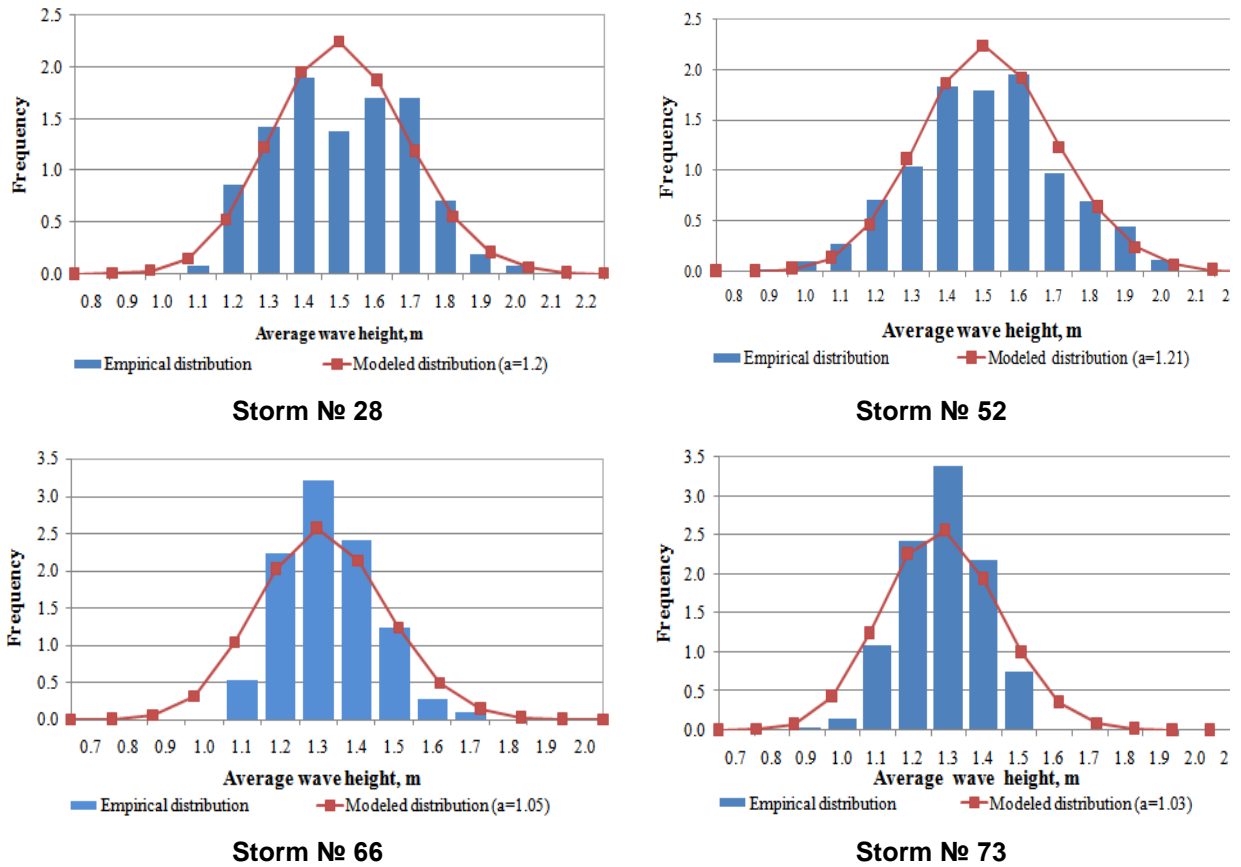


Figure 3. Examples of modeling and empirical distributions.

For the obtained intervals of the storms, the consistency of model and empirical distributions has been checked using the Kolmogorov-Smirnov criterion. Statistics of the criterion D_n was determined by the formula:

$$D_n = \sup_x |F_n(x) - F(x)|,$$

where $F_n(x)$ is the empirical probability distribution function, $F(x)$ is the modeled probability distribution function.

The critical value of the statistics D_n^* was calculated by the method described in [21].

The calculation of the wave heights of 1 % repeatability ($h_{1\%}$) was performed according to the formula:

$$h_{1\%} = a \cdot \sqrt{-2 \cdot \ln(0.01)},$$

where a is a scale parameter in the Rayleigh distribution.

The corresponding calculated wave heights of 1 % repeatability ($h_{1\%}$), the magnitude of the obtained scale parameters in the Rayleigh distribution, and the values of the measured maximum waves observed in a storm, for storms in which the empirical distribution was consistent with the modeled, are shown in Table 2.

Table 2. Parameters of storms satisfying to condition of consistency of modeled and empirical distribution.

№	Storm's №	Number of observations	Scale parameter, α	H_{max} , m	$h_{1\%}$, m	Kolmogorov-Smirnov criterion	D_n	D_n^*
1	5	204	0.79	1.9	2.4	0.65	0.046	0.105
2	9	289	0.97	2.3	2.9	0.90	0.053	0.088
3	10	324	1.09	2.6	3.3	0.70	0.039	0.084
4	11	282	1.22	3.0	3.7	1.32	0.079	0.090
5	12	183	0.95	2.2	2.9	0.84	0.061	0.108
6	13	172	1.22	2.8	3.7	1.18	0.090	0.115
7	14	510	0.79	2.0	2.4	1.30	0.058	0.067
8	16	201	0.60	1.3	1.8	1.25	0.088	0.105
9	18	201	0.74	1.8	2.2	1.03	0.071	0.104
10	19	465	0.95	2.2	2.9	0.92	0.043	0.070
11	21	100	1.12	2.4	3.4	1.46	0.138	0.142
12	22	276	1.17	2.8	3.6	0.85	0.049	0.087
13	23	387	0.92	2.1	2.8	1.47	0.074	0.075
14	25	102	0.65	1.4	2.0	0.81	0.080	0.148
15	28	254	1.20	3.0	3.6	1.05	0.065	0.093
16	29	127	0.85	2.0	2.6	1.33	0.118	0.133
17	31	181	1.52	3.6	4.6	0.55	0.041	0.112
18	32	120	1.10	2.9	3.3	1.34	0.122	0.137
19	34	105	0.68	1.7	2.1	0.38	0.037	0.146
20	35	122	0.67	1.6	2.0	0.64	0.055	0.128
21	37	127	0.73	1.7	2.2	0.67	0.059	0.133
22	38	219	0.73	1.8	2.2	1.46	0.099	0.101
23	39	113	0.84	1.9	2.5	0.95	0.087	0.137
24	40	1257	0.97	3.0	2.9	0.80	0.023	0.042
25	41	486	1.20	2.8	3.6	0.88	0.043	0.073
26	45	782	1.05	2.7	3.2	1.04	0.037	0.054
27	51	139	0.76	2.1	2.2	1.30	0.103	0.119
28	52	670	1.21	2.9	3.7	1.28	0.049	0.058
29	53	249	1.46	3.2	4.4	1.12	0.071	0.095
30	54	195	0.86	2.4	2.6	1.38	0.099	0.108
31	55	466	0.82	2.1	2.5	0.48	0.022	0.070
32	56	142	0.61	1.6	1.9	1.24	0.098	0.118
33	57	373	0.95	2.1	2.9	1.40	0.064	0.069
34	60	114	0.47	1.4	1.4	1.08	0.101	0.140
35	62	184	0.92	2.4	2.8	1.34	0.099	0.111
36	66	286	1.05	2.6	3.2	1.48	0.085	0.087
37	67	319	1.17	3.0	3.6	1.49	0.083	0.084
38	68	337	0.96	2.1	2.9	1.46	0.079	0.082
39	71	245	0.86	2.7	2.6	0.92	0.059	0.096
40	73	329	1.03	2.3	3.1	1.29	0.071	0.083
41	78	325	1.61	3.5	4.9	1.14	0.059	0.078
42	80	115	0.71	1.7	2.2	0.26	0.024	0.139

Note: H_{max} is the maximum of wave height recorded in the interval of 1 minute recorded by the FTPS gauge during the storm.

In addition, as a check, for the storms shown in Table 2, the distribution of the maximum waves recorded in the interval of 1 minute has been simulated. The obtained modal values of the distribution of the heights of the maximum waves were close to the values observed during the storm with an accuracy of 0.1 m. This also confirms the correctness of the chosen methodology.

The data presented in Table 2 shows that the calculated values of wave heights for 11 storms impacting on the structures of the FPFC of St. Petersburg during the operational period exceed the design

value of the load of 0.1 % repeatability – 3.37 m at a wind speed of up to 22 m/sec, which is less than the declared design value of 27 m/sec. Also, several storms exceeded the load value of 0.01 % repeatability at a wind speed of 22–27 m/sec. Design values are presented in Table 3.

Table 3. Parameters of extreme waves from the Gulf of Finland for the main combination of loads and impacts during normal operation of structures of navigation pass S-1.

Kronstadt Level			Parameters		
Value, m in the Baltic system	Repeatability, %	Wind speed and direction	Wave height $h_{1\%}$, m	Wave period \bar{T} , sec	Wave length $\bar{\lambda}$, m
0.00	–	15 m/sec, West	1.86	4.2	10.2
4.55	0.1	27 m/sec, West	3.37	5.9	18.5
5.15	0.01	27 m/sec, West	4.15	5.9	19.4

Since the calculated wave heights of 1 % repeatability was obtained by the indirect method, and not by direct observation of the heights of individual waves obtained from the waveforms, the above results require further investigation.

4. Conclusions

1. Authors could not find the articles are describing methods of statistical estimation of wave parameters during the storm from the average and maximum wave heights in open publications, and for with purpose a special methodology has been developed.

2. The developed methodology for estimating wave heights shows satisfactory convergence with field observations, although it requires verification with the data obtained with the use of other methods.

3. Some of the obtained wave heights of 1 % repeatability for the considered period exceed the maximum design values. The above-mentioned methodology for determining the wave heights of 1 % repeatability is indirect, based on the solution of an inverse problem, and the values obtained from it should be considered indicative, requiring further detailed study.

References

1. SP 38.13330.2012 Loads and impaction Hydraulic structures (from wave, ice and ships). (rus)
2. Stont, Zh.I., Ulyanova, M.O., Krek, E.V., Churin, D.A., Gubareva, D.E. Storm activity during autumn-winter period of 2018–2019 in the south-eastern Baltic sea. KSTU News. 2019. No. 53. Pp. 61–72.
3. Kuznetsov, K.I., Kovalev, P.D., Kurkin, A.A., Pelinovsky, E.N. Features of wind waves at the southeastern coast of Sakhalin according to bottom-pressure measurements. Izvestiya. Atmospheric and oceanic physics. 2014. Vol. 50. Pp. 213–220. DOI: 10.1134/S0001433814020066
4. Myslenkov, S.A., Arkhipkin, V.S., Pavlova, A.V., Dobrolyubov, S.A. Wave climate in the Caspian sea based on wave hindcast. Russian meteorology and hydrology. 2018. No. 10. Pp. 670–678. DOI: 10.3103/S1068373918100060
5. Kishchenko, A.A. Analysis of the Wind Wave Parameter Calculation Algorithm Using the Hydrostatic Level Gauge Data. Fundamental and applied hydrophysics. 2009. Vol. 2. No. 1. Pp. 64–70.
6. Markina, M.Y., Gavrikov, A.V. Wave climate variability in the North Atlantic in recent decades in the winter period using numerical modeling. Oceanology. 2016. Vol. 56. No. 3. Pp. 320–325. DOI: 10.1134/S0001437016080014
7. Ivonin, D.V., Telegin, V.A., Chernyshov, P.V., Kuklev, S.B., Myslenkov, S.A. Possibilities of X-band nautical radars for monitoring of wind waves near the coast. Oceanology. 2016. Vol. 56. No. 4. Pp. 591–600. DOI: 10.1134/S0001437016030103
8. Gippius, F.N., Arkhipkin, V.S. Interannual variability of storm waves in the black sea according to numerical modeling results. Moscow university bulletin. Series 5. Geography. 2017. No. 1. Pp. 38–47.
9. Kantardgi, I.G., Kuznetsov, K.I. Field measurement of waves for defining loads on marine hydraulic structures. Magazineofcivilengineering. 2014. No. 4 (48). Pp. 49–62. DOI: 10.5862/MCE.48.6
10. Garmashov, A.V. Wind wave in northwest part of the black sea in summer period. International research journal. 2018. No. 8(74). Pp. 74–86. DOI: 10.23670/IRJ.2018.74.8.014
11. Myslenkov, S., Medvedeva, A., Arkhipkin, V., Markina, M., Surkova, G., Krylov, A., Dobrolyubov, S., Zilitinkevich, S., Koltermann, P. Long-term Statistics of Storms in the Baltic, Barents and White Seas and Their Future Climate Projections. Geography, Environment, Sustainability. 2018. Vol. 11. No. 1. Pp. 93–112. DOI: 10.24057/2071-9388-2018-11-1-93-112
12. Bobykina, V.P., Stont, Z.I. Winter storm activity in 2011–2012 and its consequences for the southeastern Baltic coast. Water resources. 2015. Vol. 42. No. 3. Pp. 371–377. DOI: 10.1134/S0097807815030021
13. Medvedeva, A.Yu., Arkhipkin, V.S., Myslenkov, S.A., Zilitinkevich, S.S. Wave climate of the Baltic Sea following the results of the SWAN spectral model application. Moscow university bulletin. Series 5. Geography. 2015. No. 1. Pp. 12–22.
14. Churin, D.A., Stont, Z.I., Ulyanova, M.O. Effect of storm situations on the variability of water level in the Curonian lagoon (Baltic sea) in 2019. Materials of the VII International Baltic sea forum. Moscow. 2019. Pp. 408–415. URL: http://bmf.kltu.ru/wp-content/uploads/mat_forum/2019/tom_3_2.pdf (reference date: 13.08.2020)
15. Lopatukhin, L.I., Mironov, M.Ye., Pomeranetz, K.S., Trapeznikov, Yu.A., Tchernishova, Ye.S. Assessment of extreme wind and waving in the eastern part of the Finish gulf. Izvestiya B.E. Vedeneev VNIIG. 2005. Vol. 245. P. 145–155.

16. Kurennoy, D., Ryabchuk, T. 2011. Wind wave conditions in Neva Bay. Journal of Coastal Research, SI 64 (Proceedings of the 11th International Coastal Symposium), 1438–1442. Szczecin, Poland, ISSN 0749-0208. URL: <https://www.jstor.org/stable/26482413> (reference date: 13.08.2020)
17. Medvedeva, A.Yu., Arkhipkin, V.S., Myslenkov, S.A. Features of wind waves in the Baltic sea following the results of numerical modeling. Youth scientific conference "integrated researches of the seas of Russia: operational oceanography and forwarding researches". Sevastopol. 2016. Pp. 320–325.
18. P 74-2000.Rekomendatsii po provedeniyu naturnykh nablyudeniyy issledovaniy krepleniyy otkosov gruntovykh sooruzheniy i beregovykh sklonov. [Recommendations for producing field observations and studies of fastenings of slopes and soil structures and coastal slopes.]. VNIIG, SPb. 2000. (rus)
19. RD 52.10.865-2017 Guidance on the calculation of operational characteristics of sea wind waves. (rus)
20. Russian State Standard GOST R 55615.3-2013 Renewable power engineering. Tidal power plants. Part 3. Sea hydraulic structures. Requirements for loads and actions. (rus)
21. Bol'shev, L.N., Smirnov, N.V. Tablitsy matematicheskoy statistiki. [Tables of mathematical statistics] – M.: Nauka. Glavnaya redaktsiya fiziko-matematicheskoy literatury. 1983. – 416 p. (rus)

Contacts:

Alexandra Kozhurova, bagmut_alex@list.ru

Aleksandr Shipilov, a.shipilov@yahoo.com

© Kozhurova, A.V., Shipilov, A.V., 2021



DOI: 10.34910/MCE.105.11

Long-term properties of cement mortar under compression, tension, and 3-point bending

A. Sprince^a , R. Gailitis^a , L. Pakrastins^{*a} , T. Kozlovskis^a , N. Vatin^b 

^a Riga Technical University, Riga, Latvia

^b Peter the Great St. Petersburg Polytechnic University, St. Petersburg, Russia

*E-mail: leonids.pakrastins@rtu.lv

Keywords: long-term properties, creep, shrinkage, compression, tension, 3-point bending, digital image correlation, PVA fibre, OPC mortar

Abstract. Cement composite long-term property assessment usually is limited to the compression strain state due to the difficulty of performing long-term tests in tension and 3-point bending. This paper shows the difference in long-term properties in compression, tension, and 3-point bending for plain ordinary Portland cement mortar (OPC). The obtained results were compared to reinforced specimen results to determine whether the PVA refibres improve the long-term properties of OPC mortar in various stress-strain conditions. Cylinders, compact tension specimens (CT), and beams – plates were prepared to evaluate material properties and the role of fibre reinforcement in these different stress states. Additionally, to conventional surface-attached strain gauges, 2D-DIC was employed to observe the creep strain of specimens in tension. This paper aim to determine long-term property differences in compression, tension and 3-point bending and, also, to see if low amount PVA fibre incorporation improve long-term properties in previously stated stress-strain states. It was determined that the usage of 1 % of PVA fibres increases creep strains in compression on average by 15 % and reduced by 7 % in tension. It reduces shrinkage strain by 18 % in compression and 8 % in tension. The long-term deflection for the PVA fibre-reinforced specimens are, on average by 55 % higher than for plain OPC mortar specimens in 3-point bending.

1. Introduction

Long-term properties like creep and shrinkage is an essential phenomenon to human-made materials such as concrete. They affect the stress and deformation distribution within concrete structures [1–4]. Concrete creep, and shrinkage strain can influence the lifetime of a concrete structure. It is commonly assumed as a process that leads to increased deformations without significant damage development [3, 5].

Many factors do affect the nature of creep and shrinkage in concrete. The main factors are mixture proportions, curing age, environmental temperature, relative humidity, and applied stress level [1].

Shrinkage is the factor that influences creep strains. It has been discovered that shrinkage strains are caused by capillary pressure in the pore walls, according to capillary tension theory [6–8].

A common way to improve material mechanical properties and restrain creep and shrinkage effects is to use refibre reinforcement. Polymer fibres such as polyvinyl alcohol (PVA) and polypropylene (PP) fibres instead improve fracture toughness and resistance. They do not have significant gains to strength [6, 9–13]. It has been noted that PVA fibres, unlike the PP fibres, better increase ordinary Portland cement mortar (OPC) based material mechanical strength. It turns their brittle behaviour into more ductile. This fibre inclusion is significant to structures that could be subjected to tensile stress [14–19].

Sprince, A., Gailitis, R., Pakrastins, L., Kozlovskis, T., Vatin, N. Long-term properties of cement mortar under compression, tension, and 3-point bending. Magazine of Civil Engineering. 2021. 105(5). Article No. 10511. DOI: 10.34910/MCE.105.11

© Sprince, A., Gailitis, R., Pakrastins, L., Kozlovskis, T., Vatin, N., 2021. Published by Peter the Great St.Petersburg Polytechnic University



This work is licensed under a CC BY-NC 4.0

PVA is considered one of the most promising synthetic fibres for cement composite mechanicals. For the enhancement of cement composite mechanical properties. Some of the advantages of these fibres are ductility, resistance to corrosion, strong bonding with the cement matrix, and low cost. The main benefit of fibre addition is the increase of load-bearing tension capacity. The effect on compressive strength increase from PVA fibre addition can be only unequivocally seen when a more considerable amount of the fibres were used in the cement composite mix. There are also several reports regarding the mentioned effect and an increase of porosity in the structure and, therefore, loss of compressive strength and increase of shrinkage strains. In this case, the bending strength and tensile strength are not affected. Depending on the essential purpose and fibre dimensions, the proper amount of fibre addition is from 0.5 % to 2 % by volume. If the fibres' amount is optional, then even with the relative increase in porosity, the fibres would take care of redistributed stresses in the element [20–24]. It also has to be taken into account that many large scale fibres reduce workability. It has also been claimed that increasing the interaction surface of fibre and matrix by reducing the scale of fibre is an effective way to improve mechanical properties [25].

Long-term properties and especially creep and shrinkage, are essential for concrete at an early age. Internal and external restraints at an early age that appear due to the hydration process can cause internal stress development, leading to premature microcracking [2].

Based on the previous scientific assumptions, the theory of linear visco-elasticity is sufficient for creep deformation modelling. The condition here is that the stresses in concrete have to be limited to a level not higher than 40 % of the concrete compressive strength as it has been required in Eurocode 2 [3].

Most used strain measurement methods employ surface-attached mechanical or electrical gauges that are physically fixed to a test specimen's facet or embedded. In many cases, direct gauge attachment technology can be cumbersome or even irrelevant since a surface-attached gauge usually gives a single measurement along one axis (strictly limited to the gauge length) [26, 27]. Furthermore, in stress states such as tension, the specimen's geometry tends to be more complicated than those in compression or bending. Thus, it requires alternative solutions for trustable gauge attachment methods. To observe the deformation behaviour of an object more complete, non-contact displacement measurement systems of 2D/3D-DIC (Digital Image Correlation for bidirectional/tridirectional displacement measurements respectively) can be applied [28, 29]. Even 2D-DIC ultimately allows precisely measure strains (detectable on the surface of a test specimen) along various axes within a plain. DIC was claimed to be a more cost-effective surface deformation research method than conventional methods in less strict limitations for maximal displacements and versatility of acquired data [28].

2. Materials and Methods

2.1. Materials and specimens

Two different OPC mortar mixes were made using Aalborg white cement. The compositions of mixes are shown in Table 1.

Table 1. Prepared mix compositions.

Plain OPC mortar		1 % PVA fiber-reinforced OPC mortar	
Material	Mass for 1m ³ , kg	Material	Mass for 1m ³ , kg
Aalborg Portland cement 52.5 R	450.00	Aalborg Portland cement 52.5 R	450.00
Quartz sand 0.3/2.5	900.00	Quartz sand 0.3/2.5	900.00
Water	180.00	Water	180.00
Plasticizer VINPLAST CL 10	3.60	Plasticizer VINPLAST CL 10	3.60
PVA fibres	–	PVA fibers	15.79
W/C	0.40	W/C	0.40

Three groups of specimens were prepared. For strain of creep in compression and shrinkage strain determination, Ø 46 × 250 mm cylinders were made. The cube was prepared with dimensions 150 × 150 × 150 mm and later was cut into CT plates for strain in tension and shrinkage strain determination. For displacement determination in a 3-point bending, the plate was designed with dimensions 500 × 500 × 20 mm and subsequently was cut into beam specimens. All the specimens were unmolded 24 hours after casting and were submerged in water for four days. On the 5th day, specimen preparation for long-term property tests was started.

2.2. Test specimen preparation

When cylinders were unmolded, they were $\varnothing 46 \times 250$ mm. Specimens at the age of 5 days were cut according to RILEM code requirements for long-term testing in compression [30]. For this necessity, specimens were cut to the length of 194 mm approximately. Their top and bottom faces were ground. Specimen height was 190 mm, and top and bottom plains were perpendicular to the specimen's longitudinal axes. The diameter to height ratio was approximately 1/4.

Afterwards, the specimens intended for creep strain six aluminium plates (10 × 15 mm) were glued on. One aluminium plate was glued on the top and bottom for specimens intended for shrinkage strain measurements. For shrinkage intended specimens, aluminium plates were glued in the middle of the specimen upper and bottom parts and then in the centre [31].

For long-term property testing in tension, compact tension (CT) specimens were used [32]. Each cube was cut into 15 mm thick CT plates. According to Fig. 1, the notch was sawn, and the holes were drilled.

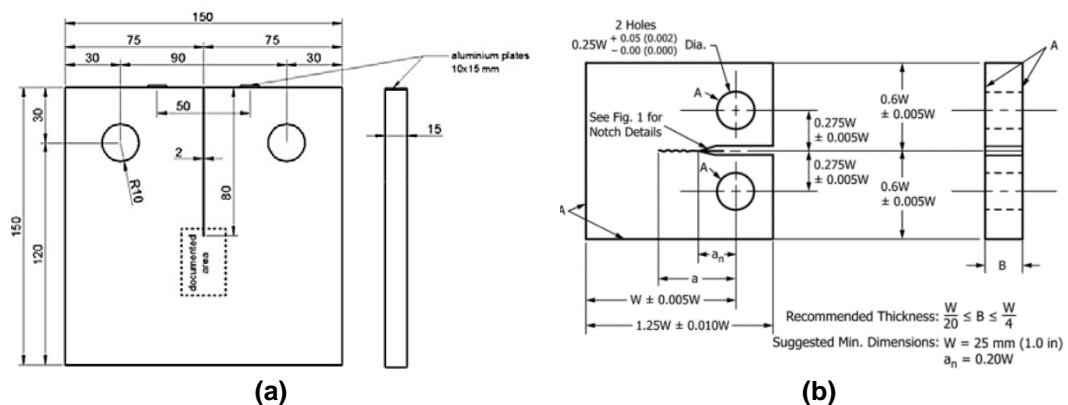


Figure 1. Geometry of the Compact Tension (CT) specimen [31, 32].

The notch in the specimen was sawn by Proxxon MICRO MBS 240/E bandsaw and was 2 mm wide. According to Fig. 1, 2 aluminium plates were glued to the specimen's facet on both sides of the notch. Additionally, the black paint speckle pattern was created on the surface of 2D-DIC specimens.

For the long-term property testing in 3-point bending, each plate was cut into 20 × 75 × 450 mm pieces. The thickness to length ratio is 0.044 [11, 33].

There were 20 cylinders, 5 CT specimens, and 6 beam-plate specimens for each prepared mortar mix.

2.3. Experimental setup

When all the specimens were prepared, the compressive strength, tensile strength, and ultimate load value in 3-point bending were determined. The procedure is shown in Fig. 2, and the results are compiled in Table 2.

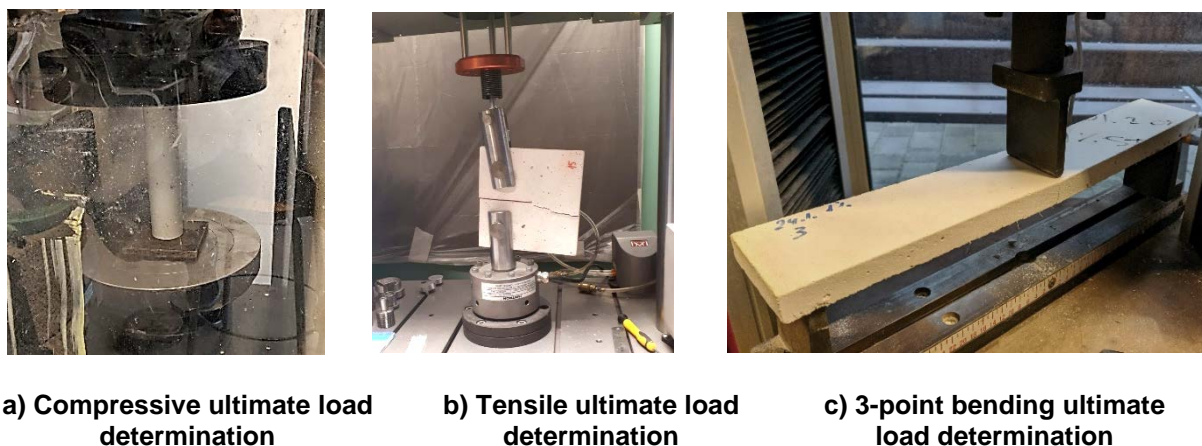


Figure 2. Experimental test setups for the determination of ultimate load values.

Afterwards, specimens were placed on their test stands. Compression and tension specimens were placed in the creep lever test stands, but 3-point bending specimens were placed in the deflection test

stand (see Fig. 3). Additionally, to a mechanical strain gauge, a single digital SLR camera was placed facing a CT specimen to acquire displacement images that were later processed using commercial software (developed by GOM GmbH). In compression and tension, specimens were loaded with 20 % of the compressive/tensile ultimate load value, whereas 3-point bending 40 % of the ultimate load value. The specimens were loaded as previously described to be within the linear strain state [3].

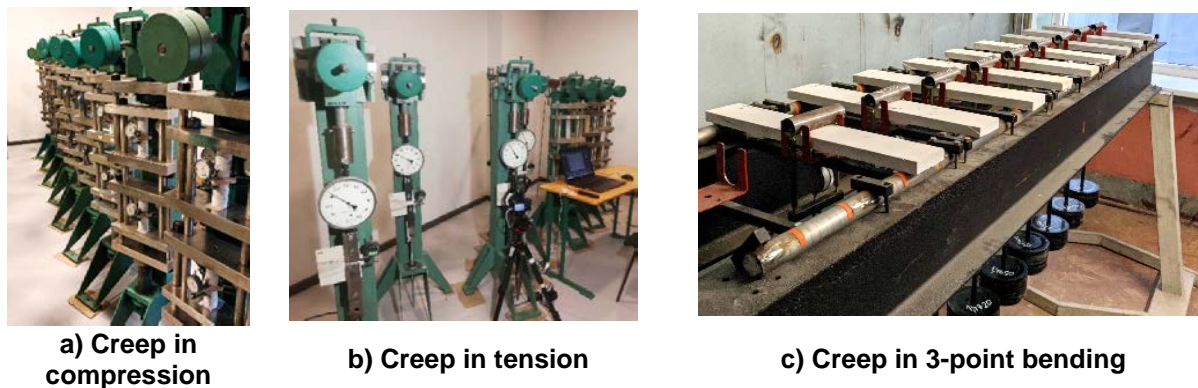


Figure 3. Creep specimens placement in the test stands.

For creep in compression and 3-point bending and shrinkage measurements for all specimens, strain gauges were used with an error margin of ± 0.01 mm. For creep in tension, digital strain gauges were used with an error margin of ± 0.001 mm. For the operating principles of the creep lever test stand, see Fig. 4. All specimens were kept in a dry atmosphere of controlled relative humidity in standard conditions: temperature 20 ± 1 °C and relative humidity 30 ± 7 %.

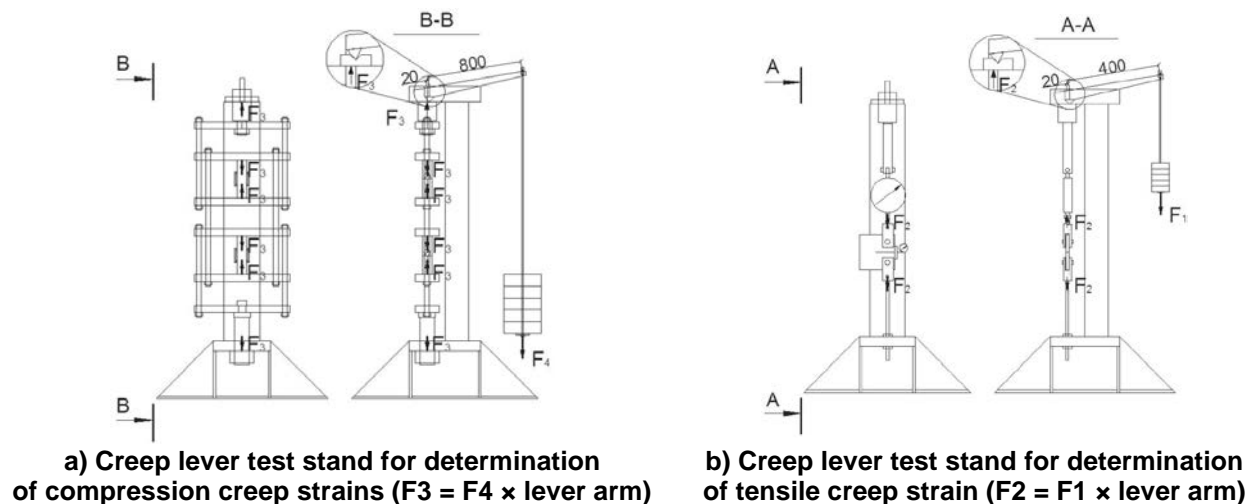


Figure 4. Compression (a) and tension (b) creep lever test stand schemes.

Simultaneously to creep strain tests also shrinkage strain measurements of compression and tension specimens were carried out. The test setup for both strain measurements is shown in Fig. 5.

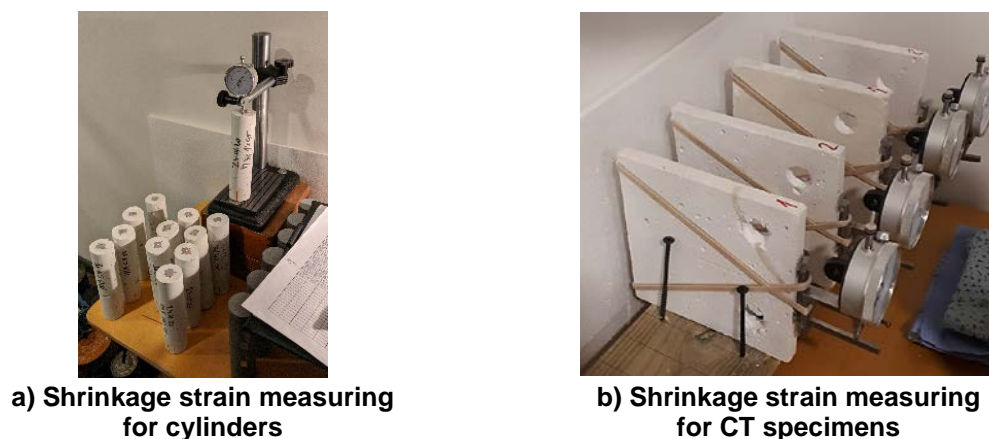


Figure 5. Shrinkage specimen placement in the test stands.

3. Results and Discussion

Before the creep tests, the specimen compressive, tensile, and bending ultimate load values were determined. The obtained results are shown in Table 2.

Table 2. Ultimate load values for all tested specimen types.

Test type	Specimen type	Average ultimate load, kN
Compression	Plain OPM	61.2
	OPM with 1 % PVA	61.0
Tension	Plain OPM	0.32
	OPM with 1 % PVA	0.34
3-point bending	Plain OPM	0.27
	OPM with 1 % PVA	0.30

According to these values, the amount of load was calculated that creep specimens were loaded in their test stands.

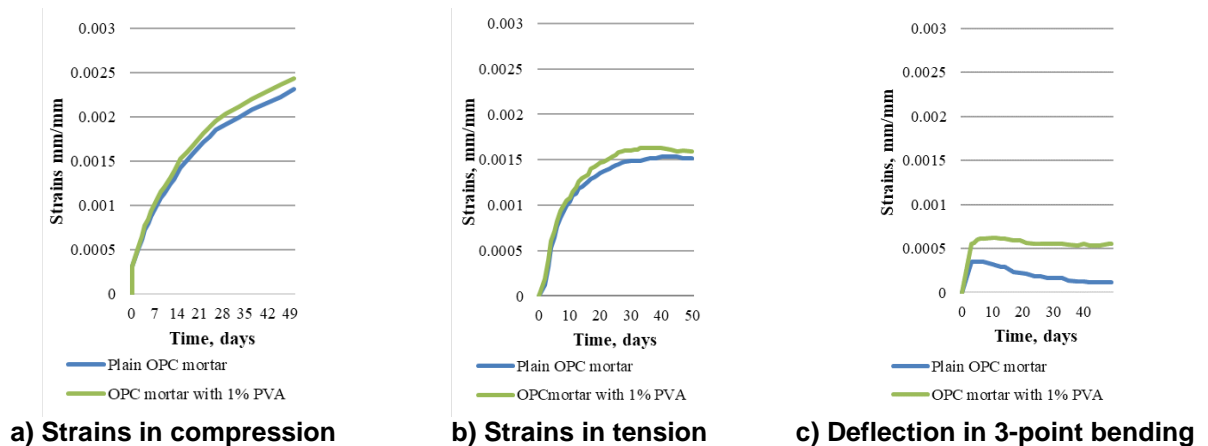


Figure 6. Full strains in compression, tension, and full deflection in 3-point bending.

Fig. 6 shows the curves of the deformations that have been measured for specimens that have not been wrapped in any way to prevent moisture evaporation from the specimen in any way. The fibre-reinforced mortar reached higher strains than plain OPC mortar. Long-term property caused strains to PVA fibre-reinforced specimens to increase around 12 days of testing in compression and tension. Still, in 3-point bending, the deflection of PVA fibre reinforced specimens overcomes plain OPC mortar specimens in the elastic state. The difference between plain and PVA fibre-reinforced specimen strains at its peak in compression is 9.1 % but in tension 8.6 %. The only positive effect of PVA reinforcement – the specimens had more significant elastic strains than plain specimens. As shown in Fig. 8 (a) and (b), the reinforced specimens in cases of compression and tension when loaded had small differences in immediate strains. Still, when unloaded, the difference is much more visible. In 3-point bending, the deflection differences between plain and PVA fibre-reinforced mortar were much more significant.

To get a more thorough look at the creep and shrinkage impact in the specimens loaded in compression and tension in Fig. 7 (a) and (b) is shown curves of creep with and without shrinkage strain part.

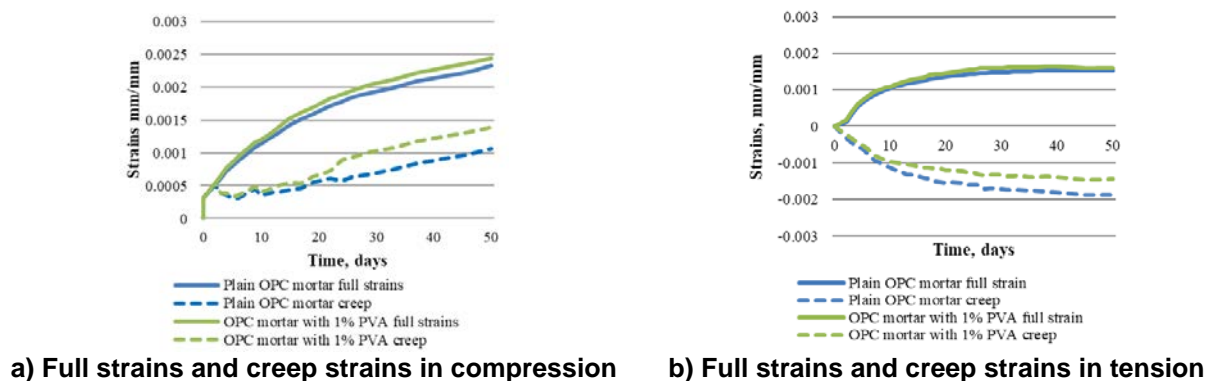


Figure 7. Full strains and creep strains in compression and tension.

Fig. 7 shows that the shrinkage effect of compression and tension specimens is reasonably different. It is possibly due to the specimens' shape and the ability to move the moisture through the specimens. In contrast to Fig. 7 (a) shown long-term properties and raw creep strains in compression, the curves in Fig. 7 (b) representing long-term properties and raw creep in tension show that the shrinkage effect to the tension specimens is significantly higher than for the compression specimens. The creep curves in tension are with downward characteristics, unlike compression creep specimens. Curves show that tension creep was opening the notch, but shrinkage (Fig. 8b) tightens and close down the notch with more significant effort. The mean value of creep curves in tension is around 2 % smaller than those in compression. The shrinkage mean value, in contrast, to creep in tension is 41 %.

In this research work, the use of 2D-DIC application aimed to obtain experimental data of cement composite creep data and conclude whether this method's usage is suitable for such application. According to the authors' knowledge, DIC is not widely used in long-term tests as a measuring tool. Obtained strain data of specimens in tension show close similarity with conventionally registered (using surface-attached gauges) results. Characteristics of graph curves correspond, but numerical data closely deviate since a virtual strain gauge cannot be applied entirely at the same spot as a mechanical system.

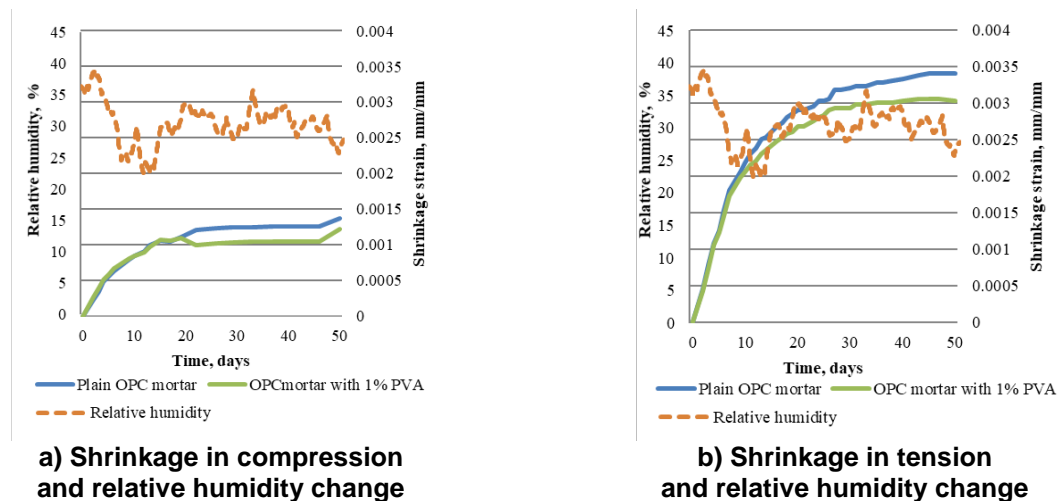


Figure 8. Shrinkage strains in compression and tension and relative humidity change.

In further, analyze shrinkage strains in compression (Fig. 8 (a)) and tension (Fig. 8 (b)) and the strain dependence from changes in relative humidity. In that case, specimens in compression react to humidity changes more rapidly than specimens in tension. Furthermore, compression specimens have very rapid strain characteristics when the moisture content increases, unlike tension specimens. For tension specimens, the strain changes from humidity level changes were more aimed to seek a balance point for specimen when the humidity level in the environment matches in the specimen. Then it would slowly react to humidity changes and deform. Farah M et al. [2] stated that creep testing for concrete at an early age leads to high creep displacements due to shrinkage and water movement into the concrete. Also, the shrinkage amount in compression is significantly less than in tension. The difference in peak shrinkage values is 70.5 % higher in tension. Fig. 6 to Fig. 8 fully shows this statement.

To further analyze obtained creep curves, the elastic strains at the beginning of the testing were taken away to evaluate raw creep strains. These curves are shown in Fig. 9.

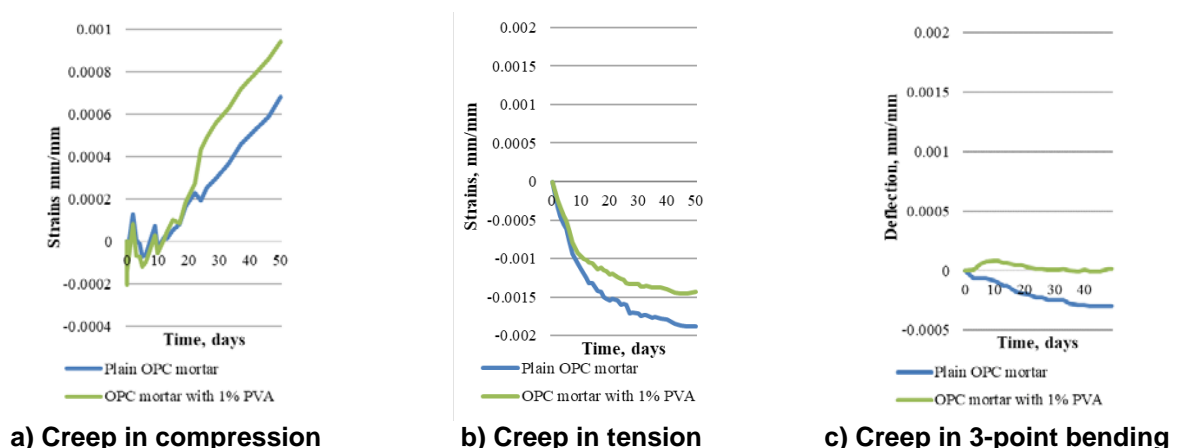


Figure 9. Creep strains without elastic strain part.

Fig. 9 clearly shows that mean creep values are close and within a 5 % margin in general in compression and tension. It has to be mentioned that the 1 % PVA fiber-reinforced OPC mortar specimens show higher strains in compression than in tension and vice versa for plain OPC mortar. The difference here is 17.89 % and 20.21 % for PVA fiber-reinforced and plain OPC mortar correspondingly. The strains in 3-point bending in contrast to strains in compression and tension are significantly less and at peak value is only about 25 % from the highest strain value in tension (plain OPC mortar specimens).

The further see moisture influence to the mortar mechanical properties. Half of the specimens were subjected to water saturation for 24 hours. The results are shown in Table 3 and Table 4.

Table 3. Water absorption characteristics of specimens.

Specimen type	Specimen mix type	Average weight before H ₂ O, kg	Average weight after 24 hours in H ₂ O, kg	Average absorbed H ₂ O weight, kg
Cylinder specimen of creep in compression	1 % PVA	0.6483	0.6878	0.0395
	Plain	0.6468	0.6858	0.0390
Cylinder specimen of shrinkage	1 % PVA	0.6455	0.6865	0.0410
	Plain	0.6693	0.7093	0.0400
CT specimen of creep in tension	1 % PVA	0.5065	0.5540	0.0475
	Plain	0.6070	0.6530	0.0460
CT specimen of shrinkage	1 % PVA	0.5585	0.6075	0.0490
	Plain	0.6465	0.6965	0.0500
Beam-plate specimen of creep in 3-point bending	1 % PVA	1.4065	1.4820	0.0755
	Plain	1.4620	1.5425	0.0805

As shown in Table 3, whether the specimen has been loaded does not significantly affect the water absorption ability. The difference of same mix specimen water absorption differing from the test they had been subjected to is within 4 % margin for specimens that were used to test creep and shrinkage in compression. Within 8 % for specimens used to test creep and shrinkage in tension and within 5 % for specimens used to test creep in 3-point bending. A shrinkage test in 3-point bending was not conducted.

Table 4. Water absorption effect to ultimate load.

Specimen type	Specimen mix type	Average strength for air-dry specimens, kN	Average strength for water-saturated specimens, kN	Average strength loss due to water saturation, %
Cylinder specimen of creep in compression	1 % PVA	70.1	49.8	29.06
	Plain	72.9	43.1	41.88
Cylinder specimen of shrinkage	1 % PVA	53.2	43.5	18.24
	Plain	63.4	38.7	39.96
CT specimen of creep in tension	1 % PVA	0.38	0.35	7.89
	Plain	0.46	0.39	15.22
CT specimen of shrinkage	1 % PVA	0.46	0.40	13.04
	Plain	0.55	0.38	30.91
Beam-plate specimen of creep in 3-point bending	1 % PVA	0.305	0.225	26.23
	Plain	0.320	0.220	31.25

From Table 4, it becomes clear that loaded specimens have significantly higher compressive load than the ones that have been used as shrinkage specimens (without load). As stated previously, when the compressive strength values for creep tests were determined, the 1 % PVA fibre incorporation into the mix did not show immediate improvement to the mechanical properties in compression. The only slight improvement that becomes apparent was that when specimens were subjected to water for 24 hours, then for those specimens, the loss of ultimate compressive load was from 12.82 to 21.72 % lower than for the plain OPC mortar. In the air-dry state difference between compressive load values to specimens are 4.9 and 16.1 %, but in water-saturated, this difference favours the PVA fibre-reinforced specimens 15.5 and 11.1 %, respectively. A similar tendency is apparent with tension and 3-point bending specimens. The PVA fibre-reinforced specimens have from 4.6 % lower bending strength load up to 17.4 % maximum tensile load in the air-dry state than plain specimens. Water-saturated PVA fibre-reinforced specimens showed a different situation when PVA reinforced specimens show more considerable ultimate tension and bending

load values than plain specimens. The decline of the maximum load value for PVA fibre-reinforced specimens is significantly less than the plain mortar ones. In general, it seems that 1 % PVA fibre by weight addition does not only decrease compressive strength as J.J. Ekaputri et al. and J. Topic et al. [34, 35] had stated but also the decrease in tensile strength as well.

If the values in Table 2 and Table 4 were compared, the plain specimens that were not subjected to load had increased their compressive strength, but PVA fiber-reinforced had lost it. It can be due to the nature of fibre reinforcement and uneven fibre distribution in the specimen. All of the loaded specimen compressive load values had risen significantly and are 16.1 and 13.0 % higher for plain and PVA fibre-reinforced ones, respectively.

4. Conclusions

This article's main primary purpose is to determine the difference of long-term strains in compression, tension and 3-point bending to OPC mortar with and without PVA fibre reinforcement. The overall conclusions are:

- In compression specimens with 1 % PVA fibre, it only improves compressive strength in a water-saturated state and is 11 to 13.5 %. In other cases, specimens show from 3.8 to 10.2 % less compressive strength than plain OPC mortar specimens;
- Initially, tension specimens with 1 % PVA fibres show higher tensile strength than plain OPC mortar specimens. After long-term testing, specimens with fibres show superior strength in tension only when the specimens were wet. At the beginning of testing, air dry PVA fibre specimens were 5.9 % resistant to tension, but plain specimens show from 16.4 to 17.4 % higher strength in tension at the end of testing. In a water-saturated state, plain specimens that have been tested to creep show 12.8 % higher strength in tension, but shrinkage test PVA fibre-reinforced specimens show 5 % higher strength in tension than plain OPC mortar specimens;
- For specimens that were used in the 3-point bending, the strength situation is similar to tension specimens. At the beginning of testing, specimens are 10 % with a higher strength than plain OPC mortar specimens. Still, after testing plain specimens in the air-dry state, they show a 4.7 % maximum load value. In water saturate state, fibre-reinforced specimens show a 2.2 % higher ultimate load value;
- Specimens with PVA fibre reinforcement show less strength loss due to water saturation than plain OPC mortar specimens. On average, it is 23.65 % and 40.92 % in compression for PVA and plain specimens, 10.47 % and 23.07 % in tension for PVA and plain OPC mortar specimens 26.23 % and 31.25 % in three-point bending for PVA and plain specimens correspondingly;
- Creep strains in tension and creep deflection in 3-point bending specimens with PVA fibres are reduced than without them. The creep strains are, on average, 21 % larger than plain OPC mortar specimens with a peak difference of 25 % in compression. The increase of creep strains in tension is less, but PVA fibre specimens on average show 7 % higher strains with a peak value of 29 % in the early loading stages. In 3-point bending, the long-term strains are on average 55 % less to the plain OPC mortar specimens with a peak value of 73 % in the late stages of loading. In compression, it is the other way around, with the increase in creep for the PVA fibre-reinforced specimens by 15.2 % at the peak;
- In shrinkage specimens with PVA, fibres show their superiority – in compression strains. PVA fibre specimens are on average 18 % less with a peak value of 42 % in late testing stages. The superiority is only 8 % to plain OPC mortar specimens with its peak value of 29 % in the late testing stages in tension;
- The 2D-DIC displacement measuring system is well applicable to monitor the creep behaviour of cement composite materials.

For further research, it is planned to have the same test procedure as it was described in this article. The test subject would be geopolymer composite. The results would then be compared with the results obtained in this article and determined whether geopolymer composite holds significantly better long-term properties at an early age.

5. Acknowledgements

This work has been supported by the Latvian Council of Science within the scope of the project 'Long term properties of innovative cement composites in various stress-strain conditions' No. lzp-2018/2-0249.

This publication was supported by Riga Technical University's Doctoral Grant programme.

This work has been supported by the European Regional Development Fund within the Activity 1.1.1.2 "Post-doctoral Research Aid" of the Specific Aid Objective 1.1.1 "To increase the research and innovative capacity of scientific institutions of Latvia and the ability to attract external financing, investing in human resources and infrastructure" of the Operational Programme "Growth and Employment" (No.1.1.1.2/VIAA/3/19/401).

Conflicts of Interest: The authors declare no conflict of interest.

References

1. Liang, S., Wei, Y. Methodology of obtaining intrinsic creep property of concrete by flexural deflection test. *Cement and Concrete Composites*. 2019. 97 (April 2018). Pp. 288–299. DOI: <https://doi.org/10.1016/j.cemconcomp.2019.01.003>
2. Farah, M., Grondin, F., Alam, S.Y., Loukili, A. Experimental approach to investigate creep-damage bilateral effects in concrete at early age. *Cement and Concrete Composites*. 2019. 96 (November 2018). Pp. 128–137. DOI: <https://doi.org/10.1016/j.cemconcomp.2018.11.022>
3. Boumakis, I., Di Luzio, G., Marcon, M., Vorel, J., Wan-Wendner, R. Discrete element framework for modeling tertiary creep of concrete in tension and compression. *Engineering Fracture Mechanics*. 2018. 200(July). Pp. 263–282. DOI: <https://doi.org/10.1016/j.engfracmech.2018.07.006>
4. Rossi, P., Tailhan, J.L., Le Maou, F. Comparison of concrete creep in tension and in compression: Influence of concrete age at loading and drying conditions. *Cement and Concrete Research*. 2013. 51. Pp. 78–84. DOI: <http://dx.doi.org/10.1016/j.cemconres.2013.04.001>
5. Ibragimov, R., Fediuk, R. Improving the early strength of concrete: Effect of mechanochemical activation of the cementitious suspension and using of various superplasticizers. *Construction and Building Materials*. 2019. 226. Pp. 839–848. DOI: <https://doi.org/10.1016/j.conbuildmat.2019.07.313>
6. Nizina, T.A., Balykov, A.S. Experimental-statistical models of properties of modified fiber-reinforced fine-grained concretes. *Magazine of Civil Engineering*. 2016. 62(2). Pp. 13–25. DOI: 10.5862/MCE.62.2
7. Lee, N.K., Jang, J.G., Lee, H.K. Shrinkage characteristics of alkali-activated fly ash/slag paste and mortar at early ages. *Cement and Concrete Composites*. 2014. 53. Pp. 239–248. DOI: <http://dx.doi.org/10.1016/j.cemconcomp.2014.07.007>
8. Kuenzel, C., Li, L., Vandeperre, L., Boccaccini, A.R., Cheeseman, C.R. Influence of sand on the mechanical properties of metakaolin geopolymers. *Construction and Building Materials*. 2014. 66. Pp. 442–446. DOI: 10.1016/j.conbuildmat.2014.05.058
9. Falliano, D., De Domenico, D., Ricciardi, G., Gugliandolo, E. Compressive and flexural strength of fiber-reinforced foamed concrete: Effect of fiber content, curing conditions and dry density. *Construction and Building Materials*. 2019. 198. Pp. 479–493. DOI: <https://doi.org/10.1016/j.conbuildmat.2018.11.197>
10. Vrijdaghs, R., di Prisco, M., Vandewalle, L. Creep of polymeric fiber reinforced concrete: A numerical model with discrete fiber treatment. *Computers and Structures*. 2020. 233. Pp. 106233. DOI: <https://doi.org/10.1016/j.compstruc.2020.106233>
11. Das, C.S., Dey, T., Dandapat, R., Mukharjee, B.B., Kumar, J. Performance evaluation of polypropylene fibre reinforced recycled aggregate concrete. *Construction and Building Materials*. 2018. 189. Pp. 649–659. DOI: <https://doi.org/10.1016/j.conbuildmat.2018.09.036>
12. Amran, M., Fediuk, R., Vatin, N., Lee, Y.H., Murali, G., Ozbakkaloglu, T., Klyuev, S., Alabduljabber, H. Fibre-reinforced foamed concretes: A review. *Materials*. 2020. 13(19). Pp. 1–36. DOI: 10.3390/ma13194323
13. Fediuk, R.S., Klyuev, A. V., Liseitsev, Y.L., Timokhin, R.A. Fiber concrete on greenest cementitious binders for road construction. 95Far Eastern Federal University, Vladivostok, Russian Federation, 2021.
14. Afroughsabet, V., Teng, S. Experiments on drying shrinkage and creep of high performance hybrid-fiber-reinforced concrete. *Cement and Concrete Composites*. 2020. 106(November 2019). Pp. 103481. DOI: <https://doi.org/10.1016/j.cemconcomp.2019.103481>
15. Liu, F., Ding, W., Qiao, Y. Experimental investigation on the tensile behavior of hybrid steel-PVA fiber reinforced concrete containing fly ash and slag powder. *Construction and Building Materials*. 2020. 241. Pp. 118000. DOI: <https://doi.org/10.1016/j.conbuildmat.2020.118000>
16. Paegle, I., Minelli, F., Fischer, G. Cracking and load-deformation behavior of fiber reinforced concrete: Influence of testing method. *Cement and Concrete Composites*. 2016. 73. Pp. 147–163. DOI: <http://dx.doi.org/10.1016/j.cemconcomp.2016.06.012>
17. Pupure, L., Varna, J., Joffe, R., Berthold, F., Miettinen, A. Mechanical properties of natural fiber composites produced using dynamic sheet former. *Wood Material Science and Engineering*. 2020. 15(2). Pp. 76–86. DOI: 10.1080/17480272.2018.1482368
18. Klyuev, S., Klyuev, A., Vatin, N. Fine-grained concrete with combined reinforcement by different types of fibers. *MATEC Web of Conferences*. 2018. 245. DOI: 10.1051/mateconf/201824503006
19. Fediuk, R., Mochalov, A., Timokhin, R. Review of methods for activation of binder and concrete mixes. *AIMS Materials Science*. 2018. 5(5). Pp. 916–931. DOI: 10.3934/matricsci.2018.5.916
20. Said, M., Abd El-Azim, A.A., Ali, M.M., El-Ghazaly, H., Shaaban, I. Effect of elevated temperature on axially and eccentrically loaded columns containing Polyvinyl Alcohol (PVA) fibers. *Engineering Structures*. 2020. 204 (December 2019). Pp. 110065. DOI: <https://doi.org/10.1016/j.engstruct.2019.110065>
21. Ling, Y., Zhang, P., Wang, J., Chen, Y. Effect of PVA fiber on mechanical properties of cementitious composite with and without nano-SiO₂. *Construction and Building Materials*. 2019. 229. Pp. 117068. DOI: <https://doi.org/10.1016/j.conbuildmat.2019.117068>
22. Wang, J., Dai, Q., Si, R., Guo, S. Investigation of properties and performances of Polyvinyl Alcohol (PVA) fiber-reinforced rubber concrete. *Construction and Building Materials*. 2018. 193. Pp. 631–642. DOI: <https://doi.org/10.1016/j.conbuildmat.2018.11.002>
23. Noushini, A., Samali, B., Vessalas, K. Effect of polyvinyl alcohol (PVA) fibre on dynamic and material properties of fibre reinforced concrete. *Construction and Building Materials*. 2013. 49. Pp. 374–383. DOI: <http://dx.doi.org/10.1016/j.conbuildmat.2013.08.035>
24. Liu, F., Ding, W., Qiao, Y. Experimental investigation on the flexural behavior of hybrid steel-PVA fiber reinforced concrete containing fly ash and slag powder. *Construction and Building Materials*. 2019. 228. Pp. 116706. DOI: <https://doi.org/10.1016/j.conbuildmat.2019.116706>

25. Ranjbar, N., Mehrali, M., Mehrali, M., Alengaram, U.J., Jumaat, M.Z. High tensile strength fly ash based geopolymer composite using copper coated micro steel fiber. *Construction and Building Materials*. 2016. 112. Pp. 629–638. DOI: <http://dx.doi.org/10.1016/j.conbuildmat.2016.02.228>
26. Biscaia, H., Franco, N., Chastre, C. Stainless Steel Bonded to Concrete: An Experimental Assessment using the DIC Technique. *International Journal of Concrete Structures and Materials*. 2018. 12(1). DOI: 10.1186/s40069-018-0229-8
27. del Rey Castillo, E., Allen, T., Henry, R., Griffith, M., Ingham, J. Digital image correlation (DIC) for measurement of strains and displacements in coarse, low volume-fraction FRP composites used in civil infrastructure. *Composite Structures*. 2019. 212. Pp. 43–57. DOI: 10.1016/j.compstruct.2019.01.024
28. Smrkić, M.F., Koščak, J., Damjanović, D. Application of 2D digital image correlation for displacement and crack width measurement on RC elements. *Gradjevinar*. 2018. 70(9). Pp. 771–781. DOI: 10.14256/JCE.2407.2018
29. A Good Practices Guide for Digital Image Correlation Standardization, Good Practices, and Uncertainty Quantification Committee. 2018. DOI: 10.32720/idics/gpg.ed1/print.format
30. Acker, P., Agullo, L., Auperin, M., Carol, I., J. Carreira, D., M.R. Catarino, J., Chem, J.-C., A. Chiorino, M., W. Dougill, J., Huet, C., Kanstad, T., Kim, J.-K., Křístek, V., Republic, C., S. Muller, H., Byung, G., Oh, H., Ožbolt, J., Reid, S., Wittmann, F. RILEM TC 107-CSP: CREEP AND SHRINKAGE PREDICTION MODELS: PRINCIPLES OF THEIR FORMATION Recommendation Measurement of time-dependent strains of concrete. *Materials and Structures*. 1998. 31. Pp. 507–512.
31. Sprince, A., Pakrastins, L., Baskers, B., Gaile, L. Crack development research in extra fine aggregate cement composites. *Vide. Tehnologija. Resursi – Environment, Technology, Resources*. 2015. 1. Pp. 205–208. DOI: 10.17770/etr2015vol1.199
32. ASTM. E647 – Standard Test Method for Measurement of Fatigue Crack Growth Rates. *ASTM Book of Standards*. 2016. 03(July). Pp. 1–49. DOI: 10.1520/E0647-15E01.2
33. Ranaivomanana, N., Multon, S., Turatsinze, A. Basic creep of concrete under compression, tension and bending. *Construction and Building Materials*. 2013. 38. Pp. 173–180. DOI: <http://dx.doi.org/10.1016/j.con-buildmat.2012.08.024>
34. Ekaputri, J.J., Limantono, H., Triwulan, Susanto, T.E.S., Abdullah, M.M.A.B. Effect of PVA fiber in increasing mechanical strength on paste containing glass powder. *Key Engineering Materials*. 2016. 673(August). Pp. 83–93. DOI: 10.4028/www.scientific.net/KEM.673.83
35. Topic, J., Prošek, Z., Indrová, K., Plachý, T., Nežerka, V., Kopecký, L., Tesárek, P. Effect of PVA modification on the properties of cement composites. *Acta Polytechnica*. 2015. 55(1). Pp. 64–75. DOI: 10.14311/AP.2015.55.0064

Contacts:

Andina Sprince, Andina.Sprince@rtu.lv

Rihards Gailitis, rihards.gailitis@rtu.lv

Leonids Pakrastins, leonids.pakrastins@rtu.lv

Tomass Kozlovskis, tomass.kozlovskis@rtu.lv

Nikolai Vatin, vatin@mail.ru



DOI: 10.34910/MCE.105.12

A deformed state of the composite frame with phased installation

A.A. Koyankin^{*a} , V.M. Mitasov^b

^a Siberian Federal University, Krasnoyarsk, Russia

^b Novosibirsk state University of architecture and construction, Novosibirsk, Russia

*E-mail: KoyankinAA@mail.ru

Keywords: reinforced concrete, compressive strength, cracks, tensile strength, experimental investigations, prefabricated-monolithic structures

Abstract. Experimental studies have been carried out to investigate the features of a composite flat frame deformation that arise in the process of its gradual installation and loading. During the first stage only precast elements (columns and beam precast parts) are assembled, which are further loaded with some weight that simulates its own weight in a real structure, the weight of other precast elements and that of monolithic concrete. Thus, at the first stage of existence the load is perceived only by the precast elements of the flat frame. Subsequently, at the second stage, without removing the previously applied load, the monolithic concrete is laid, which, having gained the required strength is included in the deformation process, taking an additional applied load that simulates the weight of floor structures, partitions, curtain walls and operational load. The motivations for conducting experimental research were as follows: the carcass of a composite building (is simulated by a flat double two-story frame in the experiment) in real conditions is built in stages, which is expressed in serial installation of individual components. These design features lead not only to the inclusion of separate parts of composite elements in the deformation process at different times, but also to a significant change in the design scheme as a whole (the formation of continuous beams and floor slabs, an appearance of a rigid junction of beams with columns, an increase in the degree of static indefinability of the system, and so on). Experimental studies of the stress-strain state of composite flat frames were performed, taking into account the phased installation process and changes in the design scheme. Precast parts of experimental flat frames (columns, beam precast parts) are made of heavy concrete, and monolithic beam parts – of light concrete (expanded- clay concrete). The conducted research allows us to state that the phased installation and involvement in the deformation process of both individual elements of the composite carcass and the constituent parts of the elements significantly change the picture of the carcass deformation.

1. Introduction

Prefabricated-monolithic housing construction is actively developing, which is reflected not only in the increase of volume of this type of construction [1–4], but in the interest of scientists in this structural system. Various scientific (theoretical, numerical, and experimental) studies of various aspects that affect the stress-strain state of individual composite elements, as well as buildings and structures in general, have been carried out. For this reason, a composite carcass was taken to be the subject of research.

For example, the authors of some contributions [5–7] have conducted research on the influence of various design features, as well as the stages of construction on the process of deformation and structural reliability of composite structures.

Of interest is work [8], where experimental studies of composite and monolithic overlappings were conducted with data on load-bearing capacity, deformability and crack resistance. At that, the estimation of



the stress-strain state was performed. The authors of some publications [1, 9–11] have also conducted a number of experimental studies of composite slabs.

In addition to considering the issues of stress-strain state, reliability and other parameters related directly to structures, scientists and engineers are also interested in the features of the technology of construction of composite structures [12, 13].

The contributions are worth noting that address the issues of load-bearing capacity, deformability and crack resistance of not only buildings and their elements as a whole, also paying attention to the reliability of individual components of the junction elements. For example, the authors of this work have previously conducted research [14], devoted to the study of the features of deformation of the junction nodes of hollow floor slabs with composite beams. In addition, the features of deformation of the junction nodes of composite beams with columns are considered. The data obtained in the course of the research made it possible to identify a number of design flaws that indicate the need for technical improvements in a number of structural systems used in modern construction of prefabricated monolithic buildings. The works of a number of other authors [15–18] are also devoted to research on the study of slab junction nodes with columns.

In addition to the above mentioned studies, various scientists and engineers have considered the problems of deformation of multilayer structures [19], including the issues of deformation of structures with external sheet reinforcement [20, 21], as well as other types of impact [22–24].

Having reviewed the current experience of prefabricated housing construction and studied the research carried out, the authors of this work concluded that a more extensive study of the stress-strain state of the building composite carcasses is required, taking into account the phased installation of both the carcass as a whole and its individual structural elements (slabs, floor beams), where, for example, the precast part is first installed, and then the monolithic one. These design features lead not only to the inclusion of individual parts of composite elements in the deformation process at different times, but also to a significant change in the design scheme as a whole (the formation of non-cut beams and floor slabs, the appearance of a rigid junction of beams with columns, an increase in the degree of static indefinability of the system, and so on).

A rather weak study of the effect of phased installation and loading, both of individual structures and of the building as a whole, on the stress-strain state of the composite carcass leads to an incorrect assessment of its performance.

These circumstances served as a reason for performing experimental studies of the stress-strain state (the subject of study) of composite gradually erected and loaded flat frame carcasses (the object of the study).

The purpose of conducted experimental studies was to study the features of formation of the stress-strain state of a composite flat frame, taking into account its phased installation and loading.

To achieve the goal, the following tasks were determined: development of the method for experimental study of the flat carcass of the composite frame taking into account the phased installation and loading, experimental tests, and analysis of received data.

2. Methods

To perform experimental studies, two flat frames R1 and R2 completely identical to each other, both in terms of design and loading were manufactured and tested.

Experimental models were produced and simultaneously loaded in two stages (Fig. 1):

1. stage 1:

- at the plant of reinforced concrete products precast parts of the frames of heavy concrete class of B25 type were manufactured: 70×70×1.200(h) mm two-storey columns, reinforced with four longitudinal Ø8A400bars and transversal Ø4B500 reinforcement with a 50 mm step; 70×70(h)×1.410 mm beam composite parts, strengthened by lower longitudinal 3Ø3B500 and the shear Ø3B500 reinforcement with a step of 100 mm in 2 rows;

- installation of precast elements of two flat two-storey two-span frames, located opposite each other at a distance of 2.0 m. The overall dimensions of each frame are as follows: 2 spans; 2 floors; a span of 1.500 mm; a floor height of 600 mm. At this stage, the flat frame is a geometrically unchangeable statically indeterminate system with the following boundary conditions: rigid pinching of the columns with the base; hinge coupling of the beam (precast part) with the column;

– loading with a preload that simulates the loading of precast elements with an assembly load in a real structure (the actual weight of the precast element itself and other elements supported on it, as well as the weight of monolithic concrete). The concentrated load was applied by hanging concrete blocks on flexible cables (average weight 0.55 kN). Loading of each beam occurred in 2 steps – 1 block for each step. Thus, at the end of the 1st stage of loading, the load was $P = 0.55$ kN.

2. stage 2:

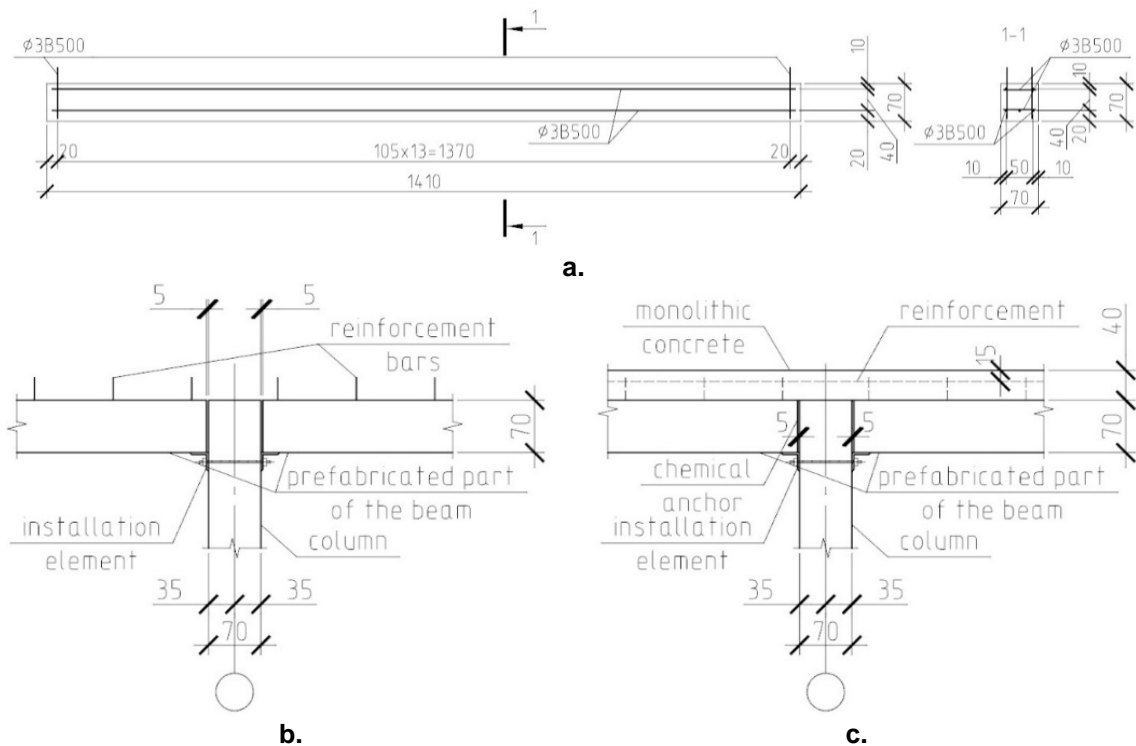
– without removing the pre-load applied during the 1st stage, longitudinal reinforcement was installed in the support zone of the beams and monolithic lightweight concrete was laid (structural expanded-clay concrete of class B12.5). The height of the concreted part of the beams was 40 mm, and the total height of composite beams of flat frames R1 and R2 was 110 mm;

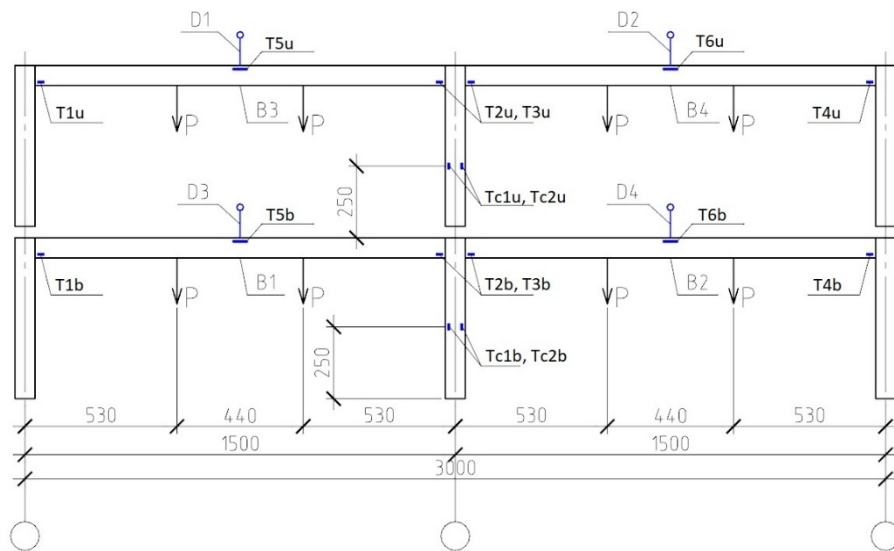
– after a set of solid concrete required strength, the flat frame is a geometrically immutable, statically indefinable system (with a greater degree of indefinability than at the 1st stage) with the following boundary conditions: rigid pinching of the column with the base and the beam with the column;

– after the required strength was set with monolithic concrete, the composite structure was loaded with an additional load that simulates the installation load, such as the weight of floor structures, partitions, curtain walls, etc., and operational loading. To do this, wooden beams were installed between the frames, on which concrete loading blocks were placed. At the same time, the location of the beams was such that the load application within the 2nd stage occurred in exactly the same places as the load application at the 1st stage. Each loading step increased the load P by 0.275 kN.

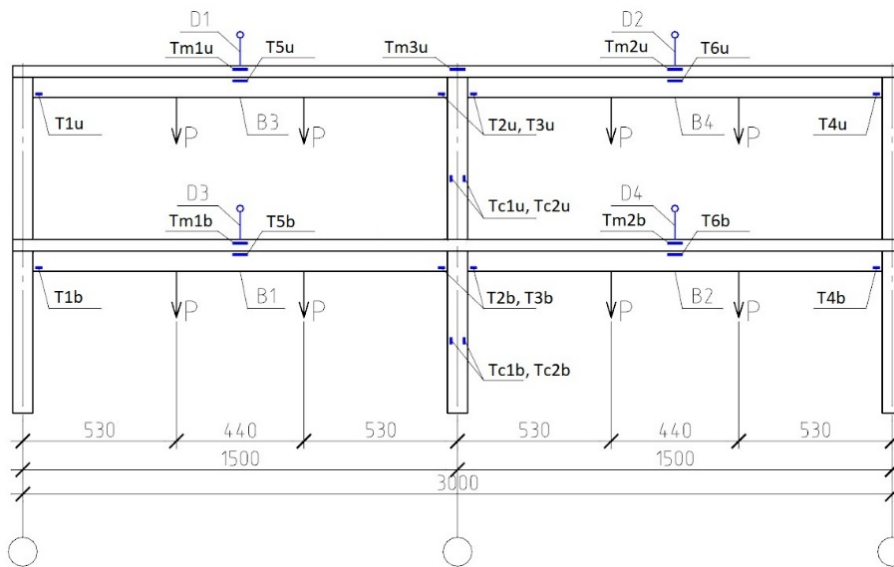
During the 2nd stage of loading, the maximum force P was: lower – tier beams – 1.65 kN; upper-tier beams – 2.2 kN and 1.925 kN for the right and left spans, respectively.

The following order of loading the beams at the 2nd stage was observed: B2, B1, B4 and B3.





d.



e.



f.



g.

Figure 1. Experimental frame: a – the scheme of reinforcement of the combined part of the beams; b – the junction of the crossbar with the column at the 1st stage; c – the junction of the crossbar with the column at the 2nd stage; d – design diagram at the 1st stage; e – design diagram at the 2nd stage; f – frames photo at the 1st stage; g – frames photo at the 2nd stage.

Concrete deformations were recorded by strain gauges with a base of 20, 50 and 60 mm. The bends were fixed by deflectors placed in the center of the beams.

3. Results and Discussion

The analysis of the results of the conducted experimental studies has shown:

- the lack of mutual displacement of the monolithic and precast parts relative to each other, i.e., compatibility of deformation of the monolithic and precast parts was ensured by friction forces at the contact surfaces of the concrete and dowel effect evenly spaced across the length of the beam shear reinforcement;
- the process of deformation of all frames and individual frame elements looks logical, which results in a uniform increase in deflections of beams and deformations of concrete (precast and monolithic) during the entire loading period. Moreover, after a set of monolithic concrete of the required strength, the intensity of the increase in deflections and deformations slows down;
- the formation of the first cracks in the beams of frames R1 and R2 occurred during the 1st stage of loading;
- there was no exhaustion of the load-bearing capacity in any element of the frame. This is evidenced by the absence of visible signs of destruction of compressed concrete, and not reaching the maximum compression deformations in concrete. In addition, the experiment did not record an intensive and non-stabilizing increase in deflections during loading.

The detailed analysis of deflections (Fig. 2) has shown the following:

- there is a different intensity of the increase in deflections at each stage of loading. At the 1st stage, when only the precast part is included in the deformation process, an increase in deflections occurs more intensively than at stage 2, when monolithic concrete has already been included in the deformation process;
- during loading at the 2nd stage, the deflection of the directly loaded beams increases, while the beams in the adjacent span, due to the continuity of the monolithic concrete, experience bending deformations, which is associated with the continuity of the composite beam;
- at the 1st stage, the deflections of the beams in the frames R1 and R2 were in the range of 0.63...0.78 mm when loading $P = 0.28$ kN and 2.47... 2.77 mm when loading $P = 0.55$ kN;
- at the 2nd stage, the deflections in the initially loaded beams B2 and B4 were 4.40 mm and 3.89 mm, respectively. After the end of direct loading of beams B2 and B4, and the beginning of loading of adjacent beams B1 and B3, the deflections in beams B2 and B4 decreased slightly, amounting to 4.14 mm and 3.73 mm, respectively, at the last step;
- in beams B1 and B3, on the contrary, at first there is a decrease in the deflection value as the adjacent beams are loaded, but later, from the moment of their direct loading, the deflections were 4.30 mm and 3.75 mm, respectively.

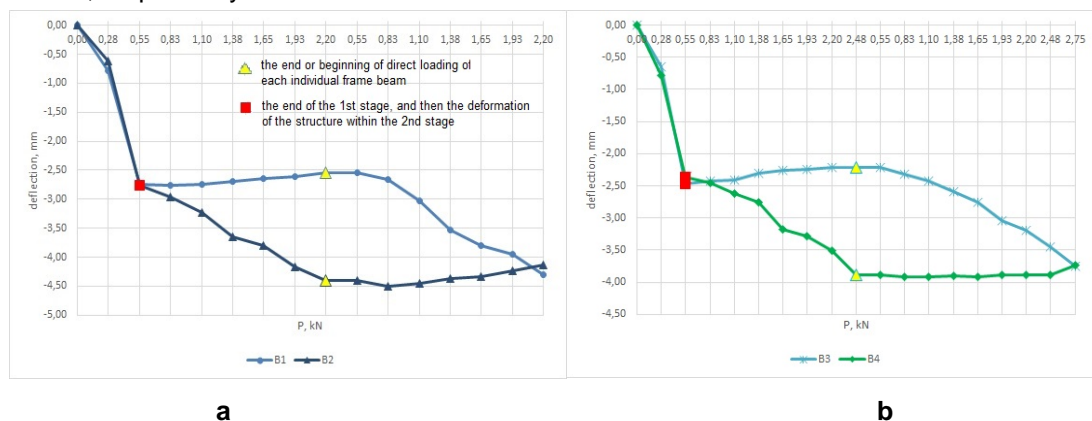


Figure 2. Frame beam deflection graph: a – beams B1, B2; b – beams B3, B4.

On the graph of the increase in deflections (Fig. 2) a large red square indicates the end of the 1st stage, and then the deformation of the structure within the 2nd stage. The yellow triangle indicates the end or beginning of direct loading of each individual frame beam.

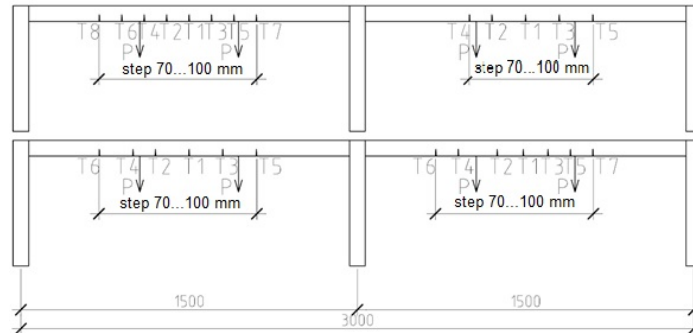
The formation of cracks was recorded in the middle of the span of the precast parts of the beams at the 1st stage of loading (Fig. 3,a), i.e. during the deformation of only the precast part at a load of $P = 0.55$ kN. The hair cracks formed at the 1st stage had a spreading height of about 20...30 mm, and the width of the opening did not exceed 0.05 mm. The step of the crack arrangement was 70...100 mm.

During the 2nd stage of loading, the opening width of previously formed cracks (Fig. 3,b) was increased without a significant increase in their height. In this case, the cracks of the precast part in the span did not reach the monolithic concrete.

In monolithic concrete, cracks were formed at a load of $P = 1.93$ kN or more above the middle support. At the same time, some of the cracks on the support at the end of loading of the 2nd stage crossed completely the monolithic part of the concrete, but did not spread to the precast part.

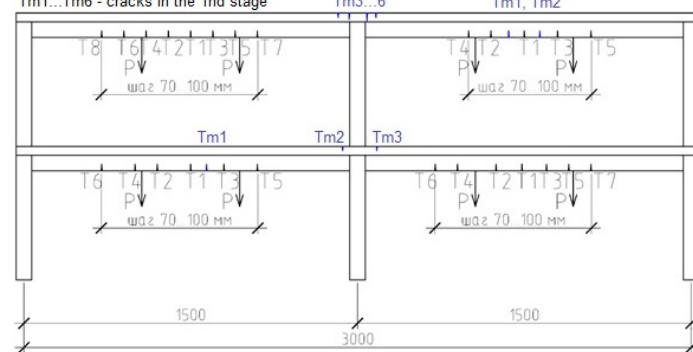
Cracks were not fixed in the columns and beams on the extreme supports, and there were no horizontal cracks, including the seam of the concrete junction.

T1...T8 - cracks in the 1st stage $P=0.55$ kN



a.

T1...T8 - cracks in the 1st stage
Tm1...Tm6 - cracks in the 1st stage



b.



c.



d.

**Figure 3. Crack formation diagram: a – stage 1; b – stage 2;
c – prefabricated part at the 1st stage; d – monolithic concrete at the 2nd stage.**

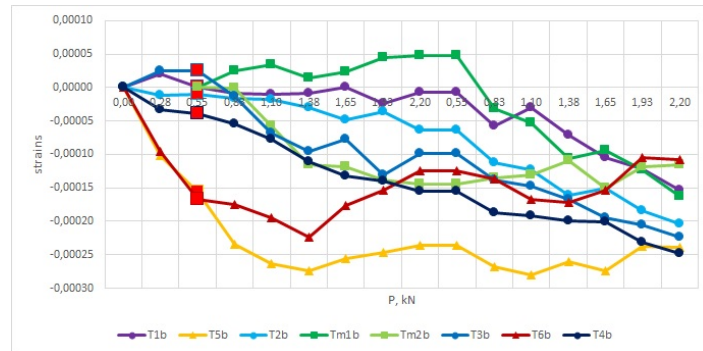
The character of deformation of the beams of experimental frames R1 and R2 is as follows:

- at the 1st stage of loading, the precast parts of the frame beams are deformed as a flexed hinge-supported single-span beam with the appearance of tensile deformations in the lower and compression deformations in the upper zones. Relative compression deformations in the upper zone of the beam precast part in the middle of the span at the end of the 1st stage of loading were 0.000121...0.000168;
- at the 2nd stage of loading, the intensity of growth of compression deformations in the upper zone of the beam precast part in the middle of the span significantly decreases, and in a number of beams, even a decrease in their value was noted. In particular, the lower level beams showed both an increase in compression, deformations from 0.000156 to 0.000239 (left beam) and a decrease from 0.000168 to 0.000108 (right beam). At the same time, on the upper beams, the relative compression deformations of the upper zones of the precast parts only increased from a value of 0.000121 to 0.000203 for the left beam and from 0.000139 to 0.000215 for the right one. Deformations in the lower zone of the beam precast part on the

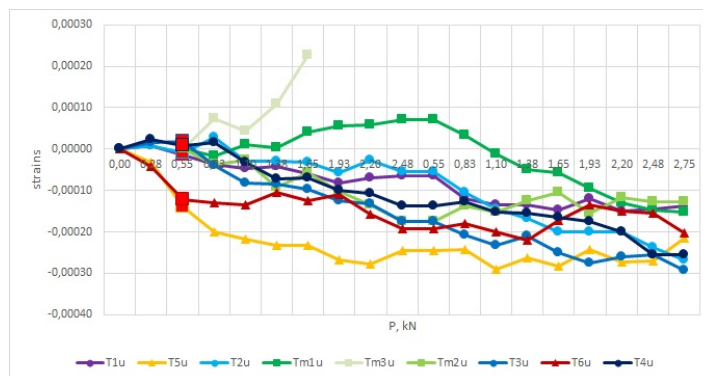
supports also began to increase, reaching values near the edge column of 0.000154...0.000248, and near the middle column – 0.000204...0.000255;

– the phased loading of the continuous beam at the 2nd stage (after the required strength is set by the monolithic concrete) affects the character of deformation of the monolithic part. In the first loaded beam, compression deformations increase in the monolithic concrete in the middle of the span to values of 0.000145...0.000175. At the same time, tensile deformations occur in the adjacent unloaded beam (values 0.000048...0.000071) in monolithic concrete, which is explained by the bending of the unloaded span. Later, after loading all the beams, final deformations in the monolithic concrete were 0.000115...0.000163;

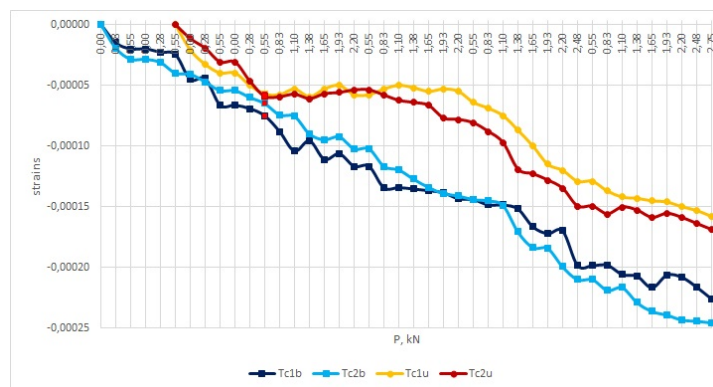
– monolithic concrete on the support undergoes tensile deformations that reach the maximum values when the load value is more than 1.38 kN. At about the same time, cracks were recorded.



a.



b.



c.

Figure 4. Graphs of relative deformations of precast and monolithic concrete elements of R1 and R2 frames: a – beams of the lower tier; b – beams of the upper tier; c – columns.

In the presented graphs (Fig. 4) relative deformations of the composite concrete, a large red square indicates the end of the 1st stage and further deformation of the structure within the 2nd stage.

Deformation of columns of R1 and R2 frames occurred logically. The lower columns began to be deformed from the first loading step, experiencing compressive deformations that reached values of 0.000065...0.000075 at the end of the 1st loading step. Columns of the upper tier are included in the deformation process after loading the upper tier beams and their deformations reached 0.000057...0.000059 at the end of the 1st stage of loading.

During the 2nd stage of deformation, the columns of the lower tier experience uniform compression. The value of relative deformations was 0.000226...0.000245. In the columns of the upper tier, the relative deformations were 0.000158...0.000169.

The results obtained in the course of experimental studies were compared with the data of other scientific papers and a good convergence was obtained. In particular, the nature of the distribution of deformations in the cross section of the composite element coincides with the data obtained during experimental studies of the hinge-supported beam [25]. In addition, similar results were obtained in [21], where numerical studies of a two-story double span frame were carried out with the phased involvement of composite concrete in the deformation process. Studies carried out in [24] have shown that it is possible to provide high shear stiffness of the joint of different-age concretes by installing transverse reinforcement.

4. Conclusions

Based on the research, the following conclusions are made:

1. Phased involvement of precast and then monolithic concrete in the deformation process significantly changes the picture of the stress-strain state of both the individual composite bent element and the structural system as a whole;
2. The corresponding reinforcement of monolithic concrete on the supports of the composite beam leads to the "transformation" of a series of single-span beams to a single multi-span continuous beam, increase in the rigidity of the beam-column interface nodes, and changes in the design scheme as a whole;
3. Uneven loading of composite beams leads to bending of unloaded beams with the appearance of tensile forces in the middle of the span of the upper zone.

References

1. Teplova, Z.S., Vinogradova, N. Combined and monolithic overlappings of "MARKO" system. Construction of Unique Buildings and Structures. 2015. 8(35). Pp. 48–59. (rus). DOI: 10.18720/CUBS.35.4.
2. Serbin, S.A., Dedyukhin, P.O., Fomin, N.I. The analysis of technological parameters of pre-cast-monolithic system with permanent formwork walls. 4th International conference on safety problems of civil Engineering critical infrastructures. Safety, 2018. DOI: 10.1088/1757-899X/481/1/012051.
3. Shmelev, G.D., Fomenko, N.A., Gavrilova, V.N. Comparative analysis of contemporary systems of establishing civil design buildings. Housing and utilities infrastructure. 2018. 3(6). Pp. 9–19. (rus).
4. Ogbul, E.K. Perspective structural solutions in fiber-reinforced concrete cast-in-place and precast floors. Vestnik grazhdanskikh inzhenerov. 2014. № 5(46). Pp. 33–38. (rus)
5. Koyankin, A., Mitsov, V. Assessment of structural reliability of precast concrete buildings. MATEC Web of Conferences. IV International Young Researchers Conference «Youth, Science, Solutions: Ideas and Prospects» (YSSIP-2017). Volume 143, 2018. DOI: <https://doi.org/10.1051/mateconf/201814301001>
6. Koyankin, A.A., Mitsov, V.M. Stress-strain state of precast and cast-in place buildings. Magazine of Civil Engineering. 2017. 6(74). Pp. 175–184. DOI: 10.18720/MCE.74.14
7. Koyankin, A.A., Mitsov, V.M. Karkas sborno-monolitnogo zdaniya i osobennosti yego raboty na raznykh zhiznennykh tsiklakh [The frame of the precast-monolithic building and the peculiarities of its work in different life cycles]. Vestnik MGSU. 2015. No. 9. Pp. 28–35. DOI: 10.22227/1997-0935.2012.4.175-180
8. Smoljago, G.A., Krjuchkov, A.A., Dronova, A.V., Drokin, C.V. Results of the experimental studies of bearing capacity, crack resistance and deformability of the precast-monolithic and monolithic overlappings. Izvestiya Yugo-Zapadnogo gosudarstvennogo universiteta. 2011. 5(38)-2. Pp. 105–109. (rus).
9. Kolchunov, V.I., Povetkin, M.S., Merkulov, D.S. Results of the experimental of the studies of the ferroconcrete constructions of the composite section. Proceedings of the Kursk state technical university. 2009. 3(28). Pp. 67–74. (rus).
10. Nedviga, E., Beresneva, N., Gravit, M., Blagodatskaya, A. Fire Resistance of Prefabricated Monolithic Reinforced Concrete Slabs of «Marko» Technology. Advances in Intelligent Systems and Computing. 2018. No. 692. Pp. 739–749.
11. Parashchenko, N.A., Gorshkov, A.S., Vatin, N.I. Partially rib precast and cast-in-situ floors with cellular-concrete blocks. Magazine of Civil Engineering. 2011. 24(6). Pp. 50–55. (rus). DOI: 10.5862/MCE.24.7
12. Vatin, N.I., Velichkin, V.Z., Kozinets, G.L., Korsun, V.I., Rybakov, V.A., Zhuvak, O.V. Pre-cast-monolithic reinforced concrete beam-slabs technology with claydit blocks. Construction of Unique Buildings and Structures. 2018. 70(7). Pp. 43-59. (rus). DOI: 10.18720/CUBS.70.4
13. Afanas'ev, A.A. Technology of erection of precast frame buildings at negative temperatures. Vestnik MGSU. 2012. No. 4. Pp. 175–180. (rus). DOI: 10.22227/1997-0935.2012.4.175-180.
14. Koyankin, A.A., Mitsov, V.M., Deordiev, S.V. The compatibility of deformation of the hollow-core slab with beams. Magazine of Civil Engineering. 2019. 3(87). Pp. 93–102. DOI: 10.18720/MCE.87.8
15. Drakatos, I.S., Muttoni, A., Beyer, K. Internal slab-column connections under monotonic and cyclic imposed rotations. Engineering Structures. 2016. No. 123. Pp. 501–516. DOI: <https://doi.org/10.1016/j.engstruct.2016.05.038>
16. Varlamov, A.A., Pivovarov, V.S., Pivovarova, O.V. Variant of keyed joint of precast-monolithic slab. Materials of the international scientific and practical conference: Architecture. Construction. Education. 2014. Pp. 249–255. (rus). <http://ace-journal.ru/wp-content/uploads/2017/04/%E2%84%961-3-2014.pdf>.
17. Sursanov, D.N., Sazonova, S.A., Ponomarev, A.B. Analysis of concrete dowel full-scale shearing tests. Vestnik PNIPU. Stroitel'stvo i arhitektura. 2015. No. 2. Pp. 7–23. (rus). DOI: 10.15593/2224-9826/2015.2.01.

18. Breccolotti, M., Gentile, S., Tommasini, M., Materazzi, A.L., Bonfigli, M.F., Pasqualini, B., Colone, V., Giancesini, M. Beam-column joints in continuous RC frames: Comparison between cast-in-situ and precast solutions. *Engineering Structures*. 2016. No. 127. Pp. 129–144. DOI: <https://doi.org/10.1016/j.engstruct.2016.08.018>.
19. Chepurnenko, A.S. Stress-strain state of three-layered shallow shells under conditions of nonlinear creep. *Magazine of Civil Engineering*. 2017. 8(74). Pp. 156–168. DOI: 10.18720/MCE.76.14
20. Garrido, M. Creep behaviour of sandwich panels with rigid polyurethane foam core and glass-fibre reinforced polymer faces: Experimental tests and analytical modeling. *Journal of Composite Materials*. 2014. Vol. 48. No. 18. Pp. 2237–2249.
21. Medvedev, V.N., Semeniuk, S.D. Durability and deformability of braced bending elements with external sheet reinforcement. *Magazine of Civil Engineering*. 2016. No. 3(63). 2016. Pp. 3–15. DOI: 10.5862/MCE.63.1
22. Olmati, P., Sagaseta, J., Cormie, D., Jones, A.E.K. Simplified reliability analysis of punching in reinforced concrete flat slab buildings under accidental actions. *Engineering Structures*. 2017. No. 130. Pp. 83–98. DOI: <https://doi.org/10.1016/j.engstruct.2016.09.061>
23. Qian, K., Li, B. Resilience of Flat Slab Structures in Different Phases of Progressive Col-lapse. *ACI Structural Journal*. 2016. No. 113. Pp. 537–548.
24. Micallef, K., Sagaseta, J., Fernandez Ruiz, M., Muttoni, A. Assessing Punching Shear Failure in Reinforced Concrete Flat Slabs Subjected to Localized Impact Loading. *International Journal of Impact Engineering*. No. 71. 2014. Pp. 17–33. DOI: <https://doi.org/10.1016/j.ijimpeng.2014.04.003>
25. Koyankin, A.A., Mitsov, V.M., Tskhay, T.A. Experimental studies of the effect of pre-loading on the stress-strain state of precast-monolithic bending element. *The Siberian Transport University Bulletin*. 2019. No. 4(51). Pp. 63–72. (rus). https://www.stu.ru/particular/get_teamwox_file.php?id=28112&ext=.pdf

Contacts:

Alexander Koyankin, KoyankinAA@mail.ru

Valery Mitsov, mitassovv@mail.ru



DOI: 10.34910/MCE.105.13

Plastic behavior particularities of structures subjected to seismic loads

O.V. Kabantsev^a, A.V. Perelmutter^b 

^a National Research Moscow State Civil Engineering University, Moscow, Russia

^b Scientific and Production Company «SCAD Soft» Ltd., Kiev, Ukraine

*E-mail: ovk531@gmail.com

Keywords: stress-strain state, limit state of structures, plastic strain, elastic brittle fracture, coefficient of reduction

Abstract. For the majority of buildings and structures, the analysis of seismic effects is performed employing the linear-spectral method, and is included into the design regulations of different countries. The linear-spectral analytical method allows for estimating the inelastic deformations in structures by reducing (decreasing) the actual seismic load by means of the coefficient of reduction. The current method of the seismic load reduction corresponds to the elastic-plastic type of structural deformation, with the coefficient of reduction applied to the load-bearing system as a whole. Nonetheless, this deformation pattern is not the only one available. There are structures and structural materials that trigger the elastic-brittle mechanism of transition to the limit state. The constructed buildings and facilities normally contain the structural elements of various deformation patterns (combined structural schemes), and that requires consideration when choosing the calculation method. Employing a universal coefficient of reduction in the design calculations of the combined structural schemes leads to an inaccurate result. Opposite to this, the authors propose herein a solution to the problem of accounting for the joint activity of elastic-plastic and elastic-brittle elements being part of the entire structure based on the energy method. Studied is the combined design model with a single degree of freedom and consisting of elements with different mechanisms of inelastic deformation. Various scenarios of conditions for the joint deformation of heterogeneous elements are analyzed. The general solution to the problem of the coefficient of reduction value for the load-bearing systems made of the elements of different types of inelastic deformation depends on the ratio of stiffness values of the elastic-plastic and elastic-brittle subsystems in structures, as well as on the ratio of bearing capacity of such subsystems. General solutions are obtained to the problem of the maximum permissible value of the coefficient of plasticity for the combined load-bearing system that is responsible for safety of the elastic-brittle sections in structures, and for the system as a whole. When employing the linear-spectral method to calculate the seismic effects for individual parts in structures, it is suggested to use differentiated coefficients of reduction, which is, in fact, complies with the actual performance pattern of structures.

1. Introduction

The prediction of the seismic response of buildings and facilities is based upon the results of the design analysis for the stress-strain state of structures experiencing the seismic impact. In this case, as a general characteristic of the limit state, the concept assuming the local damages in structural elements and nodes occurring during the operation beyond the elastic limit is applied. This approach significantly complicates the techniques and design procedures when it comes to studying the pattern of performance of structures in event of earthquake.

Available nowadays are two main methods to proceed with the design analysis for structures under seismic effects:

Kabantsev, O.V., Perelmutter, A.V. Plastic behavior particularities of structures subjected to seismic loads. Magazine of Civil Engineering. 2021. 105(5). Article No. 10513. DOI: 10.34910/MCE.105.13

© Kabantsev O.V., Perelmutter A.V., 2021. Published by Peter the Great St.Petersburg Polytechnic University



This work is licensed under a CC BY-NC 4.0

a) direct dynamic analysis based on the method of integrating the equations of motion taking into account the physically nonlinear behavior of structures/structural materials;

b) linear spectral analysis of structures.

Method a) is based on general principles of the structural dynamics [1, 2], and allows for obtaining an entirely accurate forecast for the behavior of structures in event of earthquake. Nonetheless, for the purposes of a comprehensive analysis of seismic stability of a structural system, it is required to perform a set of calculations supported by the evaluation of the representative set of earthquake accelerograms, or to perform such evaluation based on the data of seismic movements and their parameters for any particular construction site. All contemporary problem-oriented computing software complexes are equipped with a built-in modules to perform the design analysis by the direct integration method of motion equations.

Another important condition for obtaining the correct result by Method a) is modeling the process of occurrence and development of damage in structures. Meeting this requirement is ensured by implementation of the special computation techniques which take into account the deformation in structures and structural materials beyond the point of elastic strain. It is noteworthy that the design analysis beyond the elastic phase of deformation requires considerable computational capacity.

Thus, the design analysis as per Method a) is considered to be totally scientific-substantiated, yet still rather complicated in terms of its implementation, and requires the attention of high qualified specialists.

For the purposes of carrying out the mass estimation and forecast of seismic resistance, the less complicated approach, i.e. Method b), was elaborated and substantiated. This method is based on the research studies completed in the 40s of the XXth century by M.A. Biot [3, 4], and A.S. Veletsos, N.M. Newmark [5].

The research by M.A. Biot made it possible to obtain the spectra of dynamic response for the single-mass models, which served grounds for development of the design analysis techniques based on the modal analysis of multi-mass systems. The theoretical foundations for the analysis based on the modal calculation are well worked out [1]. Nonetheless, it is noteworthy that the modal calculation approach allows for obtaining the accurate results only within the framework of the elastic performance of structures.

In his research papers, Newmark came forth with the idea of carrying out calculations for inelastic systems assuming the seismic actions as elastic, but employing the lower (reduced) loads. The method of N.M. Newmark is supported by the following concept:

- for the systems demonstrating the natural vibration frequency range at $t > 0.5$ sec, the displacement of elastic and ideally elastic-plastic systems is equal. This assumption is graphically represented in Fig. 1, a);
- for the systems demonstrating the natural vibration frequency range 0.1÷0.5 sec, the energy of elastic (S1) and elastic-plastic (S2) systems is equal. This assumption is graphically represented in Fig. 1, b).

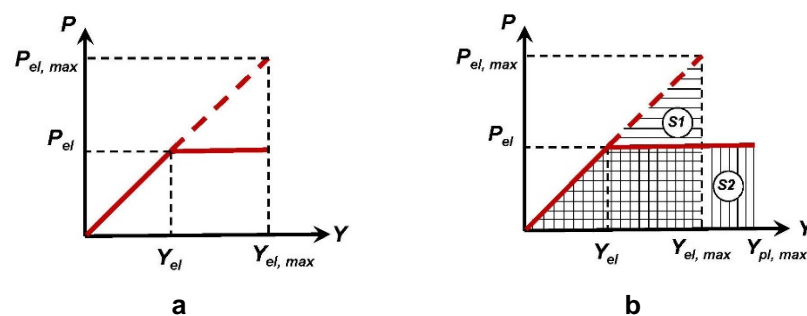


Figure 1. Graphic representation of the assumption made by N. Newmark [3] as regards the compatibility of characteristic parameters of elastic and elastic-plastic systems.

The assumption introduced by N.M. Newmark makes it possible to carry out static calculations within the framework of the elastic performance in structures, but with consideration of the possible occurrence of a certain amount of inelastic deformations taking place when the load-bearing system experiences the seismic loads of an actual level. The important aspect of using the assumption by N.M. Newmark is the opportunity to employ the modal calculation of structures taking into account the dynamic response spectra of load-bearing systems following the approach of M.A. Biot. The linear-spectral method for the design calculations of seismic effects is incorporated into the regulations of the majority of countries [6, 8–12].

The reduction in the seismic load level is ensured by multiplying its initial value by a certain coefficient which in the Russian norms [6] is known as the coefficient comprising the capacity of buildings and facilities

to withstand the inelastic strains (K_1) 6ln Eurocode-8 [8] the 'behavior factor' for structures r is mentioned accounting for the similar physical meaning but a reciprocal value ($r = 1/K_1$). Comparable methods of the seismic load reduction are referred to in the design norms of India [9], Turkey [10], Algeria [11], Ukraine [12], and many other countries.

Multiple sources [13–19, etc.] cover the problems of the coefficient of reduction. In different research papers, the attempt at assessing the accuracy of this technique was made, as well as defining more precisely the conditions of its use [20–30]. In research studies [31, 32] it is proved that the elements of the bearing system with the pronounced shear deformation pattern have significant impact upon the generalized parameter of the load reduction. Nonetheless, it should be highlighted that the entire scope of the carried out research activities pertained to the structures made of one material (either steel or reinforced concrete), the elastic-plastic response of which resulted in no loss in rigidity. At the outcome, it was concluded that the response spectral technique together with the reduction employed can be feasible while making design calculations for framed buildings of a simple geometric pattern the rigidity parameters of the bearing elements of which do not manifest a wide scatter.

With the reference to the above, the following should be stated. The reduction in seismic loading as it is represents a simulated approach based on the idea of evaluating the behavior of an elastic-plastic system through the results of calculating its elastic analogue. Indeed, the strains in elements of the system and the corresponding internal forces are limited by the yield point of the material, i.e. reduced if compared to those generated elastically. However, when shown in the way of the load reduction instead of limiting the response of the system, the idea of reduction looks as if during the vibrations of the elastic-plastic system the inertial forces decrease being the seismic loads impacting the structure, and that does not correspond to the physical side of the phenomenon.

At that, all available ways to estimate the coefficients of reduction are associated with the design model of a dynamic system with a single degree of freedom, which in fact has a single structural element the plastic behavior of which is taken into account. In fact, almost any actual structure represents a complex system, and if its dynamic deformation can still be approximated by a certain geometric shape determined with an accuracy to one parameter variable in time (the system with a single degree of freedom), then the actual content of the structure can hardly be so easily reduced to one element experiencing deformation. This is particularly true in cases when the plastic properties of various parts of the structure differ significantly one from another and, moreover, when the plasticity bears no impact whatsoever upon the load-bearing resistance of certain parts of the structure.

The purpose of this research paper is to improve the reduction approach in order to study the possibility of the combined resistance in structures in which only one part of these elements is elastic-plastic, while the other part performs elastically and breaks down in a brittle way (e.g. it loses stability). It is noteworthy that the international standard ISO 3010 [33] explicitly points to the dependency between the coefficient of reduction value and the destruction mechanism type, as well as implying a very descreet approach to the problem of assigning the value to the coefficient in question.

2. Method

In the course of this research, a nonlinear model with a single degree of freedom is mentioned as well in order to assess the behavior of the structure, but with one significant difference, i.e. the model is made of two constituents resisting the motion. The first constituent has the elastic-plastic behavior and the second one has the elastic-brittle behavior. Approximation of the use of the model with a single degree of freedom was substantiated by many authors, together alongside the corresponding reference herein [35].

The grounds of analysis lie in comparison of the deformation energy in an ideally elastic and studied systems. The assumption is made about the ideally plastic behavior of the corresponding part of the structure (Prandtl diagram) and about the instant (brittle) failure of parts showing no performance in an elastic-plastic way.

As illustrated above, as early as the classical works by Newmark [5, 34] and down to the recent times [35–43], the problem of seismic impact reduction by the plastic response of the structure proved to be a good solution for the system all elements of which functioned in the elastic-plastic mode. The solution to this problem was forming up on the assumption about the equality of the utmost displacements in plastic and elastic-plastic structures under the same seismic impact and equal initial natural frequencies. In conformity with the assumption, the design model was developed for the system of a single degree of freedom to demonstrate the reduction scenario. However, the load-bearing systems comprise the structures for which the transition to the limit state is associated with significant difference if compared to the mechanism of plasticity, i.e. the mechanism of brittle failure, rigidity loss, etc.

Is it reasonable to employ the generalized reduction coefficient supported by the elastic-plastic performance for such systems? In what way the reduction coefficient value itself depends on correlation between the rigidity of elastic-plastic and elastic-brittle subsystems?

The problem of taking into account the collaborative performance of subsystems of various mechanisms of inelastic deformation appear to be rather complicated and has not been previously considered. In order to analyze and demonstrate the distinctive features of the problem, a simplified scenario with a single degree of freedom is studied (Fig. 2) where the resistance against transition is achieved through simultaneous operation of two subsystems: marked in red is the elastic-plastic system with the idealized Prandtl diagram and rigidity of its elastic part C_1 , and marked in blue is the elastic-brittle system with its rigidity C_2 .

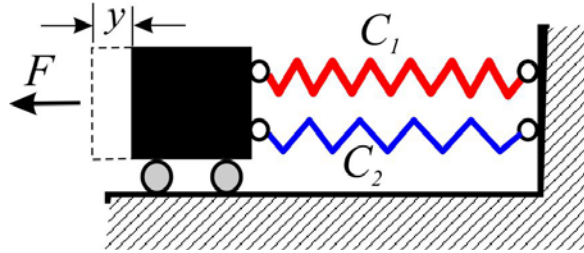


Figure 2. Design model with simultaneous performance of elastic-plastic and elastic-brittle subsystems.

3. Results and Discussion

3.1. Mechanisms of transition into limit state and impact thereof on structures

Fig. 3 introduces four possible scenarios of physical and mechanical properties correlation for these subsystems by means of the displacement-response grid coordinates. As indicated, F_T shows the tolerable limit load state for elastic-plastic subsystem; y_T depicts transition corresponding to the baseline of yield for elastic-plastic subsystem, and by y_d the displacement is introduced which is compatible with the greatest probable overlap with the zone of plasticity. Value F_{cr} stands for the tolerable limit load for elastic-brittle subsystem; y_{cr} depicts transition at which the elastic-brittle subsystem gets crumbled. Owing to the simultaneous performance of the system in general, no system failure occurs upon malfunction of one of its components. Here it should be stated that the tolerable limit state is aligned with the transition y_d for scenarios a) and c) whilst the transition y_{cr} goes along with the scenarios b) and d). At that, we shall discuss whether the defective system can function for a long period of time in the event of only one of its subsystems functioning properly. It is of paramount importance that in this state the transition shall be increasing till the moment of complete failure.

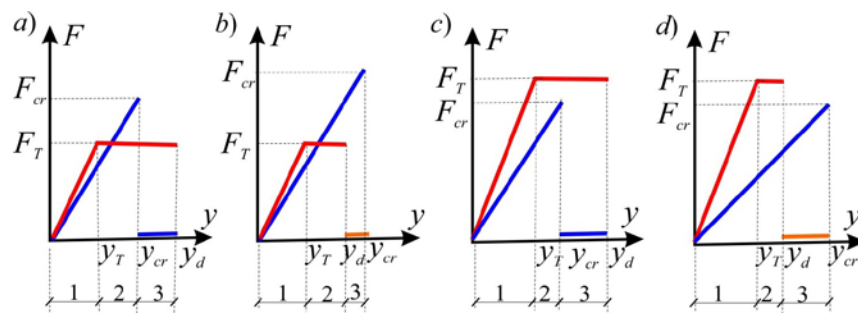


Figure 3. Possible physical and mechanical properties representation scenarios.

The value of potential cumulative energy of the system for all scenarios of physical and mechanical properties at the point when the system reaches its limit state can be estimated as follows:

$$\begin{aligned}
 W_d &= \frac{Py}{2} = F_T \left[\frac{y_T}{2} + (y_d - y_T) \right] + \frac{F_{cr}y_{cr}}{2} = \\
 &= C_1 \left(y_T y_d - \frac{y_T^2}{2} \right) + C_2 \frac{y_{cr}^2}{2}
 \end{aligned} \tag{1}$$

It is possible to work out at which value of the coefficient of reduction λ the force F would work at its elastic stage in order to enable the system with the original rigidity of C_1+C_2 to accumulate the same value of energy. The assumption of the energy balance is represented as follows:

$$\frac{(C_1 + C_2)(\lambda y_d)^2}{2} = C_1 \left(y_T y_d - \frac{y_T^2}{2} \right) + C_2 \frac{y_{cr}^2}{2} \quad (2)$$

or

$$\lambda = \sqrt{\frac{2C_1 \left[y_T y_d - \frac{y_T^2}{2} \right] + C_2 y_{cr}^2}{2(C_1 + C_2) y_d^2}} = \sqrt{\frac{(2\mu - 1)}{2(C_2/C_1)} + \frac{(y_{cr}/y_T)^2}{2}}. \quad (3)$$

The value of $\mu = y_d/y_T$ represents here the coefficient of plasticity which defines the depth of deformation progress along the yield line. If compared to just elastic-plastic system with the value of the coefficient of seismic load reduction equal to $K_1 = 1/\lambda = 1/\sqrt{2\mu - 1}$ (for reference see [5, 34]), the adjustment was obtained as regards two relative measures for the elastic-plastic part of the system and contributing to its overall performance: rigidity values ratio $\alpha = C_2/C_1$ and bearing capacity values ratio $\beta = y_{cr}/y_T$.

The design model with the simultaneous performance of elastic and elastic-plastic subsystems as discussed above is not the only possible example. Another example worth considering is when the subsystems perform sequentially (Fig. 4).

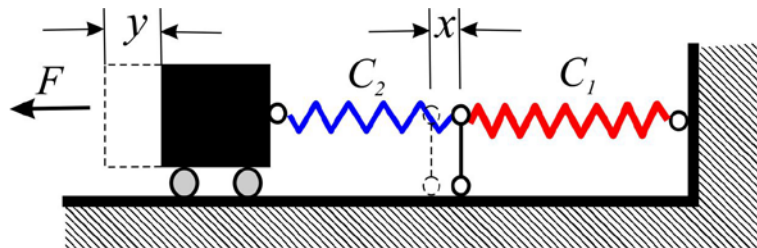


Figure 4. Design model with sequential performance of elastic-plastic and elastic-brittle subsystems. In this model the force F corresponds to the transition as follows:

$$y = F \left(\frac{1}{C_1} + \frac{1}{C_2} \right), \quad x = \frac{F}{C_1} \quad (4)$$

and besides, the values of F_{cr} and F_T are the limit values of force. In as much as for the system of this type the complete failure corresponds to the failure of the weakest element, the limit state is reached upon obtaining the lowest value of these forces., and prior to that moment both subsystems perform simultaneously at the elastic stage. Therefore, for the structure shown in Fig. 3 the coefficient of reduction is at $K_1 = 1$.

3.2. Limit values of the coefficient of plasticity

As regards the value of the coefficient of plasticity μ , its value cannot be arbitrary. Moreover, it cannot be assigned based on the conditions of the equilibrium limits in the structure [35], as the structure is not entirely elastoplastic.

At this point it would seem possible to reason as follows: the strain in the elastic part of the system should not exceed the critical value of F_{cr} as the elastic part may be completely destroyed. Still, as per Fig. 1, the system can indeed exist in this form, if in such a case the plastic strains remain within tolerable limits. It is possible to suppose that this limit is set by way of the maximum permissible value of the coefficient of plasticity μ_{max} , and in this case the elastic part transitions to the limit state and the entire load is solely born by the plastic part of the structure.

The corresponding maximum displacement $y_{\max} \leq y_T \mu_{\max}$ is representative of the force acting on the elastic system $F_{\max} \leq C_2 y_T \mu_{\max}$. The energy balance equation shall generate the value of the coefficient of reduction that corresponds to this scenario, i.e. $\lambda^* = \sqrt{2(\mu_{\max} - 1)}$.

When setting the equation equal to the value defined by the equation (3), generated will be the value of μ_{\max} limited by the condition as follows:

$$\sqrt{2(\mu_{\max} - 1)} = \sqrt{\frac{(2\mu_{\max} - 1)}{2\alpha} + \frac{\beta^2}{2}}, \quad (5)$$

which is reduced to the following:

$$\mu_{\max} = \frac{\alpha\beta^2 + 4\alpha - 1}{4\alpha - 2}. \quad (6)$$

In the case of equal scores of the elastic-plastic and elastic-brittle parts of the system, when $\alpha = 1$ and $\beta = 1$, there will be $\mu_{\max} = 1/2$.

Limiting the values of the coefficient of plasticity was also suggested previously. Thus, in the research papers [42–43], instead of the value of μ corresponding to the ultimate breaking load, it was advised to use some smaller value corresponding to the load resulting in 'tolerable' value of deformation (damage) of the structure. For this reason, naturally, it is required to be aware of the ability of the structure to exhibit the plastic stage of deformation to the extent sufficient for the operation of the damaged structure in the aftermath of seismic action. Obviously, the structures made of different materials (masonry, concrete, reinforced concrete) are capable of exhibiting significantly different values at the plastic deformation stage, within which the values of the tolerable plastic strain differ accordingly.

The actually built structures represent much more complex systems than those simplified models studied herein, the purpose of which being only the demonstration of the effects under analysis. Various structures deforming, in fact, beyond the elastic limit, may comprise the elements that do not exhibit plastic strain (brittle fracture, loss of stability, etc.). In addition, there may be critical elements integrated into the system for which the transition to the plastic stage of performance is undesirable (e.g., embedded parts). For the elements as such, the concept of a bearing capacity margin triggering the reduction in seismic loads, is improper.

The question arises whether coefficient of reduction should be attributed not to the seismic load when it affects the structure in its entirety, but to the internal strains supposing that it may have different values for different elements, as it is introduced, for instance, by means of Eurocode or in the regulations of Uzbekistan?

4. Conclusion

The outcome of the performed research studies deduce the statements as follows:

1. The linear spectral technique to model the buildings and facilities for their seismic effects using the coefficients of reduction corresponding solely to the elastic-plastic mechanism of inelastic deformation, is not of the generalised nature. When building the earthquake-resistant projects, widely used are the structures exhibiting the elastic-brittle mechanism of transition to the limit state, or the mechanism of loss of stability. Cases of collaboration in structures with different modes of deformation can take place. In such cases, implementation of the existing technique with the coefficient of reduction universal for the entire load-bearing system and considering only the elastic-plastic strain mechanism shall inevitably result in incorrect values.
2. Different scenarios for the combined pattern of structures performing the elastic-plastic and elastic-brittle deformation mechanisms are studied. On the basis of the energy balance approach, more accurate values of the coefficient of reduction are obtained taking into account various deformation mechanisms contributing to the overall inelastic performance of the load-bearing system.
3. As regards the load-bearing system comprising the set of structures with different deformation mechanisms, the restrictions in view of the coefficient of plasticity values are proposed.
4. Approaches to use differentiated coefficients of reduction while calculating the seismic impacts following the linear spectral technique are introduced. Using the coefficients of reduction corresponding to

the inelastic deformation in structures under study shall ensure reliability of the complex systems performance with parallel or sequential operation of heterogeneous parts of the structures.

References

1. Clough, R., Penzien, J. Dynamics of structures. CSI Computers & Structures, Inc. Berkeley, Calif., 2003. 731 p.
2. Chopra, A. Dynamics of structures : theory and applications to earthquake engineering. 3rd ed. Prentice Hall: Pearson, cop. New Jersey, 2007. 1657 p.
3. Biot, M.A. A mechanical analyzer for the prediction of earthquake stresses. Bull. Seism. Soc. Amer. 1941. 31. Pp. 151–171.
4. Biot, M.A. Analytical and Experimental Methods in Engineering Seismology. Trans. ASCE. 1943. 108. Pp. 365–408.
5. Veletsos, A.S., Newmak, N.M., Chelapati, C.V. Deformation spectra for elastic and elastoplastic systems subjected to ground shock and earthquake motions. Proc. of the Third World Conference on Earthquake Engineering. Auckland and Wellington. 1965. 7. Pp. 663–682.
6. SP 14.13330.2018 SNIP II-7-81* Stroitel'stvo v seysmicheskikh rayonakh [Construction Rules 14.13330.2018. Civil Design Code II-7-81*. Construction in Earthquake-prone Regions]. Moscow: Minstroy Rossii, 2018.
7. Tyapin, A.G. Sovremennyye normativnyye podkhody k raschetu otvetstvennykh sooruzheniy na seysmicheskiye vozdeystviya [Modern regulatory approaches to the calculation of critical structures for seismic effects]. Moscow: Izdatel'stvo ASV, 2018. 518 p. (rus)
8. EN 1998-1. Eurocode 8: Design of structures for earthquake resistance-Part 1: General rules, seismic actions and rules for buildings. CEN. Brussels, 2005. 102 p.
9. Sudhir, K.J., Murty, C. Proposed Draft Provisions and Commentary on Indian Seismic Code IS 1893 (Part 1). Indian Institute of Technology Kanpur. Kanpur, 2002. 158 p.
10. Specification for Structures to be Built in Disaster Areas. Part III – Earthquake Disaster Prevention. Ministry of Public Works and Settlement Government of Republic of Turkey. 1997. 84 p.
11. DTR B C 2 48. Regles Parasismiques Algeriennes RPA 99/Version 2003. Document Technique Reglementaire. Algerie, 2003. 117 p.
12. DBN V.1.1-12:2014 Budivnytstvo u seysmichnykh rayonakh Ukrayiny [Construction of seismic regions of Ukraine]. Kyiv: Ministerstvo rehional'noho rozvytku, budivnytstva ta zhytlovo-komunal'noho hospodarstva Ukrayiny. Kyiv, 2014. 110 p.
13. Nazarov, Y.P., Oyzerman, V.I. Metod trekh modeley v raschetakh sooruzheniy na seysmicheskiye vozdeystviya [Method of three models in the design of structures for seismic effects]. Stroitel'naya mekhanika i raschet sooruzheniy. 2007. 6. Pp. 6–8.
14. Mazzolani, F., Piluso, V. Theory and design of seismic resistant steel frames. E&FN Spon Press. London, 1996. 498 p.
15. Sosnin, A.V. Ob utochnenii koefitsiyenta dopuskayemykh povrezhdeniy K1 i yego soglasovannosti s kontseptsiyey reduktzii seysmicheskikh sil v postanovke spektral'nogo metoda [On the refinement of the permissible damage coefficients K1 and its consistency with the concept of reduction of seismic forces in the formulation of the spectral method]. Vestnik grazhdanskikh inzhenerov. 2017. 60(1). Pp. 92–114.
16. Khatavkar, A.S., Ghadi, A.P., Barbude, P. Comparative study of response reduction factor for reinforced concrete and steel frame. International Journal of Computer Applications. 2015. ICQUEST 20(7). Pp. 12–14.
17. Brahmavathan, D., Arunkumar, C. Evaluation of Response Reduction Factor of Irregular Reinforced Concrete Framed Structures. Indian Journal of Science and Technology. 2016. 9(23). DOI: 10.17485/ijst/2016/v9i23/95981
18. Riddell, R., Hidalgo, P., Cruz, E. Response modification factors for earthquake resistant design of short period buildings. Earthquake Spectra. 1989. 5(3). Pp. 571–590. DOI: 10.1193/1.1585541
19. Salem, Y.S., Lomiento, G., Khan, J. Assessment of Response Modification Factor of Reinforced Concrete Table Top Frames Structures Subjected to Seismic Loads. International Congress and Exhibition "Sustainable Civil Infrastructures: Innovative Infrastructure Geotechnology", GeoMEast 2017: Facing the Challenges in Structural Engineering. 2018. Pp. 55–71. DOI: 10.1007/978-3-319-61914-9_5
20. Borzi, B., Elnashai, A.S. Refined force reduction factors for seismic design. Engineering Structures. 2000. 22(10). Pp. 1244–1260. DOI: 10.1016/S0141-0296(99)00075-9
21. Elnashai, A.S., Mwafy, A.M. Overstrength and force reduction factors of multistorey reinforced-concrete buildings. Structural Design of Tall Buildings. 2002. 11(5). Pp. 329–351. DOI: 10.1002/tal.204
22. Melo, C., Sharma, S. Seismic Coefficients for Pseudostatic Analysis. 3th World Conference on Earthquake Engineering. Vancouver, B.C., Canada. 2004. Pp. 369.
23. Vielma-Perez, J.-C., Barbat, H.B., Oller, S. Confinamiento y ductilidad de los edificios de hormigón armado. Zuncho. 2008. 15. Pp. 22–29.
24. Olteanu, I., Ciongradi, I.-P., Anechitei, M., Budescu, M. The ductile design concept for seismic actions in miscellaneous design codes. Buletinul Institutului Politehnic din Iași, Tomul LV (LIX), Fasc. 4. Secția Construcții. Arhitectură. 2009. Pp. 55–62.
25. Lasley, S.J., Green, R.A., Rodriguez-Marek, A. New Stress Reduction Coefficient Relationship for Liquefaction Triggering Analyses. Journal of Geotechnical and Geoenvironmental Engineering. 2016. 142(11). Pp. 06016013. DOI: 10.1061/(ASCE)GT.1943-5606.0001530
26. Lasley, S.J., Green, R.A., Rodriguez-Marek, A. New stress reduction coefficient relationship for liquefaction triggering analyses. Journal of Geotechnical and Geoenvironmental Engineering. 2016. 142(11). DOI: 10.1061/(ASCE)GT.1943-5606.0001530
27. Reyes-Salazar, A., Bojórquez, E., Bojórquez, J., Valenzuela-Beltran, F., Ramon Gaxiola-Camacho, J., Haldar, A. Seismic Reduction Factor Evaluation and its Components for Steel Buildings Undergoing Nonlinear Deformations. Current Science. 2019. 116(11). Pp. 1860. DOI: 10.18520/cs/v116/i11/1850-1860
28. Reyes-Salazar, A. Ductility and ductility reduction factor for MDOF systems. Structural Engineering and Mechanics. 2002. 13(4). Pp. 369–385. DOI: 10.12989/sem.2002.13.4.369
29. Karmakar, D., Gupta, V.K. Estimation of strength reduction factors via normalized pseudo-acceleration response spectrum. Earthquake Engineering & Structural Dynamics. 2007. 36(6). Pp. 751–763. DOI: 10.1002/eqe.651
30. Simbort, E. Comparison of nonlinear dynamic analyses performed by both single and multi degree of freedom system. Magazine of Civil Engineering. 2011. 24(6). Pp. 23–27. DOI: 10.5862/MCE.24.5

31. Zerbin, M., Aprile, A., Spacone, E. New formulation of ductility reduction factor of RC frame-wall dual systems for design under earthquake loadings. *Soil Dynamics and Earthquake Engineering*. 2020. 138. DOI: 10.1016/j.soildyn.2020.106279
32. Zerbin, M., Aprile, A., Beyer, K., Spacone, E. Ductility reduction factor formulations for seismic design of RC wall and frame structures. *Engineering Structures*. 2019. 178. Pp. 102–115. DOI: 10.1016/j.engstruct.2018.10.020
33. ISO 3010:2017. Bases for design of structures – Seismic actions on structures. International Organization for Standardization. Geneva, 2017. 60 p.
34. Newmark, N., Rozenbluet, E. *Osnovy seysmostoykogo stroitel'stva*. Moscow: Stroyizdat, 1980. 344 p.
35. Rutman, Y.L., Simport, E. Vybory koefitsiyentov reduktsii seysmicheskikh nagruzok na osnove analiza plasticheskogo resursa konstruksii [Selection of the seismic load reduction factor based on the analysis of the plastic resource of the structure]. *Vestnik grazhdanskikh inzhenerov*. 2011. 27(2). Pp. 78–81. (rus)
36. Simbort, E. Selection procedure of seismic-load reduction factor K1 at a given level of ductility factor. *Magazine of Civil Engineering*. 2012. 27(1). Pp. 44–52. DOI: 10.5862/MCE.27.6
37. Kabantsev, O.V., Useinov, E.S., Sharipov, S. O metodike opredeleniya koefitsiyenta dopuskayemykh povrezhdeniy seysmostoykikh konstruksiy [On the method of determining the coefficient of permissible damage to seismic-resistant structures]. *Vestnik of Tomsk state university of architecture and building*. 2016. 2. Pp. 117–129.
38. Zharnitskiy, V.I., Golda, Y.L., Avdeyeva, S.O. Otsenka seysmostoykosti zdaniy i povrezhdeniy yego konstruksiy na osnove dinamicheskogo rascheta s ucheto plasticheskikh deformatsiy materialov [Assessment of the seismic resistance of buildings and damage to its structure based on dynamic analysis taking into account plastic deformations of materials]. *Seysmostoykoye stroitel'stvo. Bezopasnost' sooruzheniy*. 1999. 4(7–8). (rus)
39. Vatin, N.I., Ivanov, A.Y., Rutman, Y.L., Chernogorskiy, S.A., Shvetsov, K. V. Earthquake engineering optimization of structures by economic criterion. *Magazine of Civil Engineering*. 2017. 76(8). Pp. 67–83. DOI: 10.18720/MCE.76.7
40. Belash, T.A., Yakovlev, A.D. Seismic stability of a tsunami-resistant residential buildings. *Magazine of Civil Engineering*. 2018. 80(4). Pp. 95–103. DOI: 10.18720/MCE.80.9
41. Perel'muter, A.V., Kabantsev, O.V., Pichugin, S.F. *Osnovy metoda raschetnykh predel'nykh sostoyaniy* [Basics of the calculated limit states method]. Moscow: Izd-vo SKAD Soft, Izdatel'stvo ASV, 2019. 237 p.
42. Banon, H., Veneziano, D. Seismic safety of reinforced concrete members and structures. *Earthquake Engineering & Structural Dynamics*. 1982. 10(2). Pp. 179–193. DOI: 10.1002/eqe.4290100202
43. Banon, H., John, M. Biggs Seismic Damage in Reinforced Concrete frame. *Journal of Structural Deviation*. 1981. 107(ST9). Pp. 1713–1729.

Contacts:

Oleg Kabantsev, ovk531@gmail.com

Anatoly Perel'muter, anatolyperel'muter@gmail.com



DOI: 10.34910/MCE.105.14

Thin-walled compressed steel constructions under fire load

M.V. Gravit^a , I.I. Dmitriev^{*b} 

^a Peter the Great St. Petersburg Polytechnic University, St. Petersburg, Russia

^b Graz University of Technology, Graz, Austria

*E-mail: i.i.dmitriev@yandex.ru

Keywords: steel construction, thin walled structures, cold-formed steel, structural design, fire, fire safety, fire protection, fire design

Abstract. The article demonstrates the both theoretical and actual fire resistance limits of the composite I-shaped and box-shaped thin-walled steel structures in compression conditions under the standard fire load. The calculation was based on the Eurocode 3 and finite element modeling of high-temperature fields in SOFiSTiK PC. The experimental tests were carried out on the basis of design data to validate the results of both the calculation and modeling. It is shown that the static part of the calculation of the critical temperature, upon irreversible plastic deformations occur, is solved not completely correctly by means of regulations. In average the calculated critical temperature exceeds the actual one on 50-80 °C. It is shown that the assumption of a critical temperature equals to 350 °C is unreasonably low. The complex graphs of the temperature growth for each steel construction are given according to the paragraphs of normative documents, the finite-element modeling and results of thermocouple indicators for the fire tests. The solution of thermophysical part of calculation according to Eurocode 3 showed good convergence with the results of the experimental data, including the samples with effective fire protection, but strongly depend on the step of calculation. The accurate results were reached only when the time step equals 1 sec. The finite element modeling predicted the correct time to achieve the critical temperature of the tested sample without any additional assumptions. The MBOR-16F material produced by TIZOL JSC was used as a flame protection. This is new material, which has not been previously studied yet. The recommendations on application of the finite element programs are given in the thermophysical part of the fire resistance calculation.

1. Introduction

Bearing and enclosing structures based on the thin-walled galvanized steel profiles are rapidly spreading in construction area. The light gauge steel framing (LGSF or LSF) is widely used in low-rise constructions because of the wide architectural capabilities and excellent technical and economical qualities that allow operating in dynamic conditions of a changing market with maximum accuracy, flexibility and efficiency.

The classical formulas of structural mechanics and theory of elasticity are commonly used in the calculation of steel sections, however taking into account specificity of thin-walled elements such as reduction of the area for some elements under the load or particular work outside of elastic deformation zone.

The LGSF constructions have great perspectives in the construction area [1, 2], but low level of fire resistance and also insufficient research on both unprotected and different types of fire-protective materials for various structures inhibit their implementation. The fire resistance of thin-walled rods is actively discussed throughout the world but despite the numerous investigations of these structures, this issue has not been fully studied and remains relevant nowadays.

Gravit, M.V., Dmitriev, I.I. Thin-walled compressed steel constructions under fire load. Magazine of Civil Engineering. 2021. 105(5). Article No. 10514. DOI: 10.34910/MCE.105.14

© Gravit, M.V., Dmitriev, I.I., 2021. Published by Peter the Great St.Petersburg Polytechnic University



This work is licensed under a CC BY-NC 4.0

The majority of studies connected with the given designs have theoretical character and some experimental data on strength characteristics (including those connected with issues of local and general stability, resistance to compression, bending, torsion in the whole profile and its elements) only at room temperatures [2–7].

It is necessary to pay more attention to measures for maintaining fire safety and ensuring the standard fire resistance of all structures, especially in case of designing metal frame buildings and structures [8, 9]. This problem is extremely relevant for thin-walled structures due to the high thermal conductivity of steel and the small value of the reduced thickness of the cross-section. Rapid temperature rise in the thin-wall cross section will lead to sharp deterioration of mechanical characteristics.

There is a limited number of works devoted to studying the behavior of thin-walled structures under the influence of high temperatures. There are some studies, which show the influence of the value of the limiting deviation of geometric dimensions [10] or influence on the load-bearing capacity by the value of imperfection of structures [11]. Nowadays, EN1993-1.2 [12] does not include a simplified method for calculating of thin-walled structures, but only offers recommendations for cold-formed sections (class 4) to take the critical heating temperature as 350 °C.

The results of this work, as well as examples of similar studies [13–18], show these values to be unreasonably low. For example, under certain boundary conditions, columns and beams (especially composite ones) made of high-strength steel can retain their bearing capacity at temperatures up to 700 °C.

There is a small number of works concerning the fire resistance of LSF, which includes consideration of the regulatory framework, modelling and experimental studies of authors such as N.I. Vatin, M.R. Garifullin [19–21], M.V. Gravit [22, 23], M.Z. Naser [24, 25], W. Chen, J. Ye [26–30], Y. Dias [31, 32]. Only few studies have investigated the behavior of thin-walled steel structures under the fire load, but most of them came to the conclusion that cold-formed steel constructions have higher fire resistance than the Eurocode 3 limit of 350 °C.

The aim of the article is to substantiate the fire resistance limit of composite I-shaped and box-shaped thin-walled steel structures under compression conditions under standard fire load in cases of absence and presence of the effective fire protection.

To achieve this goal, the following tasks are solved:

- 1) Analytical calculation of the structure on the basis of Eurocode 3;
- 2) Finite-element modeling of the high-temperature fields for each complex cross-section in SOFiSTiK PC;
- 3) Fire tests based on theoretical calculation;
- 4) Deviation analysis of both analytical and finite element calculations with thermocouple results in experimental tests.

Profiles were tested under load. Two cross-sections were considered as the tested samples (Table 1):

1. I-shaped section consists of two C-shaped profiles 380×125×30×3.5 connected through a flange 10 mm by bolt fastening.
2. Box-shaped section consists of two Σ -shaped profiles 245×80×20×3 connected through a flange 1.5 mm by bolt fastening.

Profiles were tested both without fire protection and with the use of special flame-protection roll material MBOR-16F produced by TIZOL JSC.

The effective characteristics of the profiles in compression conditions are presented in Table 1.

2. Method

2.1. Analytical calculation

The basic principle of calculation for the steel structures on the fire resistance is to provide necessary and sufficient durability (bearing capacity) throughout the required time period. The most common analytical method is to determine the critical heating temperature of a structure for a given load. The material temperature θ_d during the fire load have to be less (or equal) to the design critical material temperature.

$$\theta_d < \theta_{cr,d} \quad (1)$$

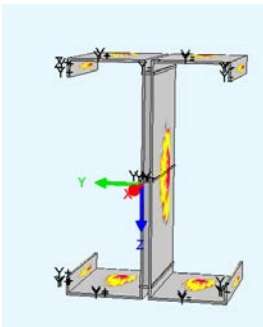
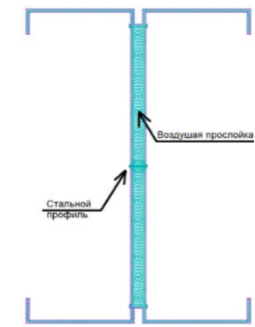
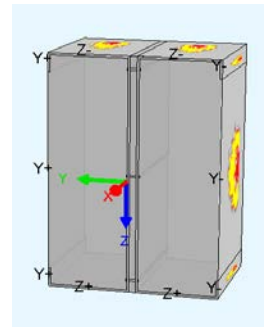
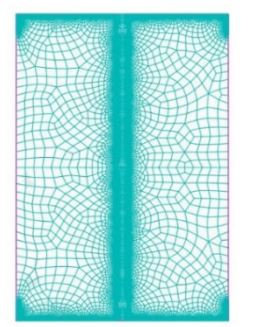
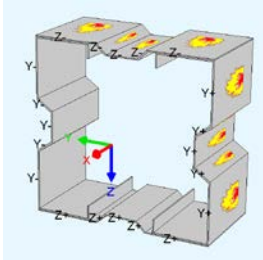
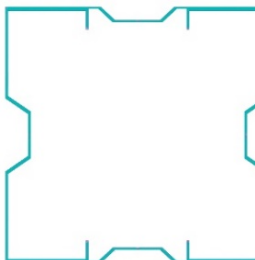
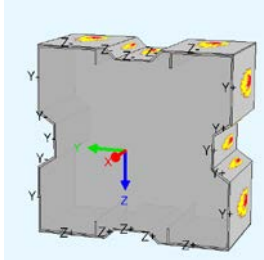
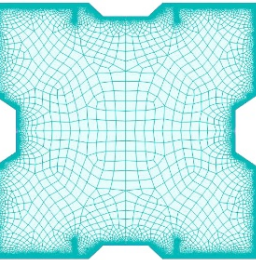
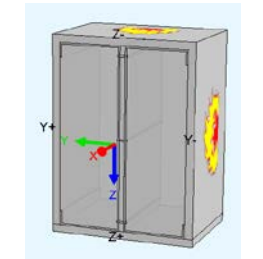

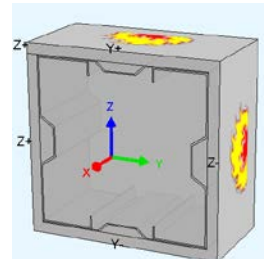
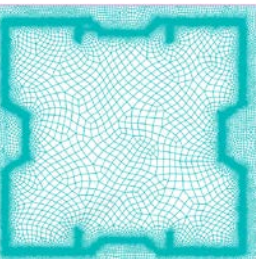
Based on this thesis, the strength calculation determines the reduced bearing capacity after the necessary time. A comparison on time parameters is used to determine the need of the fire protection for each element.

2.2. Modelling

All calculations of a structure are carried out by a method of finite elements on the basis of spatial model. The section elements used for calculation of a steel rod construction are given in Table 3. The Hydra module of the SOFiSTiK software package (ver. 2020) was used for the analysis of temperature distribution over the cross-section of the considered structure. Data input was made using the internal instrumental programming language CADINP in the text editor Teddy. Boundary conditions of the considered models correspond to boundary conditions of the experimental program (temperature is equal to 20 °C, thermal resistance is equal to 9.000 W/K/m²). The grid is quadrangular. Cell size is not constant with higher density in the area of material and model boundaries. Grid resolution is equal at least 0.01 m.

In sections without fire protection two alternative models with and without air gap were considered.

Table 3. Calculated finite element models.

N	Calculated scheme and finite element models			
1				
2				
3				

The properties and geometric dimensions of the structures are set in accordance with the real properties of materials and the samples' overall dimensions. Thermal characteristics of materials specified in the design model. Thermal Conductivity and Heat Capacity of steel are presented in Fig. 1. Numerical dependencies of fire protection are given as equation (2, 3).

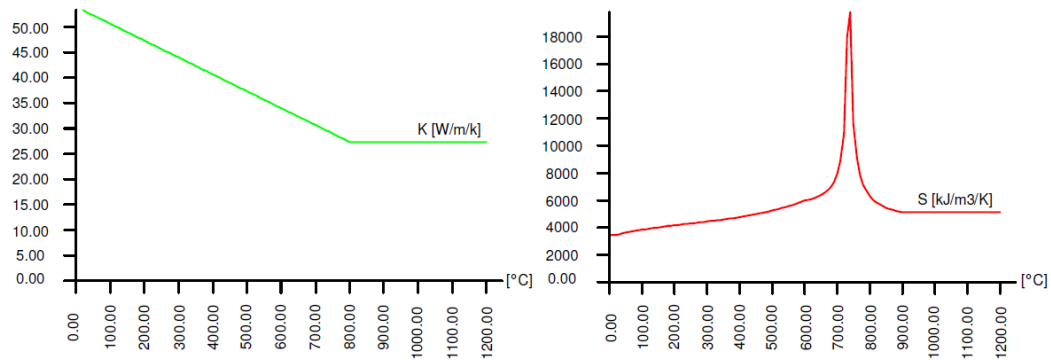


Figure 1. Thermal Conductivity and Heat Capacity of Structural Steel.

Thermal properties of fire protection:

Specific heat capacity c_p of fire protection in dependence of the temperature θ_p (°C):

$$c_p = 582 + 0.63(\theta_p + 273) = 754 + 0.63 \cdot \theta_p \frac{\text{J}}{\text{kg} \cdot \text{K}} \quad (2)$$

Thermal conductivity λ_p of fire protection in dependence of the temperature θ_p (°C) based on an analysis of the manufacturer's data:

$$\lambda_p = 0.0284 + 0.0002 \cdot \theta_a \frac{\text{W}}{\text{m} \cdot \text{K}} \quad (3)$$

Density of fire protection $p_p = 100 \frac{\text{kg}}{\text{m}^3}$.

The system is uniformly heated by the external heat flow; all energy is used to increase the system temperature taking into account its heat capacity. The heating process stops when the temperature at the external boundaries is equalized with the temperature of the external irradiating medium, which corresponds to the standard fire mode and the set temperature in the furnace.

2.3. Fire test

The furnace for fire tests in the Tizol JSC laboratory is a fire chamber lined with fireclay bricks with a loading device for creating compressive forces in the cross-section of the structure and a mechanism for fixation and support. The chrome-aluminum thermocouples were used in the middle section of the structure for the I-beam type and between the profile and the connecting plate for the box type to measure the temperature. The general view of the fire-testing machine in the Fig. 2. The thermocouples of I-shaped construction are located in the center between of C-shaped profiles. The thermocouples of box-shaped sections are in between of steel plates.



Figure 2. Test furnace.

The test method consists of determining the time of the limit state of load-bearing capacity (R) due to caving or critical deformation. The fixed time will be considered the actual fire resistance limit of the structure under test. The R limit state according to the Russian government standard GOST 30247.1-94

comes when vertical deformation reaches one hundredth of the length of the structure, which in our case is 30 mm. The standard fire mode according to the Russian government standard GOST 30247.0-94 and international standard ISO 834 was considered:

$$\theta_g = 20 + 345 \lg(8t + 1) \quad (4)$$

t is time, min;

θ_g is temperature inside the furnace t , °C.

3. Results and Discussion

3.1. The samples without fire protection

3.1.1. Static part of calculation

The bearing capacity of the steel structure is assumed to be preserved after the time t for the specified fire mode when the condition is fulfilled:

$$E_{fi,d} < R_{fi,d} \quad (5)$$

$R_{fi,d}$ is calculated value of the fire resistance at the moment of time $t = 0$.

The calculation is performed taking into account the yield strength analysis for cross sections Class 4 and the effective cross-sectional area of the thin-walled structure. The results are given in according to the static load for each cross-section (Table 1). The critical temperature is a linear interpolation between the calculated load-carrying capacity and actual one [12]. The critical temperature is equal to:

1st sample: $\theta_{cr} = 547.27$ °C (static load is 31.0 t);

2nd sample: $\theta_{cr} = 713.08$ °C (static load is 15.1 t).

3.1.2. Thermophysical part of calculation

3.1.2.1. Analytical solution

The load-bearing capacity is considered exhausted when the material of construction reaches the temperature θ_d with value higher than the critical temperature. The calculation is performed for temperatures with a time interpolation step not exceeding the recommended value until the structure reaches the critical temperature. The temperature growth delta is determined on the basis of the absorbed heat flow taking into account the convection and radiant heat exchange as well as the thermophysical properties of materials.

$$\Delta\theta_{a,t} = k_{sh} \cdot \frac{A_m}{Vc_a\rho_a} \dot{h}_{net}\Delta t$$

The results of the thermophysical calculation by the analytical method are given in the graphical form on the final graph (Fig. 5) at the end of the section. The results depends on the time step and the most accurate results were reached only with the time step equals to 1 sec.

3.1.2.2. Finite element solution with the SOFiSTiK PC (ver. 2020)

The value in the center of the section for the I-shaped and between the steel plates for the box-shaped section was taken as the design temperature.

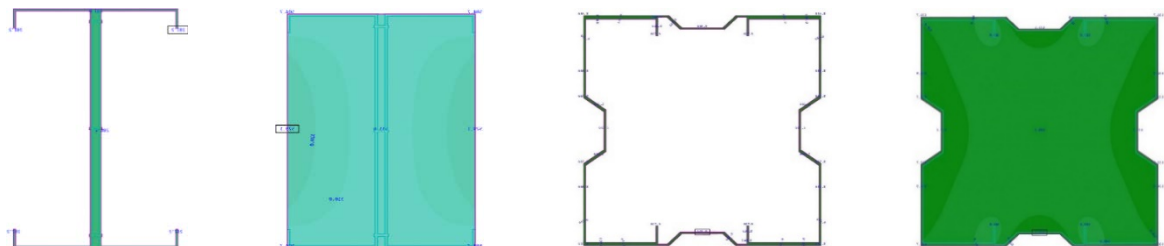


Figure 3. Simulated cross-sections of the samples.













The modeling results are graphs with temperature gradient over the cross-section (Fig. 3). Modeling results for the I-beam section show a significant difference between the sample with and without air gap.

For the box section the accounting of the internal air did not effect on the temperature gradient in the steel parts of the structure.

3.1.3. Fire test

Together with Tizol JSC, fire tests of the unprotected profiles were conducted. There are some photos of the tested samples and a diagram of temperature rise in field tests (Table 4). The tested samples are installed in the furnace chamber arranged according to the Russian government standard GOST 30247.1-94. The load is set at least 30 minutes before the start of the test and is maintained (with an accuracy of $\pm 5\%$) constant throughout the test. Static load for the 1st sample is equal to 31.0 t and for the 2nd sample is equal to 15.1 t.

Table 4. Test samples during the fire load.

No	Test samples		
1			
			
2			
			

Critical deformations of the first specimen were observed at 9 minutes 33 seconds of testing. The maximum average temperature of the specimen is 451.3 °C. For the second specimen, the critical temperature is 649.9 °C and the time to reach the limit state is 12 minutes 10 seconds respectively. The temperature changes of the furnace thermocouples and the specimen are shown in Fig. 4.



Figure 4: Graphic of temperature changes at thermocouples (monitor of test equipment TIZOL JSC):

Red – upper limit of temperature deviation tolerance from ISO curve;
 Blue (dark) – lower limit of temperature deviation tolerance from ISO curve;
 Green – set temperature in the furnace;
 Black – actual average temperature in the furnace;
 Blue – average sample heating temperature.

The accuracy of experimental results is ensured by the sufficient number of thermocouples and the experimental error does not exceed 10 %.

A summary of results of the static, thermophysical calculations and the results of fire tests are presented in Table 5.

Table 5. Summary data on critical temperatures and fire resistance limits for unprotected samples.

Calculation method	Sample 1		Sample 2	
	Calculation	Fire test	Calculation	Fire test
Static calculations				
Critical temperatures °C	547.27	451.3°C	713.08°C	649.9°C
Thermophysical calculations. Fire resistance limits, min (min)				
Analytical solution	8.942		14.790	
Simulation (including air gap)	9.231		15.150	
Calculation with $k_{sh} = 1$ (without shadow effect)	7.055	09:33	–	12:10
Simulation (without air gap)	7.440		15.150	

The calculated fire exposure curves and actual thermocouple values are shown in Fig. 5.

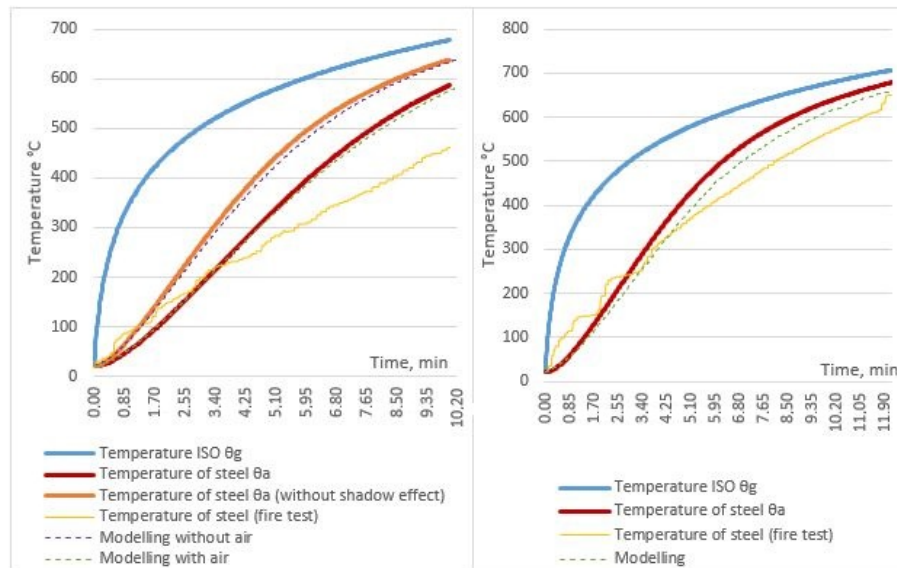


Figure 5. Fire exposure curves (calculated and actual) for unprotected samples.

Finite element modeling has shown excellent convergence with the results of calculations according to European standard EN 1993-1-2. In the case of the I-shaped section, the air gap modeling showed compliance with the curve, which calculation included shading factor, and without air for a conservative solution (without shade effect). The actual high-temperature curve obtained during the fire tests are mostly below than calculated values due to additional convective effects realized in the present tests in the fire chamber, imperfection of thermocouples and other external independent factors, which cannot be completely excluded from the experiment data. In general, the convergence between the calculated and actual curves for the first (I-shaped) sample can be considered satisfactory, and for the second (box-shaped) sample good.

3.2. The samples with fire protection

3.2.1. Thermophysical part of calculation

3.2.1.1. Analytical solution

The area A_p of fire protective material is taken as the area of its inner surface. In case of uniform temperature distribution in the cross-section of the steel protected structure, the temperature increase $\Delta\theta_{a,t}$ for the period of time Δt is determined from the following expression (§4.2.5.2, EN 1993-1-2):

$$\Delta\theta_{a,t} = \frac{A_p}{V} \frac{\lambda_p}{d_p} \cdot \frac{(\theta_{g,t} - \theta_{a,t})}{c_a \rho_a (1 + \frac{\varphi}{3})} \cdot \Delta t - (e^{\frac{\varphi}{10}} - 1) \cdot \Delta\theta_{g,t} \text{ where } \varphi = \frac{c_p \rho_p}{c_a \rho_a} d_p \frac{A_p}{V}$$

A_p is inner surface area of the fire protection material per unit of construction length (m²/m);

V is volume of the unit of construction length (m³/m);

c_a is specific heat capacity of steel depending on temperature (J/(kg K));

c_p is specific heat capacity of fire protective material independent of temperature (J/(kg K));

d_p is thickness of the fire protection (m);

Δt is time interval (s), not exceeding 30 s;

$\theta_{a,t}$ is steel temperature at time t (°C);

$\theta_{g,t}$ is ambient gas temperature at time t (°C);

$\Delta\theta_{g,t}$ is ambient gas temperature increase during the time period Δt (K);

λ_p is thermal conductivity of the fire protection system (W/(m K));

ρ_a is steel density (kg/m³);

ρ_p is fire protective material density (kg/m³).

The Eurocode prescribes to take the specific heat capacity of the fire protective material independent of the temperature. The thermal conductivity varies depend on the temperature of fire protection. The results depends on the iteration step and the most accurate results were reached only with the time step equals to $\Delta t = 1$ sec. The solution of the thermophysical problem by the analytical method is given in graphical form on the final graph at the end of the section.

3.2.1.2. Finite element solution with the SOFiSTiK PC (ver. 2020)

The value in the center of the section was taken as the design temperature. The simulation results are graphs with a temperature gradient across the section (Fig. 6). The internal filling of the profile is air.

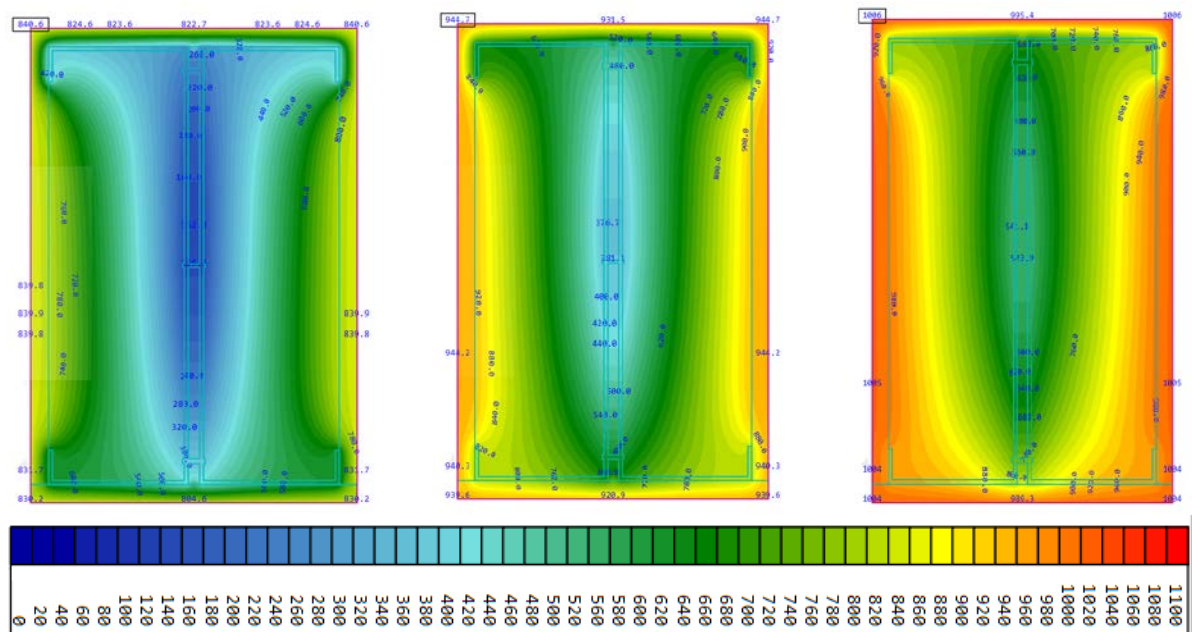


Figure 6. Temperature gradient at 30, 60 and 90 minutes.

Similarly, the fire resistance limit was calculated for the box-shaped section. Calculation point is located between steel plates (Fig. 7).

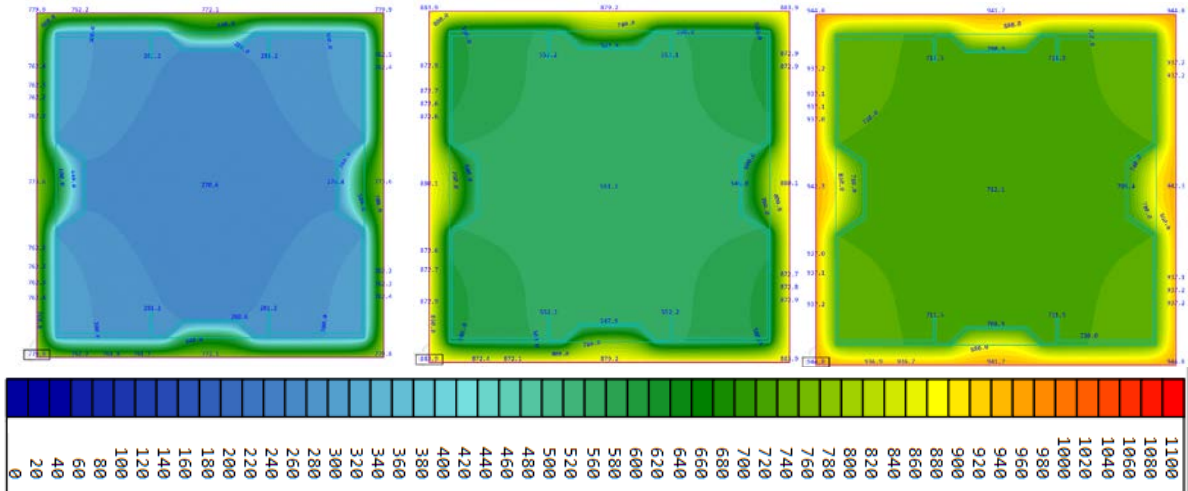


Figure 7. Temperature gradient at 20, 40 and 60 minutes.

3.2.2. Fire test

Together with Tizol JSC, fire tests of the profiles with effective fire protection MBOR-16F were conducted. Below you can see photos of the tested samples and a diagram of temperature rise in field tests.

Table 6. Test samples before and during fire test.

No	Test samples		
1			
			
2			



Figure 8. Graphic of temperature changes at thermocouples on protected samples (monitor of test equipment TIZOL JSC).

Critical deformations of the I-shaped cross section occurred at 74 minutes 27 seconds of testing. The average temperature of the cross section according to the results of thermocouples is 567.7 °C and it is accepted as critical. For the box-shaped section, the critical temperature is 624.5 °C and it reached at 57 minutes 10 seconds. The accuracy of experimental results is ensured by the sufficient number of thermocouples and the experimental error does not exceed 10 %.

The summary table of the solution of the both static, thermophysical problems and results of fire tests are presented in Table 7.

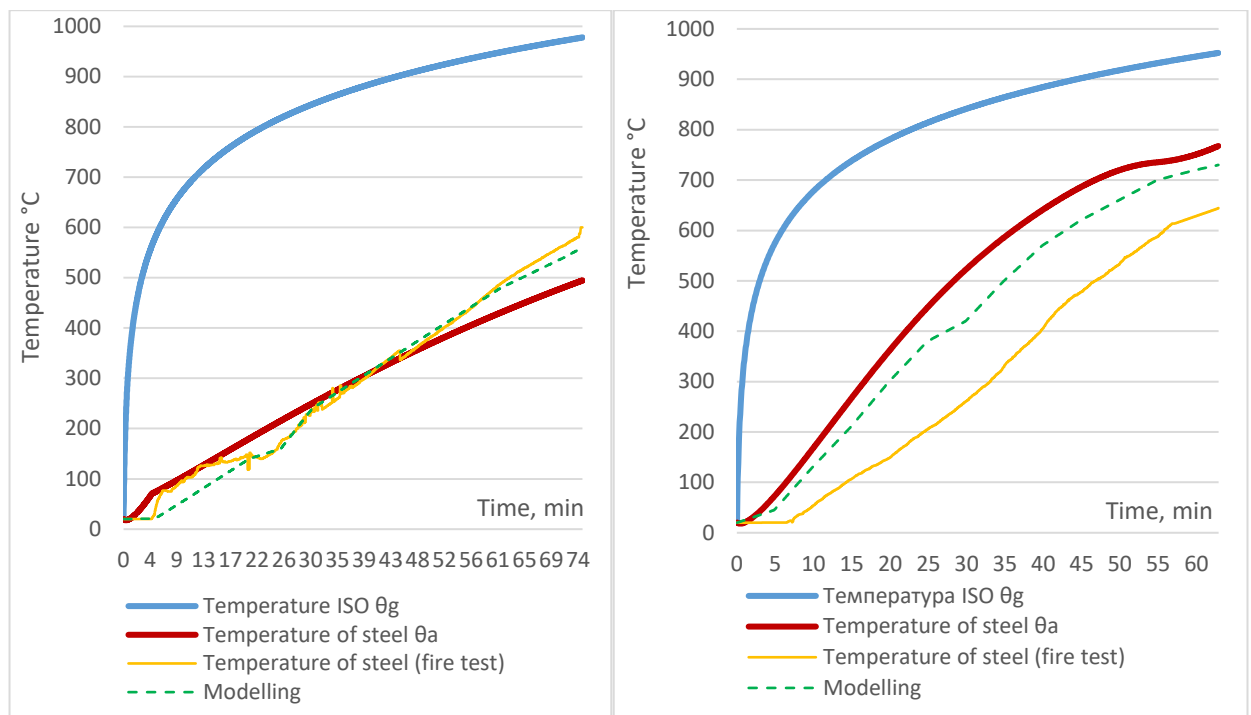


Figure 9. Fire exposure curves (calculated and actual) for protected samples.

Table 7. Data summary on critical temperatures and fire resistance limits for protected samples.

Calculation method	Sample 1		Sample 2	
	Calculation	Fire test	Calculation	Fire test
Static calculation. Critical temperatures, °C				
Critical temperatures °C	547.27°C	567.7°C	713.08°C	624.5°C
Thermophysical calculations. Fire resistance limits, min				
Analytical solution	86	74:27	49	57:10
Simulation	75		58	

The best convergence to the actual results of fire tests was shown by the simulation in the software package. This is due to the implementation of the air gap in the design model inside the fire protected structure and a comprehensive accounting of changing properties of fire protection. Analytical methods do not take these points into account to simplify the calculation scheme.

4. Conclusions

The paper analyzes the applicability of existing numerical methods for calculating of the fire resistance limits of thin-walled constructions, including those with fire protection. It is shown that when solving the static part of the calculation, the assumption of a critical temperature of 350 °C represents a significant underestimation of the structure's bearing capacity. This result is familiar with the studies [13–18] and shows that some complex structures (like 2xC columns or beams) made of high-strength steel can retain their bearing capacity at temperatures up to 500-600°C at least as normal thick-walled construction.

Validation of the static and thermophysical parts of the fire resistance calculation shows that the solution of the thermophysical problem on the basis of finite element modeling of temperature fields is the most precise method to estimate time of critical deformations in accordance to the criteria of structure heating up to the critical temperature. The most applicable C and Σ cross-sections of building structures with and without fire protection are considered.

The recommendations are given on application of program complexes in solving thermophysical problem of fire resistance calculation.

5. Acknowledgments

The research is partially funded by the Ministry of Science and Higher Education of the Russian Federation as part of World-class Research Center program: Advanced Digital Technologies (contract No. 075-15-2020-934 dated or 17.11.2020)

The authors are grateful for providing the results of the fire experiments to the management of TIZOL JSC, and also thank the specialists of Andrometa LLC for providing technical and informational support in carrying out this work.

References

1. Musorina, T.A., Gamayunova, O.S., Petrichenko, M.R., Soloveva, E. Boundary layer of the wall temperature field. *Advances in Intelligent Systems and Computing*. 2020. Vol. 1116. Pp. 429–437.
2. Musorina, T., Gamayunova, O., Petrichenko, M. Thermal regime of enclosing structures in high-rise buildings. *Vestnik MGSU*. 2018. Vol. 13. Pp. 935–943.
3. Dinis, P.B., Camotim, D. Local distortional mode interaction in cold-formed steel lipped channel beams. *Thin-Walled Structures*. 2010. 48. Pp. 771–785.
4. Narayanan, S., Mahendran, M. Ultimate capacity of innovative cold-formed steel columns. *Journal of Constructional Steel Research*. 2003. 59. Pp. 489–508.
5. Pan, C-L, Shan, M-Y. Monotonic shear tests of cold-formed steel wall frames with sheathing. *Thin-Walled Structures*. 2011. 49. Pp. 363–370.
6. Wang, H., Zhang, Y. Experimental and numerical investigation on cold-formed steel C-section flexural members. *Journal of Constructional Steel Research*. 2009. 65. Pp. 1225–1235.
7. Zaharia, R., Dubina, D. Stiffness of joints in bolted connected cold-formed steel trusses. *Journal of Constructional Steel Research*. 2006. 62. Pp. 240–249.
8. Terekh, M., Tretyakova, D. Primary energy consumption for insulating. *E3S Web of Conferences*. 2020. Vol. 157. P. 8.
9. Zemitis, J., Terekh, M. Optimization of the level of thermal insulation of enclosing structures of civil buildings. *MATEC Web of Conferences*. 2018. Vol. 245.
10. Kaitila, O. Imperfection sensitivity analysis of lipped channel column sat high temperatures. *Journal of Constructional Steel Research*. 2002. 58. Pp. 333–351.
11. Ranawaka, T., Mahendran, M. Numerical modeling of light gauge cold-formed steel compression members subjected to distortional buckling at elevated temperatures. *Thin-Walled Structures*. 2010. 48, Pp. 334–344.
12. EN 1993-1-2:2005. Eurocode 3. Design of steel structures Part 1-2. General rules. Structural fire design.
13. Kankanamge, N.D., Mahendran, M. Behaviour and design of cold-formed steel beams subject to lateral-torsional buckling at elevated temperatures. *Thin-Walled Structures*. 2012. 61. Pp. 213–228.
14. Kankanamge, N.D. Structural behaviour and design of cold-formed steel beams at elevated temperatures [Ph.D. Thesis]. Brisbane, Australia: Queensland University of Technology; 2010.
15. Laím, L., Rodrigues, J.P.C. Fire behaviour of cold-formed steel beams for industrial buildings. *Proceedings of the 1st Ibero-Latin-American congress on fire safety, Natal, Brazil*. 2011. 1. Pp. 53–62.
16. Lu, W., Mäkeläinen, P., Outinen, J. Numerical simulation of catenary action in cold-formed steel sheeting in fire. *Proceedings of the fifth international conference on thin-walled structures*. Brisbane, Australia. 2008. Pp. 713–720.

17. Laím, L., Rodrigues, J.P.C., Simões, D.V. Experimental and numerical analysis on the structural behaviour of cold-formed steel beams. *Thin-Walled Structures*. 2013. 72. Pp. 1–13.
18. Gravit, M., Dmitriev, I. Fire Resistance of Loaded I-Section Column from Light Gauge Steel Thin-Walled Profiles. In: Anatolijs B., Nikolai V., Vitalii S. (eds) *Proceedings of ECECE 2019*. ECECE 2019. Lecture Notes in Civil Engineering. 2020. Vol. 70. Springer, Cham.
19. Vatin, N. et al. Simulation of cold-formed steel beams in global and distortional buckling. *Applied Mechanics and Materials*. 2014. Vol. 633–634. Pp. 1037–1041.
20. Garifullin, M., Nackenhorst, U. Computational analysis of cold-formed steel columns with initial imperfections // *Procedia Engineering*. 2015. Vol. 117. No. 1. Pp. 1073–1079.
21. Garifullin, M. et al. Buckling analysis of cold-formed c-shaped columns with new type of perforation. *Advances and Trends in Engineering Sciences and Technologies – Proceedings of the International Conference on Engineering Sciences and Technologies, ESaT 2015*. 2016. Pp. 63–68.
22. Gravit, M., Dmitriev, I., Lazarev, Y. Validation of the Temperature Gradient Simulation in Steel Structures in SOFiSTiK. *Advances in Intelligent Systems and Computing*. 2019. Vol. 983. Pp. 929–938.
23. Gravit, M.V., Nedryshkin, O.V. Full-scale tests for the simulation of fire hazards in the building with an atrium. *Advances and Trends in Engineering Sciences and Technologies III- Proceedings of the 3rd International Conference on Engineering Sciences and Technologies, ESaT 2018*. 2019. Pp. 375–380.
24. Naser, M.Z., Degtyareva, N.V. Temperature-induced instability in cold-formed steel beams with slotted webs subject to shear. *Thin-Walled Struct.* 2019. Vol. 136. Pp. 333–352. DOI: 10.1016/j.tws.2018.12.030
25. Naser, M.Z., Uppala, V.A. Properties and material models for construction materials post exposure to elevated temperatures. *Mech. Mater.* 2020. Vol. 142. DOI: 10.1016/j.mechmat.2019.10329318.
26. Zhou H. et al. Behavior of prestressed stayed steel columns under fire conditions. *Int. J. Steel Struct.* 2017. Vol. 17. No. 1. Pp. 195–204. DOI: 10.1007/s13296-015-0074-4
27. Chen, W. et al. Full-scale experiments of gypsum-sheathed cavity-insulated cold-formed steel walls under different fire conditions. *J. Constr. Steel Res.* Elsevier. 2020. Vol. 164. Pp. 105809. DOI: 10.1016/J.JCSR.2019.105809
28. Chen, W., Ye, J., Zhao, Q. Thermal performance of non-load-bearing cold-formed steel walls under different design fire conditions. *Thin-Walled Struct.* Elsevier. 2019. Vol. 143. Pp. 106242. DOI: 10.1016/J.TWS.2019.106242
29. Chen, W., Ye, J., Li, X. Fire experiments of cold-formed steel non-load-bearing composite assemblies lined with different boards. *J. Constr. Steel Res.* 2019. Vol. 158. Pp. 290–305. DOI: 10.1016/j.jcsr.2019.04.003
30. Chen, W., Ye, J., Li, X. Thermal behavior of gypsum-sheathed cold-formed steel composite assemblies under fire conditions. *J. Constr. Steel Res.* 2018. Vol. 149. Pp. 165–179. DOI: 10.1016/j.jcsr.2018.07.023
31. Chen, W. et al. Improved fire resistant performance of load bearing cold-formed steel interior and exterior wall systems. *Thin-Walled Struct.* Elsevier. 2013. Vol. 73. Pp. 145–157. DOI: 10.1016/J.TWS.2013.07.017
32. Dias, Y., Keerthan, P., Mahendran, M. Fire performance of steel and plasterboard sheathed non-load bearing LSF walls. *Fire Saf. J.* 2019. Vol. 103. Pp. 1–18. DOI: 10.1016/J.FIRESAF.2018.11.005
33. Dias, Y., Mahendran, M., Poologanathan, K. Full-scale fire resistance tests of steel and plasterboard sheathed web-stiffened stud walls. *Thin-Walled Struct.* 2019. Vol. 137. P. 81–93. DOI: 10.1016/j.tws.2018.12.027

Contacts:

Marina Gravit, marina.gravit@mail.ru

Ivan Dmitriev, i.i.dmitriev@yandex.ru



ПОЛИТЕХ

Санкт-Петербургский
политехнический университет
Петра Великого

Инженерно-строительный институт
Центр дополнительных профессиональных программ

195251, г. Санкт-Петербург, Политехническая ул., 29,
тел/факс: 552-94-60, www.stroikursi.spbstu.ru,
stroikursi@mail.ru

**Приглашает специалистов проектных и строительных организаций,
не имеющих базового профильного высшего образования
на курсы профессиональной переподготовки (от 500 часов)
по направлению «Строительство» по программам:**

П-01 «Промышленное и гражданское строительство»

Программа включает учебные разделы:

- Основы строительного дела
- Инженерное оборудование зданий и сооружений
- Технология и контроль качества строительства
- Основы проектирования зданий и сооружений
- Автоматизация проектных работ с использованием AutoCAD
- Автоматизация сметного дела в строительстве
- Управление строительной организацией
- Управление инвестиционно-строительными проектами. Выполнение функций технического заказчика

П-02 «Экономика и управление в строительстве»

Программа включает учебные разделы:

- Основы строительного дела
- Инженерное оборудование зданий и сооружений
- Технология и контроль качества строительства
- Управление инвестиционно-строительными проектами. Выполнение функций технического заказчика и генерального подрядчика
- Управление строительной организацией
- Экономика и ценообразование в строительстве
- Управление строительной организацией
- Организация, управление и планирование в строительстве
- Автоматизация сметного дела в строительстве

П-03 «Инженерные системы зданий и сооружений»

Программа включает учебные разделы:

- Основы механики жидкости и газа
- Инженерное оборудование зданий и сооружений
- Проектирование, монтаж и эксплуатация систем вентиляции и кондиционирования
- Проектирование, монтаж и эксплуатация систем отопления и теплоснабжения
- Проектирование, монтаж и эксплуатация систем водоснабжения и водоотведения
- Автоматизация проектных работ с использованием AutoCAD
- Электроснабжение и электрооборудование объектов

П-04 «Проектирование и конструирование зданий и сооружений»

Программа включает учебные разделы:

- Основы сопротивления материалов и механики стержневых систем
- Проектирование и расчет оснований и фундаментов зданий и сооружений
- Проектирование и расчет железобетонных конструкций
- Проектирование и расчет металлических конструкций
- Проектирование зданий и сооружений с использованием AutoCAD
- Расчет строительных конструкций с использованием SCAD Office

П-05 «Контроль качества строительства»

Программа включает учебные разделы:

- Основы строительного дела
- Инженерное оборудование зданий и сооружений
- Технология и контроль качества строительства
- Проектирование и расчет железобетонных конструкций
- Проектирование и расчет металлических конструкций
- Обследование строительных конструкций зданий и сооружений
- Выполнение функций технического заказчика и генерального подрядчика

По окончании курса слушателю выдается диплом о профессиональной переподготовке
установленного образца, дающий право на ведение профессиональной деятельности

